IN VITRO AND *IN VIVO* IMPACT OF SILICA NANOPARTICLE DESIGN ON BIOCOMPATIBILITY

by

Tian Yu

A dissertation submitted to the faculty of
The University of Utah
in partial fulfillment of the requirements for the degree of

Doctor of Philosophy

Department of Pharmaceutics and Pharmaceutical Chemistry

The University of Utah

August 2012

The University of Utah Graduate School

STATEMENT OF DISSERTATION APPROVAL

The dissertation of **Tian Yu**

has been approved by the following supervisory committee members:

Hamidreza Ghandehari	, Chair	**04/17/2012** Date Approved
Darin Furgeson	, Member	**04/17/2012** Date Approved
David Grainger	, Member	**04/17/2012** Date Approved
Philip Moos	, Member	**04/17/2012** Date Approved
Ilya Zharov	, Member	**04/17/2012** Date Approved

and by **David Grainger** , Chair of the Department of **Pharmaceutics and Pharmaceutical Chemistry**

and by Charles A. Wight, Dean of The Graduate School.

ABSTRACT

Silica nanoparticles (SiO_2) have utility in a wide range of applications, such as biologic delivery platforms, imaging and diagnostic agents, and targeted therapeutic carriers. Recent improvements in regulating the geometry, porosity, and surface characteristics of SiO_2 have further facilitated their biomedical applications. Concerns however remain about the toxic effects of SiO_2 upon exposure to biological systems. The impacts of geometry, porosity, and surface characteristics of SiO_2 on cellular toxicity and hemolytic activity were explored. It was shown that surface characteristics and porosity govern cellular toxicity. The cellular association of SiO_2 increased in the following order: mesoporous SiO_2 (aspect ratio 1, 2, 4, 8) < amine-modified mesoporous SiO_2 (aspect ratio 1, 2, 4, 8) < amine-modified nonporous Stöber SiO_2 < nonporous Stöber SiO_2. Geometry did not seem to influence the extent of SiO_2 cellular association. Hemolysis assay showed that the hemolytic activity was porosity- and geometry-dependent for pristine SiO_2 and surface charge-dependent for amine-modified SiO_2.

The acute toxicity, biodistribution, and pharmacokinetics of SiO_2 of systematically varied geometry, porosity, and surface characteristics were evaluated in immune-competent mice when administered intravenously. Results suggest that *in vivo* toxicity, biodistribution and pharmacokinetics of SiO_2 were mainly influenced by nanoparticle porosity and surface characteristics. The maximum tolerated dose (MTD) increased in the following order: Mesoporous SiO_2 (aspect ratio 1, 2, 8) at 30 – 65 mg/kg

< amine-modified mesoporous SiO_2 (aspect ratio 1, 2, 8) at 100 – 150 mg/kg < unmodified or amine-modified nonporous SiO_2 at 450 mg/kg. The adverse reactions above MTDs were primarily caused by the mechanical obstruction of SiO_2 in the vasculature that led to congestion in multiple vital organs and subsequent organ failure. The nanoparticles were taken up extensively by the liver and spleen. Mesoporous SiO_2 exhibited higher accumulation in the lung than nonporous SiO_2 of similar size. This accumulation was reduced by primary amine modification. Increasing the aspect ratio of amine-modified mesoporous SiO_2 from 1 to 8 resulted in increased accumulation in the lung.

These studies provide critical guidelines in rational design of SiO_2 for nanomedicine applications.

TABLE OF CONTENTS

LIST OF TABLES

LIST OF FIGURES

LIST OF ABBREVIATIONS

Abbreviation	Full name
^{125}I-BHR	Hydrolyzed product of monoiodinated Bolton-Hunter Reagent
^{125}I-SiO_2	Radiolabeled SiO_2
2A	Amine-modified mesoporous nanorods with aspect ratio of 2
4A	Amine-modified mesoporous nanorods with aspect ratio of 4
8A	Amine-modified mesoporous nanorods with aspect ratio of 8
Al	Aluminum
Al_2O_3	Aluminum oxide
ANOVA	Analysis of variance
APTES	(3-aminopropyl)triethoxysilane
APTS	(3-aminopropyl)trimethoxysilane
AR	Aspect ratio
AR2	Mesoporous silica nanorods with aspect ratio of 2
AR4	Mesoporous silica nanorods with aspect ratio of 4
AR8	Mesoporous silica nanorods with aspect ratio of 8
ATP	Adenosine triphosphate
BCA	Bicinchoninic acid
BET	Brunauer–Emmett–Teller method
BJH	Barrett, Joyner, and Halenda method

BSA	Bovine serum albumin
CO_2	Carbon dioxide
C_2H_5OH	Ethanol
CPM	Counts per minute
CTAB	Cetyltrimethylammonium bromide
DETA	Diethylenetriamine
DI	De-ionized
DLS	Dynamic light scattering
DMEM	Dulbecco's modified eagle medium
DNA	Deoxyribonucleic acid
D-PBS	Dulbecco's phosphate buffered saline
EPR	Enhanced permeability and retention
EU	Endotoxin unit
FBS	Fetal bovine serum
f-SWNT	Functionalized single wall carbon nanotubes
FTIR	Fourier transform infrared spectroscopy
H&E	Hematoxylin and eosin staining
$HAuCl_4 \cdot 3H_2O$	Gold chloride
HF	Hydrofluoric acid
HSSS	Hybrid solid silica sphere
IACUC	Institutional Animal Care and Use Committee
IC_{50}	Concentration leading to 50% inhibition on cell growth
ICP-MS	Inductively coupled plasma mass spectrometry

IP	Intraperitoneal
IV	Intravenous
LAL	Limulus amebocyte lysate test
LC_{10}	Concentration leading to 10% hemolysis
LD_{50}	Lethal dose that causes 50% animal death
LDH	Lactate dehydrogenase
M#	Mouse #
MA	Amine-modified mesoporous nanospheres
MCDA	Multi-criteria decision analysis
MCM-41	Mobil Composite Material 41
Meso S	Mesoporous silica nanospheres
MHSN	Mesoporous hollow silica nanoparticle
MPTMS	(3-mercaptopropyl)trimethoxysilane
MTD	Maximum tolerated dose
MTT	3-(4,5-Dimethylthiazol-2-yl)-2,5-diphenyltetrazolium bromide
$NaBH_4$	Sodium borohydride
NH_4OH	Ammonium hydroxide
PBS	Phosphate buffered saline
PDI	Polydispersity index
PEG	Poly(ethylene glycol)
PLGA	Poly(lactic-co-glycolic acid)
QSAR	Quantitative structure-activity relationship

RBC	Red blood cells
RES	Reticulo-endothelial system
RGDfK	Arg-Gly-Asp-D-Phe-Lys
RNA	Ribonucleic acid
RPM	Revolutions per minute
SA	Amine-modified Stöber nanoparticles
SD	Standard deviation
SEM	Scanning electron microscopy
$SiCl_4$	Tetrachlorosilane
SiO_2	Silica nanoparticles
SNT	Silica nanotube
Stöber	Nonporous silica nanospheres
TEM	Transmission electron microscopy
TEOS	Tetraethyl orthosilicate
Tg	Glass transition temperature
TLC	Thin layer chromatography
TNF	Tumor necrosis factor
TSD	*N*-[3-(trimethoxysilyl)propyl] ethylenediamine
V_{ss}	Volume of distribution at steady state
WST-8	2-(2-methoxy-4-nitrophenyl)-3-(4-nitrophenyl)-5-(2,4-disulfophenyl)-2H-tetrazolium
XRD	X-ray diffraction

ACKNOWLEDGMENTS

I would like to express my whole-hearted appreciation for having been a member of the Department of Pharmaceutics and Pharmaceutical Chemistry at the University of Utah and working on an explorative and exciting project. It has been a great journey to learn how to conduct science and challenge my potential limits. The most important things I learned through this experience were that interest is the major driving force which inspires me to accomplish goals and we should enjoy life as even daily, usual things have their own precious meanings.

I owe great gratitude to my graduate advisor, Dr. Hamid Ghandehari, who is very diligent and goal-driven. He trained me to build my leadership skills and establish the project in the lab, and gave me the opportunity to conduct research independently. I am very grateful to him for creating opportunities for me to get exposed to the forefront of the scientific field and instilling and growing my professional instincts and skills.

I thank all my committee members, Drs. David Grainger, Darin Furgeson, Ilya Zharov, and Philip Moos, who generously served on my committee and provided valuable insights and comments for my research.

I was admitted to University of Maryland, Baltimore before I moved to this university. I would like to express my sincere thanks to my former mentors in Maryland, Dr. Anjan Nan and the late Dr. Angelika Burger, for their generous teachings about the knowledge of pharmaceutical sciences. That was a starting point for me to take on this

journey and I still remember the excitement I had at that time. The passaging of knowledge is the greatest thing I've ever known about in science or in life.

I am obligated to acknowledge Dr. Sajo Naik, a former professor of engineering at the University of Utah, for his kindness of sharing his in-depth research experience of nanoparticle synthesis with me. His voluntary input was a turning point in my research.

I would like to express my genuine thanks to Dr. Alexander Malugin, who had critical conversations with me about design and trouble-shooting of *in vitro* experiments. Without his input in my research, I could never have finished my project on time. I thank Dr. Khaled Greish for his input in our collaborative *in vivo* work.

I am deeply thankful to Shanshan Liu (M. D.) and Jinping Guo (M. D.) at the University of Utah for their experience and knowledge about histology. I learned a lot from them and their input greatly facilitated the progress of my experiments.

I also would like to give my thanks to all my lab members, whom I closely worked with or consulted about my research project, for their unselfish sharing of knowledge, expertise, and experience.

Last but not the least, I want to give my deepest thanks to my family and friends, who unconditionally and continuously provided me their love and support. They were always at my side and no words could express my gratefulness to them.

CHAPTER 1

INTRODUCTION

1.1 Introduction

Silica-based nanomaterials have attracted much attention in biomedical applications as cell markers, gene transfection agents, imaging moieties, as well as drug carriers [1-5]. They possess a variety of unique properties, such as ease of synthesis, availability of surface modification, robust mechanical properties, and relatively inert chemical composition [6, 7]. Recent advances in manipulating the geometry, porosity, and surface characteristics of silica nanoparticles (SiO_2) have further enabled their utility in nanomedicine [8-11]. Despite these advantages, the influence of physicochemical factors such as geometry, pore size, and surface functional groups of SiO_2 still needs to be carefully examined for successful utility of these constructs in biomedical applications [12].

The variations in physicochemical characteristics play a crucial role in determining the compatibility of SiO_2 with biological systems and hence their development for diagnostic or therapeutic applications [13-17]. Previous studies have revealed that biodistribution of nonporous SiO_2 varies according to particle size and only smaller SiO_2 of 70 nm in diameter accumulated in the placenta and fetus of pregnant mice compared to 300 nm or 1,000 nm nanoparticles [13]. Other studies on particle size

and toxicity relationship using a similar set of nonporous SiO_2 demonstrated that 70 nm nanoparticles induced liver injury at 30 mg/kg animal weight while 300 nm or 1,000 nm SiO_2 exerted no adverse effect at 100 mg/kg [14, 15]. The difference in the toxicity level could be due to the differential biodistribution pattern of SiO_2 in mice since studies have shown that smaller SiO_2 tend to have higher accumulation in the reticulo-endothelial system (RES) and cause specific organ toxicity [16]. It has also been shown that surface modification of 70 nm SiO_2 by either primary amine or carboxylic moieties prevent fetotoxicity even though the modified SiO_2 were found in placenta and fetus of mice [13]. The surface modification of SiO_2 could also alleviate liver injury and avoid hepatic fibrosis [17]. Thus, it is of great interest to systematically evaluate the interdependent influence of geometry, porosity, and surface functionality on toxicity of SiO_2.

Recent studies have demonstrated that geometry of nanocarriers can influence their circulation half-life and other pharmacokinetic parameters [18-21]. For example, pegylated polymeric micelles of long, filamentous shape persisted in the circulation up to 1 week after intravenous injection, approximately 10 times longer than their spherical counterparts [18]. It was suggested that the spherical micelles were taken up by the cells more readily than the long filaments under fluid flow conditions since the cellular entry of the latter was opposed by flow [18]. Cyclic polymers composed of α-cholo-ε-caprolactone and ε-caprolactone, which had molecular weights greater than the renal threshold, showed longer blood circulation time in mice than linear polymers of similar composition and comparable molecular weight [19]. This effect was attributed to the fact that linear polymers traverse nanopores in glomeruli by end-on motion of one chain end, while cyclic polymers transit through by entering the pores with two chain segments

since they lack chain ends [19]. While the studies above relate to more flexible polymeric systems, the influence of geometry on biological fate has also been studied for more rigid nanoparticles. For example, it has been shown that the anti-intercellular adhesion molecule 1 elliptical polystyrene disks (0.1 × 1 × 3 μm) had higher endothelial targeting specificity in the lung than spheres of different sizes (0.1, 1, 5 μm) [20]. Further, it has previously been demonstrated that pegylated gold nanorods (10 × 45 nm, 1.13 mV) exhibited longer blood circulation half-life and higher tumor accumulation than pegylated gold nanospheres (50 nm, -27.1 mV) in orthotopic ovarian tumor xenograft mice [21]. These studies suggest that geometry and carrier architecture can influence the *in vivo* behavior of nanoscale platforms. However, much needs to be examined in this area since factors such as porosity and surface characteristics can further influence biodistribution and pharmacokinetics.

This dissertation is centered on the systematic variation of SiO_2 geometrical features, porosity, and surface chemistry to understand their influence on nanoparticle toxicity and biodistribution. The results can provide baseline information about how to rationally engineer SiO_2 to minimize toxicity. In the long term, such an approach can be used for the design and development of advanced drug delivery systems involving SiO_2.

1.2 Hypothesis and aims of this dissertation

The global hypothesis of this dissertation is that by tailoring the shape, porosity, and surface functionality of SiO_2, their *in vitro* and *in vivo* toxicity, biodistribution, and pharmacokinetics can be altered to reduce adverse effects in potential biomedical applications. To test this hypothesis, the following Specific Aims were undertaken (Figure 1.1):

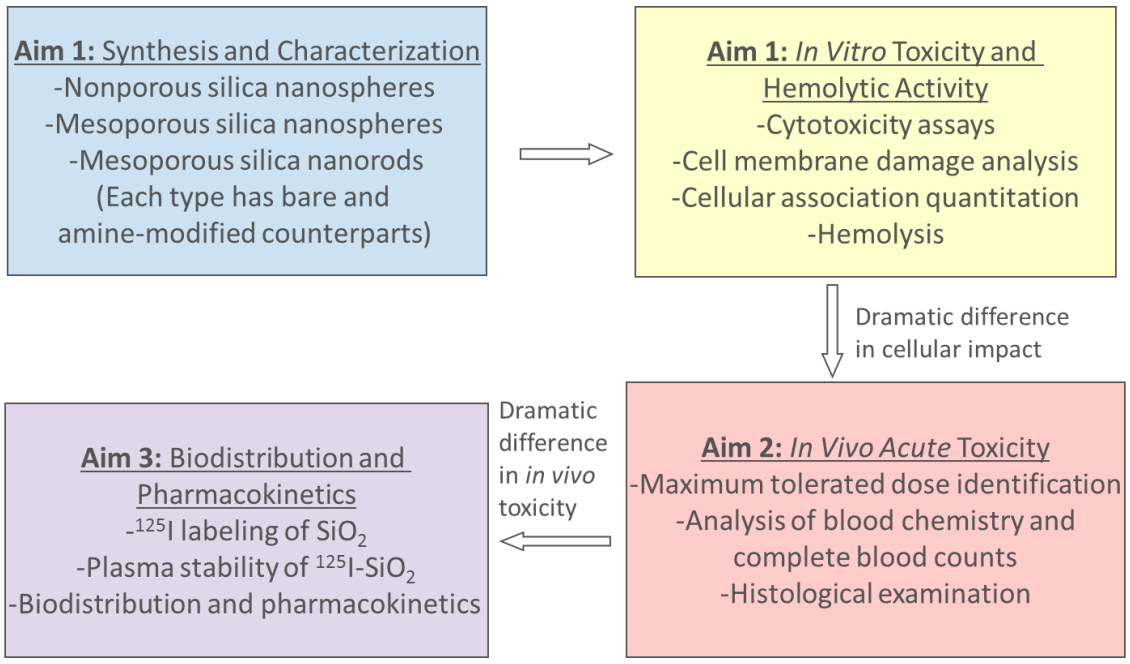

Figure 1.1 Specific Aims and corresponding experimental design for the dissertation.

Specific Aim 1: To synthesize and characterize nonporous and mesoporous SiO_2 of distinct geometrical features and surface properties, and to evaluate their cellular toxicity and blood biocompatibility.

Specific Aim 2: To evaluate the *in vivo* toxicity of systemically injected-SiO_2 with different shapes, porosity, and surface chemistry through maximum tolerated dose identification, hematology, and histology.

Specific Aim 3: To evaluate the biodistribution and pharmacokinetics of SiO_2 of various physicochemical features and to relate these parameters with *in vitro* and *in vivo* toxicity.

1.3 Scope and organization of this dissertation

Chapter 2 of this dissertation provides a current review of the literature on development of nanotoxicology as a field with a focus on the toxicity of SiO_2 on biological systems. The origin of nanotoxicology and its implication in public health and research application, multiple nanoparticle systems toxicity issues, and factors that contribute to the onset of toxicity are discussed with focus on SiO_2 physicochemical parameters and the resultant toxicity impact. Chapter 3 describes the synthesis and characterization of a series of nonporous and mesoporous SiO_2 with distinct geometrical features and surface properties and evaluates their effects on cellular toxicity and blood biocompatibility [22]. In Chapter 4, maximum tolerated doses (MTDs) of selected SiO_2 were determined *in vivo* and the adverse reactions beyond MTDs were examined and related with the physicochemical properties of SiO_2 [23]. In Chapter 5, the biodistribution and pharmacokinetics of SiO_2 as a function of geometry, porosity, and surface characetristics in immune-competent CD-1 mice was discussed and correlated with *in*

vitro and *in vivo* toxicity [24]. In Chapter 6, the key findings of this dissertation are summarized and comments are made about the future direction for this research. In Appendix A, the cytotoxicity of silica nanotubes (SNTs) was evaluated in a pilot study as a function of size and surface charge. Appendix B describes synthesis and characterization of silica-coated gold nanorods as alternative elongated-shaped silica nanomaterials to study the effect of SiO_2 shape on biological systems.

1.4 References

[1] C. Barbé, J. Bartlett, L. Kong, K. Finnie, H. Lin, M. Larkin, S. Calleja, A. Bush, G. Calleja, Silica particles: a novel drug-delivery system, Adv. Mater., 16 (2004) 1-8.

[2] M. Liong, J. Lu, M. Kovochich, T. Xia, S.G. Ruehm, A.E. Nel, F. Tamanoi, J.I. Zink, Multifunctional inorganic nanoparticles for imaging, targeting, and drug delivery, ACS Nano, 2 (2008) 889-896.

[3] J.L. Vivero-Escoto, Slowing, II, B.G. Trewyn, V.S. Lin, Mesoporous silica nanoparticles for intracellular controlled drug delivery, Small, 6 (2010) 1952-1967.

[4] J. Lu, M. Liong, Z. Li, J.I. Zink, F. Tamanoi, Biocompatibility, biodistribution, and drug-delivery efficiency of mesoporous silica nanoparticles for cancer therapy in animals, Small, 6 (2010) 1794-1805.

[5] L. Li, F. Tang, H. Liu, T. Liu, N. Hao, D. Chen, X. Teng, J. He, *In vivo* delivery of silica nanorattle encapsulated docetaxel for liver cancer therapy with low toxicity and high efficacy, ACS Nano, 4 (2010) 6874-6882.

[6] C.-P. Tsai, C.-Y. Chen, Y. Hung, F.-H. Chang, C.-Y. Mou, Monoclonal antibody-functionalized mesoporous silica nanoparticles (MSN) for selective targeting breast cancer cells, J. Mater. Chem., 19 (2009) 5737–5743

[7] S.-H. Cheng, C.-H. Lee, M.-C. Chen, J.S. Souris, F.-G. Tseng, C.-S. Yang, C.-Y. Mou, C.-T. Chen, L.-W. Lo, Tri-functionalization of mesoporous silica nanoparticles for comprehensive cancer theranostics-the trio of imaging, targeting and therapy, J. Mater. Chem., 20 (2010) 6149–6157.

[8] A. Nan, X. Bai, S.J. Son, S.B. Lee, H. Ghandehari, Cellular uptake and cytotoxicity of silica nanotubes, Nano Lett, 8 (2008) 2150-2154.

[9] S.J. Son, X. Bai, A. Nan, H. Ghandehari, S.B. Lee, Template synthesis of multifunctional nanotubes for controlled release, J Control Release, 114 (2006) 143-152.

[10] C.-C. Chen, Y.-C. Liu, C.-H. Wu, C.-C. Yeh, M.-T. Su, Y.-C. Wu, Preparation of fluorescent silica nanotubes and their application in gene delivery, Adv. Mater., 17 (2005) 404-407.

[11] F. Buyukserin, C.D. Medley, M.O. Mota, K. Kececi, R.R. Rogers, W. Tan, C.R. Martin, Antibody-functionalized nano test tubes target breast cancer cells, Nanomedicine (Lond), 3 (2008) 283-292.

[12] S.P. Hudson, R.F. Padera, R. Langer, D.S. Kohane, The biocompatibility of mesoporous silicates, Biomaterials, 29 (2008) 4045-4055.

[13] K. Yamashita, Y. Yoshioka, K. Higashisaka, K. Mimura, Y. Morishita, M. Nozaki, T. Yoshida, T. Ogura, H. Nabeshi, K. Nagano, Y. Abe, H. Kamada, Y. Monobe, T. Imazawa, H. Aoshima, K. Shishido, Y. Kawai, T. Mayumi, S. Tsunoda, N. Itoh, T. Yoshikawa, I. Yanagihara, S. Saito, Y. Tsutsumi, Silica and titanium dioxide nanoparticles cause pregnancy complications in mice, Nat Nanotechnol, 6 (2011) 321-328.

[14] H. Nishimori, M. Kondoh, K. Isoda, S. Tsunoda, Y. Tsutsumi, K. Yagi, Silica nanoparticles as hepatotoxicants, Eur J Pharm Biopharm, 72 (2009) 496-501.

[15] X. Lu, Y. Tian, Q. Zhao, T. Jin, S. Xiao, X. Fan, Integrated metabonomics analysis of the size-response relationship of silica nanoparticles-induced toxicity in mice, Nanotechnology, 22 (2011) 055101.

[16] G. Xie, J. Sun, G. Zhong, L. Shi, D. Zhang, Biodistribution and toxicity of intravenously administered silica nanoparticles in mice, Arch Toxicol, 84 (2010) 183-190.

[17] K. Isoda, T. Hasezaki, M. Kondoh, Y. Tsutsumi, K. Yagi, Effect of surface charge on nano-sized silica particles-induced liver injury, Pharmazie, 66 (2011) 278-281.

[18] Y. Geng, P. Dalhaimer, S. Cai, R. Tsai, M. Tewari, T. Minko, D.E. Discher, Shape effects of filaments versus spherical particles in flow and drug delivery, Nat Nanotechnol, 2 (2007) 249-255.

[19] N. Nasongkla, B. Chen, N. Macaraeg, M.E. Fox, J.M. Frechet, F.C. Szoka, Dependence of pharmacokinetics and biodistribution on polymer architecture: effect of cyclic versus linear polymers, J Am Chem Soc, 131 (2009) 3842-3843.

[20] S. Muro, C. Garnacho, J.A. Champion, J. Leferovich, C. Gajewski, E.H. Schuchman, S. Mitragotri, V.R. Muzykantov, Control of endothelial targeting and intracellular delivery of therapeutic enzymes by modulating the size and shape of ICAM-1-targeted carriers, Mol Ther, 16 (2008) 1450-1458.

[21] Arnida, M.M. Janat-Amsbury, A. Ray, C.M. Peterson, H. Ghandehari, Geometry and surface characteristics of gold nanoparticles influence their biodistribution and uptake by macrophages, Eur J Pharm Biopharm, 77 (2011) 417-423.

[22] T. Yu, A. Malugin, H. Ghandehari, Impact of silica nanoparticle design on cellular toxicity and hemolytic activity, ACS Nano, 5 (2011) 5717-5728.

[23] T. Yu, K. Greish, L.D. McGill, A. Ray, H. Ghandehari, Influence of geometry, porosity, and surface characteristics of silica nanoparticles on acute toxicity: their vasculature effect and tolerance threshold, ACS Nano, 6 (2012) 2289-2301.

[24] T. Yu, D. Hubbard, A. Ray, H. Ghandehari, *In vivo* biodistribution and pharmacokinetics of silica nanoparticles as a function of geometry, porosity and surface characteristics, J Control Release, accepted (2012).

CHAPTER 2

LITERATURE BACKGROUND

2.1 Introduction

Advances in nanotechnology have led to the development of novel nanoparticles for pharmaceutical applications aimed at improving diagnosis and treatment of diseases and the quality of human life [1, 2]. Many nanoparticle systems have found uses in drug delivery, imaging, and other applications [2]. However, the fast growing pace in nanotechnology has also brought to bear short- and long-term safety issues [3, 4]. From this perspective, it is essential to carefully study the toxicity profiles of nanoparticles and how such adverse effects relate to their function.

Recent advances in synthesis and fabrication have enabled the production of nanoparticles with high control over geometry, porosity, and surface characteristics, and other physicochemical features [5]. By utilizing top-down or bottom-up synthetic strategies, nanoparticles with distinct shape, porosity, or surface functionality are readily produced at a large scale in a time-efficient manner [6]. Considering their potential applications in various areas, it is intuitive to evaluate the toxicity aspects and to engineer the physicochemical properties of nanoparticles to minimize such effects.

2.2 Nanotoxicology

Nanomaterials such as silica and titanium dioxide nanoparticles and carbon nanotubes are widely used in electronics, catalysis, foods, cosmetics, and drug delivery [7, 8]. The increasing use of nanomaterials has raised concerns for their impact on public health [9]. It has been reported, for example, that carbon nanotubes can induce mesothelioma-like lesions in mice, similar to those induced by asbestos [10]. It is necessary to evaluate the toxicity of nanoparticles which can also help to identify the origins of certain human diseases due to nanoparticle exposure.

2.2.1 Origin

2.2.1.1 Environmental hazards

With the industrialization of modern society, human beings are subject to exposure of nanosized particulates either by occupational exposure or from the environment [11]. Contamination in the ambient environment is an important public health issue. Epidemiologic studies reveal that increased level of ambient nanoparticles is associated with an increase in the incidence of respiratory and cardiovascular diseases [12]. However, it is particularly difficult to identify a direct linkage between a specific human disease and exposure to ambient particulates since their composition, size, and other physicochemical parameters are complicated and variable. By engineering nanoparticles and correlating structure and physicochemical properties with biological effect, it is possible to find correlations between potential adverse effects to humans on one hand and particulate exposure on the other. For example, it has been reported that inhalation of manufactured SiO_2 causes pulmonary and cardiovascular symptoms in mice, including pulmonary inflammation, myocardial ischemic damage, arterio-ventricular

blockage, increase in fibrinogen concentration and blood viscosity [13]. The risk of physiological damage increases in the order of adult < young < old individuals, indicating the increased susceptibility of older populations to diseases upon exposure to environmental hazards [13]. Studies of nanoparticles with known parameters may provide information about the correlation between the epidemiologic findings and the effects of environmental particulates on human health.

2.2.1.2 Nanoparticles as delivery systems

Previous research on toxicology of nanosized materials is largely focused on the effects of nanoparticles that enter the body accidentally. Nowadays, toxicology studies have also been applied to major drug and imaging agent carriers that are used by patients or in clinical trials. A number of pharmaceutical products that use nanoparticulates have been approved for commercial production, or are at different stages of clinical trials (Table 2.1) [14], or are undergoing preclinical studies (Table 2.2) [15]. The emergence of novel methods to fabricate or manipulate nanoparticles is accompanied by the recognition of underlying toxicity issues associated with their utilization. These include toxicity mechanisms that are related to frustrated phagocytosis, changes in protein structure and function, immune activation, fibrogenesis and tissue remodeling, blood clotting, vascular injury, neurotoxicity, and other adverse effects (Table 2.3) [16]. Research shows that the compatibility of nanoparticles with biological systems is mainly determined by their physicochemical properties [17]. Modifying these factors can effectively change the toxicity of nanoparticles and potentially make them promising platforms for biomedical applications.

Table 2.1 Examples of nanoparticles for diagnostic and therapeutic applications which have been approved by the FDA or are currently in clinical trials (adapted from [14])

Nanoparticle/drug	Indication	Product	FDA	Company
PEGylated liposome/doxorubicin hydrochloride	Ovarian cancer	Doxil	Approved Nov. 1995	OrthoBiotech
Nanoparticulate albumin/paclitaxel	Various cancers	Abraxane	Approved Jan. 2005	American Pharmaceutical Partners
Cyclodextrin nanoparticle	Solid tumors	Cyclosert	Phase I	Insert Therapeutics
Silver nanocrystalline	Antimicrobial	Acticoat	Approved May 2005	Smith and Nephew
Iron oxide	Tumor imaging	Combidex	Phase III	Advanced Magnetics
Gold nanoparticles/TNF	Solid tumors	Aurimune	Phase II	CytImmune Sciences
Gold nanoshell	Solid tumors	AuroLase	Phase I	Nanospectra Biosciences
Quantum dot	Melanoma	Cornell dot	Phase I	Hybrid Silica Technologies

TNF, Tumor necrosis factor

Table 2.2 Representative nanoparticles in preclinical studies (adapted from [15])

Nanoparticle	Physicochemical properties	Animals	Administration routes	Experimental time
Gold	10, 50, 100, 250 nm	Mice	IV	24 h
Silver	2 nm, BSA coated	Rats	IP	7 d
Ferric oxide	144 nm	Mice	Pulmonary	50 d
Quantum dots	13 nm	Mice	IV	28 d
Carbon	29.7 nm	Rats	Pulmonary	24 h
Silica	20 nm, -25.5 mV, PEG modified	Mice	IV	24 h
Polystyrene	20, 100, 1000 nm, surface carboxylated	Mice	IV Pulmonary	90 d
PLGA	133.5 nm, -54.2 mV	Mice	IV	24 h
f-SWNTs	1 × 300 – 1000 nm, ammonium functionalized	Mice	IV	24 h

PLGA, poly(lactic-co-glycolic acid); f-SWNTs, functionalized single wall carbon nanotubes; BSA, bovine serum albumin; PEG, poly(ethylene glycol); IV, intravenous; IP, intraperitoneal.

Table 2.3 Experimental summary of major toxicological pathways which are associated with nanomaterial toxicity (adapted from [16])

Toxicological pathway	**Nanomaterials**
Membrane damage/leakage/thinning	Cationic nanoparticles
Protein binding/unfolding responses/loss of function/fibrillation	Metal oxide nanoparticles, polystyrene, dendrimer, carbon nanomaterials
DNA cleavage/mutation	Nano-Ag
Mitochondrial damage	Ultrafine particles, cationic nanoparticles
Lysosomal damage: proton pump activity/lysis/frustrated phagocytosis	Ultrafine particles, cationic nanoparticles, carbon nanotubes
Inflammation: signaling cascades/cytokines/chemokines/adhesion	Metal oxide nanoparticles, carbon nanotubes
Fibrogenesis and tissue remodeling injury	Carbon nanotubes
Blood platelet, vascular endothelial and clotting abnormalities	SiO_2
Oxidative stress injury, radical production, glutathione depletion, lipid peroxidation, membrane oxidation, protein oxidation	Ultrafine particles, carbon nanotubes, metal oxide nanoparticles, cationic nanoparticles

2.2.2 Current stage and focus of nanotoxicology

To date, the development of nanotoxicology has been centered on elucidating the relationship of nanoparticle physicochemical properties with their biological activity and correlation of *in vitro* observation with *in vivo* outcome (Figure 2.1) [16]. With an increased recognition of the need for effective approaches to control the impact of emerging nanotechnologies on the environment and human health, it is crucial to develop a framework to link research on the risk associated with nanotechnology to the decision-making needs of manufacturers, regulators, consumers, and other stake holder groups (Figure 2.2) [18]. Considering the potentially high uncertainties associated with nanoparticles, research efforts should be directed to providing information that is most meaningful to these groups. The research on nanotoxicology should be prioritized in the direction that is responsive to the recommendations on managing risks and impact of nanomaterials on the environment and human health.

2.3 Nanosystems in biomedical application and their implication in toxicity

The rapid developments in nanotechnology have raised the public‟s awareness of safety threats of the nanoparticle systems. The research community has stepped up efforts in looking into the toxicity issues of nanoparticles that are frequently used in industrial or academic settings [19, 20]. However, certain key issues should be realized for the fair judgment and decision making about nanoparticle utilization with a focus on its pharmaceutical application. First, nanoparticles could be administered through various routes, such as oral, topical, intravenous, intraperitoneal, epidural, *etc*. The toxicity of nanoparticles could be greatly varied if the delivery route is different. For example,

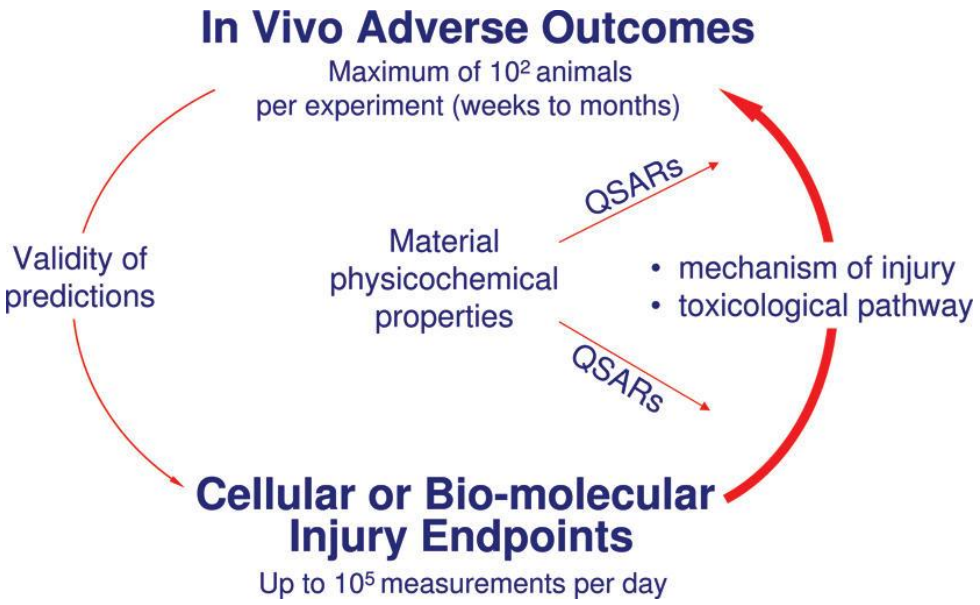

Figure 2.1 Elements of predictive toxicological paradigm for nanomaterial hazard testing. A predictive toxicological approach is defined as establishing and using *in vitro* mechanisms and pathways of injury that are directly related to the physiochemical properties of nanomaterials as well as to disease mechanisms *in vivo*. The *in vivo* output is used to validate the *in vitro* screening method as being "predictive" and therefore valid for screening large batches of materials to obtain quantitative structure-activity relationships (QSARs) that can also be applied to *in vivo* observations [16].

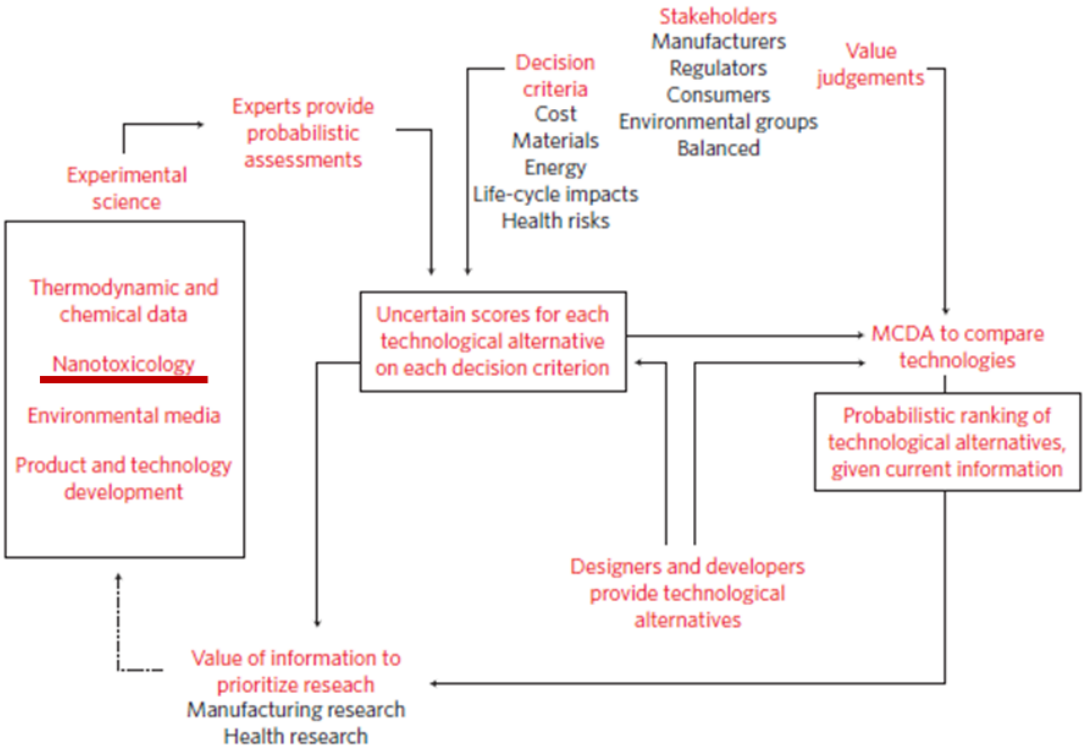

Figure 2.2 Framework for prioritizing research into the impact of nanomaterials on the environment and human health. The process could be viewed as starting at manufacturing companies, where designers and developers need to select a particular technology for a given task. Experts assess each proposed technology relative to the decision criteria through probability distributions based on experimental science or experience. This model integrates all of this information by comparing the technologies to determine which performs best on each criterion, and computes an overall preference score across criteria for each technology for each stakeholder group. This investigation explores the uncertainty in the Multi-criteria Decision Analysis (MCDA) results to determine how new information gained through research might impact the selection decision. If the overall score for a particular stakeholder group can be significantly improved by establishing technological details with certainty, then a research program that is capable of providing this information may be highly valuable to those stakeholders [18].

mesoporous silicates cause no adverse reactions through subcutaneous injection while they cause severe systemic toxicity including casualty [21]. Second, the dose selected could substantially influence the responses from biological systems [22]. If one type of nanoparticle leads to adverse reactions at high doses, it does not mean it is more toxic than the other types of nanoparticle showing no toxicity at low doses, although it could give a false impression that the nanoparticles showing no toxicity are safer. Third, the nanoparticles should be fully characterized and free of contaminants prior to any biological evaluation [23]. Otherwise, the toxicity outcome might be attributed to an irrelevant factor or may not be due to the nanoparticle itself. Fourth, time length in the study could affect toxicity level as some symptoms take time to form in order to be detected by clinical techniques. To sum up, in order to obtain accurate and comprehensive understanding on nanoparticle safety, it is essential to compare nanoparticle toxicity under equal conditions to generate valuable guidelines about designing nanoparticles with minimum adverse effects.

2.3.1 Polymeric nanosystems

Polymer-based delivery systems have been widely used as gene, drug, or dye carriers because of their potential long circulation half-lives and ready uptake by cells [24, 25]. However, such carriers can impose substantial toxicity risks [26, 27]. One such example is the use of poly(amido amine) dendrimers as drug delivery or diagnostic imaging systems due to the capacity to control the size and surface functionalities of these constructs [28]. In order to evaluate the influence of size and surface functionality of dendrimers on systemic biocompatibility, dendrimers were given to immune-competent mice via intravenous injection [27]. A clear trend in *in vivo* toxicity was

observed based on surface functionalities. Amine-terminated dendrimers caused hematological complications such as disseminated intravascular coagulation, whereas carboxyl- and hydroxyl-terminated dendrimers of similar sizes were tolerated at 50-fold higher doses [27]. These findings set caution for employing amine-terminated polymeric systems for systemic administration and have important implications in the safety of nanoparticles in biomedical application.

2.3.2 Gold nanoparticles

Gold nanoparticles are generally considered as biocompatible materials and are used in clinical trials as drug carriers or engineered devices that transform light energy into heat in hyperthermia treatment for solid tumors [29]. It has been reported that mice intravenously injected with gold nanoparticles (1.9 nm in diameter) at 2.7 g Au/kg survived over 1 year without signs of toxicity [30]. The LD_{50} for this material is approximately 3.2 g Au/kg mice. Mice subject to intravenous injection at the dose of 10 mg Au/mL blood showed normal haematology and blood chemistry for 30 days with no histological evidence of toxicity observed in any animal [30]. Biodistribution results show that the highest tissue gold concentration 15 minutes after injection was in kidneys, followed by tumor, liver, and muscle. The tumor:muscle gold ratio increased from 3.4 at 15 minutes to 9.6 at 24 hours, enabling the clear delineation of the tumor as X-ray contrast agents [30]. However, for gold nanorods which are synthesized out of the surfactant template-assisted method using a cationic surfactant such as cetyltrimethylammonium bromide (CTAB), they may be toxic to biological systems since they could perturb cell membrane if the surfactant is not completely removed [31, 32]. The salt $HAuCl_4$, the nanoparticle substrate, were toxic to the cells at ~ 10 nM

concentrations [31]. Extra attention should be paid to utilizing nanosystems for which toxic reagents are used in the synthesis, and complete purification of nanoparticles is a key step for any biological work.

2.3.3 Magnetic nanoparticles

Super paramagnetic iron-oxide nanoparticles have unique magnetic properties and are used as contrast agents in magnetic resonance imaging or as colloidal nanocarriers for targeted drug delivery in diagnosis and therapy [33]. In addition to the excellent magnetic properties, iron-oxide nanoparticles can be decomposed into free iron ions which can further incorporate in the hemoglobin of erythrocytes and be removed through normal iron recycling pathways [34]. The ultrasmall superparamagnetic iron-oxide contrast agents have been subject to safety evaluation at the dose of 0.8, 1.1, and 1.7 mg Fe/kg in phase II clinical trials [35]. The adverse events most frequently observed were dyspnea (3.8%), chest pain (2.9%), and rash (2.9%) among the participating patients. There were no clinically significant effects on vital signs, physical examination, and laboratory results. At dose administered, iron-oxide nanoparticles are considered as generally safe and well-tolerated magnetic resonance contrast agents.

2.3.4 Silica nanoparticles

SiO_2 are considered as potential therapeutic delivery systems because of their tailored pore structure, chemical stability, and ease of chemical modification [36]. The biocompatibility of mesoporous silicates of particle sizes 150 nm, 800 nm, and 4 mm and pore sizes of 3 nm, 7 nm, and 16 nm, respectively, has been examined in animals through different administration routes [21]. Following subcutaneous injection of silicates, the

amount of residual material decreased progressively with good biocompatibility, as evidenced by histology over a period of 3 months. In contrast, intraperitoneal and intravenous injections in mice resulted in death or euthanasia, probably due to pulmonary thrombosis [21]. Results suggest that local tissue reaction to mesoporous silicates was benign while they caused severe systemic toxicity. This study emphasizes the importance of chemical modification of SiO_2 in influencing systemic toxicity in animals.

2.3.5 Other nanosystems

The above are just a few examples of nanomaterials and the influence of physicochemical properties on toxicity. Other examples include quantum dots, carbon nanotubes, titanium dioxide nanoparticles, silver nanoparticles, silicon nanoparticles, *etc*. The detailed discussion of the properties and biological fate of all these constructs is beyond the scope of this dissertation. Discussion of two other examples, *i.e.*, quantum dots and carbon nanotubes is outlined below.

Quantum dots are inorganic semiconductor fluorophores comprised of atoms of elements from groups II to VI. They are currently emerging as versatile tools for biological imaging [37, 38]. However, the chemical stability of quantum dots in biological systems and the resultant toxicity issue is a serious challenge in its clinical development [39]. The use of biocompatible chemistries and reduction of toxicity are necessary in accelerating the utility of these nanoparticles in biomedical applications such as tumor imaging [40].

Carbon nanotubes are cylindrical graphene sheets which have potential applications in hyperthermic ablation of cancer tissues due to the strong optical absorption in the NIR wavelength region [41] and in drug delivery because of their high

surface areas [42]. However, there are concerns for the biodistribution and toxicity of carbon nanotubes *in vivo*, as they have shown high accumulation in liver and kidney and insufficient renal excretions [43]. There are also concerns about impurities such as non-nanotube carbon, amorphous carbon, metal residues (iron, nickel, yttrium), *etc.*, that are associated with carbon nanotubes during fabrication [44, 45] and the lack of complete removal of these contaminants could result in potential complications in the use of carbon nanotubes *in vivo* [46].

2.4 Effect of nanosystem physicochemical properties on toxicity

Nanoconstructs can possess variations in their physicochemical characteristics such as size and size distribution, core composition and structure, surface functionality, porosity, and geometry. These parameters have substantial influence on biological systems, as depicted in Figure 2.3 [14].

2.4.1 Size

Size is a major factor in influencing nanoparticle cellular interaction and *in vivo* behavior. In a study comparing the hemolysis of nonporous SiO_2 ranging from 25 to 225 nm in diameter, it was shown that smaller particles have higher hemolytic activity than the larger ones [35]. This phenomenon is attributed to the larger surface area of the nanoparticles [47]. In another study, it was shown that cellular association of mesoporous SiO_2 by cancerous epithelial cells is particle size-dependent and the maximum uptake by cells occurs at the size of 50 nm among all nanoparticles tested (50 – 280 nm) [48]. The cytotoxicity of monodisperse amorphous SiO_2 with the same morphology was strongly related to particle size [49]. Smaller nanoparticles exhibited significantly higher toxicity

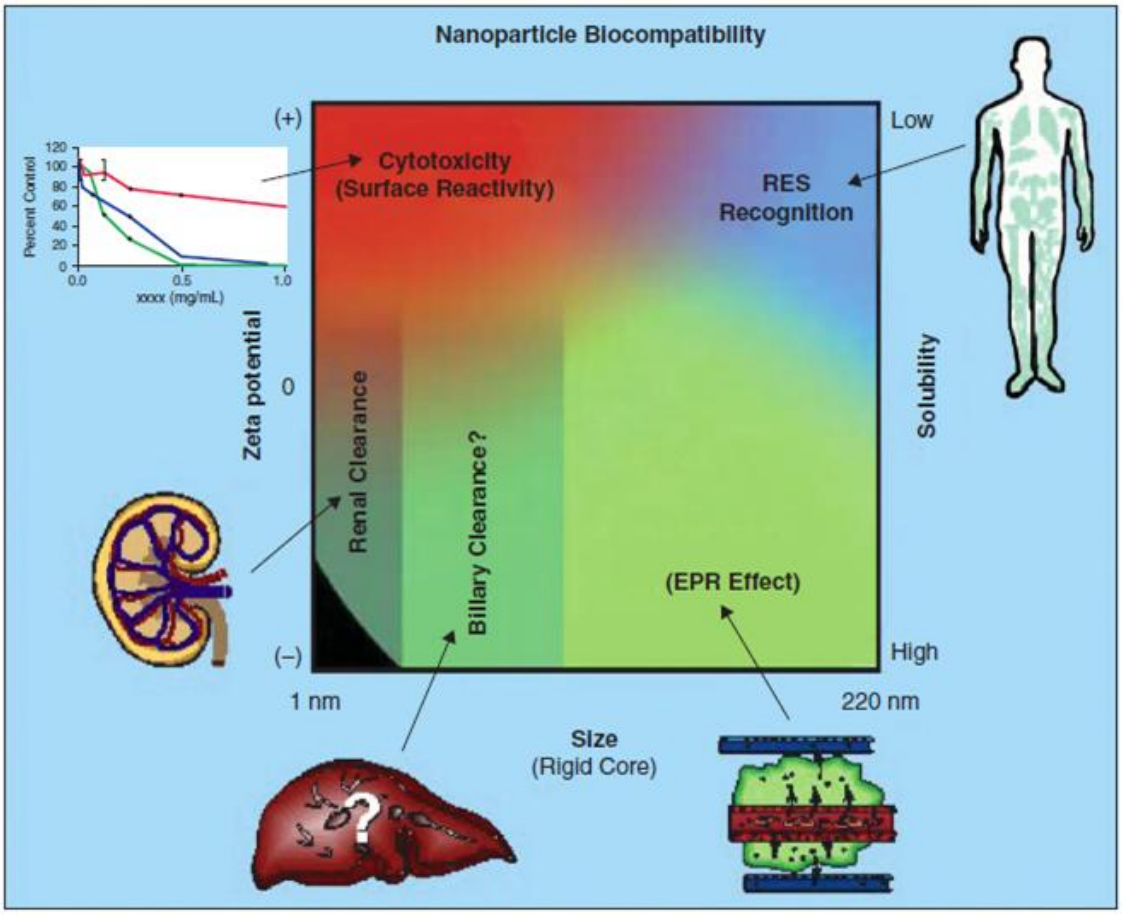

Figure 2.3 Nanoparticle physicochemical characteristics influence biocompatibility (route of uptake and clearance, green; cytotoxicity, red; and RES recognition, blue) as a function of particle size, surface charge (zeta potential), and solubility (adapted from [14]).

than the larger ones. It was concluded that the surface area of tested particles was a critical parameter in determining toxicity of amorphous SiO_2. However, how variations in surface area influence the toxicity outcome is still not fully understood and warrants further investigation.

On the basis of physiological parameters such as hepatic filtration, tissue extravasation, tissue diffusion, and kidney excretion, it is clear that particle size is a key factor in determining nanoparticle distribution *in vivo* [50]. The tissue distribution of gold nanoparticles is size-dependent with 15nm nanoparticles showing the most widespread organ distribution including blood, liver, lung, spleen, kidney, brain, heart, and stomach while 200 nm gold nanoparticles showed limited presence in organs including blood, brain, stomach, and pancreas [51]. Nanoparticles used for targeted delivery to solid tumors are defined to be in the range of 10–100 nm [35]. The lower limit is based on the threshold of the glomerular capillary wall for first-pass elimination by kidneys estimated at 10 nm or less. The upper limit on size is not well defined at this time. The "enhanced permeability and retention effect" (EPR) describes the phenomenon that nanoparticulate systems exit from the leaky blood vessels and accumulate in the tumor due to the impaired lymph system draining function and relative large size of nanoparticles [36].

2.4.2 Porosity

Porosity of inorganic nanoparticles is usually generated in the process of the template-assisted synthesis and template removal by chemical extraction or etching approaches. Mesoporous SiO_2 showed lower hemolytic activity than their nonporous counterparts of similar size, probably due to fewer silanol groups on the cell-contactable surface of mesoporous SiO_2 [47]. The level of hemolysis by mesoporous SiO_2 increased

when the pore structure was damaged by aging in salt solutions [47]. It is clear that the pore structure and stability is an important factor in determining the blood biocompatibility of nanoparticles. Since an array of proteins is present when SiO_2 are exposed to physiological media, it is expected that differential protein adsorption will occur to SiO_2 of various porosities and the biological outcome could be drastically different [52].

2.4.3 Geometry

The geometrical features of nanoparticles are usually formed as self-assembled micelles, like filomicelles [53]; with the assistance of surfactants at different concentrations, such as gold nanorods [54]; with physical compression to original particles, like polystyrene beads of different shapes [55, 56]; or in the template mold, such as SNTs [57]. The filomicelles, resembling flexible filaments, had prolonged blood circulation time up to 1 week post-intravenous injection compared with spherical systems of similar chemistry and composition [53]. This phenomenon is probably due to the reduced uptake by cells since filomicelles are extended by the circulation flow, demonstrating the merits of long shape features *in vivo*.

The influence of geometry of SiO_2 on cellular uptake and toxicity on epithelial and phagocytic cells has been analyzed using three types of amine-terminated SiO_2, namely spheres (178 ± 27 nm), worms (232 ± 22 nm × 1348 ± 314 nm), and cylinders (214 ± 29 nm × 428 ± 66 nm) [58]. The findings of the study suggest that geometry does not play a dominant role in the modes of toxicity and uptake of these particles in the size range studied.

Spherical and rod-shaped gold nanoparticles with surface PEG chains were injected intravenously to nu/nu mice bearing orthotopic ovarian tumors to compare their biodistribution pattern in vital organs [59]. Gold nanorods (10 × 45 nm, 1.1 mV) had longer circulation time, lower liver uptake, and higher tumor accumulation compared with their spherical counterparts (50 nm, -27.1 mV) (Figure 2.4). *In vitro* results showed that gold nanorods were taken up to a lesser extent by macrophages than nanospheres (Figure 2.4). Protein interaction analysis revealed that gold nanospheres exhibited more extensive interaction with proteins than nanorods, probably due to their more negative charge and enhanced interaction with lysine residues from proteins (Figure 2.4). This association with proteins might have led to the increased uptake of nanospheres by RES and reduced circulation time *in vivo* compared with nanorods.

2.4.4 Surface characteristics

Surface characteristics can have a profound influence on the interaction of nanoparticles with the local environment, leading to downstream distribution outcome or toxicity effects. Such characteristics are always manipulated by addition of steric stabilization, changes in surface charge, or addition of targeting ligands. Surface modification on SiO_2 has been shown to reduce their systemic toxicity compared to the pristine counterparts [59, 60]. For example, it has been reported that amorphous SiO_2 with diameter of 70 nm caused structural and functional abnormalities in the placenta on the maternal side when injected intravenously into pregnant mice and abolished when the surface of nanoparticles were modified with carboxyl and amine groups [60]. Previous studies also showed that the intravenous administration of pristine SiO_2 with a diameter of 70 nm caused extensive fibrosis [61]. To the contrary, the amino or carboxyl modified

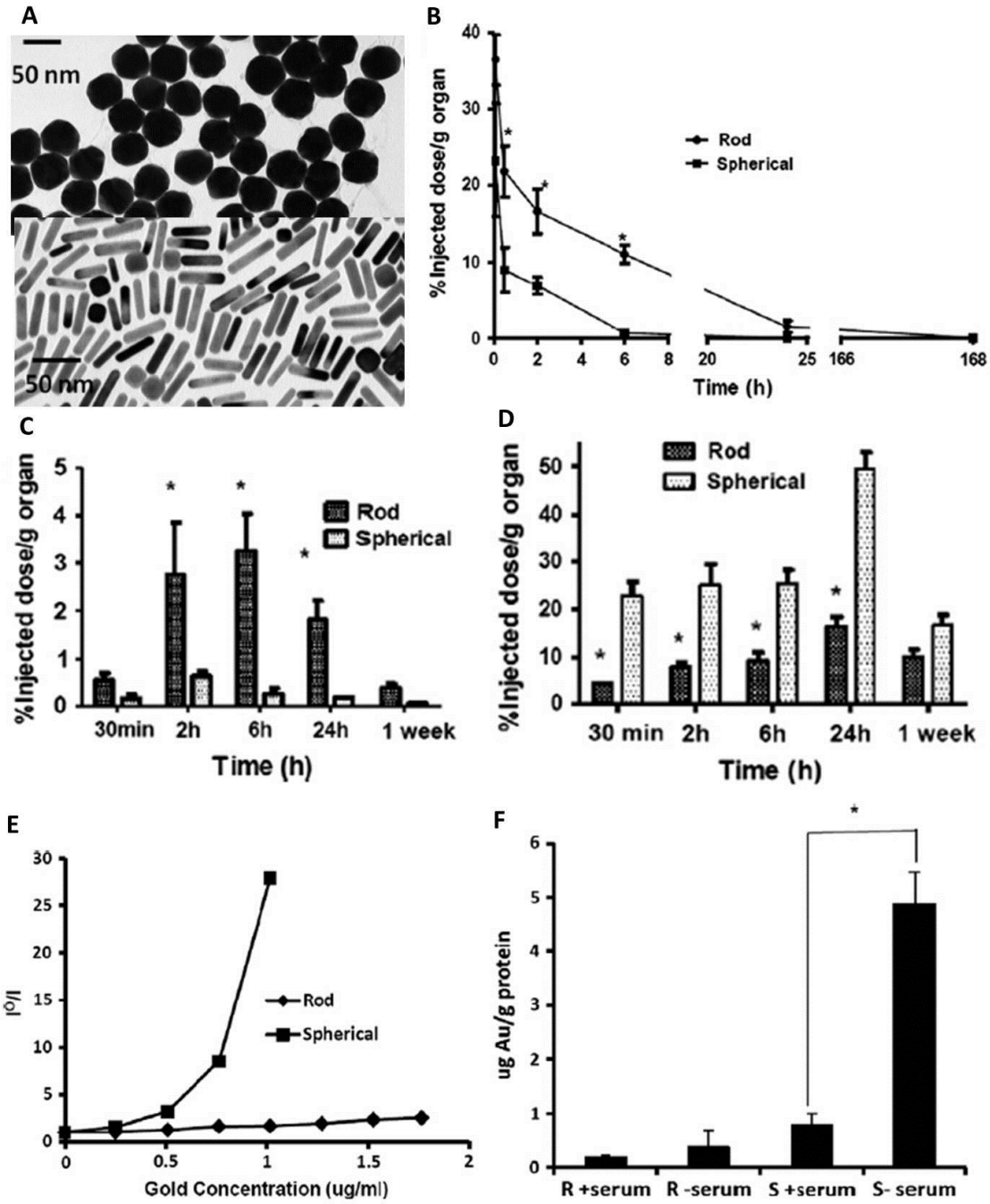

Figure 2.4 Summary of gold nanoparticle characterization and their geometry effect *in vitro* and *in vivo*. A) Transmission electron microscopy (TEM) images of pegylated gold spheres and rods. B) Their plasma profiles, distribution in C) liver and D) in tumor as a function of time are shown. $n = 3 \pm$ standard error. *Significant difference between rod and spherical particles $p < 0.05$. E) Interaction between gold nanoparticles and BSA is expressed as quenching efficiency (I_0/I), where I_0 and I are fluorescence in the absence and presence of gold nanoparticles. F) Uptake of gold nanoparticles by RAW 264.7 macrophages is compared in the presence and absence of serum. R = rod; S = spherical; $n = 3 \pm$ standard deviation (SD), $^{*}p < 0.01$ (adapted from [59]).

SiO_2 led to much less toxicity level and did not cause hepatic fibrosis. These findings indicate that the surface characteristics of nanoparticles can change toxicity profiles. It has been suggested that the change in surface characteristics influences the interaction of nanoparticles with proteins in the blood stream, which leads to alteration in hydrodynamic sizes and organ distribution patterns [59].

In addition, targeting ligands that provide specific nanoparticle–cell surface interactions can play a vital role in enhanced cellular uptake. These targeting ligands enable nanoparticles to bind to specific cell-surface receptors that are overexpressed by target cells and enter cells by receptor-mediated endocytosis. For example, cellular uptake and biodistribution of pegylated gold nanorods with or without the cyclic RGDfK (Arg-Gly-Asp-D-Phe-Lys) peptide functionalization were tested on DU145 prostate cancer cells, human umbilical vein endothelial cells, and in prostate tumor-bearing mice [62]. Targeting of the RGDfK surface-modified gold nanorods was confirmed *in vitro* due to selective binding and uptake by endothelial cells. Tumor targeting was not observed *in vivo*, however, probably due to fast clearance of the RGDfK-gold nanorods from the blood. It is possible that the presence of strong negative charges from RGDfK moieties overrides their targeting ability to the tumor, resulting in RES clearance of this system rather than enhanced uptake by the tumor. These findings corroborated with a previous study on tumor uptake of elongated gold nanocrystals that were covalently bound tumor-targeting peptides [63]. Quantitative pharmacokinetic and biodistribution data showed that the use of active targeting ligands on gold nanorods only marginally improved the total tumor uptake in comparison with control nanorods in the xenograft animal models. These results indicated that mass transport across the tumor vasculature is

a rate-limiting step for nanoparticle delivery and its kinetics is largely unaffected by active receptor binding [63].

2.4.5 Other physicochemical properties

Other physicochemical properties such as core composition, polymer architecture, *etc.*, exert critical effects on biological systems. It was hypothesized that greater degrees of nanoparticle "flexibility" improve the binding ability of particles on the cell surface [50]. Shell cross-linked nanoparticles possessed a low glass transition temperature (Tg) with a fluid-like poly(methyl acrylate) core or a high Tg with a glassy poly(styrene) core [64]. The effect of the rigidity of the polymeric core on the *in vivo* biodistribution was evaluated and results showed that high-Tg poly(styrene) core nanoparticles exhibited a significantly higher blood residence time compared to the low-Tg poly(methyl acrylate) nanoparticles, probably due to the greater flexibility and increased surface interaction that the low-Tg core nanoparticles had with the tissues [64]. Cyclic polymers composed of α-cholo-ε-caprolactone and ε-caprolactone showed longer blood circulation time in mice than linear polymers of similar composition and comparable molecular weight (> renal filtration threshold) [65]. It is probably due to the fact that linear polymers traverse nanopores in glomeruli by end-on motion of one chain end while cyclic polymers transit with two chain segments since they lack chain ends, implying the effect of polymer architecture on *in vivo* biodistriubtion and clearance [65].

2.5 Synthesis, fabrication, and characterization of silica nanoparticles

In the past decade, silica-based nanomaterials have attracted much attention in biomedical applications as cell markers, gene transfection agents, as well as drug carriers

[36, 66-70]. They possess a variety of unique properties, such as ease of synthesis and surface modification, robust mechanical properties, and relatively inert chemical composition, which make them excellent candidates for biological applications [68]. Progress in mold fabrication has further enabled the production of particles with distinct shapes [57, 71]. Reports are emerging that particle shape influences cellular uptake and biodistribution *in vivo* [72, 73].

2.5.1 Synthesis and fabrication

2.5.1.1 Top-down method

The emerging "top-down" fabrication is a robust tool adapted from the microelectronics industry for the facile production of tailor-made nanofabricated particles [5]. With the assistance of top-down fabrication techniques, the acquiring of detailed knowledge of the interdependent effect that key particle physicochemical variables have on biological toxicity become feasible. For example, with regard to SNT fabrication, the top-down strategy involving a template mold is utilized (Figure 2.5) [57]. First, a porous alumina template is prepared by electrochemical anodization on aluminum plate, where the pore dimensions could be adjusted from five to a few hundred nanometers in diameter and from tens of nanometers to hundreds of micrometers in length. Secondly, thin layers of nanomaterial are deposited onto the cylindrical wall of nanopores of an alumina membrane including surfaces of membrane through the sol-gel chemistry. Thirdly, the layer on the top of the membrane is removed by mechanical polishing. Last, free nanotubes are obtained by selectively dissolving the alumina template in 25% phosphoric acid followed by repeated filtration and collection (Figure 2.5). The template synthesis not only facilitates the production of SNTs with high control over shape, size, and size

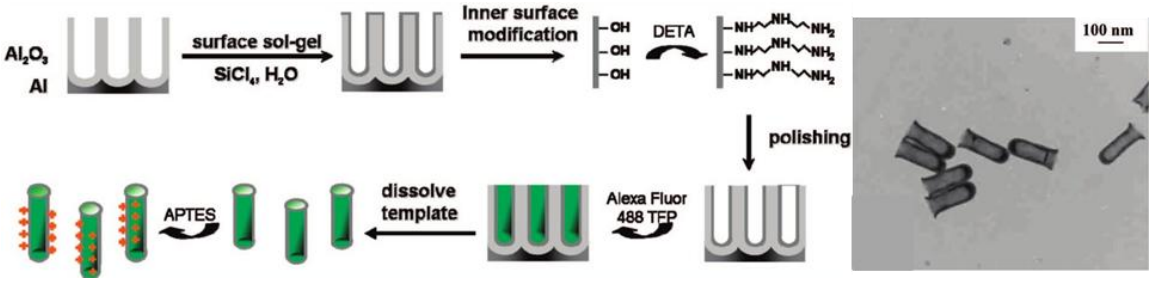

Figure 2.5 Schematic representation of template synthesis of SNTs and their TEM image (50 nm × 200 nm) (adapted from [73]). Al_2O_3, aluminum oxide; Al, Aluminum; $SiCl_4$, tetrachlorosilane; DETA, diethylenetriamine; APTES, (3-aminopropyl) triethoxysilane.

distribution, it also renders the differential functionalization of inner and outer surfaces of nanotubes feasible. The first functionalization is conducted to modify the inner surface of nanotubes before they are liberated from the template membrane (Figure 2.5). The outer surface is not accessible in the first round of functionalization because it is in contact with the template pore wall. Then, the template is dissolved to release free nanotubes; the outer surface is thus exposed and is available for a second functionalization. The differential functionalization offers multifunctionalities on nanotubes depending on their roles, *e. g.*, SNTs are modified at the inner surface with drugs or imaging agents and at the outer surface with targeting moieties [74].

2.5.1.2 Bottom-up methods

The "bottom-up" methods include the traditional ways of synthesizing SiO_2 by substrate reaction (Figure 2.6). Nonporous SiO_2 are synthesized by a Stöber method developed in the 1960s and are prepared from reacting tetraethoxysilane (TEOS) in a mixture of ammonia, water, and ethanol [75, 76]. Nonporous SiO_2 usually possesses very uniform size and the ammonia concentration greatly influences their size, that is, the higher the ammonia concentration, the larger the size of nonporous SiO_2 in a certain range (Figure 2.6A) [77]. Mesoporous SiO_2 were first synthesized by researchers in Mobil Company in 1992 [78]. The most extensively studied mesoporous SiO_2 are the MCM-41 (Mobil Composite Material 41) type, which are synthesized out of the cationic surfactant micelle template and is characteristic of the 2D-hexagonal mesopores running parallel from one end to the other in the close-packed structure of the silicate product [79]. Possible mechanistic pathways for the formation of MCM-41 type mesoporous silicates are listed as (Figure 2.6B): 1) liquid-crystal-phase-initiated pathway, which postulates

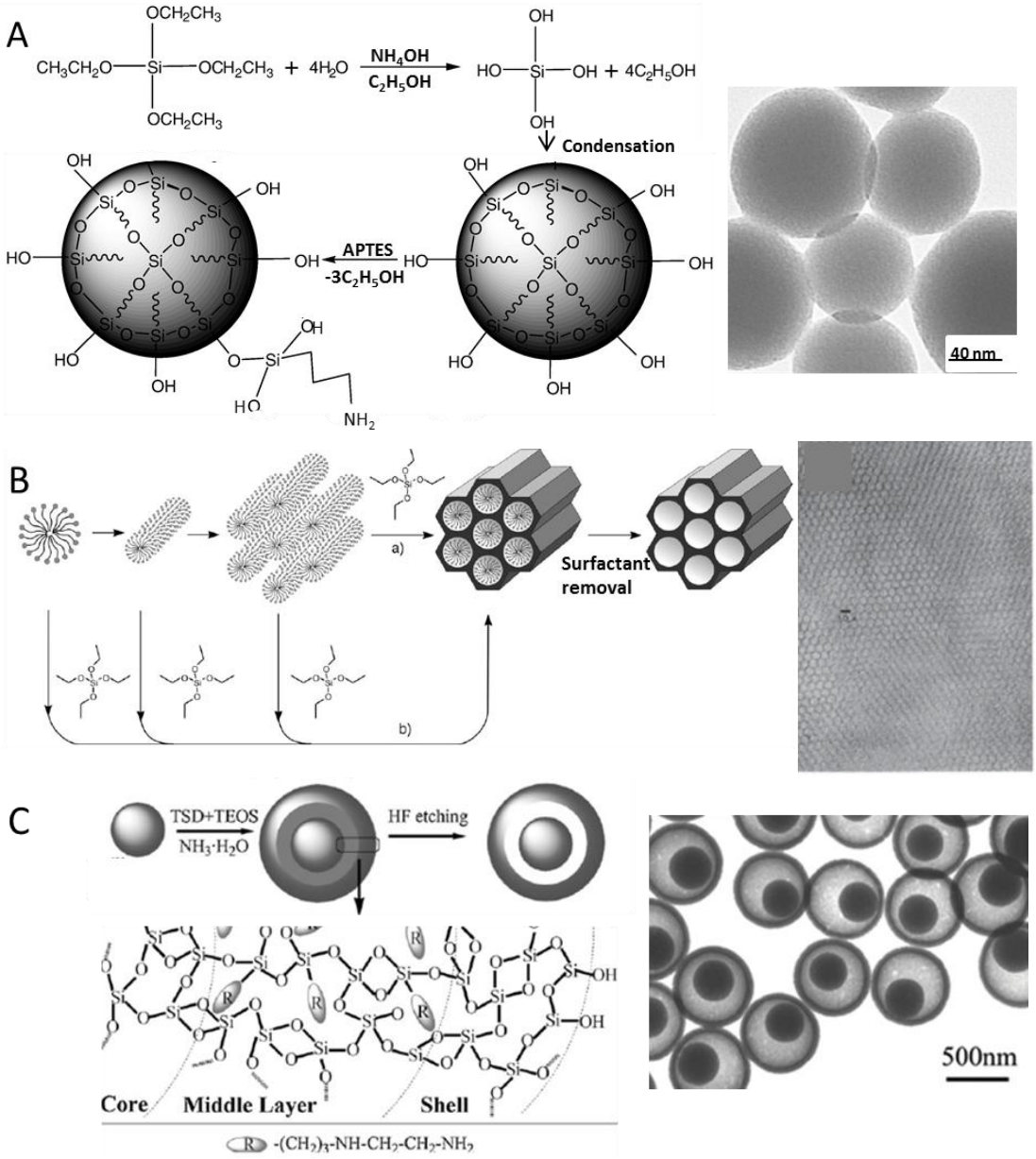

Figure 2.6 Schematic illustration for the synthesis and functionalization of A) nonporous SiO_2 (adapted from [80]), B) MCM-41 type mesoporous SiO_2 (adapted from [79, 81]), and C) silica nanorattles (adapted from [82]) and their TEM images. NH_4OH, ammonium hydroxide; C_2H_5OH, ethanol; TSD, *N*-[3-(trimethoxysilyl)propyl] ethylenediamine; HF hydrofluoric acid.

that the pre-existence of surfactant association (rod-like micelles) followed by polymerization of silicate anions led to the formation of the MCM-41 structure; 2) silicate-anion initiated pathway, which suggests that the self-assembly of the liquid-crystal-like structures results from mutual interactions between the silicate anion and the surfactant cations in solution [81]. In this synthesis, the shape of nanoparticles is mainly dependent on the CTAB concentration and the stirring rate in the reaction. The aspect ratio of nanoparticles could vary from 1 to 8 when CTAB concentration increases and stirring rate reduces. The ammonia concentration plays a crucial role in determining the diameter of nanoparticles, as the increase in ammonia concentration leads to the increase in the width of nanoparticles. Such control over synthetic conditions results in the production of nanoparticles with tailored geometrical features which lay the foundation for studying the geometry effect of nanoparticles on biological toxicity. Compared with the nonporous SiO_2, mesoporous SiO_2 have advantageous features such as large surface areas (600 – 1000 m^2/g), uniform pore sizes, and dual-modification on inner surface or outer surface, making them attractive candidates as therapeutic carriers [67, 68].

Recently, there is an emerging synthetic pathway for generating mesoporous hollow silica nanospheres (MHSNs) with unique porosity and surface features based on a template-assisted, selective etching method (Figure 2.6C) [6]. The MHSN is of silica nanorattle structure by selectively etching the middle layer of organic-inorganic hybrid solid silica spheres (HSSSs) with hydrofluoric acid (HF). To synthesize MHSNs, the HSSSs with three-layer “sandwich” structure are designed in the first step with the core and the shell as pure silica hydrolyzed from TEOS and the middle layer as organic silica co-condensed from TEOS and *N*-[3-(trimethoxysilyl)propyl] ethylenediamine (TSD). In

the second step, the HSSSs are changed into silica nanorattles with an appropriate amount of aqueous HF, which diffuses into the middle layer of HSSSs *via* micropores in the shell and selectively etches away the middle layer. This selective-etching strategy could readily produce monodisperse nanorattles on a large scale with tailored size, shell thickness, and core diameter. By rationally choosing functional nanoparticles as core materials, such as gold nanoparticles, this strategy could be developed as a general tool to synthesize multifunctional hybrid nanorattles for a variety of applications in nanomedicine and catalysis [68].

2.5.2 Characterization

Nanoparticle characterization is a crucial step in determining physicochemical properties in the relevant medium. Appropriate and systematic characterization provides a foundation for correlating physicochemical properties of nanoparticles with biological outcome and generates valid guidelines in designing nanoparticles with desirable features. Commonly used methods include electron microscopy and dynamic light scattering (DLS) measurements for size or geometry identification, X-ray diffraction (XRD) analysis for pore structure and ordering determination, nitrogen adsorption desorption isotherm analysis for surface area and pore size measurement, and other important assays before the samples are ready for biological evaluation (Table 2.4).

2.5.2.1 Electron microscopy

Transmission electron microscopy (TEM) is a standard technique to image the morphology and particle size distribution for micro- or nanosized solid particles. Particle sizing by TEM yields valid size and shape information and provides visual evidence of

Table 2.4 Commonly used characterization methods for SiO_2 (adapted from [84])

Physicochemical properties	**Assays**	**Function**	**Limitation**
Size	Electron microscopy	Visualizes the size or shape at dry state	Time consuming, influence of sample preparation
	Dynamic light scattering	Measures the hydrodynamic size in medium	Not appropriate for very polydisperse population, influence of aggregates
Surface characteristics	Surface functionality quantification	Quantifies the amount of functional groups on nanoparticles	Complexity of experimental preparation
	Zeta potential	Measures the surface charge in presence of medium	Influence of aggregates or salt, pH conditions
Porosity	X-ray diffraction	Records the pore arrangement and orderliness	Large amount of samples required Setup optimization required
Surface area	Nitrogen adsorption/desorption isotherm	Measures the surface area, pore size/distribution in samples	Large amount of samples required, time consuming, restricted material (liquid nitrogen) required
Impurity	Fourier transform infrared spectroscopy	Obtains the infrared spectrum from functional moieties in the sample	Limited sensitivity
	Inductively coupled plasma mass spectrometry	Analyzes the content of trace elements in the sample	High background noise for certain elements (proton, oxygen, *etc.*)
	Endotoxin detection assay	Detects and quantifies the bacterial endotoxin level in the sample	Sample auto-absorbance, soluble sample referred, cost

internal structure for inorganic nanoparticles *via* the penetrating electron beams at high voltage [83]. However, TEM only assesses the size of samples prepared at dry state, does not provide size information of nanoparticles suspended in aqueous medium, and it is laborious to obtain multiple TEM images from the same sample to obtain sizing information of statistical significance [23]. The same holds true for scanning electron microscopy (SEM), which gives information about the surface features and sizes of nanoparticles. Electron microscopy technique is usually coupled with dynamic light scattering analysis to generate the overall picture of nanoparticle sizing in various media.

2.5.2.2 Zeta potential and dynamic light scattering measurement

The physicochemical state of nanoparticles in suspension, such as surface charge and hydrodynamic size, is commonly identified by zeta potential or DLS measurement. Since nanoparticles could be exposed to various media, including water, saline, cell medium, serum solution, or whole blood, it is of crucial importance to identify their charge and hydrodynamic size in each condition as it significantly influences the interaction of nanoparticles with the local environment [85].

2.5.2.3 X-ray diffraction

XRD is a technique in crystallography in which the patterns produced by the diffraction of X-rays through the closely spaced lattice of atoms in the solid state sample are examined [86]. The electrons that surround the atoms are the entities which physically interact with the incoming X-ray photons. The spacing in the lattice could be determined using Bragg‟s law. The pattern of diffraction peaks could be used to identify the crystal size, purity, and textures of the sample tested [86]. This technique is widely used in

chemistry or materials science to determine the structures of various crystalline molecules, including inorganic compounds, DNA, and proteins [87]. It is one of the basic characterization steps to evaluate the hexagonal pore structure and orderliness for mesoporous SiO_2.

2.5.2.4 Nitrogen adsorption and desorption isotherm analysis

Nitrogen adsorption desorption isotherm analysis is used to measure the BET (Brunauer-Emmett-Teller) and Langmuir surface area and BJH (Barrett, Joyner, and Halenda) pore size distribution of a solid sample at dry state [88, 89]. In a typical characterization experiment, the sample is contained in an evacuated sample tube, cooled to cryogenic temperature (77K), and is then exposed to analysis gas at a series of precisely controlled pressures. With each incremental pressure increase, the number of gas molecules adsorbed on the surface increases. The pressure at which adsorption equilibrium occurs is recorded and the changing quantity of gas adsorbed on the solid surface is quantified. Then, the desorption process begins in which pressure is systematically reduced, leading to the liberation of the adsorbed molecules. A plot of relative pressure vs. volume adsorbed is thus obtained by measuring the amount of nitrogen gas that adsorbs onto the surface and the subsequent amount that desorbs at a constant temperature [88]. Analysis of the isotherms provides information about the surface area and pore size information of the material [90].

2.5.2.5 Other characterization techniques

Several techniques which address other important issues such as absence of contaminants are applied in nanoparticle characterization. These include: Fourier

Transform Infrared Spectroscopy (FTIR) used to identify an infrared spectrum of impurity, Inductively Coupled Plasma Mass Spectrometry (ICP-MS) used to measure the amount of trace element impurities from the environment, and Endotoxin detection assay used to detect the level of possible biological contaminants from bacteria in nanoparticle stocks by Limulus Amebocyte Lysate (LAL) detection assay.

2.6 Impact of silica nanoparticle design on toxicity in biological systems

Physicochemical properties of carriers, such as surface functionality, size, chemical composition, and texture, play important roles in determining the extent of toxicity *in vitro* and *in vivo* (Figure 2.7). However, the interdependent role of shape, pore size, and surface modification of the carriers on toxicity *in vitro* and *in vivo* still remains largely unknown. A comprehensive study that evaluates the impact of multiple physicochemical characteristics of SiO_2 on cellular and *in vivo* toxicity, biodistribution, and pharmacokinetics is needed.

2.6.1 *In vitro* evaluation

SiO_2 induced *in vitro* toxicity involves an incremental series of cellular responses that could be classified as anti-oxidant defense, pro-inflammatory effects, and cytotoxicity [16]. Cytotoxicity occurs at the highest level of oxidative stress, which means that the interference in mitochondrial inner membrane electron transfer or changing open/closed status of the permeability transition pore could lead to effects on adenosine triphosphate (ATP) synthesis and release of pro-apoptotic factors [16]. Common assays that reflect the extent of cytotoxicity in cell population include MTT (3-(4,5-Dimethylthiazol-2-yl)-2,5-diphenyltetrazolium bromide) assays and propidium

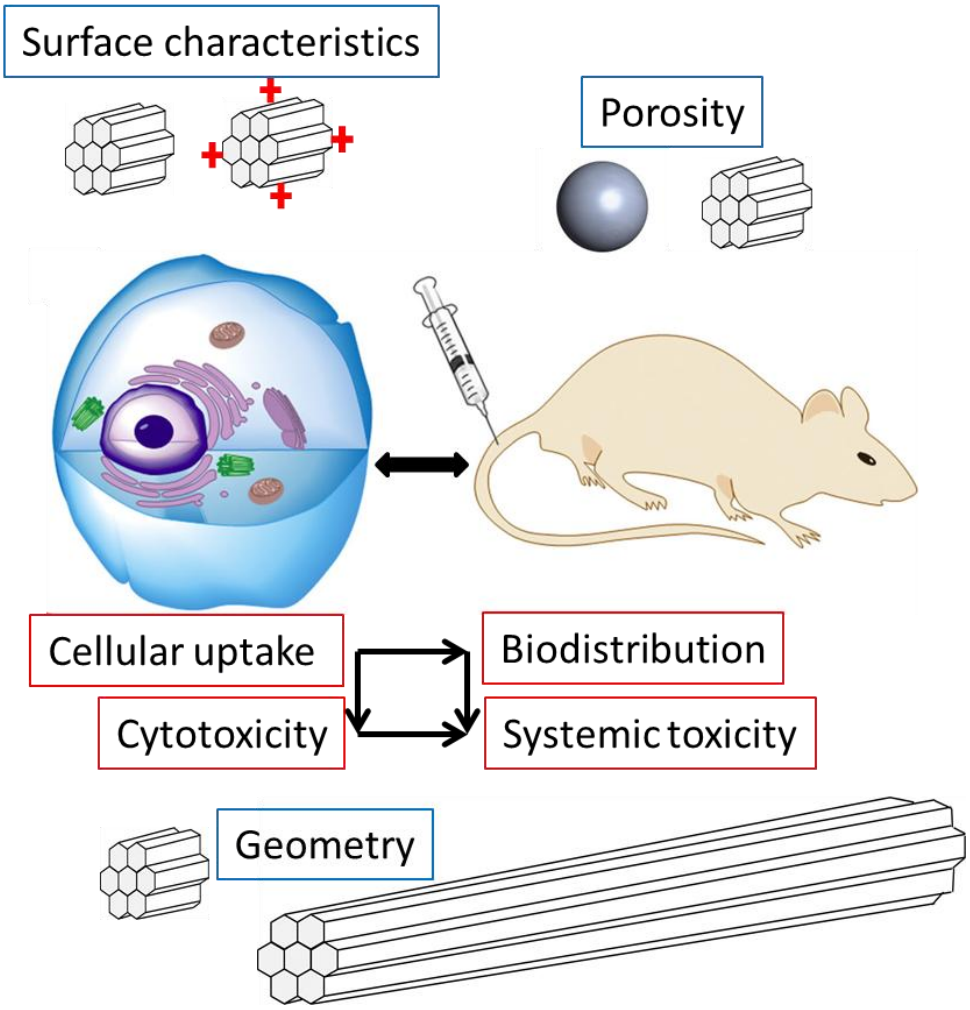

Figure 2.7 Schematic illustration of biocompatibility of SiO_2 as a function of physicochemical properties, such as particle size, pore size, geometry, and surface properties. These parameters have a complex influence on *in vitro* cellular uptake, subcellular location and cytotoxicity, and *in vivo* biodistribution, excretion, and toxicity.

iodine uptake, *etc.* [91]. The impact of nanoparticles on the cellular level could also be reflected by the extent of nanoparticle uptake by cells, which are quantitatively measured by flow cytometry analysis for fluorescently labeled nanoparticles, gamma counter for radiolabeled nanoparticles, and ICP-MS for metal or metallic oxide nanoparticles. Subcellular location and fate of nanoparticles could also indicate the potential interference with cellular processes and is frequently identified by phase contrast microscopy or TEM imaging [92], or confocal microscopy for nanoparticles with fluorescence capability [93].

2.6.2 *Ex vivo* evaluation

Ex vivo analysis of nanoparticles evaluates how the effect of nanoparticle physicochemical parameters influences their interaction with blood constituents. The plasma protein binding is crucial in determining the *in vivo* organ biodistribution and clearance of nanoparticles. It has been reported that the adsorption of plasma proteins depends primarily on nanoparticle surface hydrophobicity or charge [94]. Nanoparticles whose surface is not modified, *e. g.*, pegylated, to avoid opsonization can be cleared from the circulation rapidly by macrophages in the RES [94]. Hence, nanoparticle-serum protein interaction is generally the focus of *ex vivo* studies. Another common *ex vivo* assessment evaluates the interaction of nanoparticles with erythrocytes and platelets, which are key components involved in blood coagulation. Typical assays include hemolysis, platelet aggregation, or neutrophil activation studies. Understanding the particle structure-activity relationships at the level of interaction with cellular and protein components in circulation greatly facilitates the correlation of nanoparticle parameters with *in vivo* toxicity outcome.

2.6.3 *In vivo* toxicity

The *in vivo* toxicity of nanoparticles is usually examined in animals by a selected administration route according to the arranged dosing regimen:

1) The toxicity studies can be conducted at a single dose, which is usually within the therapeutic window of the drug concentration they are able to load. As long as the nanoparticles do not exhibit any adverse reactions at this specific dose by the end of the study, they are considered as safe. For example, the systemic toxicity of pegylated silica nanorattles at a single dose of 40 mg/kg has been evaluated and their biocompatibility was confirmed by histology. The drug nanocarrier was then loaded with Docetaxel (32 wt %) and injected into animals at the same nanoparticle dose (equivalent to 20 mg/kg Docetaxel) to compare the toxicity and efficacy with a commercial Taxotere group (20 mg/kg Docetaxel) [95].

2) The toxicity studies can also be conducted at multiple doses of the same nanoparticles on an escalating scale. The dosing increase is stopped when adverse reactions are identified at the highest dose tested and a MTD is determined based on the absence of adverse reactions at a lower dose. Even though it might not be directly translated to a drug efficacy dose in preclinical settings, the MTD could reflect the intrinsic toxicity level the nanoparticles impose on the biological system and can be used in comparison with nanoparticles of different physicochemical features, generating useful guidelines [96, 97]. However, there are emerging concerns since adverse reactions in animals eventually happen under this study design [27]. Thus, careful planning for the study is needed to minimize the risks the animals are exposed to during the study period.

2.6.4 *In vivo* biodistribution and pharmacokinetics

The tracking of nanoparticle biodistribution and pharmacokinetics is usually conducted in two ways, *i.e.*, by tracing labeling agents that are covalently conjugated to nanoparticles (either fluorescent dyes or radioisotopes), or by measuring the elements of nanoparticles themselves, in this case, measuring silicon atoms from SiO_2 *via* ICP-MS. There are advantages and disadvantages associated with each type of detection method. For tracing labeling agents, the detection is fast and simple; however, there are always concerns about the stability of the conjugate and whether it is tracking nanoparticles or the free labeling agents that are in the original stock or have become dissociated due to hydrolysis or enzyme cleavage [98-101]. This becomes an outstanding issue if the study is aimed at examining the excretion of nanoparticles into urine or feces as the breakage of the bond partially occurs during this process. For tracing nanoparticle elements, the measurement is quantitative and directly reflects the concentration of nanoparticles in tissues or organs. However, due to the prevalent presence of silica in the body and in the environment, the background noise level from the control groups is high and may interfere with the readings from nanoparticle samples, especially if they are not or could not be dosed at a high concentration [72, 102]. It has been reported that the silicon content in the feces and urine of the control group were very high and fluctuating since the mice had free access to water and commercial laboratory food [72]. This interfered with the calculation of excretion percentage. Careful selection for a specific detection method is needed to facilitate accurate and efficient probe measurement.

2.7 Silica nanoparticles in biomedical applications and further consideration

SiO_2 offer a useful alternative to organic systems in the field of nanomedicine. Their intrinsic chemical stability, capacity for multifunctional modification, and low cost of production make them a promising candidate for such applications. Recent progress has enabled the production of SiO_2 with distinct shape, porosity, and surface characteristics. To develop SiO_2 as effective carriers, there are still significant challenges remaining and it is critical to fully analyze the effect of various physicochemical features on toxicity to generate rational guidelines to design SiO_2 for applications in nanomedicine.

2.8 References

[1] R.A. Petros, J.M. DeSimone, Strategies in the design of nanoparticles for therapeutic applications, Nat Rev Drug Discov, 9 (2010) 615-627.

[2] G. Konstantatos, E.H. Sargent, Nanostructured materials for photon detection, Nat Nanotechnol, 5 (2010) 391-400.

[3] V.E. Kagan, H. Bayir, A.A. Shvedova, Nanomedicine and nanotoxicology: two sides of the same coin, Nanomedicine : Nanotechnology, Biology, and Medicine, 1 (2005) 313-316.

[4] A. Nel, T. Xia, L. Madler, N. Li, Toxic potential of materials at the nanolevel, Science, 311 (2006) 622-627.

[5] S.E. Gratton, P.A. Ropp, P.D. Pohlhaus, J.C. Luft, V.J. Madden, M.E. Napier, J.M. DeSimone, The effect of particle design on cellular internalization pathways, Proc Natl Acad Sci U S A, 105 (2008) 11613-11618.

[6] C.-P. Tsai, C.-Y. Chen, Y. Hung, F.-H. Chang, C.-Y. Mou, Monoclonal antibody-functionalized mesoporous silica nanoparticles (MSN) for selective targeting breast cancer cells, J. Mater. Chem., 19 (2009) 5737–5743

[7] M.A. Augustin, P. Sanguansri, Nanostructured materials in the food industry, Adv Food Nutr Res, 58 (2009) 183-213.

[8] D.M. Bowman, G. van Calster, S. Friedrichs, Nanomaterials and regulation of cosmetics, Nat Nanotechnol, 5 (2010) 92.

[9] B. Fadeel, A.E. Garcia-Bennett, Better safe than sorry: Understanding the toxicological properties of inorganic nanoparticles manufactured for biomedical applications, Adv Drug Deliv Rev, 62 (2010) 362-374.

[10] C.A. Poland, R. Duffin, I. Kinloch, A. Maynard, W.A. Wallace, A. Seaton, V. Stone, S. Brown, W. Macnee, K. Donaldson, Carbon nanotubes introduced into the abdominal cavity of mice show asbestos-like pathogenicity in a pilot study, Nat Nanotechnol, 3 (2008) 423-428.

[11] K.R. Martin, The chemistry of silica and its potential health benefits, J Nutr Health Aging, 11 (2007) 94-97.

[12] G. Oberdorster, J.N. Finkelstein, C. Johnston, R. Gelein, C. Cox, R. Baggs, A.C. Elder, Acute pulmonary effects of ultrafine particles in rats and mice, Res Rep Health Eff Inst, (2000) 5-74; disc 75-86.

[13] Z. Chen, H. Meng, G. Xing, H. Yuan, F. Zhao, R. Liu, X. Chang, X. Gao, T. Wang, G. Jia, C. Ye, Z. Chai, Y. Zhao, Age-related differences in pulmonary and cardiovascular responses to SiO_2 nanoparticle inhalation: nanotoxicity has susceptible population, Environ Sci Technol, 42 (2008) 8985-8992.

[14] S.E. McNeil, Nanoparticle therapeutics: a personal perspective, Wiley Interdiscip Rev Nanomed Nanobiotechnol, 1 (2009) 264-271.

[15] M. Li, K.T. Al-Jamal, K. Kostarelos, J. Reineke, Physiologically based pharmacokinetic modeling of nanoparticles, ACS Nano, 4 (2010) 6303-6317.

[16] H. Meng, T. Xia, S. George, A.E. Nel, A predictive toxicological paradigm for the safety assessment of nanomaterials, ACS Nano, 3 (2009) 1620-1627.

[17] M.A. Dobrovolskaia, S.E. McNeil, Immunological properties of engineered nanomaterials, Nat Nanotechnol, 2 (2007) 469-478.

[18] I. Linkov, M.E. Bates, L.J. Canis, T.P. Seager, J.M. Keisler, A decision-directed approach for prioritizing research into the impact of nanomaterials on the environment and human health, Nat Nanotechnol, 6 (2011) 784-787.

[19] G. Oberdorster, E. Oberdorster, J. Oberdorster, Nanotoxicology: an emerging discipline evolving from studies of ultrafine particles, Environ Health Perspect, 113 (2005) 823-839.

[20] H.F. Krug, P. Wick, Nanotoxicology: an interdisciplinary challenge, Angew Chem Int Ed Engl, 50 (2011) 1260-1278.

[21] S.P. Hudson, R.F. Padera, R. Langer, D.S. Kohane, The biocompatibility of mesoporous silicates, Biomaterials, 29 (2008) 4045-4055.

[22] T. Liu, L. Li, X. Teng, X. Huang, H. Liu, D. Chen, J. Ren, J. He, F. Tang, Single and repeated dose toxicity of mesoporous hollow silica nanoparticles in intravenously exposed mice, Biomaterials, 32 (2011) 1657-1668.

[23] C.F. Jones, D.W. Grainger, *In vitro* assessments of nanomaterial toxicity, Adv Drug Deliv Rev, 61 (2009) 438-456.

[24] D.B. Pike, H. Ghandehari, HPMA copolymer-cyclic RGD conjugates for tumor targeting, Adv Drug Deliv Rev, 62 (2010) 167-183.

[25] J.L. Frandsen, H. Ghandehari, Recombinant protein-based polymers for advanced drug delivery, Chem Soc Rev, (2012).

[26] A.C. Hunter, S.M. Moghimi, Therapeutic synthetic polymers: a game of Russian roulette?, Drug Discov Today, 7 (2002) 998-1001.

[27] K. Greish, G. Thiagarajan, H. Herd, R. Price, H. Bauer, D. Hubbard, A. Burckle, S. Sadekar, T. Yu, A. Anwar, A. Ray, H. Ghandehari, Size and surface charge significantly influence the toxicity of silica and dendritic nanoparticles, Nanotoxicology, (2011).

[28] N. Malik, R. Wiwattanapatapee, R. Klopsch, K. Lorenz, H. Frey, J.W. Weener, E.W. Meijer, W. Paulus, R. Duncan, Dendrimers: relationship between structure and biocompatibility *in vitro*, and preliminary studies on the biodistribution of ^{125}I-labelled polyamidoamine dendrimers *in vivo*, J Control Release, 65 (2000) 133-148.

[29] H.C. Huang, S. Barua, G. Sharma, S.K. Dey, K. Rege, Inorganic nanoparticles for cancer imaging and therapy, J Control Release, 155 (2011) 344-357.

[30] J.F. Hainfeld, D.N. Slatkin, T.M. Focella, H.M. Smilowitz, Gold nanoparticles: a new X-ray contrast agent, Br J Radiol, 79 (2006) 248-253.

[31] C.J. Murphy, A.M. Gole, J.W. Stone, P.N. Sisco, A.M. Alkilany, E.C. Goldsmith, S.C. Baxter, Gold nanoparticles in biology: beyond toxicity to cellular imaging, Acc Chem Res, 41 (2008) 1721-1730.

[32] A.M. Alkilany, C.J. Murphy, Toxicity and cellular uptake of gold nanoparticles: what we have learned so far?, J Nanopart Res, 12 (2010) 2313-2333.

[33] E. Ruiz-Hernandez, A. Baeza, M. Vallet-Regi, Smart drug delivery through DNA/magnetic nanoparticle gates, ACS Nano, 5 (2011) 1259-1266.

[34] R. Weissleder, D.D. Stark, B.L. Engelstad, B.R. Bacon, C.C. Compton, D.L. White, P. Jacobs, J. Lewis, Superparamagnetic iron oxide: pharmacokinetics and toxicity, AJR Am J Roentgenol, 152 (1989) 167-173.

[35] R. Sharma, S. Saini, P.R. Ros, P.F. Hahn, W.C. Small, E.E. de Lange, A.E. Stillman, R.R. Edelman, V.M. Runge, E.K. Outwater, M. Morris, M. Lucas, Safety profile of ultrasmall superparamagnetic iron oxide ferumoxtran-10: phase II clinical trial data, J Magn Reson Imaging, 9 (1999) 291-294.

[36] J.L. Vivero-Escoto, Slowing, II, B.G. Trewyn, V.S. Lin, Mesoporous silica nanoparticles for intracellular controlled drug delivery, Small, 6 (2010) 1952-1967.

[37] M.V. Yezhelyev, L. Qi, R.M. O'Regan, S. Nie, X. Gao, Proton-sponge coated quantum dots for siRNA delivery and intracellular imaging, J Am Chem Soc, 130 (2008) 9006-9012.

[38] S.B. Rizvi, S. Ghaderi, M. Keshtgar, A.M. Seifalian, Semiconductor quantum dots as fluorescent probes for in vitro and in vivo bio-molecular and cellular imaging, Nano Rev, 1 (2010).

[39] R. Hardman, A toxicologic review of quantum dots: toxicity depends on physicochemical and environmental factors, Environ Health Perspect, 114 (2006) 165-172.

[40] P. Pericleous, M. Gazouli, A. Lyberopoulou, S. Rizos, N. Nikiteas, E.P. Efstathopoulos, Quantum dots hold promise for early cancer imaging and detection, Int J Cancer, (2012).

[41] H.K. Moon, S.H. Lee, H.C. Choi, *In vivo* near-infrared mediated tumor destruction by photothermal effect of carbon nanotubes, ACS Nano, 3 (2009) 3707-3713.

[42] Z. Liu, A.C. Fan, K. Rakhra, S. Sherlock, A. Goodwin, X. Chen, Q. Yang, D.W. Felsher, H. Dai, Supramolecular stacking of doxorubicin on carbon nanotubes for *in vivo* cancer therapy, Angew Chem Int Ed Engl, 48 (2009) 7668-7672.

[43] R. Singh, D. Pantarotto, L. Lacerda, G. Pastorin, C. Klumpp, M. Prato, A. Bianco, K. Kostarelos, Tissue biodistribution and blood clearance rates of intravenously administered carbon nanotube radiotracers, Proc Natl Acad Sci U S A, 103 (2006) 3357-3362.

[44] C.W. Lam, J.T. James, R. McCluskey, S. Arepalli, R.L. Hunter, A review of carbon nanotube toxicity and assessment of potential occupational and environmental health risks, Crit Rev Toxicol, 36 (2006) 189-217.

[45] K. Kostarelos, The long and short of carbon nanotube toxicity, Nat Biotechnol, 26 (2008) 774-776.

[46] K. Yang, Z. Liu, *In vivo* biodistribution, pharmacokinetics, and toxicology of carbon nanotubes, Curr Drug Metab, (2012).

[47] Y.S. Lin, C.L. Haynes, Impacts of mesoporous silica nanoparticle size, pore ordering, and pore integrity on hemolytic activity, J Am Chem Soc, 132 (2010) 4834-4842.

[48] F. Lu, S.H. Wu, Y. Hung, C.Y. Mou, Size effect on cell uptake in well-suspended, uniform mesoporous silica nanoparticles, Small, 5 (2009) 1408-1413.

[49] D. Napierska, L.C. Thomassen, V. Rabolli, D. Lison, L. Gonzalez, M. Kirsch-Volders, J.A. Martens, P.H. Hoet, Size-dependent cytotoxicity of monodisperse silica nanoparticles in human endothelial cells, Small, 5 (2009) 846-853.

[50] F. Alexis, E. Pridgen, L.K. Molnar, O.C. Farokhzad, Factors affecting the clearance and biodistribution of polymeric nanoparticles, Mol Pharm, 5 (2008) 505-515.

[51] G. Sonavane, K. Tomoda, K. Makino, Biodistribution of colloidal gold nanoparticles after intravenous administration: effect of particle size, Colloids Surf B Biointerfaces, 66 (2008) 274-280.

[52] G. Jia, Z. Cao, H. Xue, Y. Xu, S. Jiang, Novel zwitterionic-polymer-coated silica nanoparticles, Langmuir, 25 (2009) 3196-3199.

[53] Y. Geng, P. Dalhaimer, S. Cai, R. Tsai, M. Tewari, T. Minko, D.E. Discher, Shape effects of filaments versus spherical particles in flow and drug delivery, Nat Nanotechnol, 2 (2007) 249-255.

[54] B.P. Khanal, E.R. Zubarev, Purification of high aspect ratio gold nanorods: complete removal of platelets, J. Am. Chem. Soc., 130 (2008) 12634-12635.

[55] J.A. Champion, Y.K. Katare, S. Mitragotri, Particle shape: a new design parameter for micro- and nanoscale drug delivery carriers, J Control Release, 121 (2007) 3-9.

[56] J.A. Champion, S. Mitragotri, Shape induced inhibition of phagocytosis of polymer particles, Pharm Res, 26 (2009) 244-249.

[57] S.J. Son, X. Bai, A. Nan, H. Ghandehari, S.B. Lee, Template synthesis of multifunctional nanotubes for controlled release, J Control Release, 114 (2006) 143-152.

[58] H.L. Herd, A. Malugin, H. Ghandehari, Silica nanoconstruct cellular toleration threshold *in vitro*, J Control Release, 153 (2011) 40-48.

[59] Arnida, M.M. Janat-Amsbury, A. Ray, C.M. Peterson, H. Ghandehari, Geometry and surface characteristics of gold nanoparticles influence their biodistribution and uptake by macrophages, Eur J Pharm Biopharm, 77 (2011) 417-423.

[60] K. Yamashita, Y. Yoshioka, K. Higashisaka, K. Mimura, Y. Morishita, M. Nozaki, T. Yoshida, T. Ogura, H. Nabeshi, K. Nagano, Y. Abe, H. Kamada, Y. Monobe, T. Imazawa, H. Aoshima, K. Shishido, Y. Kawai, T. Mayumi, S. Tsunoda, N. Itoh, T. Yoshikawa, I. Yanagihara, S. Saito, Y. Tsutsumi, Silica and titanium dioxide nanoparticles cause pregnancy complications in mice, Nat Nanotechnol, 6 (2011) 321-328.

[61] K. Isoda, T. Hasezaki, M. Kondoh, Y. Tsutsumi, K. Yagi, Effect of surface charge on nano-sized silica particles-induced liver injury, Pharmazie, 66 (2011) 278-281.

[62] A.J. Gormley, A. Malugin, A. Ray, R. Robinson, H. Ghandehari, Biological evaluation of RGDfK-gold nanorod conjugates for prostate cancer treatment, J Drug Target, 19 (2011) 915-924.

[63] X. Huang, X. Peng, Y. Wang, D.M. Shin, M.A. El-Sayed, S. Nie, A reexamination of active and passive tumor targeting by using rod-shaped gold nanocrystals and covalently conjugated peptide ligands, ACS Nano, 4 (2010) 5887-5896.

[64] X. Sun, R. Rossin, J.L. Turner, M.L. Becker, M.J. Joralemon, M.J. Welch, K.L. Wooley, An assessment of the effects of shell cross-linked nanoparticle size, core composition, and surface PEGylation on in vivo biodistribution, Biomacromolecules, 6 (2005) 2541-2554.

[65] N. Nasongkla, B. Chen, N. Macaraeg, M.E. Fox, J.M. Frechet, F.C. Szoka, Dependence of pharmacokinetics and biodistribution on polymer architecture: effect of cyclic versus linear polymers, J Am Chem Soc, 131 (2009) 3842-3843.

[66] S.-H. Cheng, C.-H. Lee, M.-C. Chen, J.S. Souris, F.-G. Tseng, C.-S. Yang, C.-Y. Mou, C.-T. Chen, L.-W. Lo, Tri-functionalization of mesoporous silica nanoparticles for comprehensive cancer theranostics-the trio of imaging, targeting and therapy, J. Mater. Chem., 20 (2010) 6149–6157.

[67] J.M. Rosenholm, V. Mamaeva, C. Sahlgren, M. Linden, Nanoparticles in targeted cancer therapy: mesoporous silica nanoparticles entering preclinical development stage, Nanomedicine (Lond), 7 (2012) 111-120.

[68] F. Tang, L. Li, D. Chen, Mesoporous silica nanoparticles: synthesis, biocompatibility and drug delivery, Adv Mater, (2012).

[69] S.H. Wu, Y. Hung, C.Y. Mou, Mesoporous silica nanoparticles as nanocarriers, Chem Commun (Camb), 47 (2011) 9972-9985.

[70] F. Torney, B.G. Trewyn, V.S. Lin, K. Wang, Mesoporous silica nanoparticles deliver DNA and chemicals into plants, Nat Nanotechnol, 2 (2007) 295-300.

[71] S.E. Gratton, P.D. Pohlhaus, J. Lee, J. Guo, M.J. Cho, J.M. Desimone, Nanofabricated particles for engineered drug therapies: a preliminary biodistribution study of PRINT nanoparticles, J Control Release, 121 (2007) 10-18.

[72] X. Huang, L. Li, T. Liu, N. Hao, H. Liu, D. Chen, F. Tang, The shape effect of mesoporous silica nanoparticles on biodistribution, clearance, and biocompatibility *in vivo*, ACS Nano, 5 (2011) 5390-5399.

[73] A. Nan, X. Bai, S.J. Son, S.B. Lee, H. Ghandehari, Cellular uptake and cytotoxicity of silica nanotubes, Nano Lett, 8 (2008) 2150-2154.

[74] X. Bai, S.J. Son, S. Zhang, W. Liu, E.K. Jordan, J.A. Frank, T. Venkatesan, S.B. Lee, Synthesis of superparamagnetic nanotubes as MRI contrast agents and for cell labeling, Nanomedicine (Lond), 3 (2008) 163-174.

[75] W. Stöber, A. Fink, E. Bohn, Controlled growth of monodisperse silica spheres in the micron size range, Journal of Colloid and Interface Science, 26 (1968) 62-69.

[76] A.V. Blaaderen, J.V. Geest, A. Vrij, Monodisperse colloidal silica spheres from tetraalkoxysilanes: particle formation and growth mechanism, Journal of Colloid and Interface Science, 154 (1992) 481-501.

[77] A.v. Blaaderen, A. Vrij, Synthesis and characterization of colloidal dispersions of fluorescent, monodisperse silica spheres, Langmuir, 8 (1992) 2921-2931.

[78] C.T. Kresge, M.E. Leonowicz, W.J. Roth, J.C. Vartuli, J.S. Beck, Ordered mesoporous molecular sieves synthesized by a liquid-crystal template mechanism, Nature, 359 (1992) 710-712.

[79] J.S. Beck, J.C. Vartuli, W.J. Roth, M.E. Leonowicz, C.T. Kresge, K.D. Schmitt, C.T.W. Chu, D.H. Olson, E.W. Sheppard, A new family of mesoporous molecular sieves prepared with liquid crystal templates, J. Am. Chem. Soc., 114 (1992) 10834–10843.

[80] H.B. Lu, Y. Hu, M.H. Gu, S.C. Tang, H.M. Lu, X.K. Meng, Synthesis and characterization of silica–acrylic–epoxy hybrid coatings on 430 stainless steel, Surface & Coatings Technology, 204 (2009) 91-98.

[81] P. Selvam, S.K. Bhatia, C.G. Sonwane, Recent advances in processing and characterization of periodic mesoporous MCM-41 silicate molecular sieves, Ind. Eng. Chem. Res., 40 (2001) 3237-3261.

[82] D. Chen, L. Li, F. Tang, S. Qi, Facile and scalable synthesis of tailored silica „„nanorattle‟‟ structures, Adv. Mater., 21 (2009) 3804-3807.

[83] R. Erni, M.D. Rossell, C. Kisielowski, U. Dahmen, Atomic-resolution imaging with a sub-50-pm electron probe, Phys Rev Lett, 102 (2009) 096101.

[84] M. Gaumet, A. Vargas, R. Gurny, F. Delie, Nanoparticles for drug delivery: the need for precision in reporting particle size parameters, Eur J Pharm Biopharm, 69 (2008) 1-9.

[85] Y.S. Lin, N. Abadeer, C.L. Haynes, Stability of small mesoporous silica nanoparticles in biological media, Chem Commun (Camb), 47 (2011) 532-534.

[86] V. Stojanoff, B. Cappelle, Y. Epelboin, J. Hartwig, A.B. Moradela, F. Otalora, High resolution imaging as a characterization tool for biological crystals, Ann N Y Acad Sci, 1027 (2004) 48-55.

[87] M.H. Koch, P. Vachette, D.I. Svergun, Small-angle scattering: a view on the properties, structures and structural changes of biological macromolecules in solution, Q Rev Biophys, 36 (2003) 147-227.

[88] S. Brunauer, P.H. Emmett, E. Teller, Adsorption of gases in multimolecular layers, J. Am. Chem. Soc., 60 (1938) 309–319.

[89] R.B. Anderson, Pore distributions from desorption isotherms, Journal of Catalysis, 3 (1964) 50-56.

[90] C.P. Tsai, Y. Hung, Y.H. Chou, D.M. Huang, J.K. Hsiao, C. Chang, Y.C. Chen, C.Y. Mou, High-contrast paramagnetic fluorescent mesoporous silica nanorods as a multifunctional cell-imaging probe, Small, 4 (2008) 186-191.

[91] M. Vitale, L. Zamai, G. Mazzotti, A. Cataldi, E. Falcieri, Differential kinetics of propidium iodide uptake in apoptotic and necrotic thymocytes, Histochemistry, 100 (1993) 223-229.

[92] M.M. Song, W.J. Song, H. Bi, J. Wang, W.L. Wu, J. Sun, M. Yu, Cytotoxicity and cellular uptake of iron nanowires, Biomaterials, 31 (2010) 1509-1517.

[93] T. Xia, M. Kovochich, M. Liong, L. Madler, B. Gilbert, H. Shi, J.I. Yeh, J.I. Zink, A.E. Nel, Comparison of the mechanism of toxicity of zinc oxide and cerium oxide nanoparticles based on dissolution and oxidative stress properties, ACS Nano, 2 (2008) 2121-2134.

[94] R. Gref, M. Luck, P. Quellec, M. Marchand, E. Dellacherie, S. Harnisch, T. Blunk, R.H. Muller, 'Stealth' corona-core nanoparticles surface modified by polyethylene glycol (PEG): influences of the corona (PEG chain length and surface density) and of the core composition on phagocytic uptake and plasma protein adsorption, Colloids Surf B Biointerfaces, 18 (2000) 301-313.

[95] L. Li, F. Tang, H. Liu, T. Liu, N. Hao, D. Chen, X. Teng, J. He, *In vivo* delivery of silica nanorattle encapsulated docetaxel for liver cancer therapy with low toxicity and high efficacy, ACS Nano, 4 (2010) 6874-6882.

[96] J. Chen, X. Dong, J. Zhao, G. Tang, *In vivo* acute toxicity of titanium dioxide nanoparticles to mice after intraperitoneal injection, J Appl Toxicol, 29 (2009) 330-337.

[97] Z. Chen, H. Meng, G. Xing, C. Chen, Y. Zhao, G. Jia, T. Wang, H. Yuan, C. Ye, F. Zhao, Z. Chai, C. Zhu, X. Fang, B. Ma, L. Wan, Acute toxicological effects of copper nanoparticles *in vivo*, Toxicol Lett, 163 (2006) 109-120.

[98] J.S. Souris, C.H. Lee, S.H. Cheng, C.T. Chen, C.S. Yang, J.A. Ho, C.Y. Mou, L.W. Lo, Surface charge-mediated rapid hepatobiliary excretion of mesoporous silica nanoparticles, Biomaterials, 31 (2010) 5564-5574.

[99] R. Kumar, I. Roy, T.Y. Ohulchanskky, L.A. Vathy, E.J. Bergey, M. Sajjad, P.N. Prasad, *In vivo* biodistribution and clearance studies using multimodal organically modified silica nanoparticles, ACS Nano, 4 (2010) 699-708.

[100] Q. He, Z. Zhang, F. Gao, Y. Li, J. Shi, *In vivo* biodistribution and urinary excretion of mesoporous silica nanoparticles: effects of particle size and PEGylation, Small, 7 (2011) 271-280.

[101] X. He, H. Nie, K. Wang, W. Tan, X. Wu, P. Zhang, *In vivo* study of biodistribution and urinary excretion of surface-modified silica nanoparticles, Anal Chem, 80 (2008) 9597-9603.

[102] J. Lu, M. Liong, Z. Li, J.I. Zink, F. Tamanoi, Biocompatibility, biodistribution, and drug-delivery efficiency of mesoporous silica nanoparticles for cancer therapy in animals, Small, 6 (2010) 1794-1805.

CHAPTER 3

IMPACT OF SILICA NANOPARTICLE DESIGN ON CELLULAR TOXICITY AND HEMOLYTIC ACTIVITY

3.1 Introduction

It has been suggested that particle shape can influence cellular uptake and toxicity *in vitro* [1-3]. For example, it has been reported that high-aspect-ratio cationic hydrogel particles (150 × 450 nm) were internalized by HeLa cells four times faster than corresponding low-aspect-ratio particles (200 × 200 nm) [1]. In addition to geometry, porosity and surface functionality of nanoparticles are also critical factors that can influence the interaction of silica nanoparticles with biological systems [4-6]. Maurer-Jones *et al.* have demonstrated that 25 nm nonporous SiO_2 had a greater impact on cells than 25 nm porous SiO_2 since the former possessed higher "cell-contactable reactive surface area" to perturb cell function [5]. Slowing *et al.* have reported that the uptake of mesoporous silica nanoparticles by cervical cancer cells could be elevated by surface functionalization with cationic functionalities or targeting moiety [6]. Despite these initial studies, there is a need for a systematic investigation of the interdependent roles of nanoparticle geometrical effect, porosity, and surface functionality on cellular uptake and toxicity [7-9]. Such studies will enable the elucidation of predominant factors that determine the extent of toxicity, which will then provide practical guidance for rationally

designing SiO_2 for biomedical applications with minimum adverse effects.

In this chapter, multiple physicochemical parameters of SiO_2 were evaluated for their effects on cellular toxicity and hemolytic activity. In order to compare the effect of pore size, mesoporous and nonporous spherical SiO_2 of the same diameter (ca. 110 nm) were synthesized and evaluated. To demonstrate the effect of geometrical feature (represented as aspect ratio, ratio of length over width), silica nanorods were produced with similar diameters along the short axis (around 100 nm) and different lengths along the long axis (approximately 200 nm, 600 nm, 1,000 nm). SiO_2 of different porosities and aspect ratios were modified with primary amine silane groups to generate cationic charge and compared with the anionic bare silica nanoparticles to assess the impact of surface charge. SiO_2 with the engineered physicochemical features as mentioned above were subject to a series of toxicity assays on two model cell lines, namely RAW 264.7 (a model macrophage commonly used to represent the physiological scavengers of foreign nanoparticles exposed to *in vivo* systems [10]) and A549 (the non-small-cell lung cancer epithelial cells). These cells were selected as models for potential targeted delivery of bioactive and imaging agents. We further characterized the hemolytic activity of SiO_2 as an initial step to evaluate *ex vivo* blood biocompatibility.

3.2 Methods

3.2.1 Synthesis of nonporous and mesoporous SiO_2

Nonporous silica nanoparticles (Stöber) were produced using the modified Stöber method [11]. 34.82 mL water, 3.25 mL ammonium hydroxide solution (29.7%), and 100 mL ethanol were mixed and stabilized at 40 ^{o}C. 6.20 mL TEOS was added at an injection rate of 5 mL/min upon stirring at 550 rpm. The reaction was conducted for 1 hour and the

product was washed twice by ethanol and stored in ethanol. Mesoporous SiO_2 of different shapes were synthesized through a one-step condensation under a dilute silica source and low surfactant concentration conditions with ammonium hydroxide solution as the base catalyst [12-17]. CTAB was dissolved in aqueous medium with mild heating (30 ^oC). After the solution was cooled to room temperature (22 ^oC), aqueous ammonia solution was introduced and the mixture was stirred for an hour. TEOS was added at the rate of 5 mL/minute while the stirring continued. The mixture was further stirred for 4 hours and the product was autoclaved at 100 ^oC for 24 hours [18, 19]. Subsequently the product was collected by centrifugation at 15,000 rpm for 20 minutes. As-synthesized nanoparticles were suspended in ethanolic HCl (1.5 mL HCl in 150 mL ethanol) and heated at 60^oC for 6 hours to remove the surfactant. The complete removal of CTAB was confirmed by FT-IR spectroscopy.

3.2.2 Surface functionalization

To modify the surface of SiO_2 with primary amine functionalities [20], 100 mg of SiO_2 were resuspended in 100 mL of anhydrous ethanol. (3-aminopropyl)triethoxysilane APTES was introduced drip by drip to SiO_2 suspension upon stirring at 500 rpm under nitrogen flow. The mixture was stirred at room temperature for 20 hours. Amine-modified SiO_2 were collected by centrifugation and washed extensively with ethanol and water. SiO_2 were stored in ethanol at 4^oC and transferred to water immediately before use.

3.2.3 Nanoparticle characterization

TEM images were taken with a Philips Tecnai microscope operating at 120 kV. FT-IR spectra were recorded on a Varian Cary FTIR 1000 spectrometer using KBr pellets. XRD patterns of SiO_2 were analyzed on a Philips PANalytical X'Pert X-ray diffractometer (Spectris, England) using Cu Ka radiation (λ = 0.1542 nm) at 45 kV and 40 mA. The XRD spectra were recorded in the 2θ range of 2-10 with a step size of 0.02^o in a 2θ scattering angle and a scanning speed of 0.01 degree/second. The slit sizes and specimen length were also adjusted for divergence slit, antiscattered slit, and receiving slit to suit for the low angle detection. Nitrogen adsorption–desorption isotherm measurements were completed on a Micromeritics ASAP 2010 (Norcross, GA) accelerated surface area analyzer at -196 ^oC. The SiO_2 were dried at 100 ^oC overnight before analysis. The BET-specific surface areas were calculated by using adsorption data at P/P_0 = 0.05–0.20 [7, 9]. The external surface areas of mesoporous SiO_2 were calculated from the *t* plots of their N_2 adsorption isotherms [21]. Pore volume and Pore size distributions were obtained from adsorption branch by using the BJH method [7, 9].

3.2.4 Acute cytotoxicity assay

The acute toxicity effect of SiO_2 was determined by WST-8 assay on A549 cells or RAW 264.7 (ATCC, Manassas, VA). Cells from passages 5 through 20 were used with medium changing once every 3 days. A549 cells or RAW 264.7 macrophages were seeded at 8,000 cells/well or 16,000 cells/well in a 96-well plate in F-12k medium or DMEM supplemented with 10% fetal bovine serum (FBS) and maintained in a humidified incubator for 24 hours. SiO_2 at incremental concentrations of 100, 250, or 500 μg/mL were added to cells. Supernatants from nanoparticle stock solutions and respective

growth medium only were served as controls. Post-24 hours, old medium was aspirated and cells were washed three times with phosphate buffered saline (PBS). 100 μL complete medium containing 10% (v/v) Cell Counting Kit-8 (Dojindo, Rockville, MD) was added to each well and incubated with cells for 2 hours. The absorbance of the plate was recorded at 450 nm on a UV/Vis reader with a reference wavelength of 650 nm.

3.2.5 Proliferation inhibition assay

The cytotoxicity of SiO_2 was evaluated by WST-8 viability assay on A549 cells or RAW264.7 macrophages. Initially, A549 or RAW cells were seeded at 2,000 cells/well or 4,000 cells/ well in a 96-well plate and allowed settlement for 24 hours. 10, 50, 100, 250, 500, or 1,000 μg/mL of bare SiO_2 or amine-modified SiO_2 were added into the 96-well plate in triplicates. Supernatants from nanoparticle stock solutions and respective growth medium served as controls. Post 72 hours, old medium was aspirated and the following steps were the same as the procedures for acute cytotoxicity assay described above.

3.2.6 Plasma membrane integrity assay

Determination of propidium iodide uptake was used to assess the integrity of the plasma membrane of nanoparticle-dosed cells. A549 cells or RAW cells were seeded at 8×10^4 cells/well or 1.6×10^5 cells/well on a 12-well plate in triplicate. After 24 hours, selected nanoparticles were added into each well at the concentration of 250 μg/mL. 24 hours later, cells and medium from each well were collected into a 5 mL flow cytometry tube. The cell suspension was centrifuged at 1000 rpm × 5 minutes, supernatant was decanted, and the cells were resuspended in 100 μL of PBS. 5 μL of propidium iodide

solution (50 μg/mL in water) was added to each tube. The tube was gently vortexed and incubated for 15 minutes at room temperature in the dark. 400 μL of PBS was added into each tube and the samples were analyzed by flow cytometry (FACScan Analyzer, Becton Dickinson, Franklin Lakes, NJ) within an hour.

3.2.7 Quantitation of cellular association

Cellular association of SiO_2 was evaluated on A549 cells and RAW264.7 cells. A549 cells or RAW cells were seeded at 8×10^4 cells/well or 1.6×10^5 cells/well on a 12-well plate in triplicate, 24 hours before the addition of particles. Cells were incubated with 100 μg/mL of SiO_2 for 24 hours (37°C, 5% CO_2). After cell/particle incubation, the old medium was aspirated and the cells were washed three times with PBS. Then the cells were treated with 0.5 mL of 0.1% (v/v) Triton X-100 solution in water for 15 minutes. After that, the cell lysate was collected into a centrifuge tube and the wells were further washed with 0.5 mL water. The wash was also collected into the same centrifuge tube. 100 μL aliquots of cell lysate were used for protein content measurement by BCA assay (Thermo Scientific, Rockford, IL). The concentration of silicon in the cell lysate was measured by direct Si measurement using ICP-MS (Agilent 7500, Agilent Technologies, Santa Clara, CA). The amount of cellular-associated SiO_2 post-1 hour incubation at 4 ^oC or 37 ^oC was also measured. RAW cells were seeded at 3.2×10^5 cells/well on a 12-well plate in triplicate and incubated for 24 hours. After that, cells were preconditioned to 4 ^oC by incubating at 4 ^oC for a brief period of 10 minutes. Then silica nanoparticles were added to the cells at the concentration of 100 μg/mL and the cells were further incubated at 4 ^oC for another hour. Following treatment was the same as mentioned above. To make sure that relative cell viability in the 4 ^oC treated plate was not dramatically influenced by

exposure to cold temperature for the experimental duration, the relative viability from 4 ^{o}C treated plate was compared with cells incubated at 37 ^{o}C for 70 minutes by WST-8 assay.

3.2.8 Hemolysis

Heparin-stabilized human blood was freshly collected according to an approved University of Utah Institutional Review Board protocol and used within 3 hours of being drawn [22, 23]. 4 mL of whole blood was added to 8 mL of Dulbecco's phosphate buffered saline (D-PBS) and the red blood cells (RBCs) were isolated from serum by centrifugation at 10,016 × g for 5 minutes. The RBCs were further washed five times with sterile D-PBS solution. Following the last wash, the RBCs were diluted to 40 mL of D-PBS. 0.2 mL of the diluted RBC suspension was added to 0.8 mL of silica nanoparticle suspension in D-PBS at the concentrations of 12.5 μg/mL, 62.5 μg/mL, 125 μg/mL, 312.5 μg/mL, or 625 μg/mL to make the final nanoparticle concentration at 10, 50, 100, 250, or 500 μg/mL. All samples were prepared in triplicate and the suspension was briefly vortexed before leaving at static condition at room temperature for 4 hours. After that, the mixture was briefly vortexed again and centrifuged at 10,016 × g for 3 minutes. 100 μL of supernatant from the sample tube was transferred to a 96-well plate. The absorbance value of hemoglobin at 577 nm was measured with the reference wavelength at 655 nm. 0.2 mL diluted RBC suspensions incubated with 0.8 mL of D-PBS and 0.8 mL of water were used as the negative or positive control. The percent of hemolysis was calculated as: Hemolysis % = [(Sample absorbance – negative control) / (positive control – negative control)] × 100%.

3.2.9 Statistical analysis

The difference between multiple groups was analyzed by one-way analysis of variance (ANOVA); Tukey post test was used where difference was detected. For two group comparison, Student's *t*-test was used. The difference between two groups was considered significant when $p < 0.05$. The nanoparticle concentrations that led to 10% hemolysis (LC_{10}) in hemolysis assay were determined by using ED50plus v1.0 software.

3.3 Results and discussion

Nonporous SiO_2 and mesoporous SiO_2 of different geometrical features were synthesized and characterized using TEM, XRD, and nitrogen adsorption-desorption isotherm analysis for size, mesopore arrangement, surface area, and pore size measurement (Table 3.1). Mesoporous SiO_2 of different shapes were synthesized by a one-step condensation and aging method [7, 12-17]. In the first step, mesoporous SiO_2 were formed by condensation under a dilute silica source and low surfactant concentration conditions with ammonium hydroxide as the base catalyst. The shape and polydispersity of SiO_2 was mainly controlled by molar composition of reaction agents [12-16] and stirring rate [17]. By changing the concentration of TEOS, CTAB, and aqueous ammonia, and reaction stirring rate, mesoporous SiO_2 with targeted diameters (ca. 100 nm), lengths, and aspect ratios (1, 2, 4, 8) were synthesized. In general, the width of mesoporous SiO_2 was controlled by adjusting the ammonia concentration in the reaction mixture [7] with larger width obtained at increased ammonia concentration, while the length of mesoporous SiO_2 increased with increased TEOS concentration, increased CTAB concentration, increased ammonia concentration, and reduced stirring speed [16, 17]. In the second step, mesoporous SiO_2 were subject to autoclaving at

Table 3.1 Synthetic conditions of nonporous and mesoporous SiO_2 and their physical characterization of size, surface area, and pore size.*

	Stöber	**Meso S**	**AR2**	**AR4**	**AR8**
Composition (CTAB:H_2O: NH_4OH:TEOS)	See "METHODS"	0.1:1000: 7:0.7	0.2:1000: 5:0.7	0.4:1000:10: 1.4	0.4:1000:10: 1.4
Stirring rate (RPM)	550	250	230	350	250
Temperature (^oC)	40	22	22	22	22
Size by TEM (nm)	115 ± 13	120 ± 25	77 ± 9 × 198 ± 53	159 ± 49 × 594 ± 82	136 ± 26 × 1028 ± 139
Aspect ratio	1	1	2.5	3.8	7.6
Surface area (m^2/g)	24	663	443	1191	284
External surface area (m^2/g)	24	109	102	231	47
Pore volume (cm^3/g)	N/A	0.63	0.59	1.17	0.26
Pore size (nm)	N/A	2.7	2.7	2.8	2.7

*Data were mean ± SD (n = 3).

100 ^{o}C for 24 hours to promote silica matrix crosslinking and to enhance the stability of mesopore structure [18, 19].

Evident from TEM image analysis (Figure 3.1), nonporous silica nanospheres (Stöber) and mesoporous silica nanospheres (Meso S) were 115 ± 13 nm and 120 ± 25 nm in diameter, respectively. Mesoporous silica nanorods were produced with distinctly different geometrical features. They possessed similar diameter as that of nanospheres (around 100 nm), yet the aspect ratios were different (mesoporous SiO_2 with aspect ratio 2, 4, 8 were abbreviated as AR2, AR4, and AR8, respectively). The aspect ratio distribution histogram showed that each type of mesoporous SiO_2 possessed distinct shape characteristics compared with any other type of mesoporous SiO_2 (Figure 3.1G), except that AR2 and AR4 had a certain portion of overlapped aspect ratios. However, they still possessed distinct geometrical features considering their dimensions were significantly different from each other along the short or long axes.

Figure 3.2 presents the nitrogen adsorption-desorption isotherms for mesoporous SiO_2 of different shapes. Mesoporous SiO_2 exhibited type IV isotherms, which were typical of a mesopore structure. The filling of mesopores occurred at relative pressure (P/P_0) of 0.3 to 0.5. Each type of nanoparticles also exhibited an additional capillary condensation at high relative pressure ($P/P_0 > 0.90$), which was characteristic of a high degree of textural porosity [7, 9]. Mesoporous SiO_2 possessed relatively high surface area (280 – 1190 m^2/g), as calculated by the BET method (Table 3.1) [7, 9]. The external surface areas of mesoporous SiO_2, which referred to cell-contactable surface area, were calculated from the *t* plots of their N_2 adsorption isotherms (Table 3.1) [21]. Different mesoporous nanoparticles displayed a narrow distribution of pore size which centered

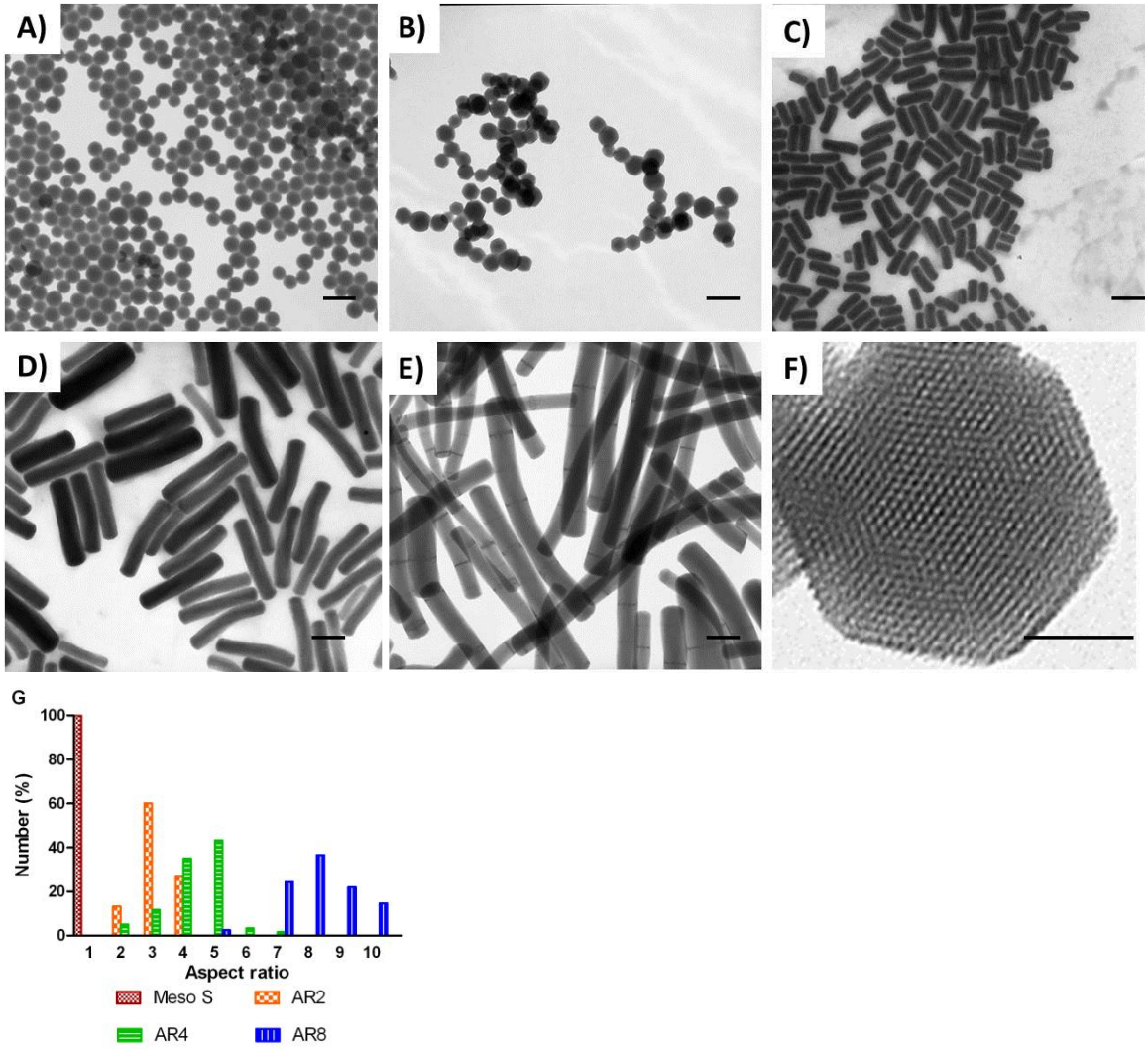

Figure 3.1 TEM images of A) Stöber SiO_2 with average diameter of 115 nm (referred to as Stöber), B) mesoporous SiO_2 with average diameter of 120 nm (Meso S), C) mesoporous silica nanorods with aspect ratio 2 (AR2), D) mesoporous silica nanorods with aspect ratio 4 (AR4), E) mesoporous silica nanorods with aspect ratio 8 (AR8), and F) high resolution image of a single particle in B), G) The percentage distribution histogram as a function of aspect ratio. Scale bars in A-E = 200 nm, scale bar in F = 50 nm.

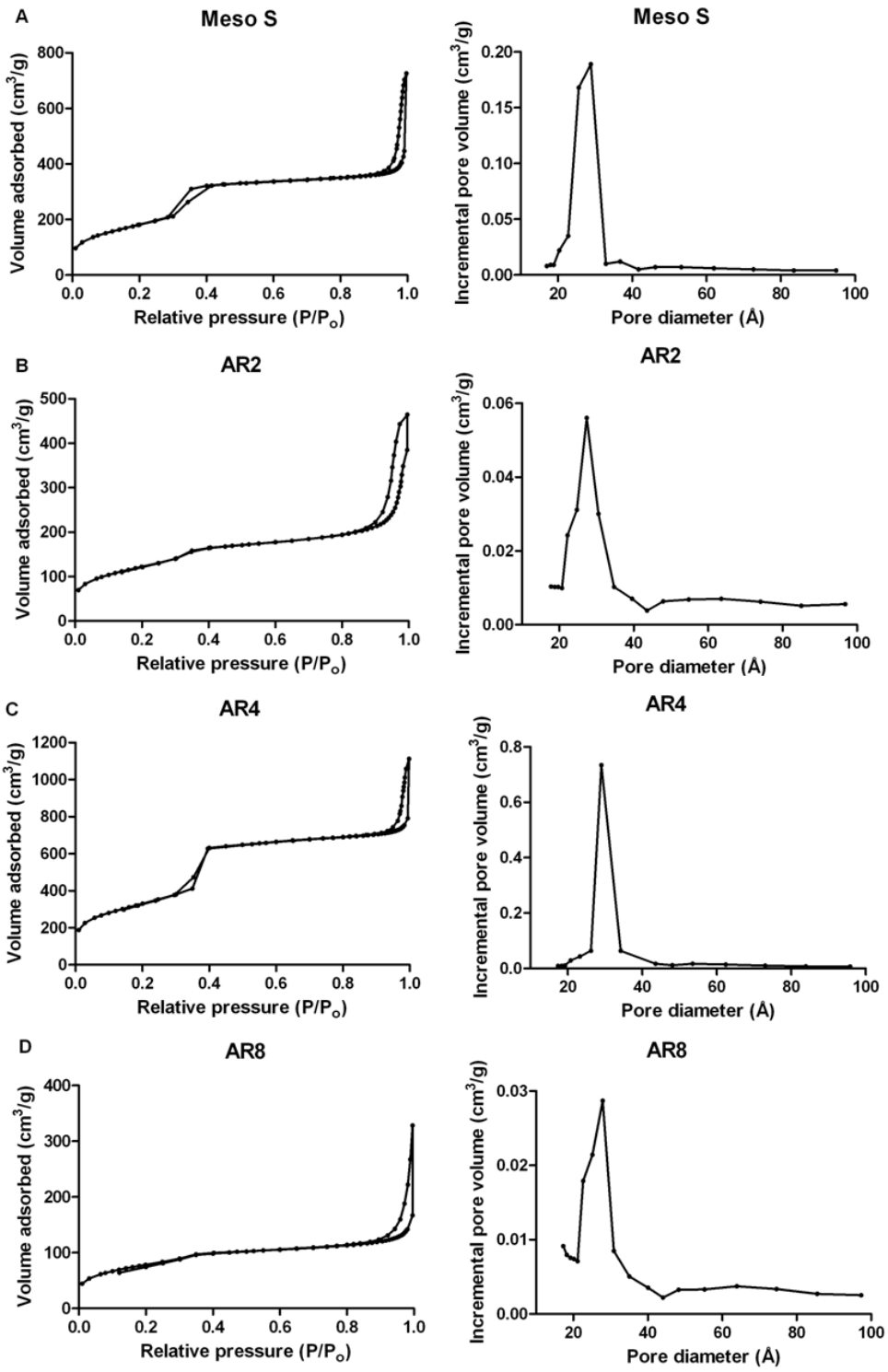

Figure 3.2 Nitrogen adsorption-desorption isotherms of: A) Meso S, B) AR2, C) AR4, D) AR8 mesoporous SiO_2. Pore size distribution plot for each type of SiO_2 is shown on the right.

around 2.7-2.8 nm in diameter, as determined by the BJH method (Table 3.1) [7, 9]. Meso S possessed typical MCM-41 type mesopore arrangement as reflected by the distinct peaks (100, 110, 200, 210) in XRD measurement (Figure 3.3A), which was in a good agreement with its high resolution TEM image (Figure 3.1F) showing 2D-hexagonal mesopores in the close-packing structure for this type of SiO_2 [16]. The mesopore structure of Meso S was also well maintained post-amine modification (Figure 3.3B). Therefore, Meso S was compared with nonporous Stöber nanoparticles to study the pore size effect on cellular toxicity and hemolytic activity.

The DLS measurements showed that the Meso S tended to agglomerate to a higher extent (257.8 ± 0.9 nm) and was thus more polydisperse in size distribution than Stöber (148.0 ± 0.4 nm) (Table 3.2). Due to the method limitations, DLS measurements are not applicable to mesoporous silica nanorod structure because such a measurement model assumes spherical shape of nanoparticles in suspension [17]. Zeta potential measurements showed that Stöber nanoparticles were highly negatively charged (-50.4 ± 1.0 mV), indicating a fairly stable suspension in aqueous medium [20]. Amine-modified Stöber (SA) nanoparticles had relatively lower positive zeta potential (17.0 ± 0.7 mV), which implied a moderate stability in aqueous suspension (Table 3.2) [19]. Mesoporous SiO_2 were highly negatively charged (< -30 mV) as bare nanoparticles and were all highly positively charged (> 30 mV) post-amine modification, which indicated a high stability within suspension (The amine-modified mesoporous nanospheres or nanorods with aspect ratio of 2, 4, 8 were abbreviated as MA, 2A, 4A, and 8A) [20]. Zeta potential measurements showed the dramatic surface charge difference between bare nanoparticles and their amine-modified counterparts, indicating the successful amine modification

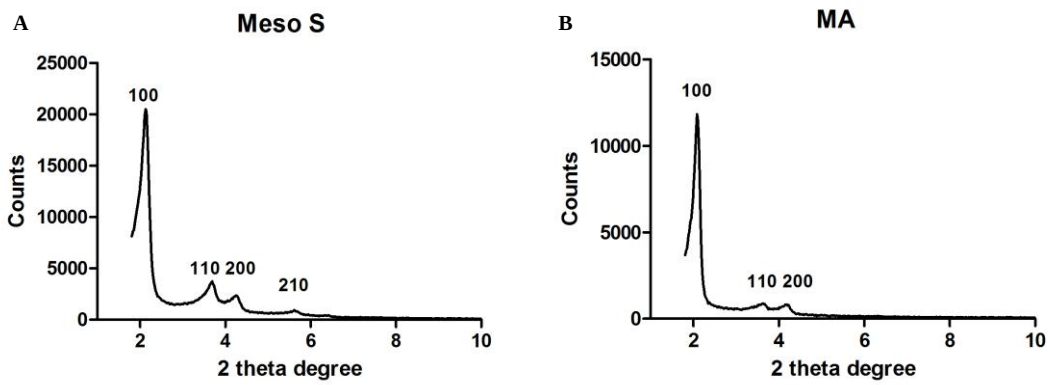

Figure 3.3 XRD patterns of A) Meso S and B) MA. Both Meso S and MA exhibited the typical diffraction patterns of MCM-41 type mesoporous SiO_2 with hexagonal symmetry. The reduction in intensity of MA diffraction pattern and the missing 210 peak might be due to the pore filling effects caused by silane modification [9].

Table 3.2 Hydrodynamic size and surface charge of SiO_2 before and after primary amine modification in aqueous suspension at pH 7.0.*

	Before APTES modification		**Post-APTES modification**	
	Size by DLS (nm)/PDI	**Zeta potential (mV)**	**Size by DLS (nm)/PDI**	**Zeta potential (mV)**
Stöber	148.0 ± 0.4/0.043	-50.4 ± 1.0	174.2 ± 1.9/0.102	17.0 ± 0.7
Meso S	257.8 ± 0.9/0.219	-39.4 ± 0.5	233.8 ± 2.2/0.145	32.4 ± 0.9
AR2	N/A	-33.5 ± 0.5	N/A	32.0 ± 1.0
AR4	N/A	-34.0 ± 1.2	N/A	40.3 ± 1.0
AR8	N/A	-36.6 ± 0.6	N/A	36.7 ± 0.5

*Data were mean of average diameter/zeta potential of each measurement ± SD (n = 1 in triplicate measurements). PDI, polydispersity index.

which allowed the comparative evaluation of the effect of surface characteristics on biological systems. However, it should be noted that the absolute value of zeta potential would shift in other media that were used in *in vitro* or *in vivo* analysis. Thus, the effect of surface characteristics in *in vitro* or *in vivo* studies was probably due to differential presence of surface functionalities rather than the absolute zeta potential values. The absence of carbon chain band (wavenumber 3000 – 2800) in the FT-IR spectrum of surfactant-removed nanoparticles confirmed the complete removal of CTAB from the products by acidic ethanol extraction method (Figure 3.4). The endpoint chromogenic Limulus amebocyte lysate (LAL) test (Lonza, Walkersville, MD) showed that there was no detectable gram negative endotoxin on any type of nanoparticles at 1 mg/mL (the detection limit was less than 0.1 EU/mL), which was the highest concentration of nanoparticles used in the *in vitro* and *ex vivo* studies. However, it must be noted that LAL assays could not effectively indicate the amount of endotoxin potentially adsorbed on nanoparticle surface [24]. Thus, the results from LAL assay showed that the level of soluble endotoxin in nanoparticle suspension was below the detection limit.

The ability of SiO_2 with the engineered physicochemical features to induce acute cellular toxicity response was tested on RAW 264.7 and A549 cells by WST-8 assay. Results demonstrated that toxicity of SiO_2 was highly cell-type and nanoparticle-concentration dependent (Figures 3.5-3.6). All types of SiO_2 at concentration as high as 500 μg/mL did not affect the relative viability of A549 cells after 24 hours exposure. For RAW 264.7 macrophages, nonporous or mesoporous SiO_2 caused dramatic toxicity post-24 hour incubation, leaving only ca. 20-40% viable cells compared with controls, while amine-modified counterparts caused limited toxicity with approximately 64-85% relative

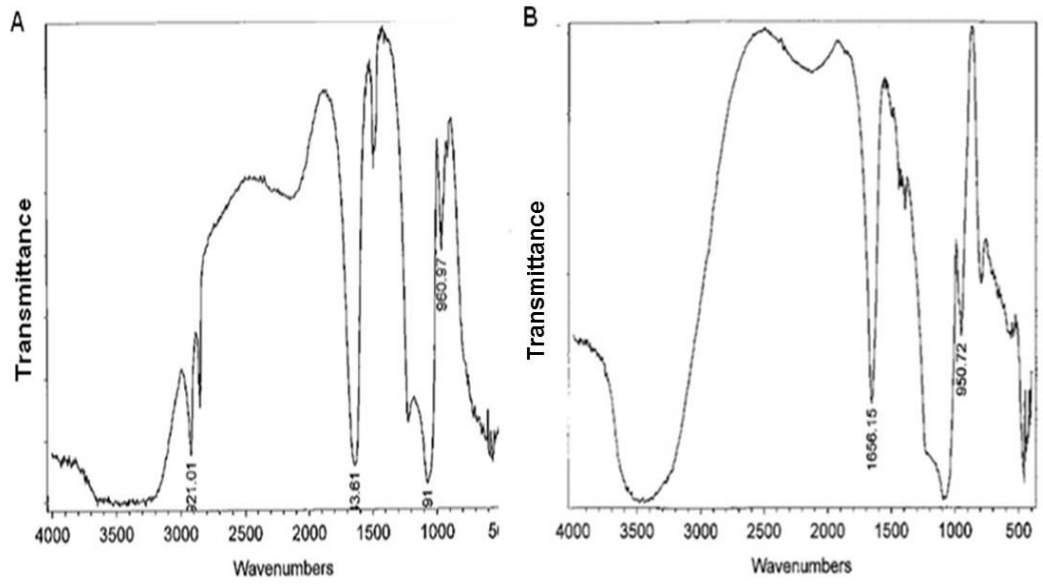

Figure 3.4 Typical FT-IR spectra of A) as-synthesized mesoporous SiO_2 and B) surfactant-removed mesoporous SiO_2.

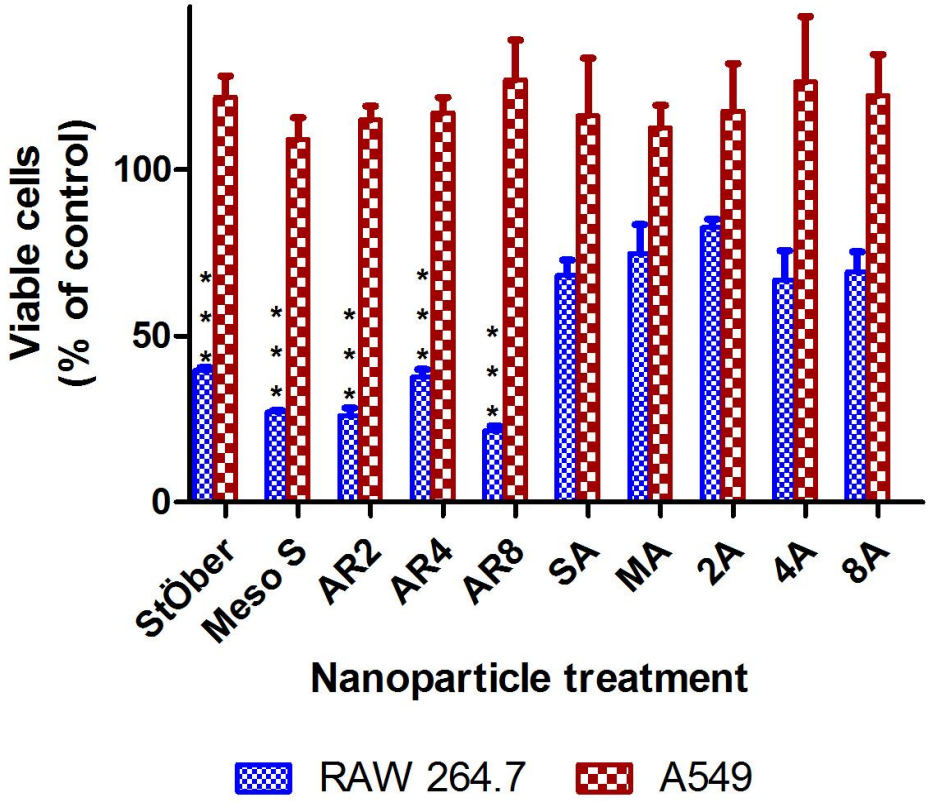

Figure 3.5 Acute cytotoxicity assay of indicated cells incubated with bare and amine-modified SiO_2 at 500 µg/mL. *** Relative viability of bare silica nanoparticle-treated cells was significantly lower than that of amine-modified counterpart-treated cells ($p < 0.001$). Data were mean ± SD ($n = 3$).

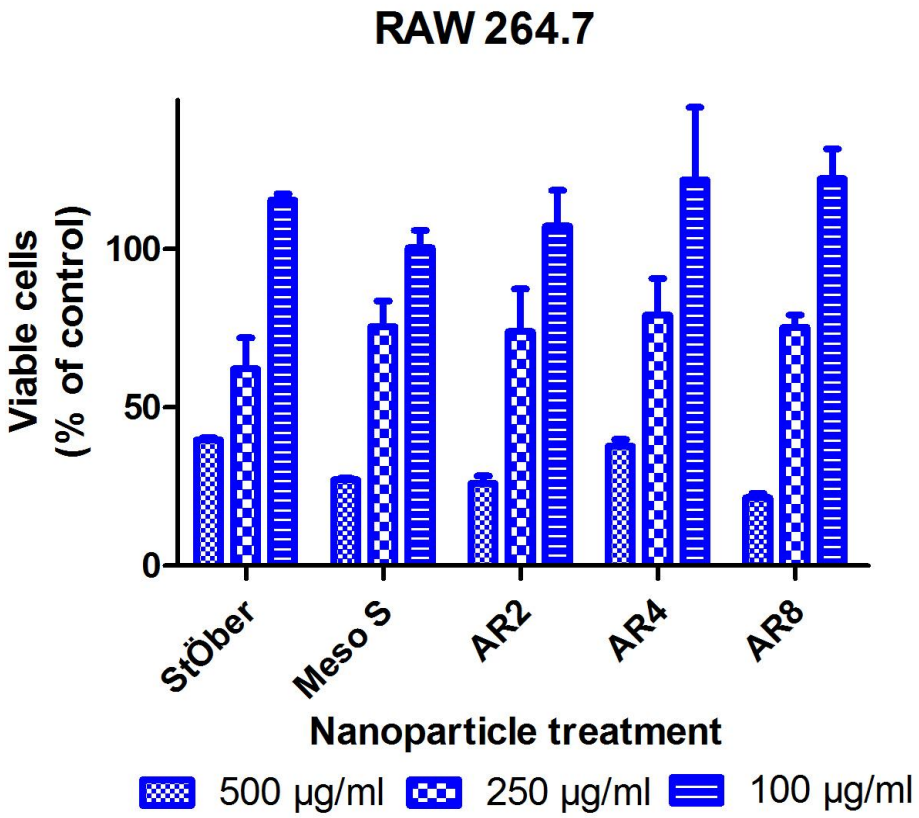

Figure 3.6 Acute cytotoxicity assay of RAW 264.7 cells after incubating with bare SiO_2 at 500 µg/mL, 250 µg/mL, and 100 µg/mL for 24 hours.

viability (Figure 3.5). Since bare SiO_2 showed higher cytotoxicity on RAW 264.7, doses that led to reduced toxicity (250 μg/mL with ca. 70% viability) or nontoxicity (100 μg/mL with ca. 100% viability) have been identified (Figure 3.6) to be used in the plasma membrane integrity assay or nanoparticle cellular association quantitation assay.

The ability of nanoparticles to inhibit cell proliferation was cell type-dependent (Figures 3.7-3.10). Cancer epithelial cells were resistant to all types of nanoparticle treatment up to 500 μg/mL post-72-hour exposure, and only cells treated with 2A and 8A at 1000 μg/mL exhibited moderate toxicity response, resulting in 60-70% viable cells compared with controls (Figures 3.7-3.8). For macrophages, the nanoparticle concentration that led to 50% inhibition on cell growth (IC_{50}) ranged approximately from 50 to 100 μg/mL post-3-day exposure for bare SiO_2 (Figure 3.9) and the IC_{50} of bare nonporous and mesoporous SiO_2 were not distinguishable from one another ($p > 0.05$). Interestingly, the reduction of IC_{50} was not observed for nanoparticles post-amine modification. Instead, several-fold increase in IC_{50} was detected for amine-modified nanoparticles (Figure 3.10, Table 3.3). For example, the IC_{50} of AR4 and 4A were 91.6 ± 5.9 μg/mL and 184.2 ± 17.1 μg/mL, respectively and IC_{50} of AR8 and 8A were 73.7 ± 17.0 μg/mL and 224.9 ± 28.2 μg/mL, respectively. Changes in cell morphology were observed in RAW 264.7 post-nanoparticle exposure for 24 hours (Figure 3.11) or 72 hours (Figure 3.12). Reduced cell density and rounded cells were observed for bare SiO_2 treated macrophages while swollen vacuoles in cells were frequently observed in amine-modified SiO_2 treated macrophages.

To assess whether toxicity was due to soluble factors that were released from nanoparticles [25], the toxicity assay was performed on the supernatant of nanoparticle

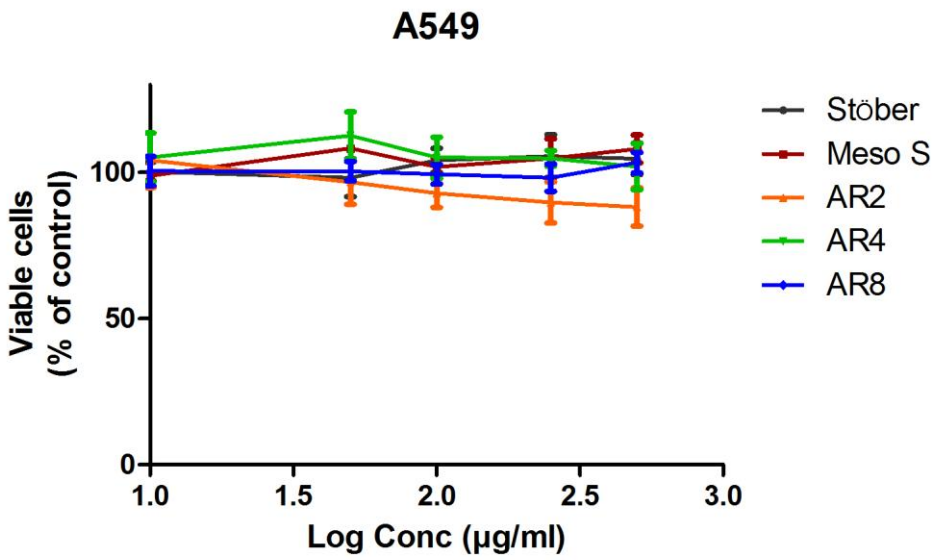

Figure 3.7 Proliferation inhibition assay of A549 cells after continuous 72 hours incubation with bare SiO_2. Data were mean ± SD (n = 3).

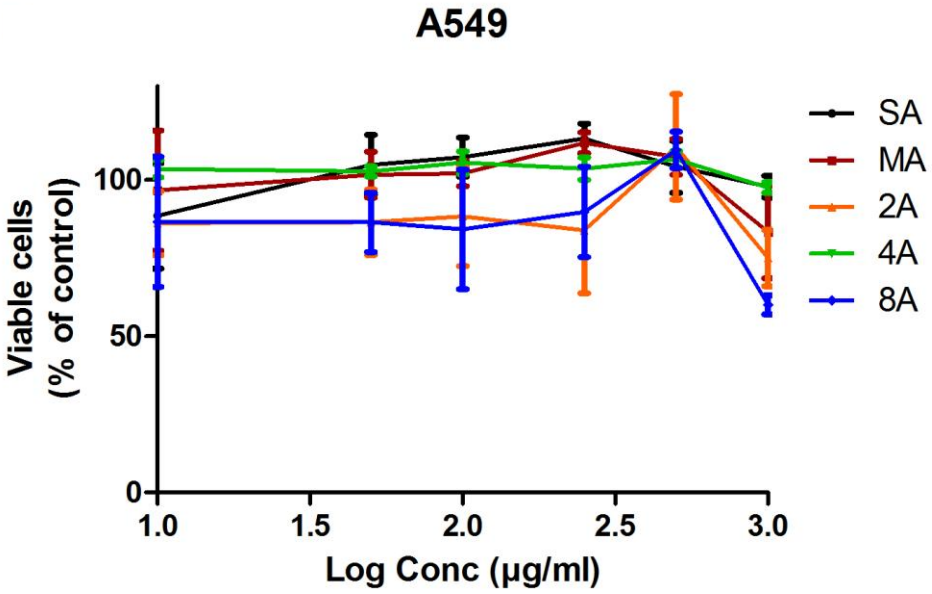

Figure 3.8 Proliferation inhibition assay of A549 cells after continuous 72 hours incubation with amine-modified SiO_2. Data were mean ± SD (n = 3).

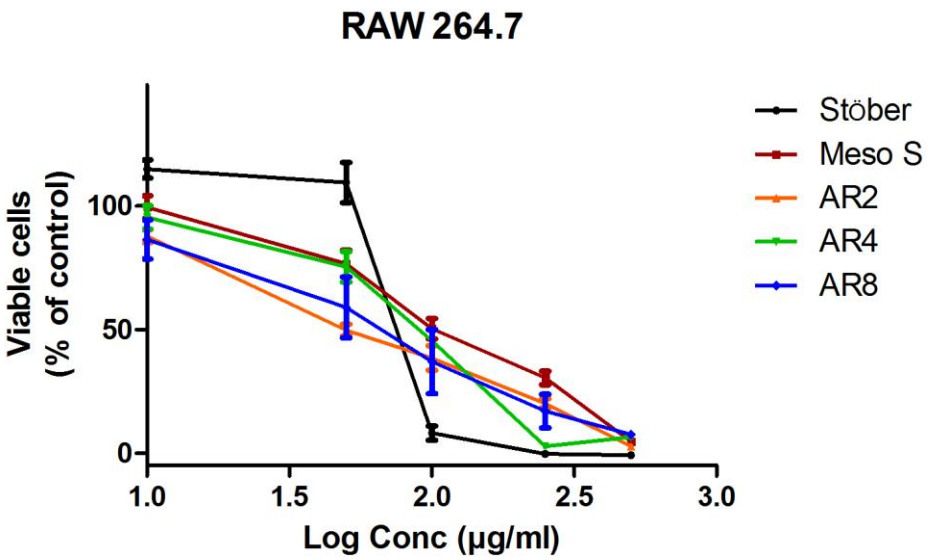

Figure 3.9 Proliferation inhibition assay of RAW 264.7 cells after continuous 72 hours incubation with bare SiO_2. Data were mean ± SD (n = 3).

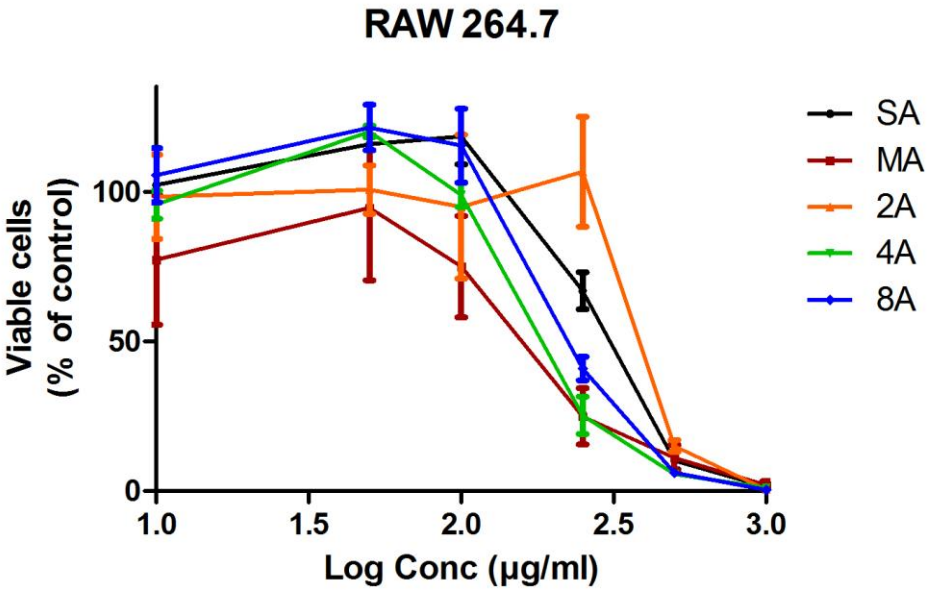

Figure 3.10 Proliferation inhibition assay of RAW 264.7 cells after continuous 72 hours incubation with amine-modified SiO_2. Data were mean ± SD (n = 3).

Table 3.3 Summary of IC_{50} values of SiO_2 on RAW 264.7 macrophages.[*]

IC_{50} values (μg/mL)	Stöber	Meso S	AR2	AR4	AR8
Bare nanoparticles[#]	73 ± 3	89 ± 4	72 ± 12	92 ± 6	74 ± 18
Amine-modified nanoparticles	254 ± 15	182 ± 38	471 ± 7	184 ± 17	225 ± 28

[*]Data were mean ± SD (n = 3).
[#]There was no significant difference in IC_{50} among all types of bare SiO_2 ($p > 0.05$), however, statistically significant differences were observed between IC_{50} of each type of bare SiO_2 and that of their amine-modified counterparts ($p < 0.001$).

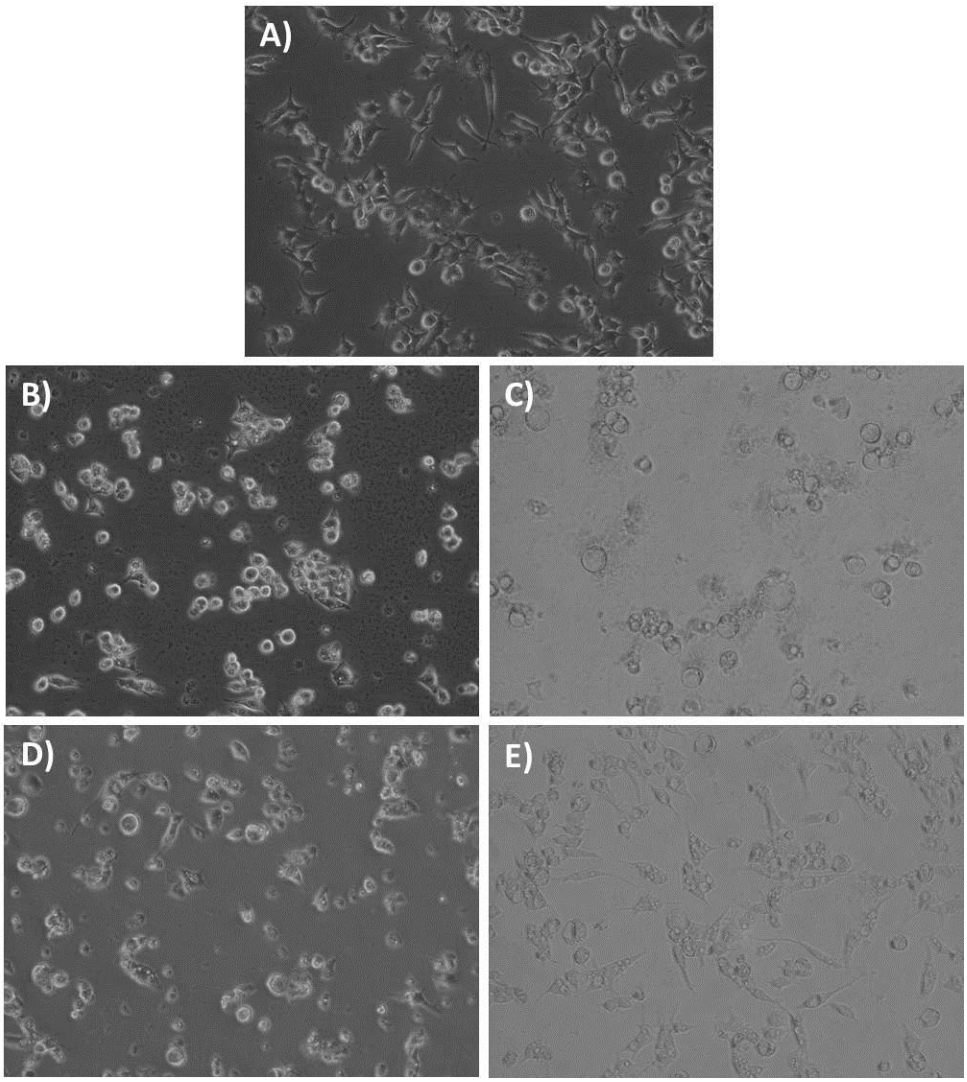

Figure 3.11 RAW 264.7 morphology post-24-hour incubation with: A) cell medium, B) Meso S 250 µg/mL, C) MA 250 µg/mL, D) Stöber 250 µg/mL, E) SA 250 µg/mL. Pictures were taken using a phase-contrast microscope with ×200 magnification.

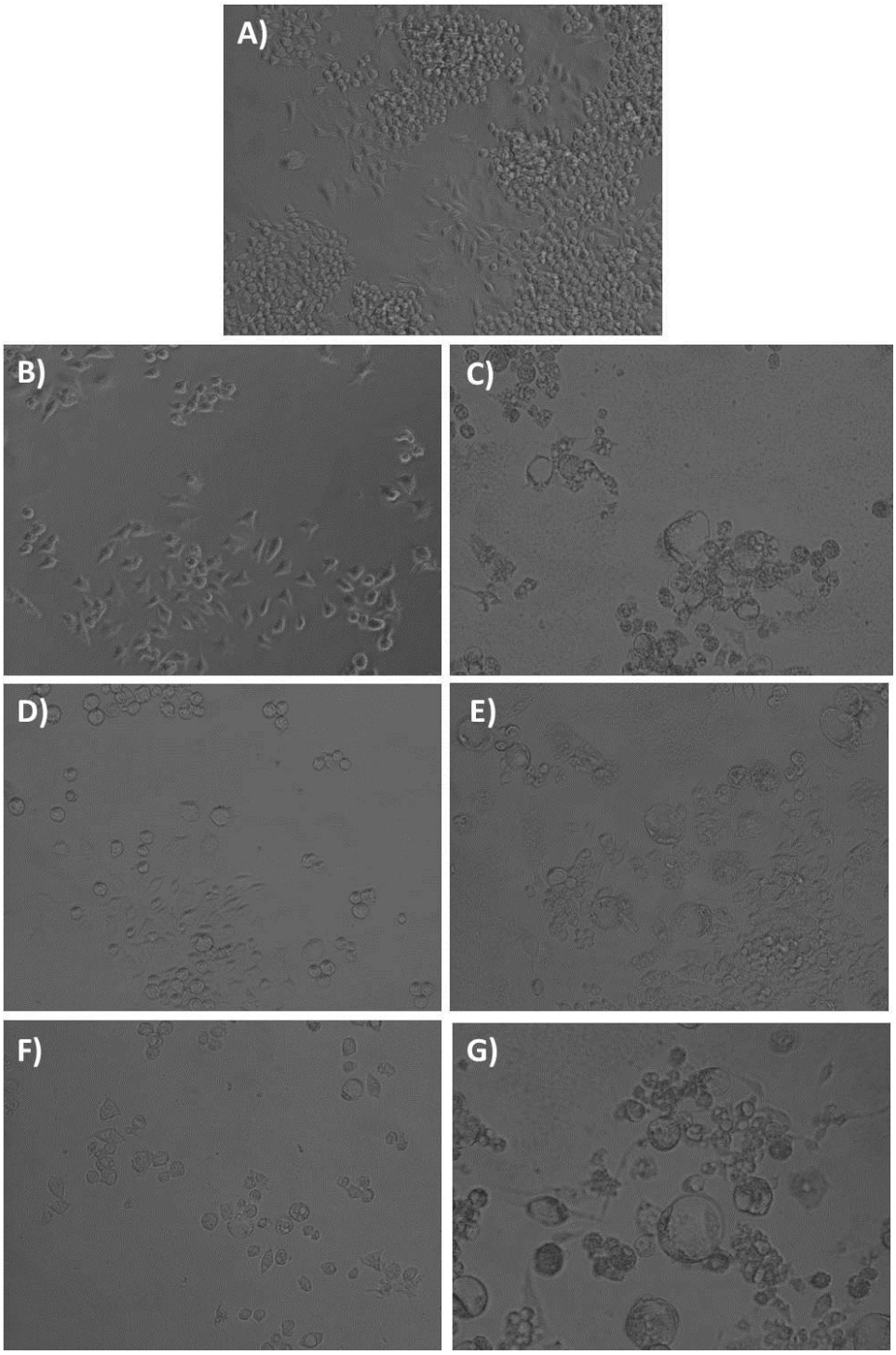

Figure 3.12 RAW 264.7 morphology post-72-hour incubation with: A) cell medium, B) Meso S 250 µg/mL, C) MA 250 µg/mL, D) AR2 250 µg/mL, E) 2A 250 µg/mL, F) AR10 250 µg/mL, G) 10A 250 µg/mL. Pictures were taken using a phase-contrast microscope with ×200 magnification.

stock aqueous suspension. Results showed that the supernatant did not affect the relative viability compared with controls (data not shown). To evaluate whether toxicity was due to adsorbed endotoxin on nanoparticles, endotoxin from reference standard *E. coli* stock was added to 500 μg/mL nanoparticle suspension to make its concentration at 0.1 EU/mL. Results showed that the relative viability post-24-hour incubation and IC_{50} of nanoparticles post-72-hour exposure were not changed in the presence of added endotoxin compared with nanoparticle treatment without addition of endotoxin (data not shown). These results indicate that the added endotoxin did not contribute to toxicity in macrophages at 24 hours or 72 hours; thus, these assays did not fully explain the potential endotoxin-induced macrophage mortality with nanoparticle incubation. It suggests that the toxicity of SiO_2 was due to cellular interaction with nanoparticles themselves, rather than a product of degradation or any associated contaminants.

Plasma membrane damage is an important aspect of cellular toxicity upon nanoparticle treatment. When cells have plasma membrane damage, the propidium iodide in the solution passively diffuses into the cytoplasm and binds with intracellular DNA or RNA. By quantitating the percentage of propidium iodide positive cells, one could deduct the percentage of cells experiencing plasma membrane damage in the total cell population [26]. The results show that the ability of nanoparticles (250 μg/mL) to compromise the integrity of the plasma membrane after 24-hour incubation was cell type-dependent (Figure 3.13). For cancer epithelial cells, the percentage of propidium iodide positive cells was less than 3% for all types of SiO_2 treatment. For macrophages, Stöber caused plasma membrane damage in 53% of the cell population, while all mesoporous SiO_2 selected for this study caused plasma membrane damage in 6-15% of the RAW

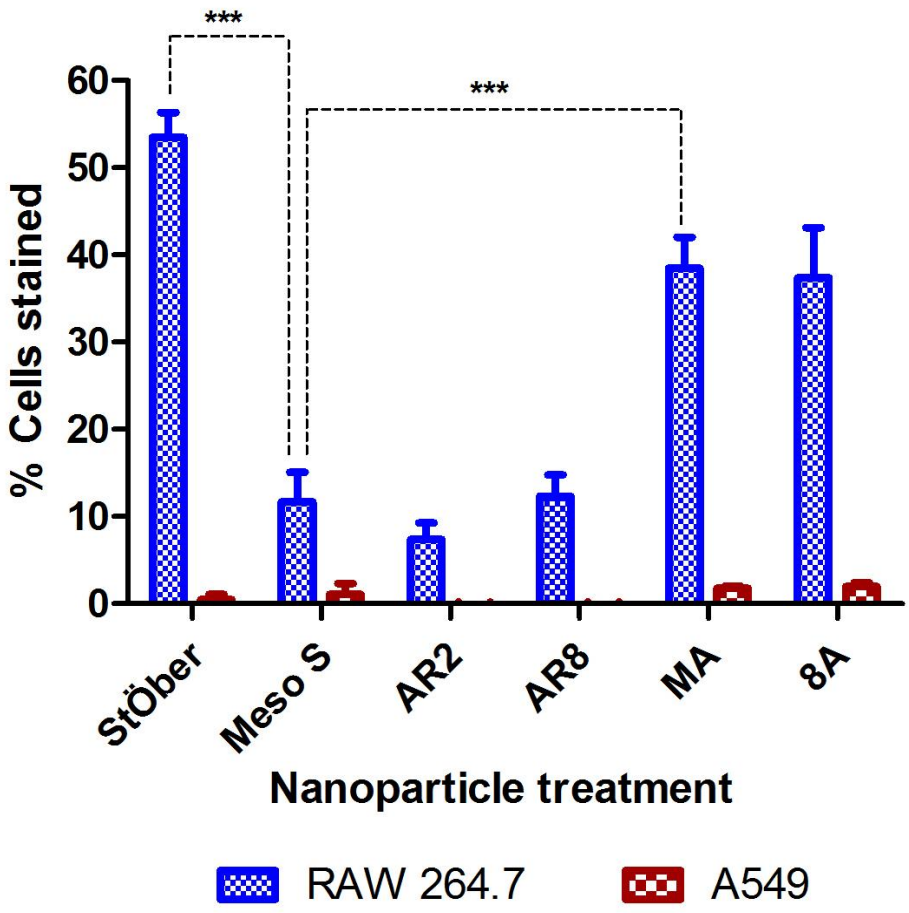

Figure 3.13 Percentage of propidium iodide stained cells in RAW 264.7 cells (blue bars) or A549 cells (red bars) after incubating with 250 µg/mL SiO_2 for 24 hours. ***Meso S led to significantly decreased percentage of propidium iodide-positive cells compared with Stöber or MA ($p < 0.001$). Data were mean ± SD ($n = 3$).

264.7 cell population. Stöber caused the highest percentage of propidium iodide positive cells, probably due to their high silanol density on the external surface that were accessible to the cell membrane, which caused significantly higher cellular impact than mesoporous SiO_2 [22]. Amine-modified mesoporous SiO_2 generated a higher extent of plasma membrane damage in ca. 38% of the cells than their bare mesoporous counterparts. Plasma membrane damage in cells was probably not due to the sedimentation of the nanoparticles, as this experiment was repeated with nanoparticles being added before cells were carefully plated on top of the nanoparticles and the observed results were very similar (Figure 3.14). Combining the results above, it seems that porosity and surface charge are the major factors that determine the extent of plasma membrane damage.

The amount of cellular associated SiO_2, which included internalized nanoparticles or nanoparticles adhering to the extracellular matrix, was quantitated by ICP-MS [7]. Results show a similar pattern of cellular association of SiO_2 with macrophages and cancer epithelial cells. However, the amount of silicon associated with macrophages was 10-15 times higher than that of the cancer epithelial cells (Figures 3.15-3.16). Stöber led to much higher cellular association than mesoporous nanoparticles both on a particle mass basis and on a particle number basis (Table 3.4). The level of cellular association was also highest for Stöber among all types of SiO_2, including the amine-modified counterparts SA. This observation was possibly due to the highest silanol density on the continuous external surface of Stöber, which was reflected by the highest magnitude of negative charge (-50 mV) for these particles [22]. The formation of porous structure or modification with primary amine groups led to reduced silanol density on the external

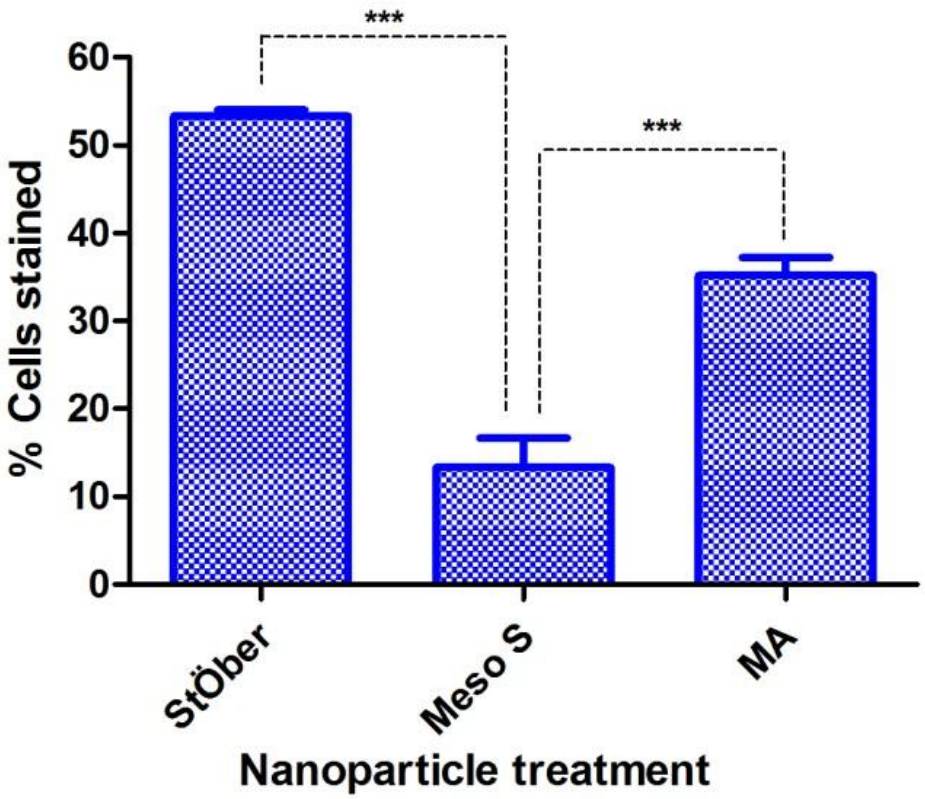

Figure 3.14 Percentage of propidium iodide stained cells in RAW 264.7 cells when cells were plated on top of SiO_2 and incubated for 24 hours . ***Meso S led to significantly less propidium iodide-stained cells compared with Stöber or MA ($p < 0.001$). Data were mean ± SD ($n = 3$).

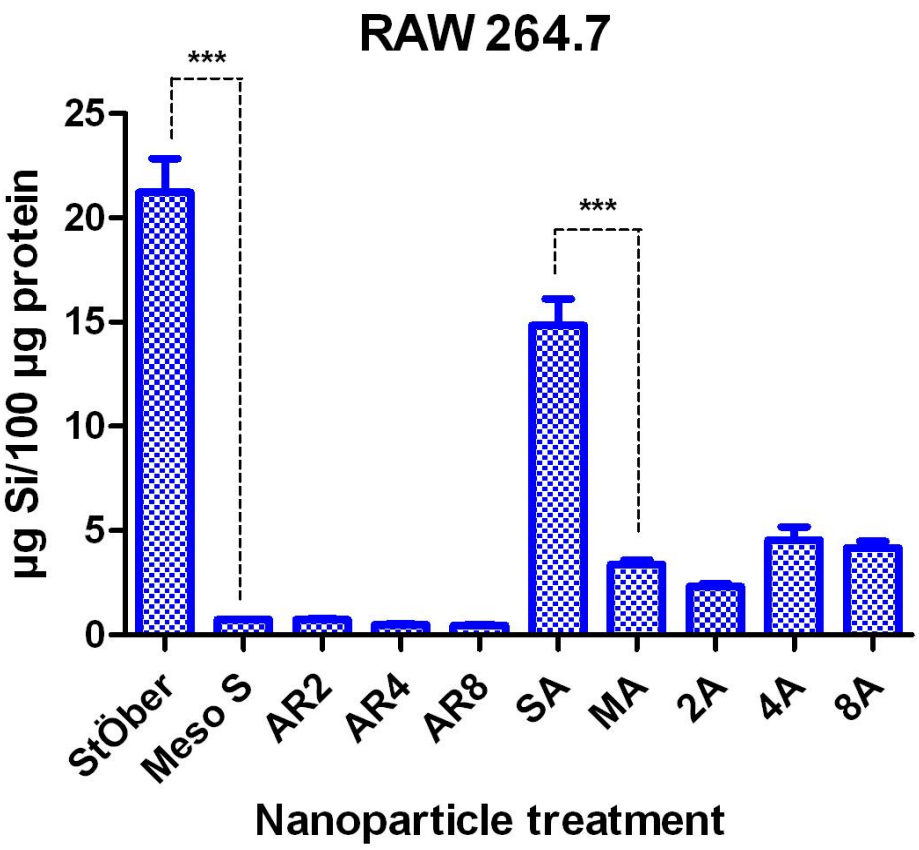

Figure 3.15 ICP-MS analysis of cellular association of SiO_2 in RAW 264.7 cells post-incubation with nanoparticles at 100 µg/mL for 24 hours. ***The level of cell-associated silicon was significantly higher in Stöber- or SA- treated cells than in the mesoporous counterpart-treated cells ($p < 0.001$). Data were mean ± SD ($n = 3$).

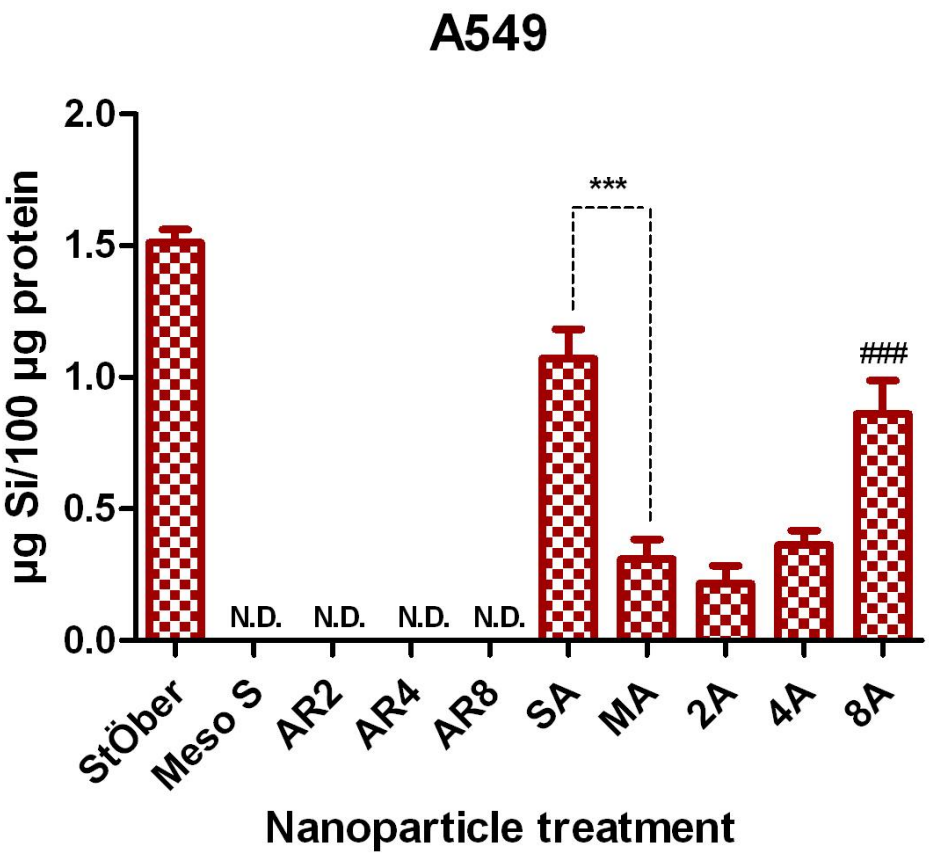

Figure 3.16 ICP-MS analysis of cellular association of SiO_2 in A549 cells post-incubation with nanoparticles at 100 µg/mL for 24 hours. ***The level of cell-associated silicon was significantly higher in Stöber- or SA- treated cells than in the mesoporous counterpart-treated cells ($p < 0.001$). $^{###}$ The level of cell-associated silicon was significantly higher in high aspect ratio, 8A treated cells than in MA, 2A, or 4A treated cells ($p < 0.001$). N.D. means "not detected". Data were mean ± SD ($n = 3$).

Table 3.4 Average cellular association of bare SiO_2 detected by ICP-MS on RAW 264.7 post-incubating with nanoparticles at 100 μg/mL for 24 hours.*

Nanoparticle treatment	Silicon content (μg)/100 μg protein	No. nanoparticles/100 μg protein
Stöber	21.2	2.6×10^{11}
Meso S	0.7	1.6×10^{10}
AR2	0.8	2.2×10^{10}
AR4	0.5	1.8×10^{9}
AR8	0.5	6.1×10^{8}

*There was no significant difference in the amount of cellular associated silicon content per 100 μg protein among various types of mesoporous SiO_2 ($p > 0.05$). Stöber nanoparticles were associated with RAW 264.7 at significantly higher levels than mesoporous SiO_2 of all types either in mass concentration or in number concentration ($p < 0.001$). Data were mean of triplicates.

surface of the particles (-33 mV to -39 mV for mesoporous SiO_2) or shielding of surface silanol by amine functionalities, which reduced the accessibility of silanol groups to cells and in turn decreased the level of cellular association [22].

On the other hand, amine-modified mesoporous SiO_2 (32 mV – 40 mV) showed significantly higher cellular association than their bare mesoprous counterparts ($p < 0.05$), which appeared to contradict the aforementioned phenomenon with SA (17 mV) and Stöber nanoparticles. This indicated that there could be a surface charge "threshold" (> 30 mV) above which the amine functionalities facilitated nanoparticle-cell interaction through electrostatic interaction of positively charged amine groups with negatively charged cell membrane, whereas below the "threshold," there were less surface amine groups available and they had electrostatic interaction with surface silanols and covered the sites of silanol [27], which eventually reduced the level of cellular association.

Bare mesoporous silica nanoparticles, irrespective of their shape features, exhibited a similar level but the lowest amount of cellular associated silicon. For A549 cells, the level of cell-associated silicon from mesoporous SiO_2 exposure was even below the detection limit of ICP-MS (< 0.1 μg/mL for silicon element). There was no significant difference in the level of cellular association among all types of mesoporous SiO_2 ($p > 0.05$). There was also no significant difference in the cellular association among all mesoporous SiO_2 post-amine modification on both cell lines ($p > 0.05$), except that 8A had significantly higher cellular association than other amine-modified mesoporous SiO_2 on A549 cells ($p < 0.001$). This suggests that the curvature of cationic SiO_2 could influence the wrapping by the cell membrane and affect the cellular association with non-phagocytic cells [1].

In order to test if porosity, geometry, and surface modification can influence the cellular association at an earlier time point, selected SiO_2 including Stöber, Meso S, AR8, and MA were incubated with RAW 264.7 cells for 1 hour and the level of cellular association was detected by ICP-MS. The experiment was done at 4 ^oC or 37 ^oC to differentiate the amount of membrane bound SiO_2 with that of internalized SiO_2, as incubation at low temperature (4 ^oC) drastically reduces the energy-dependent internalization process in cells [28]. Considering that the viability of cells could be affected upon incubation at 4 ^oC which subsequently could influence the protein content recovered, the relative viability of cells post-70-minute incubation (10-minute pre-incubation and 60-minute incubation with nanoparticles) at 4^oC was measured and the results show that the percentage of viable cells was 94 ± 8% compared with control cells treated at 37 ^oC for the same time duration. As shown in Figure 3.17, Stöber nanoparticles led to a significant increase in cellular association 24 hours post-incubation at 37 ^oC compared with 1-hour incubation at 37 ^oC ($p < 0.001$) or at 4 ^oC ($p < 0.001$), indicating that there was extensive internalization of nonporous nanoparticles over 24 hours. There was no significant difference in cellular association between Meso S and AR8 post-1-hour incubation at 37 ^oC ($p > 0.05$). Geometry did not seem to affect the level of cellular associated nanoparticles for mesoporous SiO_2 at the early time point as well. Most mesoporous SiO_2 seemed to bind to the cell membrane instead of being internalized into the cytoplasm within an hour as the level of silicon association from Meso S or AR8 exposure was similar for cells incubated at 4 ^oC or 37 ^oC for 1 hour. However, the level of cellular association significantly increased post-incubation for 24 hours compared with incubation for 1 hour at 37 ^oC for Meso S ($p < 0.001$) and AR8

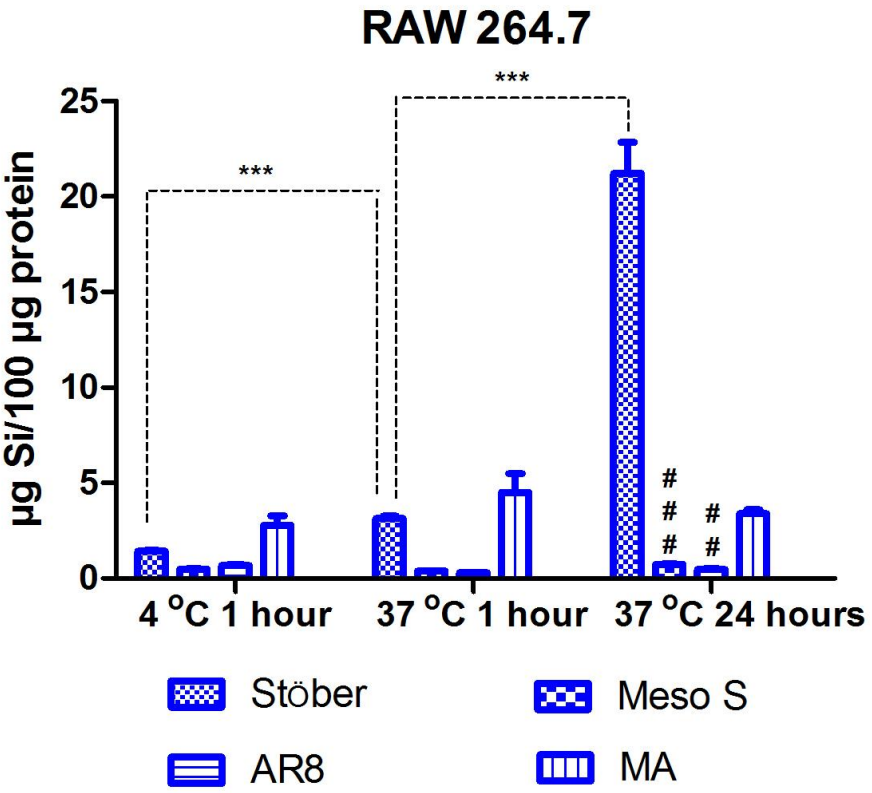

Figure 3.17 Cellular association of SiO_2 after RAW 264.7 cells were incubated with 100 µg/mL selected SiO_2 at 4 °C (1 hour) and 37 °C (1 hour or 24 hours). The level of cellular associated silicon was significantly higher at 24 hours than at 1 hour post-incubation with Stöber (***, $p < 0.001$), Meso S ($^{###}$, $p < 0.001$), or AR8 ($^{##}$, $p < 0.01$) at 37 °C. 1-hour incubation with Stöber at 37 °C led to significantly higher silicon association than incubation at 4 °C (***, $p < 0.001$). Data were mean ± SD ($n = 3$).

($p < 0.01$), which indicated that internalization of mesoporous SiO_2 had occurred. On the contrary, there was no significant difference in cellular association between 1-hour incubation and 24-hour incubation with MA at 37 ^{o}C ($p > 0.05$), which implied that the cellular association of MA almost reached the plateau within 1-hour post-incubation. The cellular association of MA post-1-hour incubation at 37 ^{o}C was not significantly higher than that at 4 ^{o}C ($p > 0.05$). The combined results suggest that there was limited internalization over 24-hour post-incubation with MA, which probably explained why there was a reduction in toxicity of amine-modified SiO_2 compared with that of bare SiO_2. It has been suggested that the strong association of cationic SiO_2 with negatively charged cell membranes, which made the cationic SiO_2 adhere to the cell membrane instead of bringing them into the cytoplasm, led to the reduction in internalization and the resultant decreased toxicity based on transmission electron microscopy [29-31] or confocal microscopy analyses [32]. Our results provide quantitative evidence by ICP-MS that there was limited internalization for amine-modified SiO_2.

In summary, it appears that surface charge and porosity mainly influenced the extent of cellular association while geometry did not seem to influence cellular association within the aspect ratio range of 1-8 studied. These observations are consistent with the experiments examining plasma membrane integrity post-nanoparticle treatment. The level of plasma membrane damage by nanoparticles was directly related to the extent of nanoparticle cellular association, which indicated a biological cause-and-effect relationship between cellular association and cell membrane damage to both cell lines.

The impact of nanoparticle porosity, geometry, and surface functionality on human RBCs was evaluated by a hemolysis assay. The quantitation of hemoglobin in the

supernatant of nanoparticle-RBC mixture was done by recording the absorbance of hemoglobin at 577 nm with a reference wavelength of 655 nm [22, 23]. Results show that the extent of hemolysis was concentration-, porosity-, and geometry-dependent for bare SiO_2 (Figure 3.18). Stöber nanoparticles caused an immediate onset of hemolysis that soon reached a plateau of 17% hemolysis at ca. 250 μg/mL, probably due to its high negative charge which might expel RBCs (-15 mV) [33] from interacting at further increased nanoparticle concentration. For mesoporous SiO_2 of all geometries tested, no hemolytic toxicity was observed below 100 μg/mL. The impact of nanoparticle geometry became pronounced as the concentration further increased. Mesoporous SiO_2 with high aspect ratio demonstrated lower hemolytic activity than spherical or low aspect ratio mesoporous SiO_2. It has been reported that the external surface area and the curvature of SiO_2 influence their hemolytic activity by affecting the magnitude of binding energy of particles with RBCs or bending energy of the membrane to wrap around nanoparticles [27]. Large external surface area and small curvature (*i.e.*, $1/r^2$ for spheres) rendered the hemolysis process thermodynamically favorable [27]. In this case, the external surface areas of Stöber and Meso S were 24 and 109 m^2/g, respectively, which agreed well with previous similar calculations [23, 27], and had similar curvature due to the similar size they possessed. However, Meso S did not lead to a higher hemolytic rate than Stöber until the mass concentration exceeded beyond ca. 190 μg/mL. This indicates that there could possibly be a threshold in the density of silanol groups on each nanoparticle only above which it could cause immediate cell membrane damage upon exposure. Hence, the hemolytic activity depends not only on external surface area and curvature but also on silanol density of each nanoparticle exposed to RBCs.

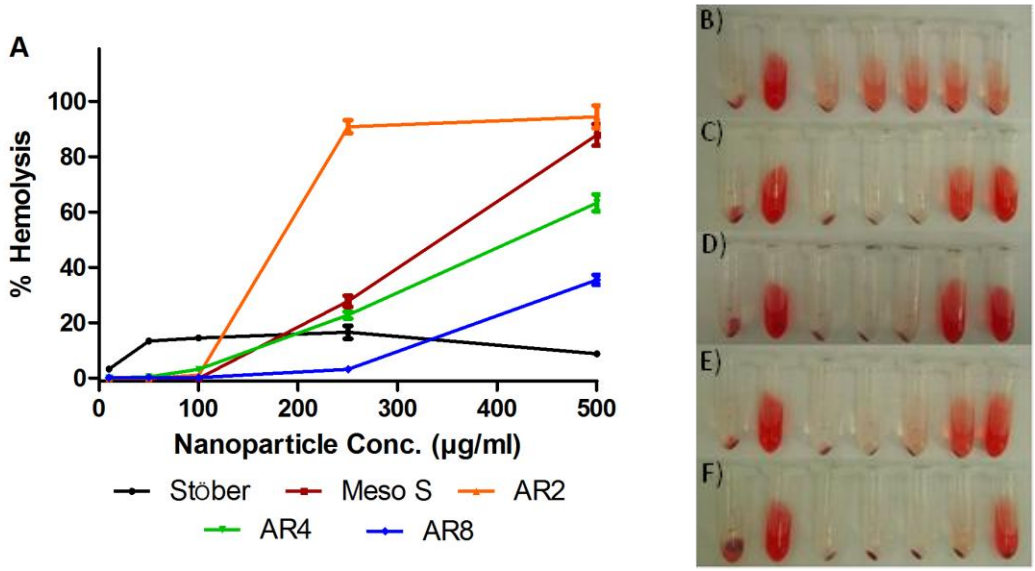

Figure 3.18 Hemolysis assay on bare SiO_2: A) Relative rate of hemolysis in human RBCs upon incubation with nanoparticle suspension at incremental concentrations. The presence of hemoglobin in the supernatant (red) was observed in: B) Stöber suspension, C) Meso S suspension, D) AR2 suspension, E) AR4 suspension, and F) AR8 suspension. The tubes were lined in a sequence (from left to right) as negative control (PBS), positive control (water), 10 µg/mL suspension, 50 µg/mL suspension, 100 µg/mL suspension, 250 µg/mL suspension, and 500 µg/mL suspension. Data were mean ± SD (n = 1 in triplicate measurements).

The hemolytic activity of amine-modified SiO_2 was surface charge- and concentration-dependent (Figure 3.19). As the concentration increased, there was a rapid onset of hemolysis for all types of nanoparticles. SA led to the lowest extent of hemolysis, possibly because of its lowest surface charge, whereas amine-modified mesoporous SiO_2 caused similar rates of hemolysis. The concentrations of SiO_2 leading to 10% hemolysis (LC_{10}) are summarized in Table 3.5. Zhao *et al.* revealed that the affinity of SiO_2 to RBCs decreased with increasing degree of surface functionality independent of surface charge (-43 mV – 7 mV) [27]. Results from our study as shown in Table 3.5 suggest that increasing the surface charge beyond a certain threshold (> 30 mV) might lead to an opposite effect, including enhanced interaction of nanoparticles with RBCs and the resultant elevated hemolysis by amine-modified mesoporous SiO_2, in agreement with the cellular association results (Figures 3.15-3.16). It must be noted that a good correlation with results of different experiments is based on a similar dose (ca. ≤ 100 μg/mL SiO_2). As the dose changes beyond a certain range, the pattern from different experiments would shift and the correlation of various experiments at that dosage need to be further validated.

3.4 Conclusion

In summary, nonporous Stöber silica nanospheres, mesoporous silica nanospheres, mesoporous silica nanorods with aspect ratio of 2, 4, and 8, as well as their cationic-charged counterparts were synthesized and characterized. The porosity, shape, and surface modification effects on cellular toxicity or hemolytic activity were evaluated on macrophages, cancer epithelial cells, or on human erythrocytes. The toxicity of SiO_2 was found to be cell-type dependent. Cancer epithelial cells were highly resistant to

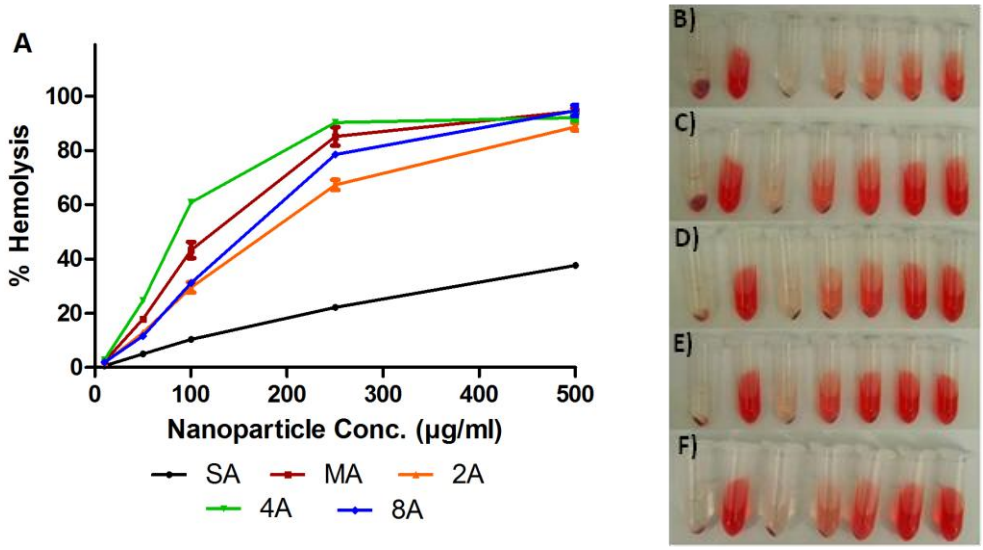

Figure 3.19 Hemolysis assay on amine-modified SiO_2: A) Relative rate of hemolysis in human RBCs upon incubation with amine-modified nanoparticle suspension at incremental concentrations. The presence of hemoglobin in the supernatant (red) was observed in: B) SA suspension, C) MA suspension, D) 2A suspension, E) 4A suspension, and F) 8A suspension. The tubes were lined in a sequence (from left to right) as negative control (PBS), positive control (water), 10 µg/mL suspension, 50 µg/mL suspension, 100 µg/mL suspension, 250 µg/mL suspension, and 500 µg/mL suspension. Data were mean ± SD (n = 1 in triplicate measurements).

Table 3.5 Summary of LC_{10} values of SiO_2 in human erythrocytes.[*]

LC_{10} values (μg/mL)	Stöber	Meso S	AR2	AR4	AR8
Bare nanoparticles[#]	36 ± 1	154 ± 4	115 ± 1	152 ± 2	302 ± 3
Amine-modified nanoparticles	97 ± 4	30 ± 1	40 ± 1	23 ± 1	43 ± 1

[*]Data were mean ± SD (n = 1 in triplicate measurements).
[#]There was significant difference between the LC_{10} value of bare SiO_2 and that of amine-modified counterparts ($p < 0.001$).

nanoparticle treatment while the toxicity on macrophages was predominantly surface-charge-dependent. The difference in toxicity between the two cell types could be due to the difference in the physiological function of each. Porosity and surface characteristics of the nanoparticles were the major factors that influenced the cellular association of the nanoparticles. Geometry did not seem to influence the extent of cellular association of the nanoparticles at either the early time point or over extended duration. Initial comparison of blood biocompatibility of nonporous and mesoporous SiO_2 with varied shapes and surface characteristics has been demonstrated using the hemolysis assay. Bare SiO_2 showed a porosity- and geometry-dependent hemolytic activity on RBCs with mesoporous SiO_2 at high aspect ratio exhibiting a reduced hemolytic activity. The extent of hemolysis was highly zeta potential-dependent among the amine-modified SiO_2 and results indicated that there could be a surface charge "threshold" below which the amine modification on SiO_2 could lead to reduced hemolysis compared with their bare counterparts. Further studies evaluating the *in vivo* toxicity of SiO_2 in animal models are needed to establish an *in vitro-in vivo* correlation for better prediction of toxicity in biological systems.

3.5 References

[1] S.E. Gratton, P.A. Ropp, P.D. Pohlhaus, J.C. Luft, V.J. Madden, M.E. Napier, J.M. DeSimone, The effect of particle design on cellular internalization pathways, Proc Natl Acad Sci U S A, 105 (2008) 11613-11618.

[2] S. Muro, C. Garnacho, J.A. Champion, J. Leferovich, C. Gajewski, E.H. Schuchman, S. Mitragotri, V.R. Muzykantov, Control of endothelial targeting and intracellular delivery of therapeutic enzymes by modulating the size and shape of ICAM-1-targeted carriers, Mol Ther, 16 (2008) 1450-1458.

[3] Arnida, M.M. Janat-Amsbury, A. Ray, C.M. Peterson, H. Ghandehari, Geometry and surface characteristics of gold nanoparticles influence their biodistribution and uptake by macrophages, Eur J Pharm Biopharm, 77 (2011) 417-423.

[4] T.P.B. Nguyen, J.-W. Lee, W.G. Shim, H. Moon, Synthesis of functionalized SBA-15 with ordered large pore size and its adsorption properties of BSA, Microporous and Mesoporous Materials, 110 (2008) 560-569.

[5] M.A. Maurer-Jones, Y.S. Lin, C.L. Haynes, Functional assessment of metal oxide nanoparticle toxicity in immune cells, ACS Nano, 4 (2010) 3363-3373.

[6] I. Slowing, B.G. Trewyn, V.S. Lin, Effect of surface functionalization of MCM-41-type mesoporous silica nanoparticles on the endocytosis by human cancer cells, J Am Chem Soc, 128 (2006) 14792-14793.

[7] F. Lu, S.H. Wu, Y. Hung, C.Y. Mou, Size effect on cell uptake in well-suspended, uniform mesoporous silica nanoparticles, Small, 5 (2009) 1408-1413.

[8] Q. He, Z. Zhang, Y. Gao, J. Shi, Y. Li, Intracellular localization and cytotoxicity of spherical mesoporous silica nano- and microparticles, Small, 5 (2009) 2722-2729.

[9] C.P. Tsai, Y. Hung, Y.H. Chou, D.M. Huang, J.K. Hsiao, C. Chang, Y.C. Chen, C.Y. Mou, High-contrast paramagnetic fluorescent mesoporous silica nanorods as a multifunctional cell-imaging probe, Small, 4 (2008) 186-191.

[10] M.A. Dobrovolskaia, P. Aggarwal, J.B. Hall, S.E. McNeil, Preclinical studies to understand nanoparticle interaction with the immune system and its potential effects on nanoparticle biodistribution, Mol Pharm, 5 (2008) 487-495.

[11] Y.S. Chung, M.Y. Jeon, C.K. Kim, Fabrication of nearly monodispersed silica nanoparticles by using poly(1-vinyl-2-pyrrollidinone) and their application to the preparation of nanocomposites, Macromol. Res., 17 (2009) 37-43.

[12] S. Giri, B.G. Trewyn, M.P. Stellmaker, V.S. Lin, Stimuli-responsive controlled-release delivery system based on mesoporous silica nanorods capped with magnetic nanoparticles, Angew Chem Int Ed Engl, 44 (2005) 5038-5044.

[13] S. Huh, J.W. Wiench, J.-C. Yoo, M. Pruski, V.S.-Y. Lin, Organic functionalization and morphology control of mesoporous silicas via a co-condensation synthesis method, Chem. Mater., 15 (2003) 4247-4256.

[14] S.P. Naik, S.P. Elangovan, T. Okubo, I. Sokolov, Morphology control of mesoporous silica particles, J. Phys. Chem. C, 111 (2007) 11168-11173.

[15] S. Yang, L. Zhao, C. Yu, X. Zhou, J. Tang, P. Yuan, D. Chen, D. Zhao, On the origin of helical mesostructures, J Am Chem Soc, 128 (2006) 10460-10466.

[16] G. Lelong, S. Bhattacharyya, S. Kline, T. Cacciaguerra, M.A. Gonzalez, M.-L. Saboungi, Effect of surfactant concentration on the morphology and texture of MCM-41 materials, J. Phys. Chem. C, 112 (2008) 10674–10680.

[17] H. Jin, Z. Liu, T. Ohsuna, O. Terasaki, Y. Inoue, K. Sakamoto, T. Nakanishi, K. Ariga, S. Che, Control of morphology and helicity of chiral mesoporous silica, Adv. Mater., 18 (2006) 593–596.

[18] J.M. Kim, J.H. Kwak, S. Jun, R. Ryoo, Ion exchange and thermal stability of MCM-41, J. Phys. Chem., 99 (1995) 16742-16747.

[19] R. Ryoo, S. Jun, Improvement of hydrothermal stability of MCM-41 using salt effects during the crystallization process, J. Phys. Chem. B, 101 (1997) 317-320.

[20] J. Kobler, K. Moller, T. Bein, Colloidal suspensions of functionalized mesoporous silica nanoparticles, ACS Nano, 2 (2008) 791-799.

[21] H.Y. Zhu, X.S. Zhao, G.Q. Liu, D.D. Do, Improved comparison plot method for pore structrue characterizatoin of MCM-41, Langmuir, 12 (1996) 6513-6517.

[22] Slowing, II, C.W. Wu, J.L. Vivero-Escoto, V.S. Lin, Mesoporous silica nanoparticles for reducing hemolytic activity towards mammalian red blood cells, Small, 5 (2009) 57-62.

[23] Y.S. Lin, C.L. Haynes, Impacts of mesoporous silica nanoparticle size, pore ordering, and pore integrity on hemolytic activity, J Am Chem Soc, 132 (2010) 4834-4842.

[24] C.F. Jones, D.W. Grainger, *In vitro* assessments of nanomaterial toxicity, Adv Drug Deliv Rev, 61 (2009) 438-456.

[25] S.P. Hudson, R.F. Padera, R. Langer, D.S. Kohane, The biocompatibility of mesoporous silicates, Biomaterials, 29 (2008) 4045-4055.

[26] C. Riccardi, I. Nicoletti, Analysis of apoptosis by propidium iodide staining and flow cytometry, Nat Protoc, 1 (2006) 1458-1461.

[27] Y. Zhao, X. Sun, G. Zhang, B.G. Trewyn, Slowing, II, V.S. Lin, Interaction of mesoporous silica nanoparticles with human red blood cell membranes: size and surface effects, ACS Nano, 5 (2011) 1366-1375.

[28] X. Xing, X. He, J. Peng, K. Wang, W. Tan, Uptake of silica-coated nanoparticles by HeLa cells, J Nanosci Nanotechnol, 5 (2005) 1688-1693.

[29] Z. Tao, B.B. Toms, J. Goodisman, T. Asefa, Mesoporosity and functional group dependent endocytosis and cytotoxicity of silica nanomaterials, Chem Res Toxicol, 22 (2009) 1869-1880.

[30] A. Petushkov, J. Intra, J.B. Graham, S.C. Larsen, A.K. Salem, Effect of crystal size and surface functionalization on the cytotoxicity of silicalite-1 nanoparticles, Chem Res Toxicol, 22 (2009) 1359-1368.

[31] T.H. Chung, S.H. Wu, M. Yao, C.W. Lu, Y.S. Lin, Y. Hung, C.Y. Mou, Y.C. Chen, D.M. Huang, The effect of surface charge on the uptake and biological function of mesoporous silica nanoparticles in 3T3-L1 cells and human mesenchymal stem cells, Biomaterials, 28 (2007) 2959-2966.

[32] H. Nabeshi, T. Yoshikawa, A. Arimori, T. Yoshida, S. Tochigi, T. Hirai, T. Akase, K. Nagano, Y. Abe, H. Kamada, S.-i. Tsunoda, N. Itoh, Y. Yoshioka, Y. Tsutsumi, Effect of surface properties of silica nanoparticles on their cytotoxicity and cellular distribution in murine macrophages, Nanoscale Research Letters, 6 (2011) 1-6.

[33] K.M. Jan, S. Chien, Role of surface electric charge in red blood cell interactions, J Gen Physiol, 61 (1973) 638-654.

CHAPTER 4

INFLUENCE OF SILICA NANOPARTICLE DESIGN ON ACUTE TOXICITY *IN VIVO*

4.1 Introduction

The relationship between biological responses from *in vitro* examination and those from *in vivo* evaluation has been less well established to date [1-3]. It has been reported that nonfunctionalized mesoporous silicates of particle sizes 150 nm – 4000 nm, which induced more toxicity to mesothelial cells and myoblasts and less toxicity to macrophages, exhibited benign local compatibility by subcutaneous injection route, but with considerable systemic toxicity when administered by the intraperitoneal or intravenous routes in mice [1]. In Chapter 3, we evaluated the cellular uptake and toxicity of nonporous silica nanospheres of 115 nm in diameter, mesoporous silica nanospheres of similar size, and mesoporous silica nanorods with aspect ratios of 2, 4, and 8 as well as their cationic counterparts [4]. *In vitro* observations showed that the cellular toxicity of nanoparticles are cell-type-dependent and that surface characteristics and porosity govern cellular uptake rather than geometric features [4]. While *in vitro* observations shed light on the potential influence of these physicochemical characteristics on biocompatibility in a live biological system, a thorough investigation in animals is needed to relate the observed *in vitro* impacts of SiO_2 with *in vivo* outcomes.

In this chapter, the single-dose, acute toxicity of engineered SiO_2 of distinct shapes, porosities, and surface characteristics upon intravenous injection into immune-competent mice is described. A series of different doses were administered to identify the MTD of nonporous or mesoporous silica nanospheres, mesoporous silica nanorods of different aspect ratios, as well as their cationic counterparts. Clinical observation, daily weight monitoring, hematological/blood chemistry tests, and histological examination were conducted to evaluate *in vivo* toxicity of SiO_2 as a function of their physicochemical properties.

4.2 Methods

4.2.1 Nanoparticle characterization and injectable preparation

Nonporous or mesoporous SiO_2 with distinct geometrical features or drastically different surface characteristics were prepared as reported in Chapter 3 (Section 3.3) [4]. Hydrodynamic sizes of SiO_2 in DI (deionized) water, physiological saline, and 50% FBS in saline were measured on a Malvern Zetasizer Nanoseries equipped with a back-scattering detector (173 degrees). Various SiO_2 were stored in ethanol and washed extensively with ethanol and DI water. SiO_2 were resuspended in water or saline to make highly concentrated stocks. Then nanoparticles were diluted in water or saline to 1 mg/mL at room temperature and their sizes measured by DLS. SiO_2 from saline stock were diluted in 50% serum (prewarmed to 37 ^{o}C) to 1 mg/mL and were incubated at 37 ^{o}C for 30 minutes followed by equilibration to room temperature (typically 5 minutes) before the measurements were taken [5]. To prepare SiO_2 injectable formulation, the nanoparticles were diluted in saline to a specific concentration, vortexed and sonicated,

and were loaded into a 1 mL syringe under sterile conditions immediately before injection.

4.2.2 Animals

All animal experiments were performed in compliance with the University of Utah Institutional Animal Care and Use Committee (IACUC). Six- to eight-week-old female CD-1 mice were purchased from Charles River Laboratories, and housed in a group of five in standard cages with free access to food and water and were subject to a 12 hour light/dark cycle. All animals were acclimated to the animal facility for at least 1 week prior to experimental procedures. CD-1 mice have an intact immune system and were expected to react to nanoparticle exposure in a closer manner as in humans.

4.2.3 MTD investigation

Animals were received in standard cages from the animal facility with five mice per cage. These cages were randomly assigned to treatment groups with one cage per treatment and the animals in each cage were randomly numbered as M1- M5. SiO_2 were suspended in sterile saline and injected through the tail vein in 200 μL suspension per mouse. Injections of sterile saline at equivalent volumes were also given to mice as controls for each dose phase. The starting dose administered into mice was chosen to be 30 mg/kg. If major adverse reactions were not observed in all five animals within 10 days, the next dose level (100 mg/kg) was applied to a new group of mice and so forth. Animals that survived were euthanized by CO_2 asphyxiation at the end of 10 days and the blood and tissues were collected. If major adverse reactions in animals were identified at a certain dose (toxic dose) within 10 days, a decreased dose (usually the mean value

between toxic dose and least tolerated dose) was used and so forth. Animals (one or more) may have shown the onset of major adverse reactions even before five animals in the same group were all injected. When this occurred, no more animals were injected and there were less than five animals in this treatment. Animals that showed major adverse reactions were immediately euthanized, and blood and tissues were collected for analysis. If the dose was reduced to a level that no major adverse reactions were observed in all five animals for 10 days, then this dose was identified as a survival dose. Histological evidence of organ damage and abnormal values of hematological/blood chemical indices, organ weight ratios, and body weight changes were also considered as evidence of major toxicity in mice. If such major toxicity was absent in animals from the survival dose, the survival dose was then considered as the MTD. Otherwise, a further decreased dose was selected until all major toxicities mentioned above were absent in all five animals subject to a specific dose, which was identified as the MTD.

4.2.4 Hematology and blood chemistry

Blood was withdrawn from the inferior vena cava immediately following euthanasia or animal death. The collected blood was stored in heparin-coated centrifuge tubes. The blood counts were measured within 4 hours post-collection, and plasma chemistry evaluated on the same day of blood collection. In the blood count analysis, major hematology markers from the whole blood, namely, erythrocyte count, platelet count, total leukocyte count, and hemoglobin level, were measured on a CBC-DIFF Instrument (Heska, Loveland, CO). In the blood chemistry analysis, blood samples (about 0.3 – 0.7 mL each mouse) were briefly centrifuged at 1000 rpm for 2 minutes to obtain plasma. Liver function indicators (albumin, aspartate aminotransferase, alanine

aminotransferase, and total bilirubin), renal function indicators (blood urea nitrogen and creatinine), and globulin and total protein levels were tested using a DRI-CHEM (Heska, Loveland, CO) veterinary blood chemistry analyzer.

4.2.5 Animal and organ weight measurements

The animals which survived the injections of nanoparticles were weighed on a daily basis. Vital organs, including heart, liver, spleen, lung, and kidney were excised and weighed post-necropsy. The normalized weight percentages of heart, liver, spleen, lung, or kidney were calculated as the ratio of wet tissue weight over total body weight.

4.2.6 Histological examination

All the organs recovered from necropsy, including heart, liver, spleen, lung, and kidney, were fixed in 10% formalin in PBS solution and stored at 4 ^{o}C. The tissues were embedded in paraffin blocks, sliced, and placed onto glass slides. The slides were stained with hematoxylin and eosin (H&E). The histological examination was performed by a pathologist who was unaware of the treatment modalities of each animal, and images were taken using a light microscope (Olympus, BH-2).

4.2.7 Calculation of dose equivalents at MTD

The dose equivalents of nanoparticles at MTD on the basis of mass, total surface area, external surface area, total number, or total volume were calculated as:

Total surface area of SiO_2 at MTD (m^2/kg animals) = MTD (mg/kg) / 1000 × Total surface area of SiO_2 (m^2/g nanoparticles).

External surface area of SiO_2 at MTD (m^2/kg animals) = MTD (mg/kg) / 1000 × External surface area of SiO_2 (m^2/g nanoparticles).

Total number of SiO_2 at MTD (nanoparticles/kg animals) = MTD (mg/kg) / 1000 × Number of SiO_2 (nanoparticles/g nanoparticles).

Total volume of SiO_2 at MTD (cm^3/kg animals) = Total number of SiO_2 at MTD (nanoparticles/kg animals) × Volume of a nanoparticle (cm^3/nanoparticle)

4.2.8 Statistical analysis

Multigroup comparisons of the means were carried out by one-way ANOVA test using Graphpad Prism. Statistical significance for all tests was set at $p < 0.05$. Results are expressed as mean ± SD (n = 3-5).

4.3 Results

Stöber, Meso S, AR2, and AR8 were previously synthesized and stored in ethanol. The pristine SiO_2 of various types were further modified with APTES to obtain their highly cationic counterparts (SA, MA, 2A and 8A). The overall physicochemical features of various SiO_2 are summarized in Figure 3.1 and Tables 3.1-3.2 in Chapter 3 [4]. The hydrodynamic sizes of selective spherical SiO_2 (Stöber, Meso S, MA) in DI water, physiological saline, and 50% serum were assessed by dynamic light scattering (DLS) to analyze the effect of porosity or surface characteristics on nanoparticle dispersive status in media. Results showed that SiO_2 had good dispersivity in water or saline except that MA exhibited some degree of agglomeration in saline (Table 4.1), probably due to decreased electrostatic repulsion in the salt solution and enhanced interaction of surface amine with salinol groups on nanoparticles [6]. When incubated in 50% serum at 37 ^oC for 30 minutes, Meso S exhibited significantly higher hydrodynamic size than in water or saline ($p < 0.001$)(Table 4.1). This indicates that protein molecules

Table 4.1 Hydrodynamic sizes of selective spherical SiO_2 in DI water, physiological saline, and 50% serum at 1 mg/mL[a]

Nanoparticle	Size in DI water (nm)/PDI	Size in saline (nm)/PDI	Size in 50% serum (nm)/PDI
Stöber	170.3 ± 0.8/0.059	139.6 ± 0.2/0.053	121.6 ± 1.6/0.053
Meso S	208.6 ± 1.2/0.145	200.6 ± 1.5/0.137	268.9 ± 6.3***/0.166
MA	206.0 ± 0.5/0.140	855.7 ± 2.8/0.498	150.3 ± 0.6$^{###}$/0.102

[a]Data are mean of average diameter of each measurement ± SD (n = 1 in triplicate measurements). ***The hydrodynamic size of Meso S was significantly higher than that of Stöber in 50% serum ($p < 0.001$). $^{###}$The hydrodynamic size of MA was significantly lower than that of Meso S in 50% serum ($p < 0.001$).

adhered to the surface of Meso S and suggests the formation of a "nanoparticle-protein corona" upon incubation with proteins [6, 7]. The hydrodynamic sizes of Stöber or MA in 50% serum were significantly lower than their sizes in water or saline ($p < 0.001$) (Table 4.1). This implied that there was limited nanoparticle association in water or saline and addition of protein molecules served as the dispersion stabilizer and resulted in a decrease in average diameter of nanoparticles [8, 9]. In this case, the protein molecules were probably adsorbed onto the nanoparticle surface and provided steric hinderance that potentially prevented nanoparticles from agglomorating [8, 9]. To compare the hydrodynamic sizes of SiO_2 in 50% serum across the board, Meso S had significantly higher size than Stöber ($p < 0.001$), while MA possessed significantly lower size than Meso S in 50% serum ($p < 0.001$) (Table 4.1).

MTD is defined as the highest dose that does not cause major adverse reactions in mice over 10 days post-intravenous injection [10, 11]. Major adverse reactions are considered to be immediate death, impaired mobility or irregular breathing that could not be recovered within a day, or over 10% weight loss over continuous days, or histological evidence of organ toxicity. In this study, toxic dose(s) were first reached as major adverse reactions were observed in a test group of five mice (named as M1 – M5) at that specific dose. Then the dose was reduced to a level identified later as MTD based on summarized clinical, hematological, blood chemical, and histological examinations. Nanoparticle treatments administered to mice are expressed as "nanoparticle type (,) dose (mg/kg)" throughout the chapter. The overall dosing procedure and animal response is summarized in Figure 4.1. The detailed record of animal adverse reactions from SiO_2 dosing is shown in Table 4.2.

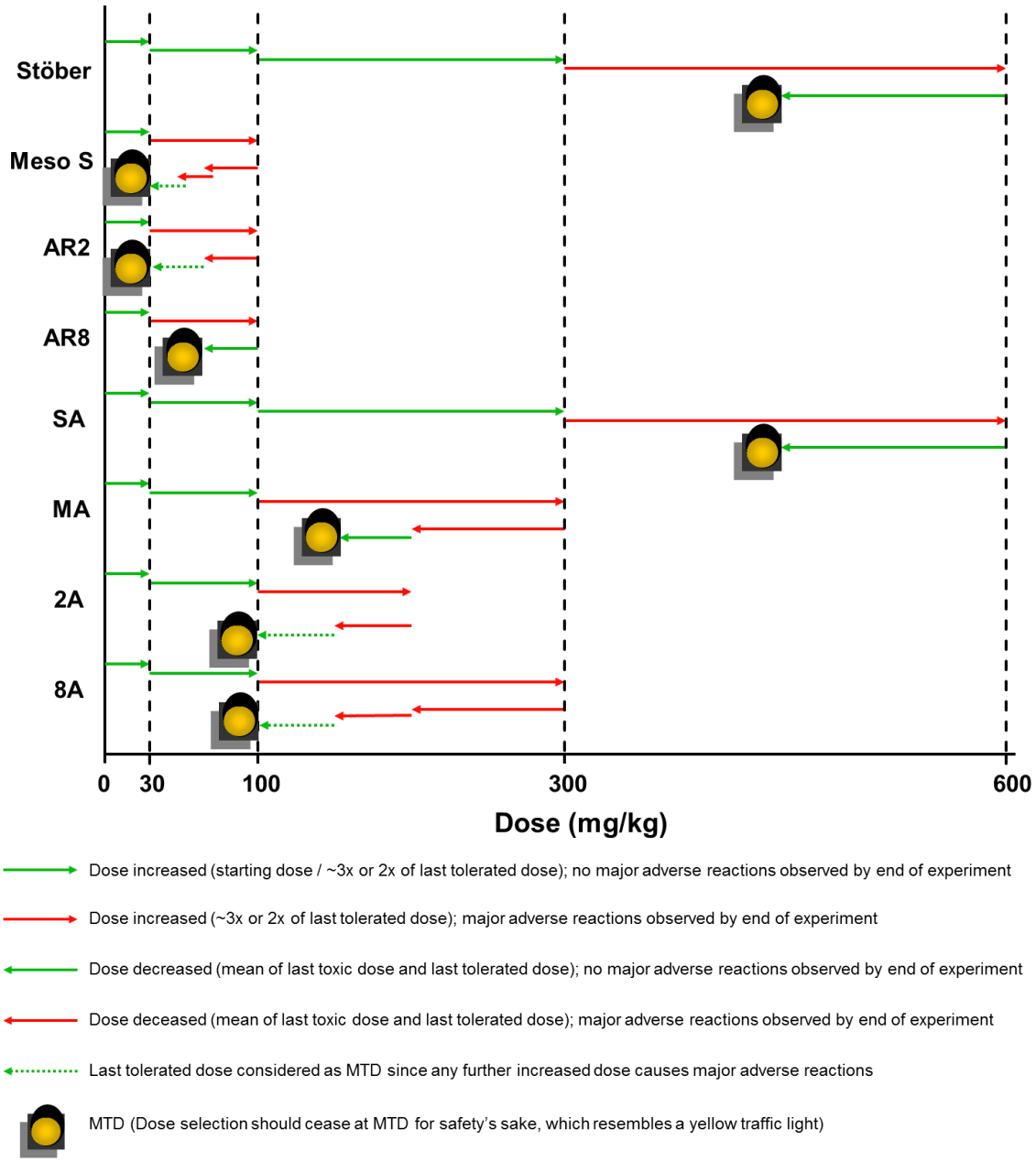

Figure 4.1 Summary of the experimental procedures and outcomes of MTD investigation of various SiO_2 in mice.

Table 4.2 Mortality rate of CD-1 mice post-intravenous injection of SiO_2 at various doses and the time to reach life termination for each animal which showed major adverse reactions (animal identity shown).

Treatment	Dose (mg/kg)	Mortality	Time to death post injection
Stöber	600	1/5	Died 2 days later (M3)
Meso S	100	1/5	Died at 27 hours (M2)
	65	1/5	Died at 20 hours (M2)
	50	1/5	Died at 24 hours (M4)
AR2[a]	100	3/5	Died at 24 hours (M4), Died 2 days later (M1, M5)
AR8	100	2/5	Sacrificed at 24 hours (M5), died 2 days later (M2)
SA	600	1/5	Died 3 days later (M3)
MA	300	2/2	Died immediately (M4), euthanized at 22 hours (M2)
	200	1/2	Died immediately (M1)
2A	200	3/5	Died 1 day later (M4) or 2 days later (M1, M5)
	150	1/4	Euthanized immediately (M5)
8A	300	1/1	Died immediately (M1)
	200	1/1	Died immediately (M1)
	150	1/1	Died immediately (M3)

[a]AR2 causes kidney injury in one animal (M1) as shown in histological evaluation at the dose of 65 mg/kg, which is then considered as a toxic dose even when it does not lead to animal life termination.

The MTDs of various types of nanoparticles are summarized in Table 4.3. As shown, the MTDs of nonporous SiO_2, either bare or amine-modified, were the highest (450 mg/kg) among all types of SiO_2 studied. Mesoporous SiO_2 had a remarkably low safety threshold with MTDs between 30 mg/kg to 65 mg/kg, irrespective of geometrical features. Any higher doses could cause major adverse reaction, which was reported by previous studies that animals had immediate death post-intravenous injection of mesoporous SiO_2 at 6 mg/mouse (approximately 240 mg/kg) [1]. Toxicity was alleviated by modifying mesoporous SiO_2 with primary amine groups, resulting in a 2-3-fold increase in MTDs to 100 – 150 mg/kg. For the animals which survived treatment, they showed normal weight gain 10 days post-injection (Figure 4.2) and there was no clinical difference in organ weight percentages between treatment groups and the control group (Figure 4.3).

In order to gain comprehensive understanding about nanoparticle impact *in vivo*, blood was collected after animal termination for the diagnosis of SiO_2 toxicity. Major hematology markers from the whole blood, including erythrocyte count, platelet count, total leukocyte count, and hemoglobin level, were measured in complete blood count analysis. Kidney and liver functions were evaluated in the blood chemistry analysis. Renal function was examined by blood urea nitrogen and creatinine concentrations, while liver function was tested through plasma levels of albumin, aspartate aminotransferase, alanine aminotransferase, and total bilirubin. Globulin level was measured as a potential indicator of an immune reaction as the increase in both total leukocyte count and globulin concentration reflected the onset of inflammation. Animals that survived showed no significant changes in blood counts or blood biochemical indices between SiO_2 treatment

Table 4.3 MTDs of SiO_2 with engineered physicochemical characteristics and the major affected organs, and the associated adverse reactions in mice post-intravenous injection at toxic doses.

Treatment	MTD (mg/kg)	Major affected organ(s) above MTD	Main adverse reaction(s) above MTD
Stöber	450	Heart, lung, spleen	Thrombosis on endocardium or in lung, anemia
Meso S	30	Kidney	Renal congestion
AR2	30	Kidney	Renal congestion
AR8	65	Kidney	Renal congestion
SA	450	Lung, kidney	Pulmonary and renal congestion
MA	150	Lung, kidney	Pulmonary and renal congestion
2A	100	Lung, kidney	Pulmonary and renal congestion
8A	100	Lung, kidney	Lung thrombosis and renal congestion

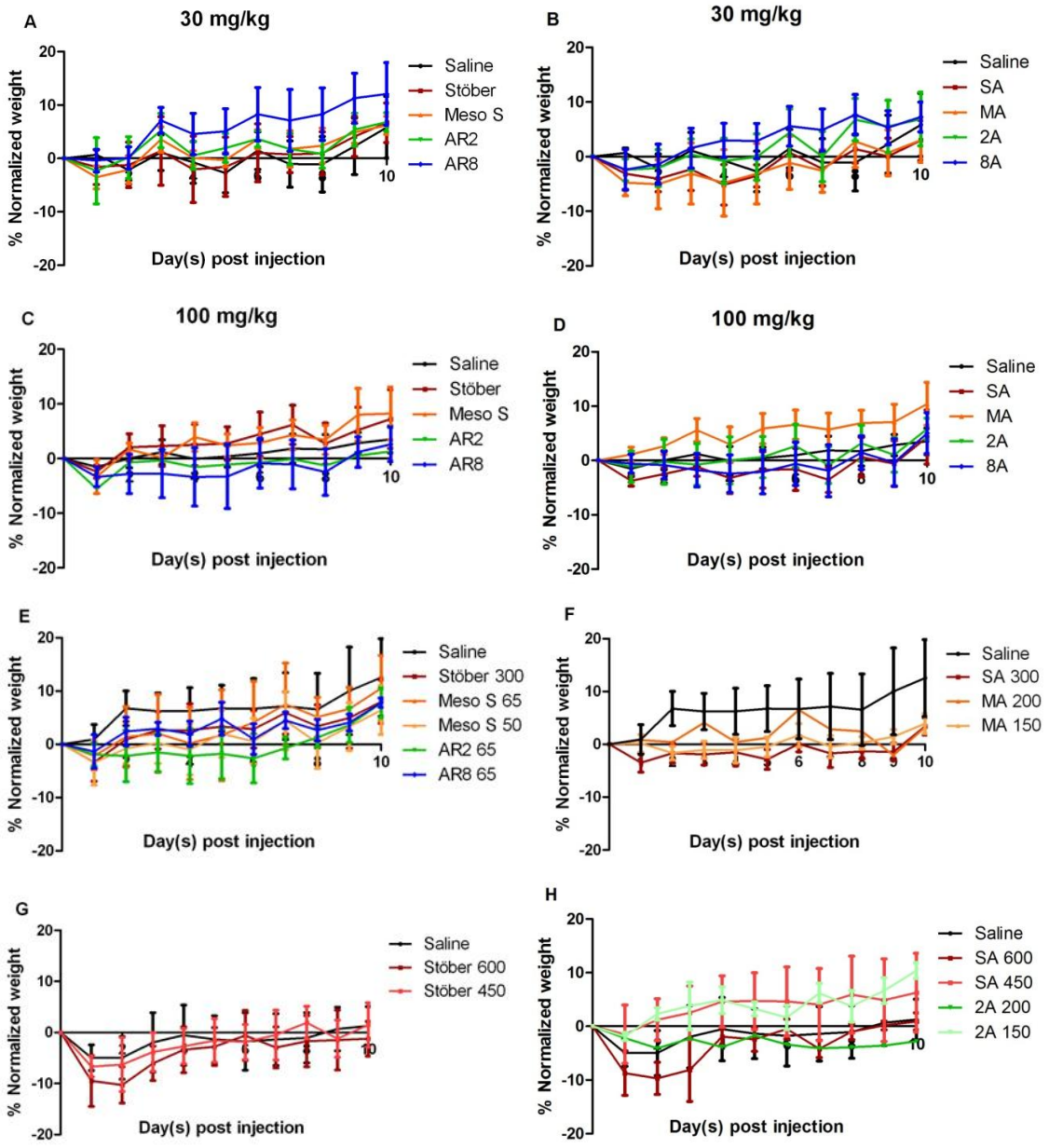

Figure 4.2 Normalized weight changes over 10 days post-intravenous injection of various SiO_2 at indicated doses. No significant difference in normalized weight gain was observed between treatment groups and the control group for each injection phase (four dosing phases were conducted in this study and four control groups were included) ($p > 0.05$).

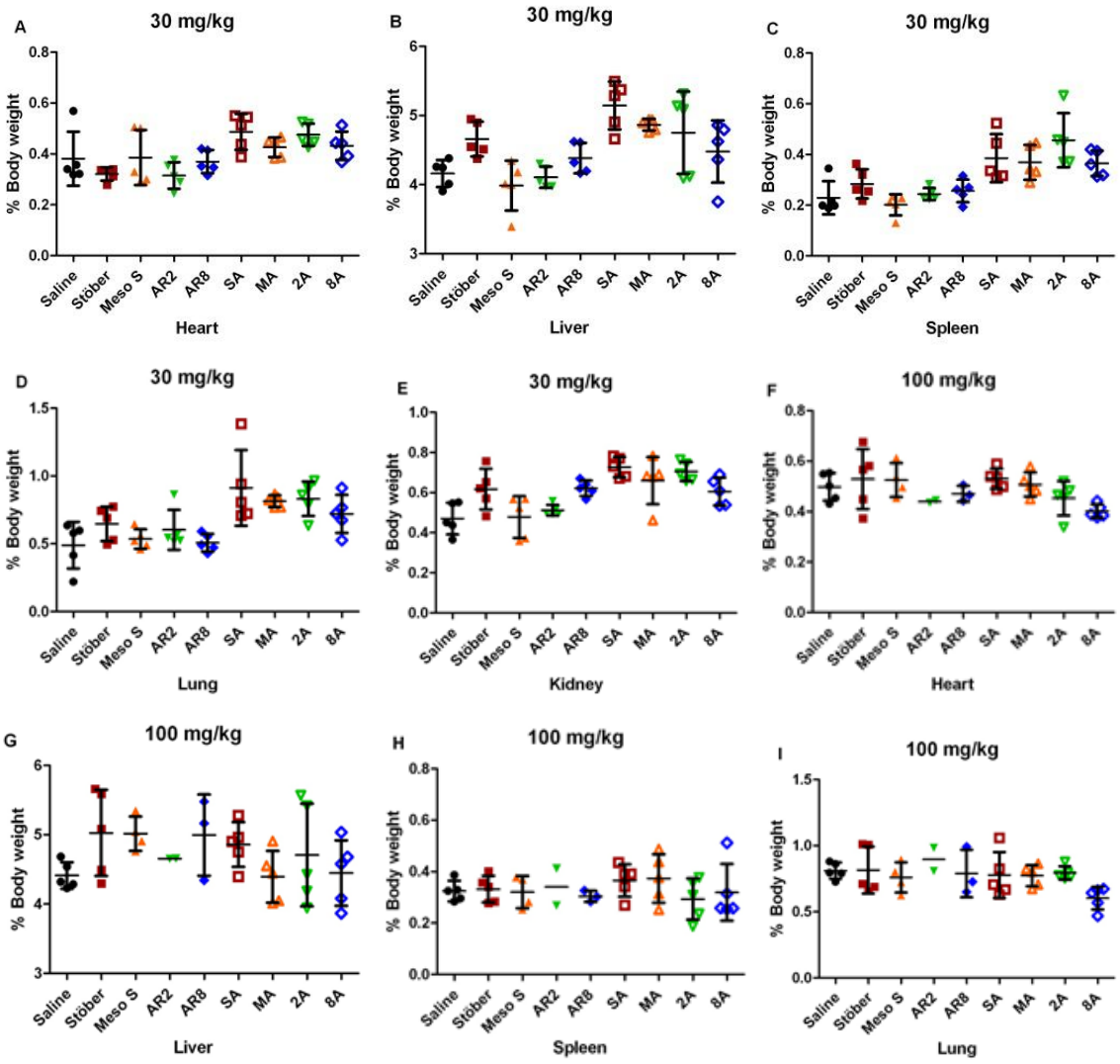

Figure 4.3 Organ weight percentage analysis of A, F, K, P) heart; B, G, L, Q) liver; C, H, M, R) spleen; D, I, N, S) lung; E, J, O, T) kidney from the survived animals subject to various SiO_2 treatment at indicated doses.

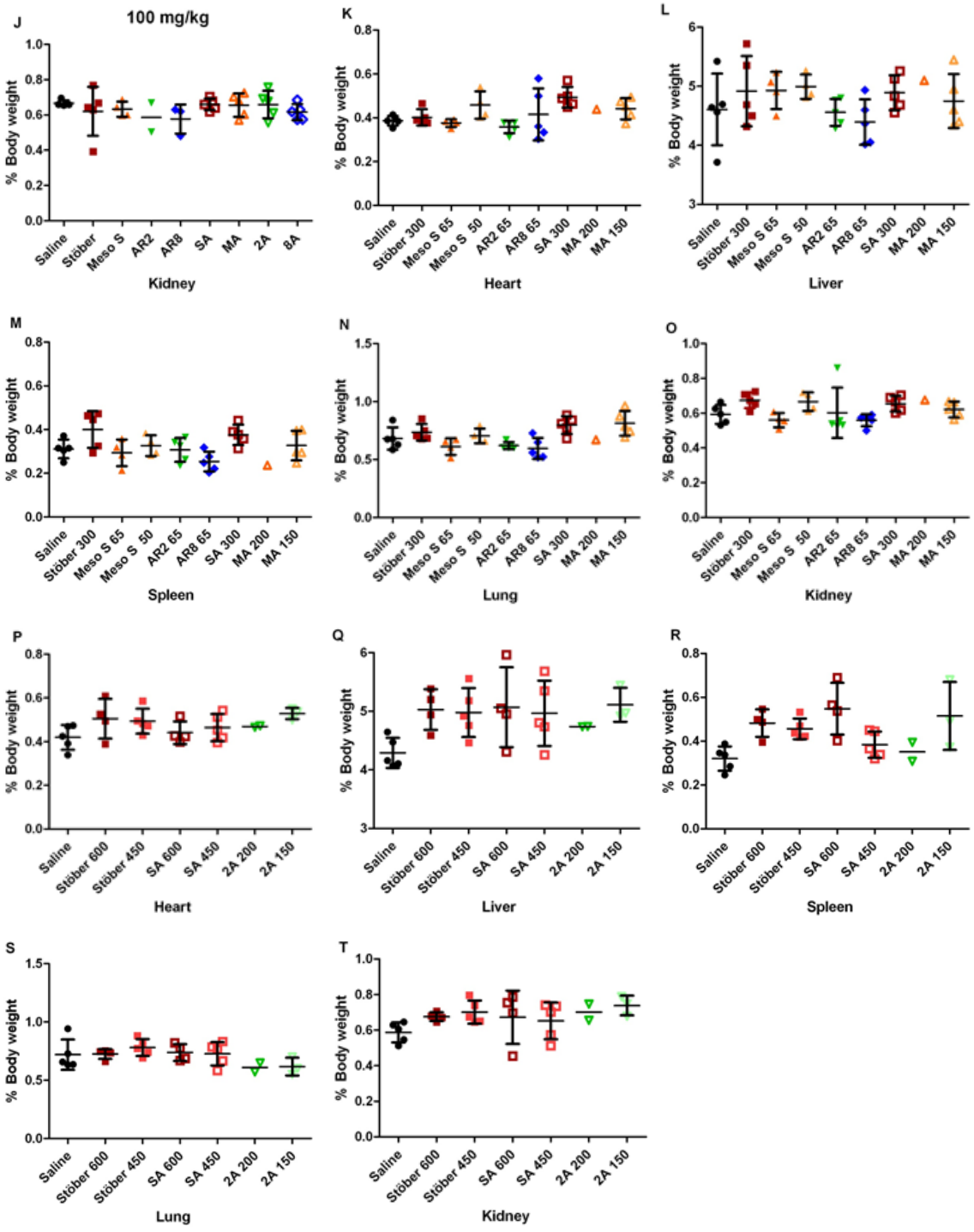

Figure 4.3 continued.

groups at all doses tested and the control groups ($p > 0.05$) (Figures 4.4-4.7), except that animals that survived from AR8 100 mg/kg showed significantly higher total bilirubin concentration than controls ($p < 0.05$) (Figure 4.5I), or animals dosed with Stöber at 600 mg/kg had significantly lower hemoglobin level ($p < 0.001$) (Figure 4.7D) coupled with significantly higher alanine aminotransferase concentration than controls ($p < 0.001$) (Figure 4.7H). Stöber caused hematological toxicity or hepatocellular injury at the high dose of 600 mg/kg. All surviving animals from the entire study had less than 0.2 mg/dL creatinine level upon euthanasia, indicating normal kidney function.

Among animals showing adverse reactions, renal compromise was the major abnormality of animals treated with mesoporous SiO_2 (Meso S, AR8) or MA, as indicated by dramatically increased blood urea nitrogen level (> 140 mg/dL *versus* 18 ± 3 mg/dL in control) or creatinine concentration (2 - 2.4 mg/dL *versus* < 0.2 mg/dL in control) (Table 4.4). Coupled with increased kidney weight percentages (0.99% - 1.19% *versus* 0.66 ± 0.01% in control), these data suggest that the kidney was the target organ of mesoporous SiO_2 intravenous toxicity, irrespective of geometrical features or surface characteristics (Table 4.4). There was an increase in liver weight percentage across the board for mesoporous SiO_2 treatments (5.75% - 6.37% *versus* 4.41 ± 0.19% in control) (Table 4.4). Combining the significantly increased total bilirubin concentrations in animals from AR8 100 mg/kg ($p < 0.05$) (Figure 4.5I), it seems that liver function was affected by exposure to mesoporous SiO_2. No inflammatory responses were observed in the animals showing acute toxicity as the total leukocyte counts remained in the normal range (Table 4.4).

In order to obtain accurate diagnosis of SiO_2 toxicity on a microscopic level,

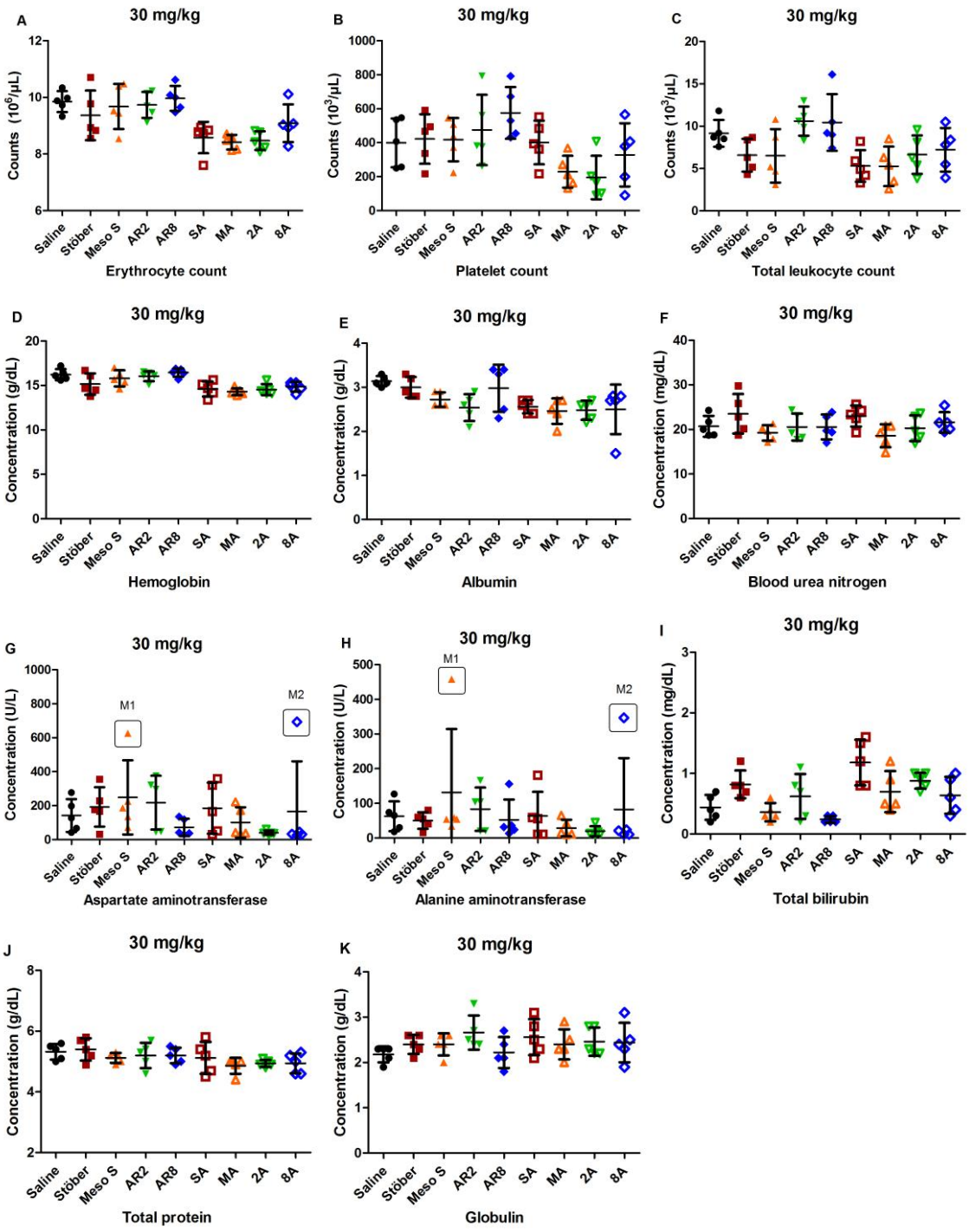

Figure 4.4 Blood counts (A-D) and blood chemistry (E-K) of animals treated at the dose of 30 mg/kg. No significant difference was observed in the hematological or chemical indices between various SiO_2 treatment groups and the control ($p > 0.05$). There were individual animals (Meso S 30 M1 or 8A 30 M2) which exhibited elevated aspartate aminotransferase or alanine aminotransferase levels (value circled with animal identity shown).

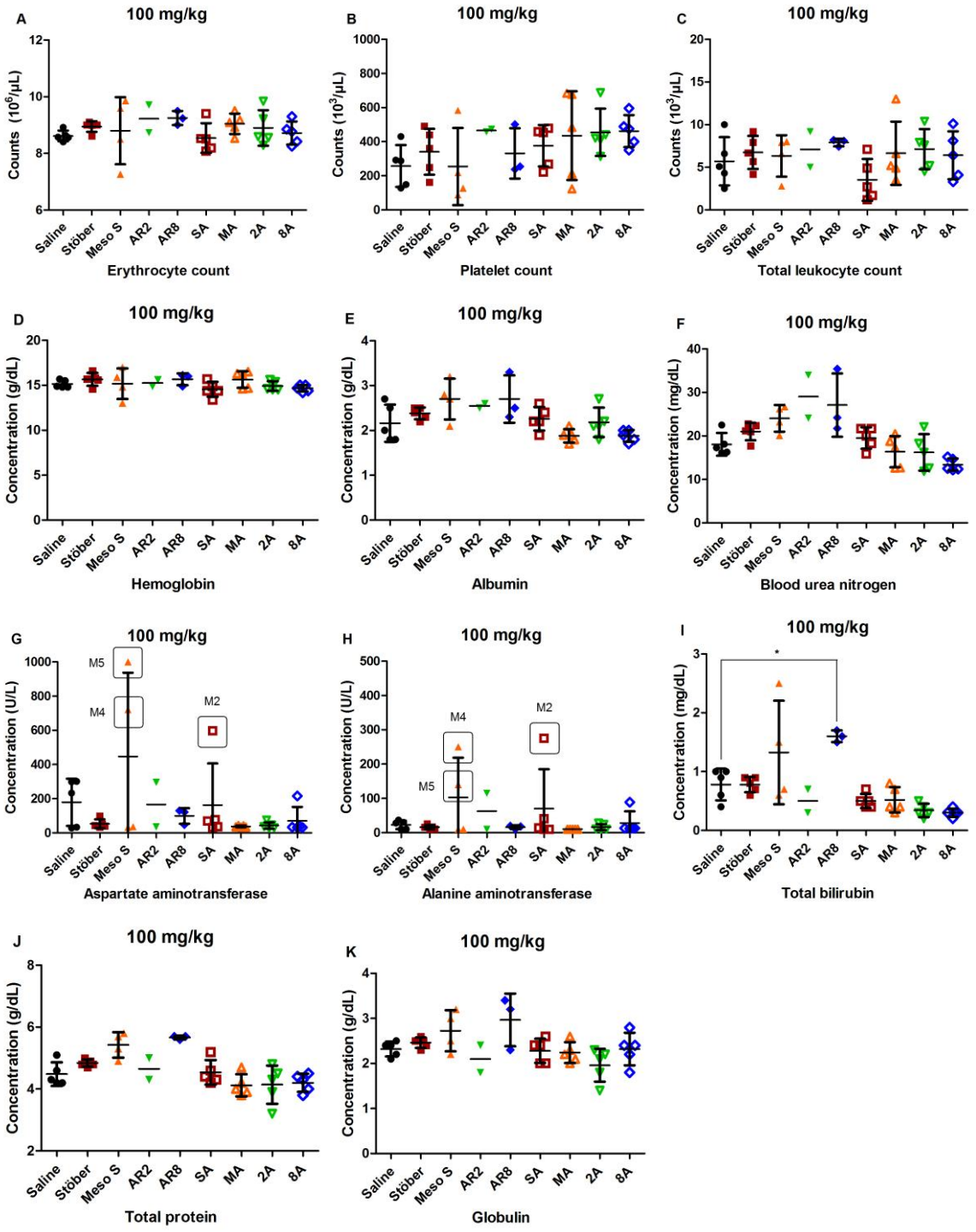

Figure 4.5 Blood counts (A-D) and blood chemistry (E-K) of animals treated at the dose of 100 mg/kg. Only the surviving animals from AR8 100 mg/kg exhibited a significant increase in total bilirubin concentration compared with the control ($^{*}p < 0.05$). There were individual animals (Meso S 100 M4, M5 or SA 100 M2) which exhibited elevated aspartate aminotransferase or alanine aminotransferase levels (value circled with animal identity shown).

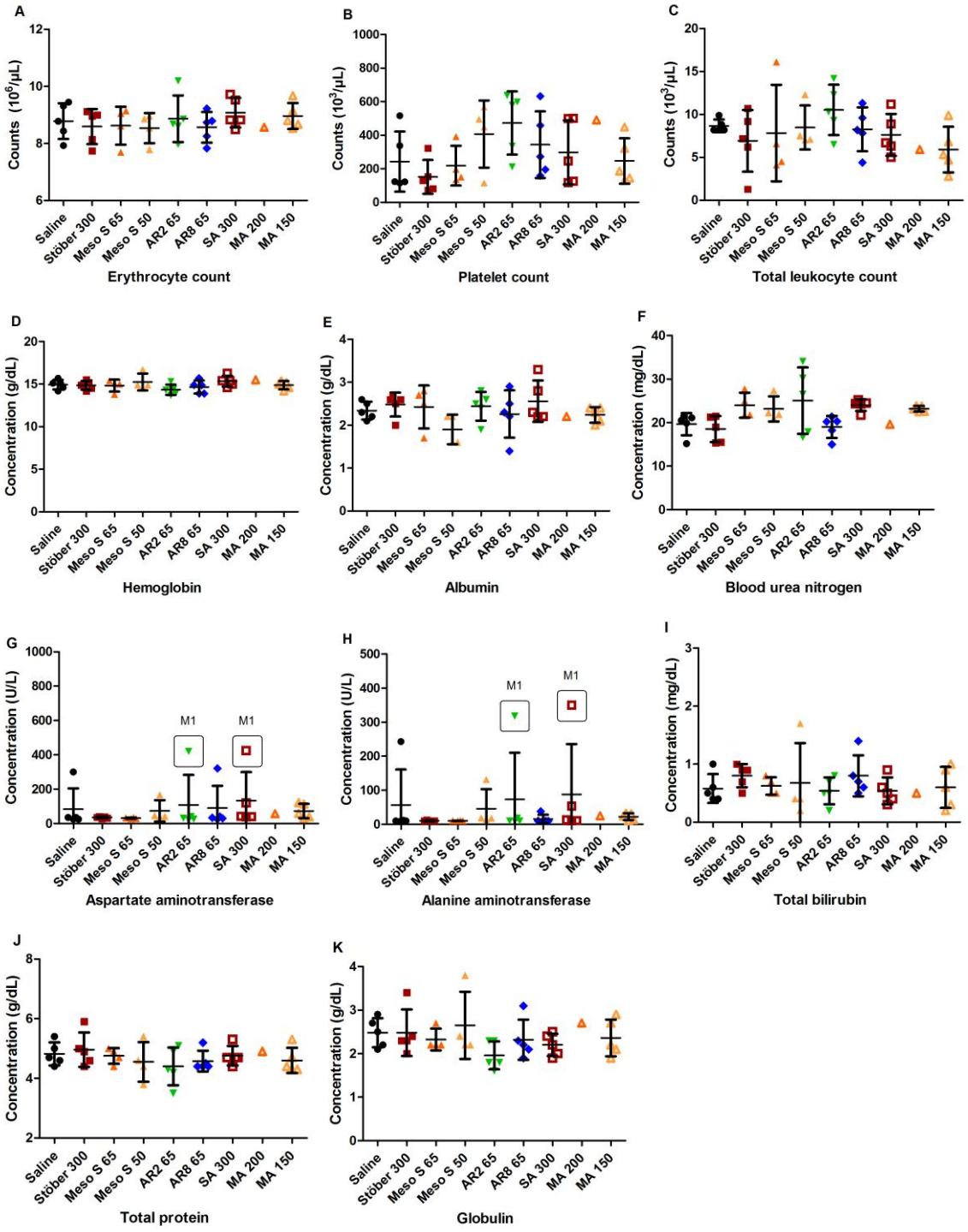

Figure 4.6 Blood counts (A-D) and blood chemistry (E-K) of animals treated at indicated dose. No significant changes were observed between each SiO_2 treatment group and the control ($p > 0.05$). There were individual animals (AR2 65 M1 or SA 300 M1) which exhibited elevated aspartate aminotransferase or alanine aminotransferase levels (value circled with animal identity shown).

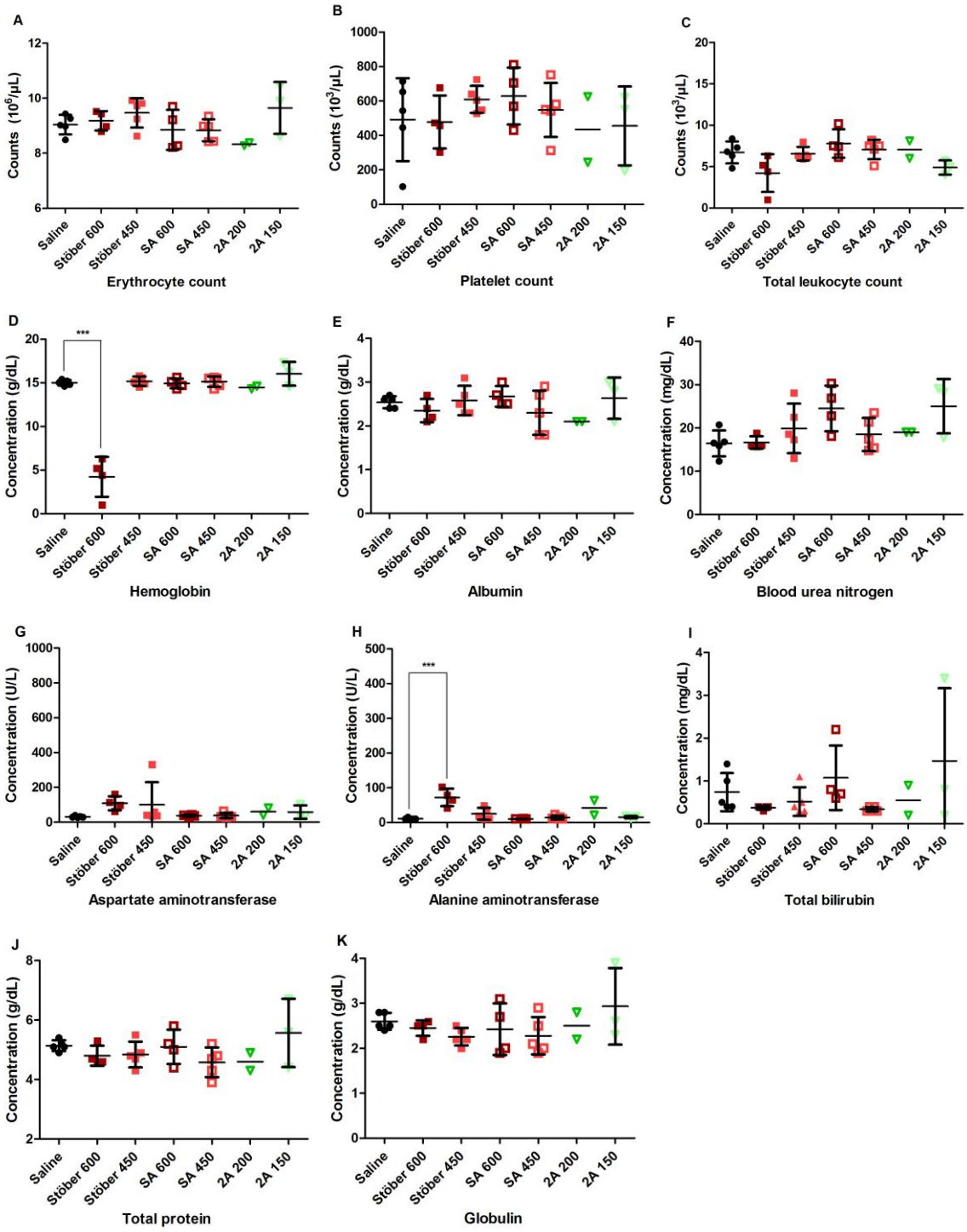

Figure 4.7 Blood counts (A-D) and blood chemistry (E-K) of animals treated at indicated dose. No significant changes were observed between each SiO_2 treatment group and the control, except that the surviving animals from Stöber 600 mg/kg showed significant decrease in hemoglobin concentration ($^{***}p < 0.001$) and significant increase in alanine aminotransferase level ($^{***}p < 0.001$) compared with the control.

Table 4.4 Hematological and blood chemical indices of selected mice which exhibited major adverse reactions post-intravenous injection of SiO_2 at toxic doses and the organ weight percentages and weight changes upon necropsy of each mouse

Treatment	Saline*	Meso S	AR2	AR8	MA
Animal identity		100 mg/kg, M2	100 mg/kg, M4	100 mg/kg, M5	300 mg/kg, M2
Complete blood count					
Erythrocyte count (10^6/μL)	8.62 ± 0.18	7.25	5.34	8.51	8.00
Platelet count (10^3/μL)	257 ± 123	163	139	262	319
Total leukocyte count (10^3/μL)	5.7 ± 2.8	2	1.9	3.1	2.7
Hemoglobin (g/dL)	15.1 ± 0.4	13.9	15.9	15.6	14.1
Blood chemistry					
Kidney function					
Blood urea nitrogen (mg/dL)	18 ± 3	>140	n/a	>140	>140
Creatinine (mg/dL)	<0.2	2.4	n/a	2	2.2
Liver function					
Albumin (g/dL)	2.2 ± 0.4	1.3	n/a	1.5	2.2
Aspartate aminotransferase (U/L)	179 ± 138	243	n/a	162	334
Alanine aminotransferase (U/L)	32 ± 5	23	n/a	20	129
Total bilirubin (mg/dL)	0.8 ± 0.3	1.1	n/a	1.3	1.8
Other biomarkers					
Globulin (g/dL)	2.3 ± 0.2	4.1	n/a	3.6	3.3
Total protein (g/dL)	4.5 ± 0.4	5.4	n/a	5.1	5.5
% Body weight					
Heart	0.49 ± 0.05	0.43	0.59	0.44	0.44
Liver	4.41 ± 0.19	5.94	6.37	5.75	4.70
Spleen	0.32 ± 0.04	0.28	0.34	0.36	0.26
Lung	0.81 ± 0.06	0.55	0.99	1.04	0.83
Kidney	0.66 ± 0.01	0.99	1.06	1.19	1.13
% Normalized weight upon death	3.50 ± 2.44	-8.52	-4.43	-4.18	-4.16

*Data were mean ± SD (n = 5) from the control group for 100 mg/kg dose phase.

major organs from animals were subject to histological evaluation. Compared with control animals that received saline (Figure 4.8), the animals treated with nonporous SiO_2 (Stöber) at a high dose of 600 mg/kg developed thrombosis on the endocardium of the heart (Figures 4.9A, 4.10A). Extensive lung hemorrhage was also observed (Figure 4.9D). The presence of macrophages with light bluish grey cytoplasm suggests that SiO_2 uptake was detected in the spleen and liver (Figure 4.10B-C). Since animals of this group also showed significantly increased alanine aminotransferase level in the plasma ($p < 0.001$) (Figure 4.7H), it could be deducted that these animals experienced moderate liver dysfunction. This may be induced by nanoparticle accumulation or by the secondary effect of obstructive damage to the circulatory and respiratory systems (mainly heart and lung) by Stöber.

Mesoporous SiO_2, irrespective of the geometrical features, caused vascular congestion in viscera of mice at the dose of 100 mg/kg (Figures 4.11-4.15), especially in the medullary interstitium of the kidney (Figures 4.11F, 4.13F, 4.14F). This change corresponded with elevated levels of renal biomarkers from these animals (Table 4.4). It could be due to compromised blood flow in the vasa recta which makes the renal interstitium a likely location for thrombosis [2]. Calcium deposition was observed as intense blue staining in the cortex in one animal (M1) from AR2 65 mg/kg treatment (Figure 4.16). This indicates that kidney damage occurred; therefore, 65 mg/kg was ruled out as MTD and the lower dose of 30 mg/kg was determined to be MTD for AR2. No histological abnormality was found in major organs of the animal (M1) from Meso S 30 mg/kg treatment (Figure 4.17) and thus, 30 mg/kg was still considered as the MTD for Meso S.

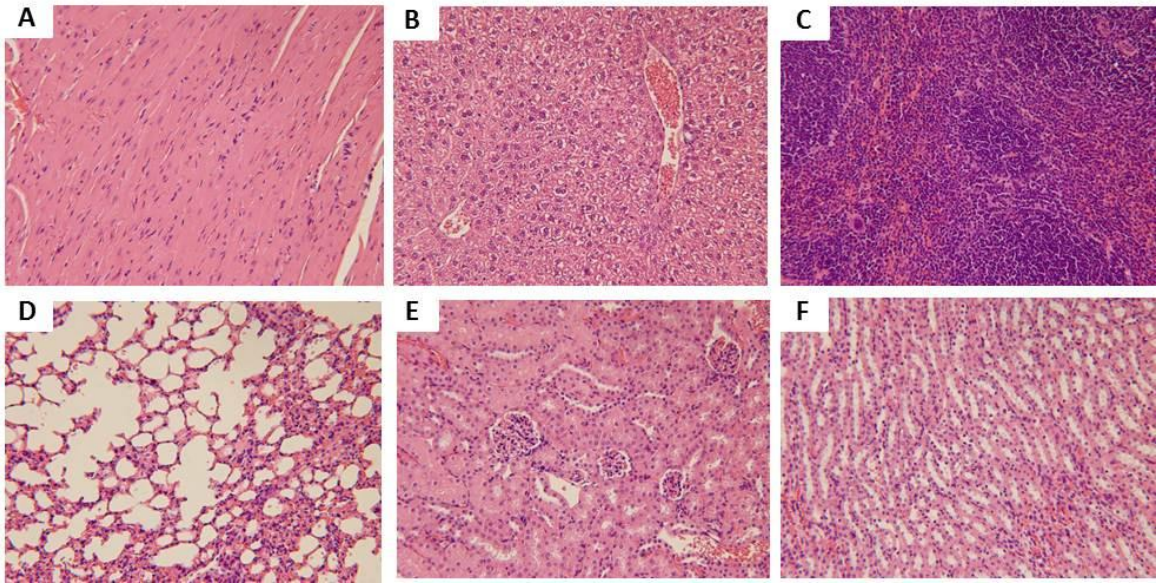

Figure 4.8 Light microscopic analysis of organs recovered from control group: A) heart, B) liver, C) spleen, D) lung, E) kidney (glomeruli), F) kidney (tubules). All H&E staining images were 200× the original magnification.

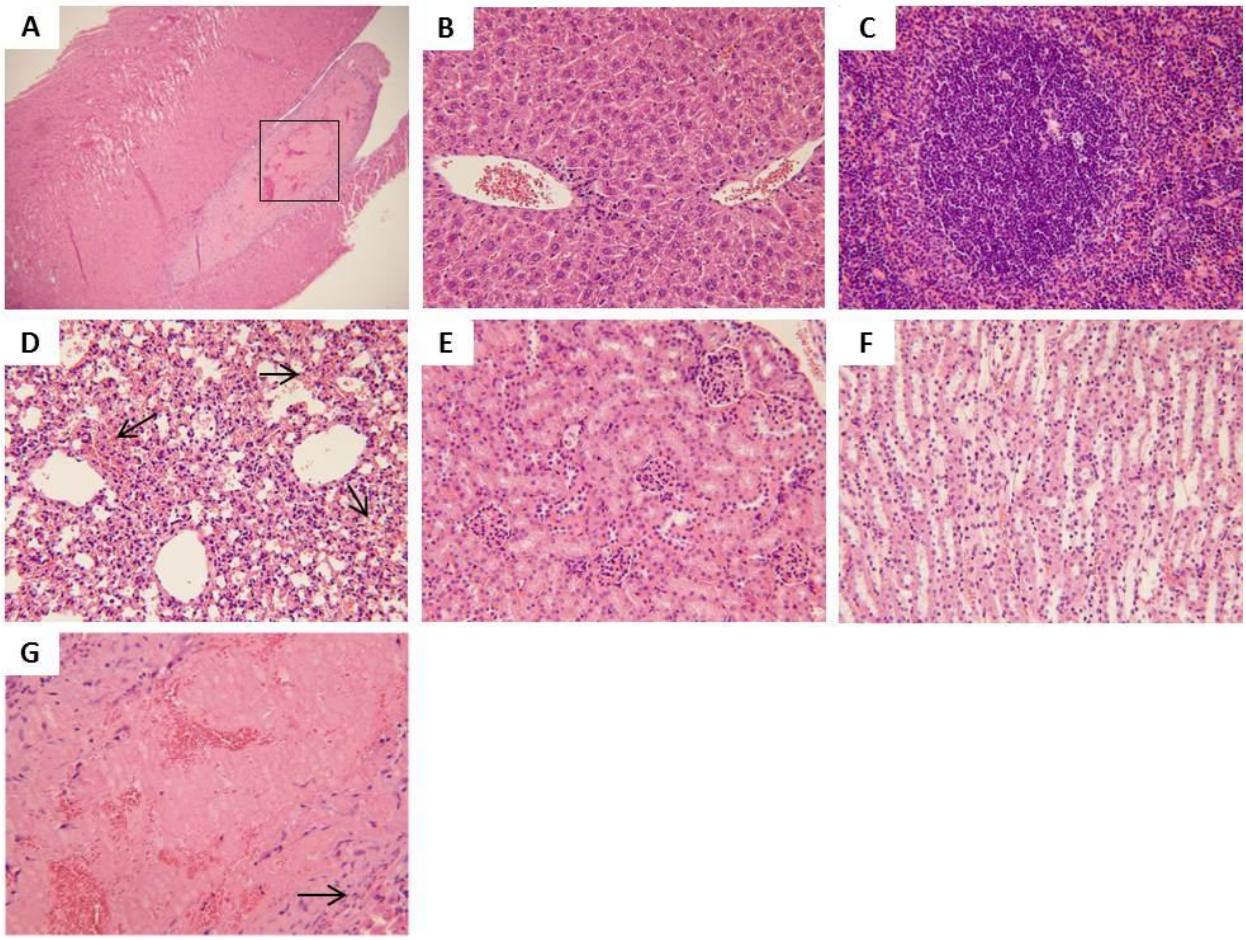

Figure 4.9 Light microscopic analysis of organs recovered from Stöber 600 mg/kg M2: A) heart (40×), rectangle box indicates the area that is amplified and shown in G, B) liver, C) spleen, D) lung, arrows indicate hemorrhage into the alveoli, E) kidney (glomeruli), F) kidney (tubules), G) heart. The arrow indicates fibrosis layer organized around the thrombus. All H&E staining images were 200× the original magnification except A (40×).

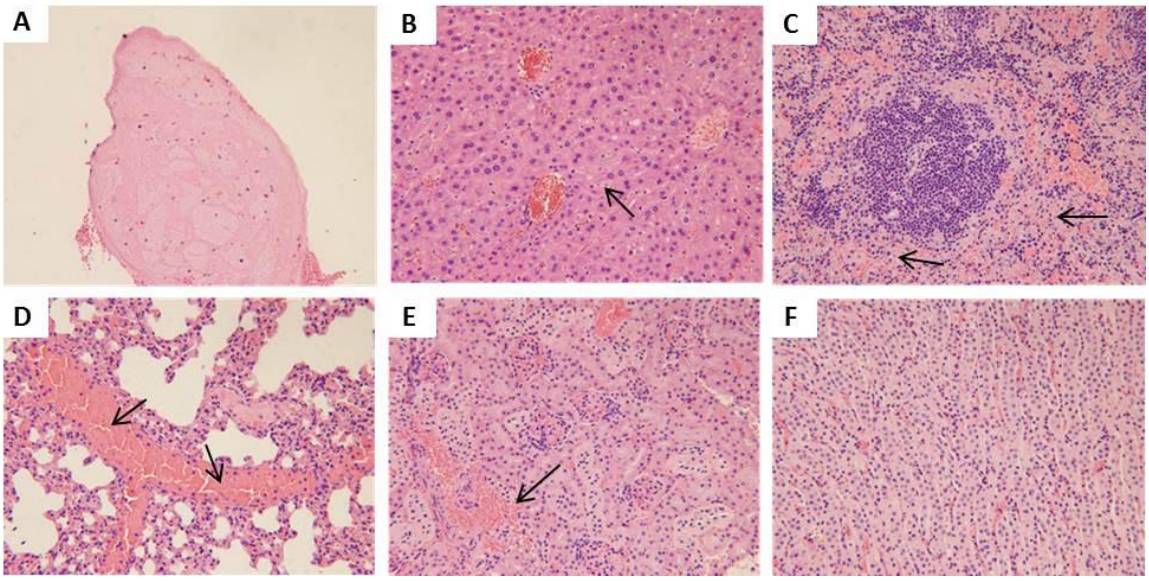

Figure 4.10 Light microscopic analysis of organs recovered from Stöber 600 mg/kg M3: A) heart (thrombus body shown), B) liver, arrow indicates macrophage with light grey cytoplasm suggesting SiO_2 presence, C) spleen, arrows indicate macrophages with light grey cytoplasm implying SiO_2 presence, D) lung, arrows indicate congestion in the pulmonary capillary, E) kidney (glomeruli), arrow indicates congestion in the interstitium, F) kidney (tubules). All H&E staining images were 200× the original magnification.

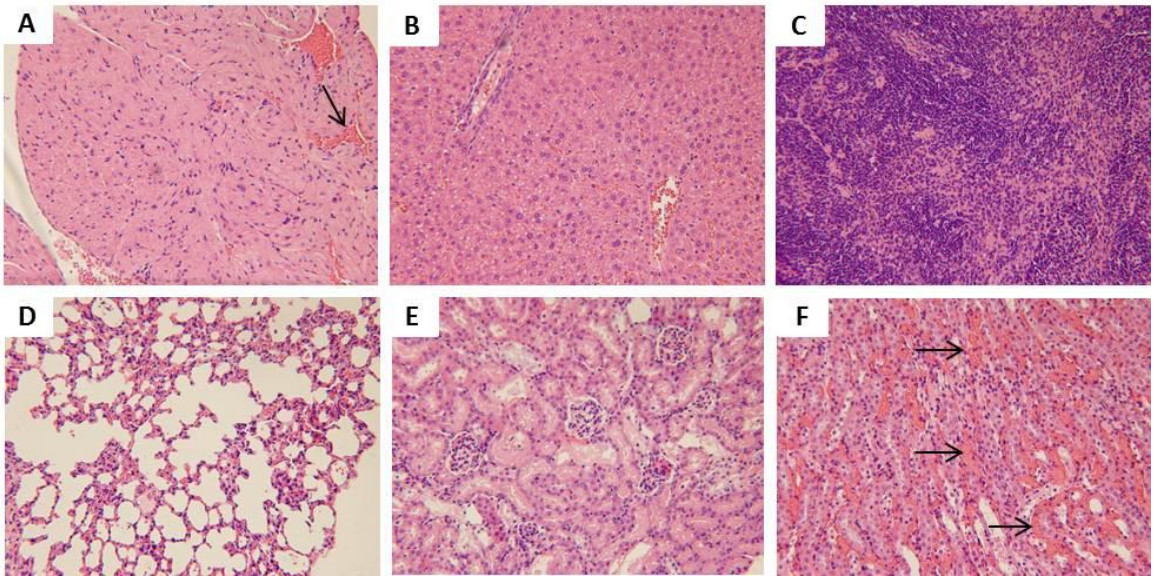

Figure 4.11 Light microscopic analysis of organs recovered from Meso S 100 mg/kg M2: A) heart, arrow indicates the congestion in the capillary, B) liver, C) spleen, D) lung, E) kidney (glomeruli), F) kidney (tubules), arrows indicate vasa recta congestion. All H&E staining images were 200× the original magnification.

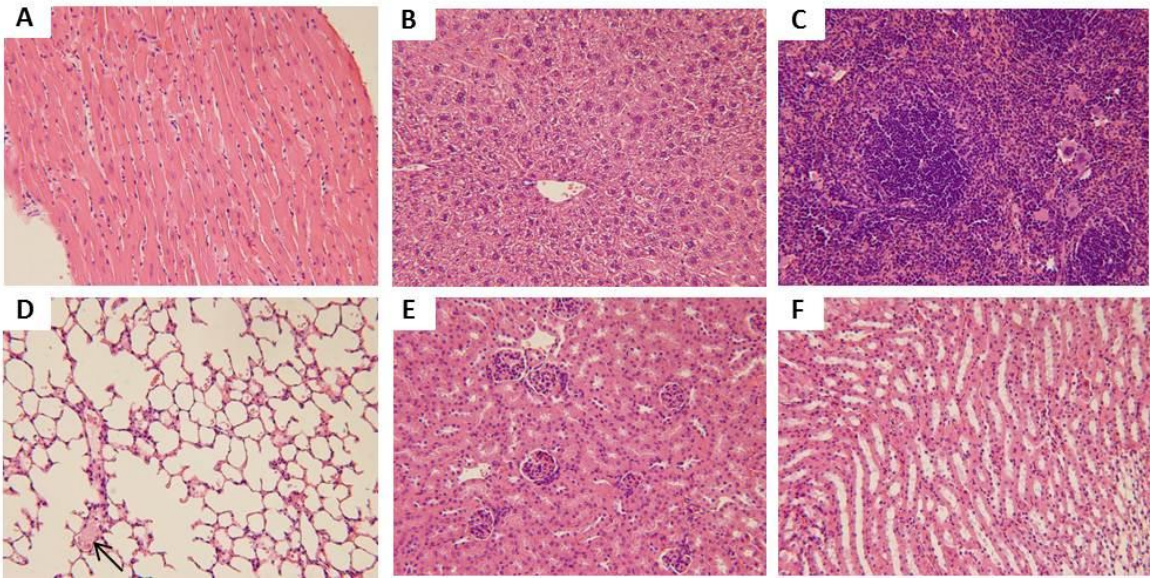

Figure 4.12 Light microscopic analysis of organs recovered from Meso S 100 mg/kg M5: A) heart, B) liver, C) spleen, D) lung, arrow indicates lung edema, E) kidney (glomeruli), F) kidney (tubules). All H&E staining images were 200× the original magnification.

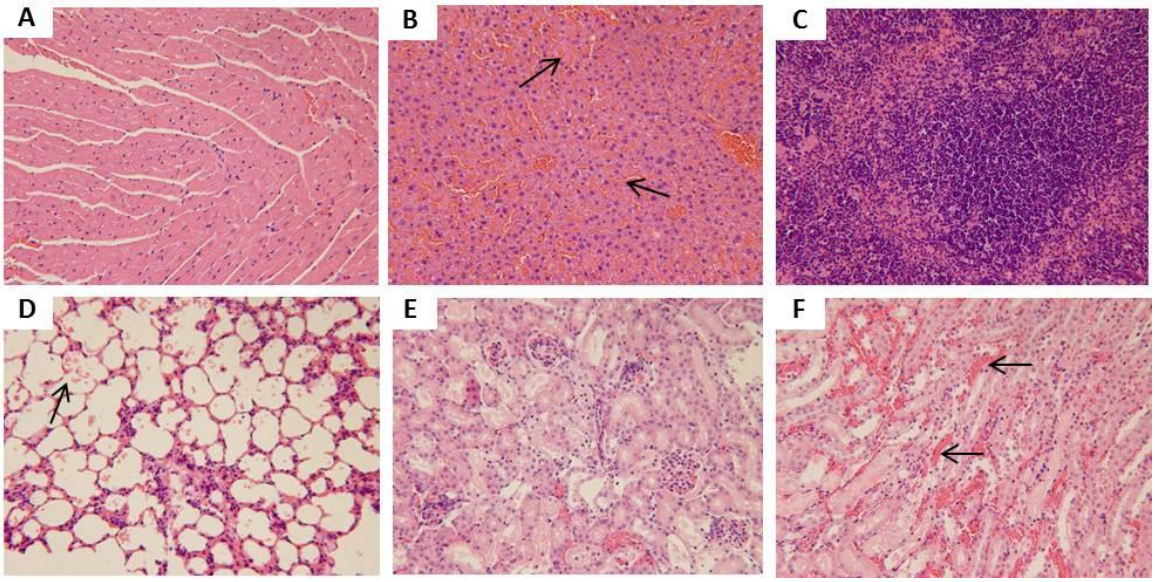

Figure 4.13 Light microscopic analysis of organs recovered from AR2 100 mg/kg M4: A) heart, B) liver, arrows indicate congestion in hepatic capillaries, C) spleen, D) lung, arrow indicates the hemorrhage in the alveoli, E) kidney (glomeruli), F) kidney (tubules), arrows indicate congestion in the renal interstitium. All H&E staining images were 200× the original magnification.

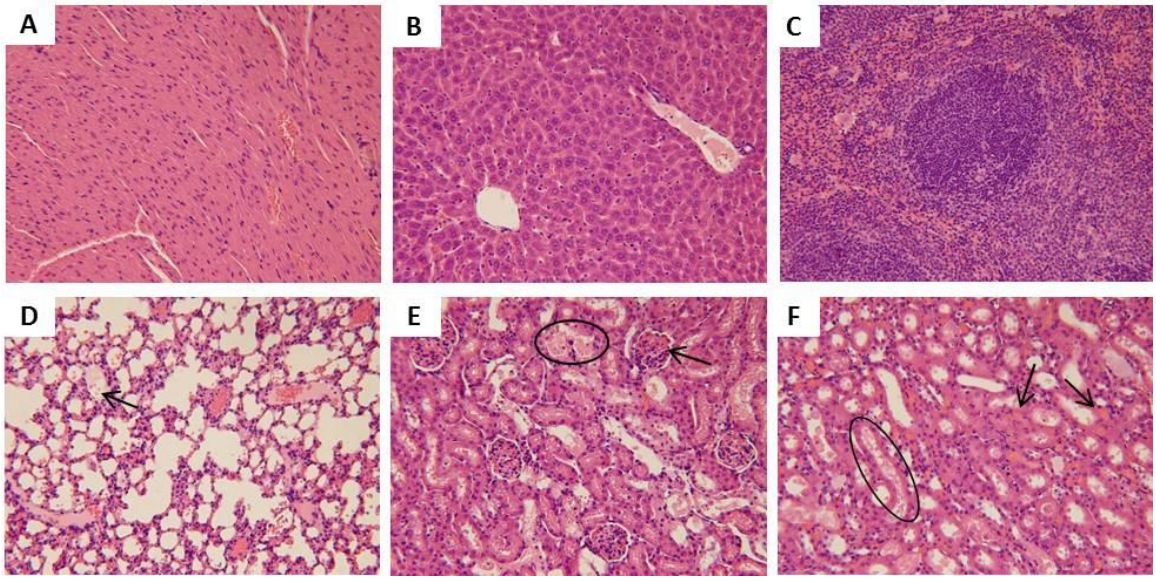

Figure 4.14 Light microscopic analysis of organs recovered from AR8 100 mg/kg M5: A) heart, B) liver, C) spleen, D) lung, arrow indicates lung edema, E) kidney (glomeruli), circle indicates the tubule that went through degeneration with protein seen in the tubule, arrow indicates congestion in the glomerulus, F) kidney (tubules), circle indicates the degeneration in the tubule with protein seen in the tubule, arrows point to the congestion in the renal interstitium. All H&E staining images were 200× the original magnification.

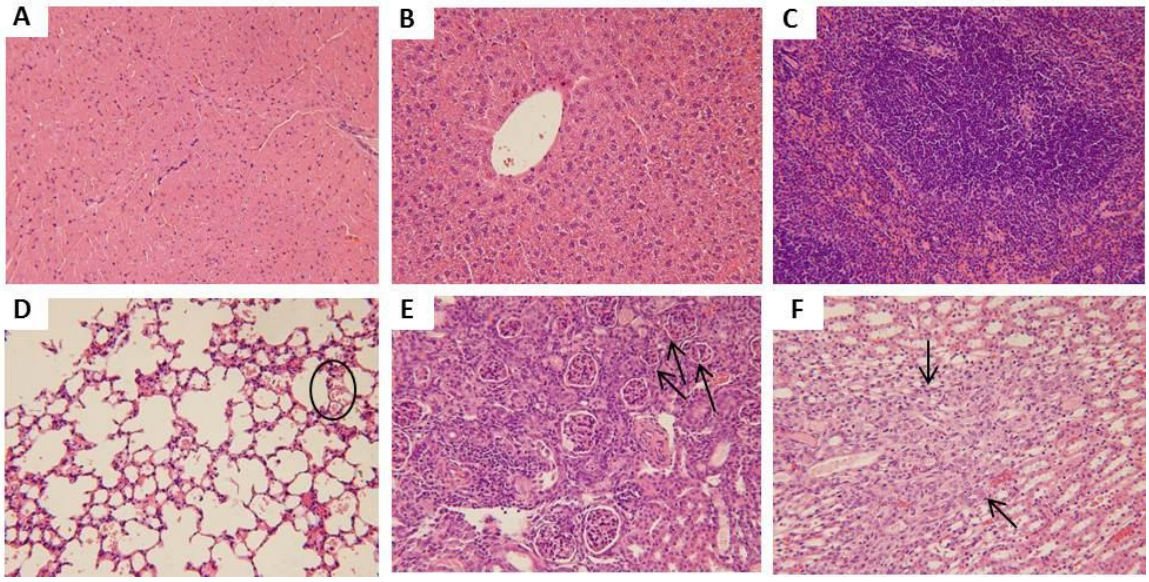

Figure 4.15 Light microscopic analysis of organs recovered from AR8 100 mg/kg M3: A) heart, B) liver, C) spleen, D) lung, circle encloses the hemorrhage in the alveoli, E) kidney (glomeruli), arrows indicate contracted glomeruli with fibrosis observed in the cortex, F) kidney (tubules), arrows indicate fibrosis formation in the medulla. All H&E staining images were 200× the original magnification.

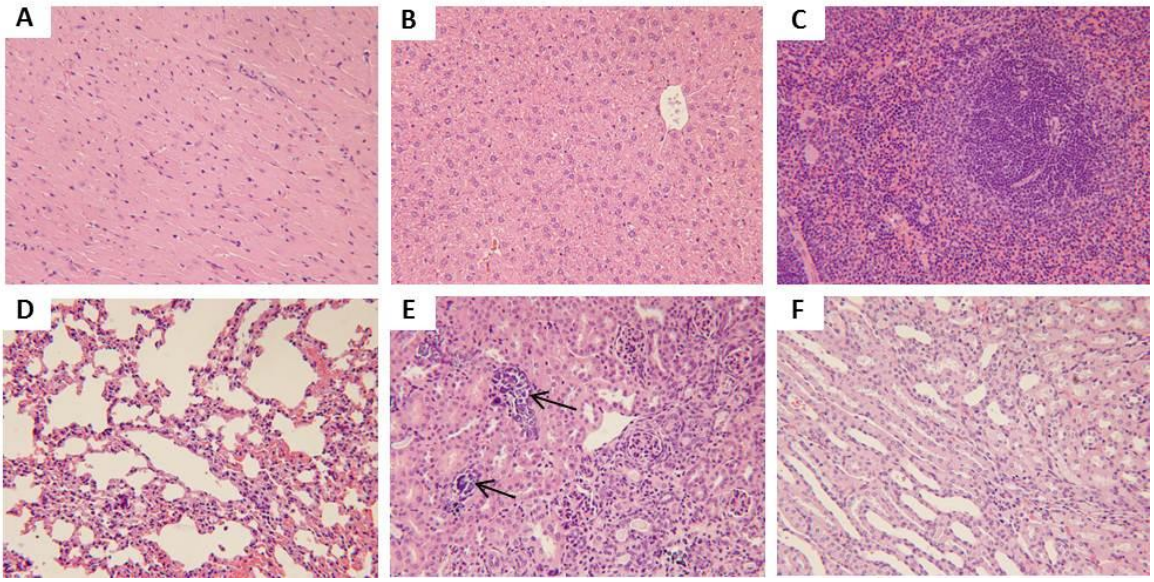

Figure 4.16 Light microscopic analysis of organs recovered from AR2 65 mg/kg M1: A) heart, B) liver, C) spleen, D) lung, E) kidney (glomeruli), arrows indicate calcium deposition, F) kidney (tubules). All H&E staining images were 200× the original magnification.

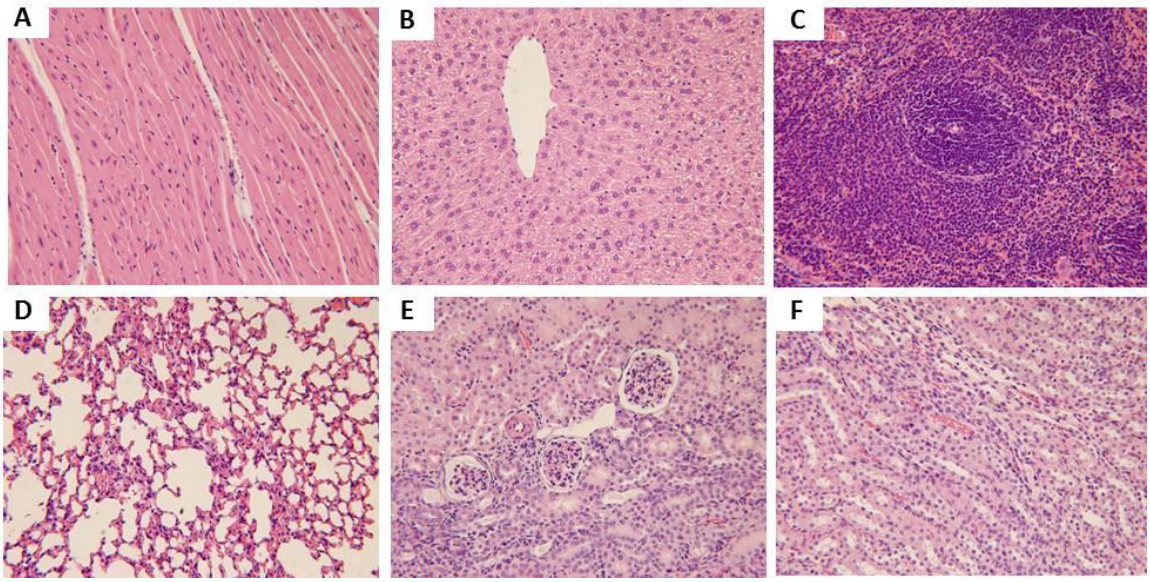

Figure 4.17 Light microscopic analysis of organs recovered from Meso S 30 mg/kg M1: A) heart, B) liver, C) spleen, D) lung, E) kidney (glomeruli), F) kidney (tubules). All H&E staining images were 200× the original magnification.

Amine-modified nonporous or mesoporous SiO_2 caused hemorrhage or congestion in the lung and kidney (Figures 4.18-4.21). Pulmonary embolism was observed in the lung in animal M2 from MA 300 mg/kg which was sacrificed 22 hours post-injection due to acute adverse reactions (Figure 4.19G). The histological examination confirmed the onset of lung thrombosis with renal congestion (Figure 4.19D, F). One mouse (M1) from 8A 300 mg/kg died immediately post-injection and pulmonary embolism was observed upon necropsy with confirmation by histologic observation of pulmonary congestion with additional symptoms of kidney congestion (Figure 4.21). The presence of macrophages with light bluish grey cytoplasm in the liver or spleen indicated the association of amine-modified SiO_2 with RES in these organs (Figures 4.18-4.19). In the animals treated with amine-modified SiO_2 at high doses, the color of red pulp in the spleen turned from pinkish red to light blue, probably because of the extensive association of amine-modified SiO_2 with macrophages (Figures 4.18C, 4.19C).

In sum, histological examination demonstrated that there was minimum cellular toxicity that occurred in major organs (heart, liver, spleen, lung, and kidney). Lesions were mainly associated with mechanical obstruction in the vasculature upon intravenous injection of various SiO_2 which resulted in congestion in major organs and consequently led to organ failure and life termination. At the MTD or even lower doses of each type of nanoparticle, no pathologic changes were found in major organs of SiO_2 treatment groups compared with control groups, including individual animals (8A 30 mg/kg M2, SA100 mg/kg M2, SA 300 mg/kg M1) which showed moderate liver enzyme level increase in plasma (Figures 4.4-4.6G-H). The major adverse reactions to intravenous injection of various SiO_2 at toxic doses are summarized in Table 4.3.

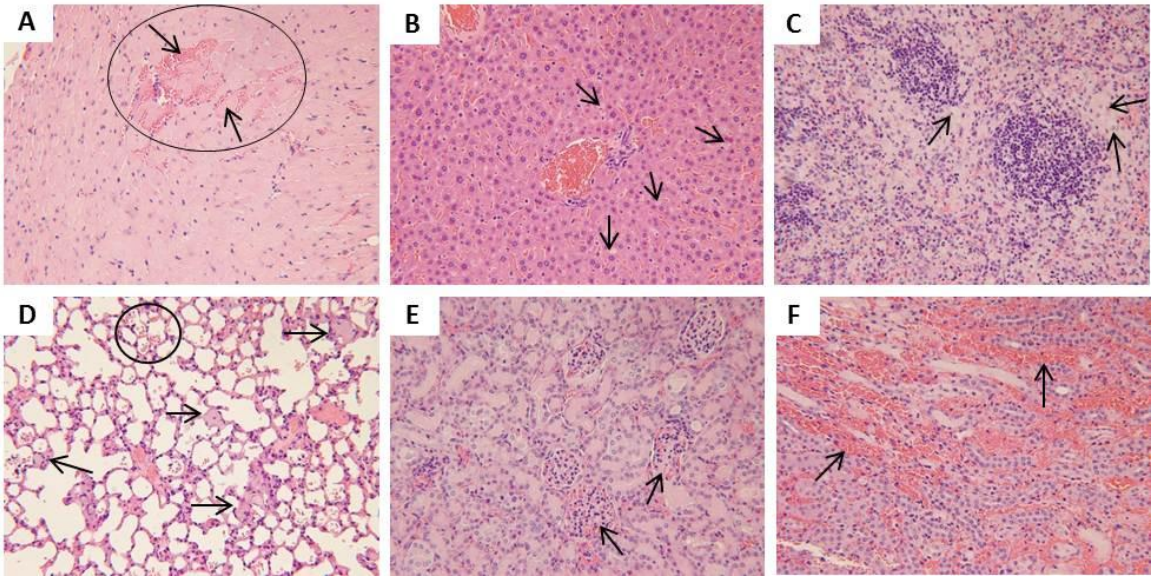

Figure 4.18 Light microscopic analysis of organs recovered from SA 600 mg/kg M3: A) heart, the circle refers to hemorrhage into the cardiac muscle, the arrow on top indicates the hemorrhage that separates the cardiac fiber, the arrow below indicates the cardiac fiber surrounded by the hemorrhage, B) liver, C) spleen, arrows in B and C indicate macrophages with light bluish grey cytoplasm implying SiO_2 internalization, D) lung, arrows indicate bluish grey congestion in the capillary suggesting SiO_2 presence and the circle encloses the hemorrhage in alveoli, E) kidney (glomeruli), arrows indicate congestion in the glomeruli, F) kidney (tubules), arrows indicate hemorrhage into renal interstitium. All H&E staining images were 200× the original magnification.

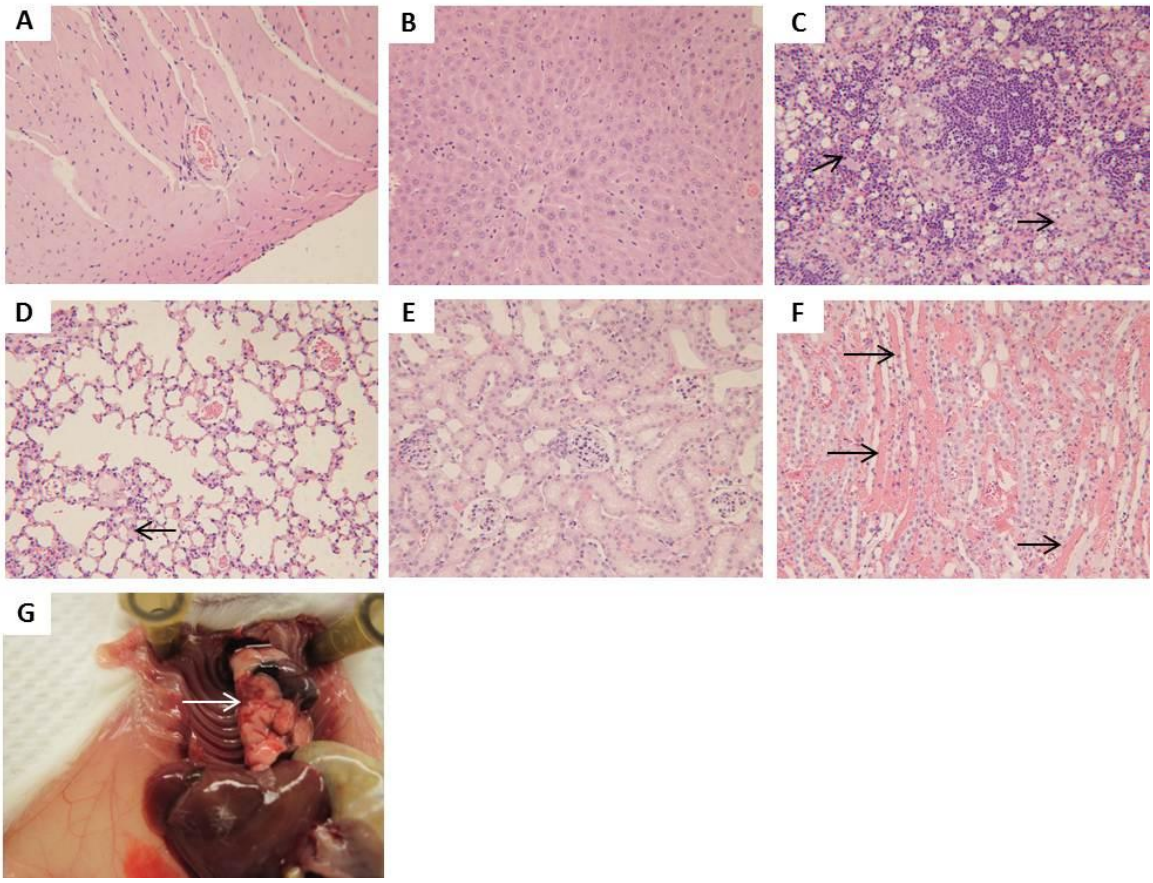

Figure 4.19 Light microscopic analysis of organs recovered from MA 300 mg/kg M2: A) heart, B) liver, C) spleen, arrows point to macrophages with light bluish grey cytoplasm indicating SiO_2 uptake, D) lung, the arrow indicates congestion in the capillary, E) kidney (glomeruli), F) kidney (tubules), arrows indicate intravasculature congestion. G) Pulmonary embolism (pointed by the arrow) was observed upon necropsy of this animal. All H&E staining images were 200× the original magnification.

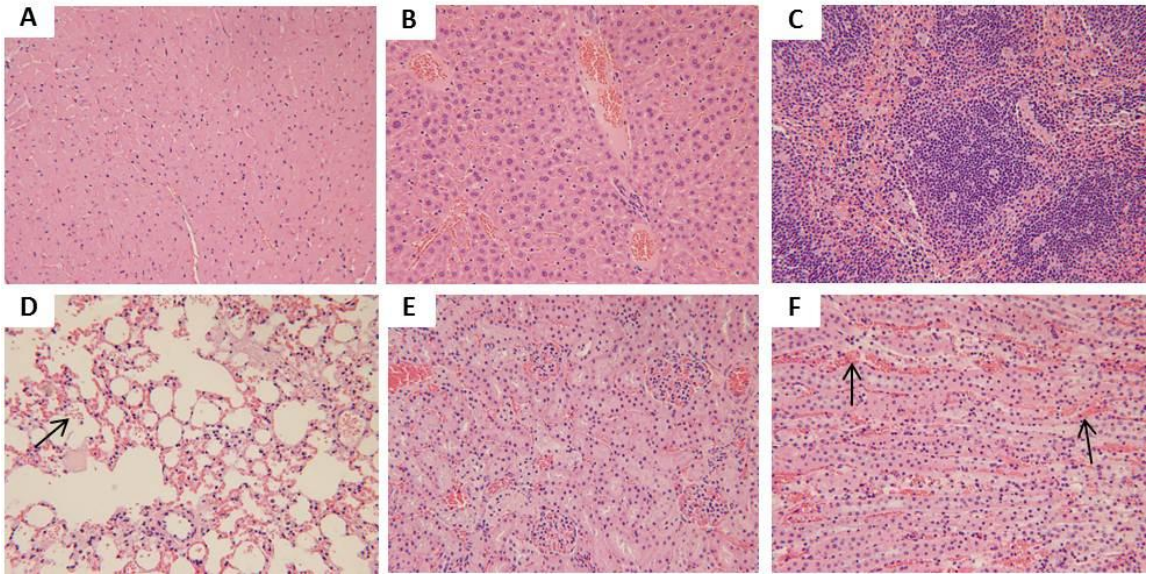

Figure 4.20 Light microscopic analysis of organs recovered from 2A 200 mg/kg M4: A) heart, B) liver, C) spleen, D) lung, arrow indicates the hemorrhage in the alveoli, E) kidney (glomeruli), F) kidney (tubules), arrows indicate congestion in the renal interstitium. All H&E staining images were 200× the original magnification.

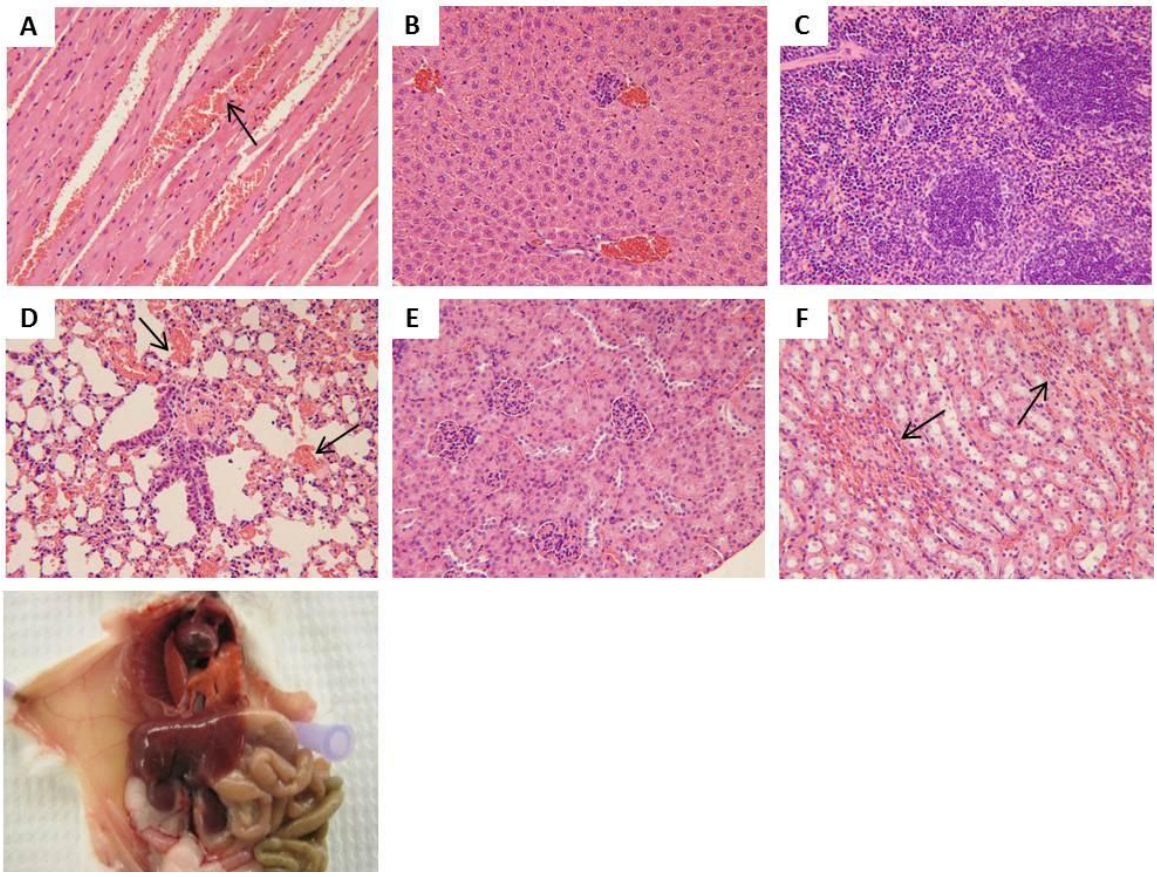

Figure 4.21 Light microscopic analysis of organs recovered from 8A 300 mg/kg M1: A) heart, arrow indicates hemorrhage into the cardiac muscle, B) liver, C) spleen, D) lung, arrows indicate pulmonary congestion, E) kidney (glomeruli), F) kidney (tubules), arrows indicate congestion in the renal interstitium. G) Pulmonary embolism was observed upon necropsy of this animal. All H&E staining images were 200× the original magnification.

Table 4.5 lists the dose equivalents of nanoparticles calculated on the basis of mass, total surface area, external surface area, total nanoparticle number, or total nanoparticle volume normalized to the animal weight [4]. It can be observed that dosing based on a total surface area was the most relevant parameter in evaluating the MTD of nanoparticles administered by the intravenous route since the variation of MTD equivalent dose expressed as total surface area per kilogram was the lowest (27%) among the five dose equivalents. This agreed well with previous studies, indicating that similar gene expression changes in cell culture [12] or similar toxicity thresholds to liver in mice [13] were achieved for nonporous SiO_2 of different sizes dosed on an equivalent surface area basis. In our case, reaching MTD, as the common biological outcome, has been achieved for SiO_2 of different porosities or geometrical features that were dosed on an equivalent total surface area basis of 15.6 ± 4.3 m^2/kg animals.

4.4 Discussion

Toxicity profile of SiO_2 is a crucial factor in determining their potential application in nanomedicine. In this chapter, we investigated the single-dose, acute toxicity of engineered SiO_2 of various shapes, porosities, and surface characteristics upon intravenous injection to immune-competent mice. In order to explain the difference in MTD and to relate it with SiO_2 physicochemical properties, representative spherical SiO_2 were incubated with 50% serum at 1 mg/mL for 30 minutes at 37 ^oC to evaluate the hydrodynamic size changes by DLS measurement. 50% serum was used to mimic the *in vivo* protein environment when nanoparticles were exposed to the circulation. SiO_2 concentration 1mg/mL was equivalent to initial blood concentration achieved at 100 mg/kg dose, which led to a drastic difference in animal response to intravenous injection

Table 4.5 The dose equivalents of nanoparticles at MTD on the basis of mass, total surface area, external surface area, total number, or total volume

Treatment	Mass (mg/kg)	Total surface area (m^2/kg)	External surface area (m^2/kg)	Total number ($\times 10^{13}$/kg)	Total volume ($\times 10^{-2}$ cm^3/kg)
Stöber	450	10.8	10.8	25.6	20.5
Meso S	30	19.9	3.2	3.0	3.3
AR2	30	13.3	3.0	4.2	3.2
AR8	65	18.4	3.0	0.4	4.7
AVG	143	15.6	5.0	8.3	7.9
ST	204	4.3	3.8	11.6	8.4
%	142	27	76	140	106

of various SiO_2. Since SiO_2 exhibited a relatively fast blood clearance and majority of SiO_2 were removed from circulation in several minutes, incubation time of SiO_2 in serum was chosen at 30 minutes to reflect the time length most SiO_2 interacted with serum protein before they were taken up by the RES system. Stöber exhibited the smallest hydrodynamic size post serum incubation, which was related to highest MTD *in vivo* among all SiO_2 tested. Meso S showed the largest hydrodynamic size post protein exposure. This could explain that it easily caused vasculature congestion in major organs at a low dose, as confirmed by histological examination, leading to the lowest MTD. The cationic MA, amine-modified counterpart of Meso S, had significantly lower hydrodynamic size than Meso S ($p < 0.001$), leading to onset of vessel congestion only at higher dose and several folds increase in MTD. It should be noted that slight agglomeration of MA was observed in saline. However, the agglomerates were dissociated when MA from the same saline stock was diluted in 50% serum, probably due to steric stabilization by protein adsorption. Nevertheless, injecting MA in saline might lead to congestion in vasculature because of lack of protein stabilization, especially at higher doses of MA. This could possibly explain why the MTD of MA was several folds lower than that of Stöber, even when their sizes in protein solution were similar. Overall porosity and surface characteristics of SiO_2 were the major factors that determined hydrodynamic size change post-protein adsorption, the related vasculature impact, and *in vivo* tolerance threshold.

Differential patterns of toxicity in major organs were observed in animals, probably due to varied physicochemical characteristics of SiO_2 combined with physiological traits of different organs. When administered through the tail vein,

nanoparticles were rushing through the inferior vena cava to the heart, resulting in damage to the endocardium of the heart leading to a series of cardiovascular complications [14], such as thrombosis as found in nonporous Stöber treated animals at high dose. The lung is the following organ which receives 100% cardiac venous output and serves as a first-pass filter capillary bed for foreign bodies [15]. Any aggregation of nanoparticles formed in the blood can then cause obstruction in the capillaries of the lung, resulting in acute embolism [15]. Injection of MA, 2A, and 8A at high doses often led to acute death in animals in such a manner. After traversing the lung, the oxygenated blood with SiO_2 returned to the heart and was distributed to the whole body. In this process, the kidney is likely the most vulnerable organ to SiO_2 exposure among five major organs examined, probably because of its specialized vasculature organization. As a selective blood filter, the kidney receives 20% of the cardiac output and compromising the blood flow in the vasa recta in renal interstitium will lead to congestion upon exposure to mesoporous SiO_2, which showed larger hydrodynamic size in the presence of protein or amine-modified SiO_2. The renal congestion leads to onset of renal failure, a consequence which was observed in mesoporous SiO_2 or amine-modified SiO_2 treated mice. Liver and spleen were the major sites where the majority of SiO_2 eventually was collected regardless of variation in physicochemical properties because of the abundant blood supply and the major presence of RES in these organs [3, 16]. It must be noted that animals from Stöber 600 mg/kg treatment experienced splenomegaly (Figure 4.3R) and anemia (Figure 4.7D) simultaneously. Histological examination revealed that this concurrence could be due to infiltration and hyperplasia of macrophages in the spleen (Figure 4.10C). The macrophage hyperactivity could be linked to anemia through one or

more of the following mechanisms: a) displacement of the hematopoietic centers in the spleen results in less erythrocyte production, b) physical spleen enlargement entraps more erythrocytes as the blood passes through the spleen, c) SiO_2 engulfment by splenic macrophages could result in hyperactivity in phagocytosis from macrophages at all locations of spleen, or d) a combination of two or more mechanisms mentioned above. Thus, SiO_2 exposure could lead to hepatic or splenic toxicity at high dose. In all, results set caution for developing SiO_2 as a functional carrier in a drug or biological delivery system, especially for nonporous SiO_2 as a heart disease targeted system [17] or for mesoporous SiO_2 as an intravascular delivery system [18]. Understanding how variations in multiple critical physicochemical factors influence toxicity helps establish guidelines for selecting appropriate compositions and properties of SiO_2 to improve biocompatibility and maximize its potential utility in nanomedicine applications.

Since most of the nanoparticle toxicity found in this study was related to vasculature damage, it was expected that toxicity could also be due to interaction of nanoparticles with the endothelium that lines the entire circulatory system. It was reported that nonporous SiO_2 caused toxicity in the primary endothelial cell culture in 24 hours at concentrations higher than 100 μg/mL [19]. Interaction of nanoparticles with macrophages could also play an important role in affecting the organ toxicity level, as reflected in previous studies that demonstrated that inhibition of phagocytosis of Kupffer cells elevated the liver injury by 70 nm nonporous SiO_2 [20]. Our previous study showed that there was a concentration threshold of safety for SiO_2 of various physicochemical properties on macrophages such that above the concentration of 100 μg/mL, SiO_2 tended to cause cellular toxicity in macrophages post-24-hour incubation [4]. In this study,

assuming the density of animal tissue is equivalent to water (1 g/cm^3) [21], the nanoparticle dose mg/kg could be converted to mg/1000 cm^3 or μg/mL to relate the *in vivo* results with *in vitro* observations. In this case, at the tested toxic dose of Meso S, AR2, and AR8 (*i.e.*, 100 mg/kg), toxicity was most likely due to vasculature obstruction since toxicity on endothelial cells or macrophages should be limited at this concentration within the time frame (1 day) in animals. For amine-modified mesoporous nanoparticles (MTDs 100 -150 mg/kg), the toxicity that was immediately observed at the doses above MTDs was basically because of pulmonary obstruction by clinical observation, while the toxicity that was found in animals at extended time points (1 day or more) could be partially derived from endothelium or macrophage dysfunction due to nanoparticle exposure above 100 μg/mL. For Stöber or SA, the toxicity at the dose (600 mg/kg) above MTDs could possibly be due to vasculature compromise as well as endothelial cell and macrophage toxicity (600 μg/mL). Liu *et al.* reported that nonporous SiO_2 given through the intravenous route were associated with increased risk of cardiovascular diseases, *i.e.*, atherosclerosis and thrombosis, by inducing endothelial cell dysfunction through oxidative stress *via* JNK/p53 pathways [19]. Our result supports this prediction that SiO_2 lead to the onset of vascular diseases besides other organ toxicities *in vivo*.

Surface area of engineered particles has been shown to play a crucial role in determining their biological activity [22, 23]. For nanosized particles, the increased surface area per mass compared with large particles could induce greater biological interaction, which could be either desirable (*e.g.*, loading capacity of therapeutics) or detrimental (*e.g.*, toxicity, cell dysfunction) [22, 23]. Our study revealed that given the same surface characteristics and bulk chemical composition, the total surface area of SiO_2

per mass is the most relevant factor that determines the MTD of SiO_2 in animals. The MTD of Stöber was surprisingly close to the maximum safety dose (500 mg/kg) of the mesoporous hollow silica nanoparticles (MHSNs, ca. 110 nm in diameter), as determined in previous dose escalation studies [24]. MHSNs were produced by a modified Stöber method and the surface of MHSNs should resemble Stöber used in our study, except that irregular pores were present on the surface with amine groups extending out from the inner cavity to produce a high cationic charge [25]. Although MHSNs possessed higher surface area per mass, they still had a high MTD which could probably be due to the different surface characteristics mentioned above. This indicates that porosity and surface characteristics are the crucial factors in determining the toxicity of SiO_2 *in vivo*, as reflected by MTD, and the equivalent total surface area dosing strategy should be applicable to SiO_2 without the presence of functional silane on the surface.

4.5 Conclusion

Of the materials studied here, nonporous SiO_2 sized 120 nm exhibited low systemic toxicity and the highest MTDs of 450 mg/kg before or after primary amine modification when exposed intravenously to animals. Mesoporous SiO_2 exerted considerable systemic toxicity with MTDs ranging from 30 – 65 mg/kg, irrespective of the geometrical features. However, toxicity was attenuated when mesoporous SiO_2 were modified with primary amine functionalities, which led to the increased MTDs of 100 – 150 mg/kg. *In vivo* toxicity of SiO_2 was mostly influenced by nanoparticle porosity and surface characteristics, and was primarily associated with vasculature obstruction as a consequence of SiO_2 protein interaction and change in hydrodynamic size in the serum. Dosing SiO_2 on an equivalent total surface area basis could achieve a common mode of

action as was quantitated as MTD here. Further studies will be focusing on the pharmacokinetics and tissue distribution of SiO_2 with distinct physicochemical features to provide confirmative evidence about the origin of organ-associated toxicity.

4.6 References

[1] S.P. Hudson, R.F. Padera, R. Langer, D.S. Kohane, The biocompatibility of mesoporous silicates, Biomaterials, 29 (2008) 4045-4055.

[2] J. Lu, M. Liong, Z. Li, J.I. Zink, F. Tamanoi, Biocompatibility, biodistribution, and drug-delivery efficiency of mesoporous silica nanoparticles for cancer therapy in animals, Small, 6 (2010) 1794-1805.

[3] G. Xie, J. Sun, G. Zhong, L. Shi, D. Zhang, Biodistribution and toxicity of intravenously administered silica nanoparticles in mice, Arch Toxicol, 84 (2010) 183-190.

[4] T. Yu, A. Malugin, H. Ghandehari, Impact of silica nanoparticle design on cellular toxicity and hemolytic activity, ACS Nano, 5 (2011) 5717-5728.

[5] S. Yadav, S.J. Shire, D.S. Kalonia, Viscosity analysis of high concentration bovine serum albumin aqueous solutions, Pharm Res, 28 (2011) 1973-1983.

[6] Y.S. Lin, N. Abadeer, C.L. Haynes, Stability of small mesoporous silica nanoparticles in biological media, Chem Commun (Camb), 47 (2011) 532-534.

[7] M.A. Dobrovolskaia, A.K. Patri, J. Zheng, J.D. Clogston, N. Ayub, P. Aggarwal, B.W. Neun, J.B. Hall, S.E. McNeil, Interaction of colloidal gold nanoparticles with human blood: effects on particle size and analysis of plasma protein binding profiles, Nanomedicine : Nanotechnology, Biology, and Medicine, 5 (2009) 106-117.

[8] P. Bihari, M. Vippola, S. Schultes, M. Praetner, A.G. Khandoga, C.A. Reichel, C. Coester, T. Tuomi, M. Rehberg, F. Krombach, Optimized dispersion of nanoparticles for biological *in vitro* and *in vivo* studies, Part Fibre Toxicol, 5 (2008) 14.

[9] Z. Ji, X. Jin, S. George, T. Xia, H. Meng, X. Wang, E. Suarez, H. Zhang, E.M. Hoek, H. Godwin, A.E. Nel, J.I. Zink, Dispersion and stability optimization of TiO_2 nanoparticles in cell culture media, Environ Sci Technol, 44 (2010) 7309-7314.

[10] Z. Chen, H. Meng, G. Xing, C. Chen, Y. Zhao, G. Jia, T. Wang, H. Yuan, C. Ye, F. Zhao, Z. Chai, C. Zhu, X. Fang, B. Ma, L. Wan, Acute toxicological effects of copper nanoparticles *in vivo*, Toxicol Lett, 163 (2006) 109-120.

[11] J. Chen, X. Dong, J. Zhao, G. Tang, *In vivo* acute toxicity of titanium dioxide nanoparticles to mice after intraperitoneal injection, J Appl Toxicol, 29 (2009) 330-337.

[12] K.M. Waters, L.M. Masiello, R.C. Zangar, B.J. Tarasevich, N.J. Karin, R.D. Quesenberry, S. Bandyopadhyay, J.G. Teeguarden, J.G. Pounds, B.D. Thrall, Macrophage responses to silica nanoparticles are highly conserved across particle sizes, Toxicol Sci, 107 (2009) 553-569.

[13] X. Lu, Y. Tian, Q. Zhao, T. Jin, S. Xiao, X. Fan, Integrated metabonomics analysis of the size-response relationship of silica nanoparticles-induced toxicity in mice, Nanotechnology, 22 (2011) 055101.

[14] D.H. Endemann, E.L. Schiffrin, Endothelial dysfunction, J Am Soc Nephrol, 15 (2004) 1983-1992.

[15] V.R. Muzykantov, Biomedical aspects of targeted delivery of drugs to pulmonary endothelium, Expert Opin Drug Deliv, 2 (2005) 909-926.

[16] Q. He, Z. Zhang, F. Gao, Y. Li, J. Shi, *In vivo* biodistribution and urinary excretion of mesoporous silica nanoparticles: effects of particle size and PEGylation, Small, 7 (2011) 271-280.

[17] M.M. Galagudza, D.V. Korolev, D.L. Sonin, V.N. Postnov, G.V. Papayan, I.S. Uskov, A.V. Belozertseva, E.V. Shlyakhto, Targeted drug delivery into reversibly injured myocardium with silica nanoparticles: surface functionalization, natural biodistribution, and acute toxicity, Int J Nanomedicine, 5 (2010) 231-237.

[18] Y. Zhao, X. Sun, G. Zhang, B.G. Trewyn, Slowing, II, V.S. Lin, Interaction of mesoporous silica nanoparticles with human red blood cell membranes: size and surface effects, ACS Nano, 5 (2011) 1366-1375.

[19] X. Liu, J. Sun, Endothelial cells dysfunction induced by silica nanoparticles through oxidative stress via JNK/P53 and NF-κB pathways, Biomaterials, 31 (2010) 8198-8209.

[20] H. Nishimori, M. Kondoh, K. Isoda, S. Tsunoda, Y. Tsutsumi, K. Yagi, Silica nanoparticles as hepatotoxicants, Eur J Pharm Biopharm, 72 (2009) 496-501.

[21] J.F. Hainfeld, D.N. Slatkin, T.M. Focella, H.M. Smilowitz, Gold nanoparticles: a new X-ray contrast agent, Br J Radiol, 79 (2006) 248-253.

[22] G. Oberdorster, E. Oberdorster, J. Oberdorster, Nanotoxicology: an emerging discipline evolving from studies of ultrafine particles, Environ Health Perspect, 113 (2005) 823-839.

[23] H.F. Krug, P. Wick, Nanotoxicology: an interdisciplinary challenge, Angew Chem Int Ed Engl, 50 (2011) 1260-1278.

[24] T. Liu, L. Li, X. Teng, X. Huang, H. Liu, D. Chen, J. Ren, J. He, F. Tang, Single and repeated dose toxicity of mesoporous hollow silica nanoparticles in intravenously exposed mice, Biomaterials, 32 (2011) 1657-1668.

[25] D. Chen, L. Li, F. Tang, S. Qi, Facile and scalable synthesis of tailored silica „„nanorattle"" structures, Adv. Mater., 21 (2009) 3804-3807.

CHAPTER 5

IN VIVO BIODISTRIBUTION AND PHARMACOKINETICS OF SILICA NANOPARTICLES AS A FUNCTION OF GEOMETRY, POROSITY, AND SURFACE CHARACTERISTICS

5.1 Introduction

Nanoparticle physicochemical properties, such as size, pegylation, and surface charge, play important roles in biodistribution and *in vivo* toxicity of SiO_2 [1-5]. It has been reported that mesoporous SiO_2 of smaller size with surface pegylation had lower capture by the RES and were more slowly degraded [6]. Organically modified silica nanoparticles with diameters of 20 – 25 nm exhibited effective clearance *via* the hepatobiliary route without any sign of organ toxicity [7]. Cationic mesoporous SiO_2 were excreted rapidly by the hepatobiliary route, probably due to charge-dependent serum protein adsorption [8]. Limited information, however, is available about the impact of geometry of SiO_2 on biodistribution and toxicity.

In previous chapters, studies on lung cancerous epithelial cells and macrophages showed that *in vitro* toxicity of spherical or rod-shaped SiO_2 was mainly determined by porosity and surface characteristics irrespective of geometric features [9]. Further *in vivo* studies demonstrated that the systemic toxicity of these nanoparticles was also mainly influenced by nanoparticle porosity and surface characteristics. Mesoporous SiO_2 tended to be less tolerated than nonporous SiO_2 while amine modification on mesoporous

nanoparticles improved the tolerated dose threshold [10]. Geometry did not make a significant difference in the mechanism or extent of the systemic toxicity. The next logical step is to investigate the distribution of these SiO_2 in animals to shed light on the causes for *in vivo* toxicity observed in mice beyond MTDs and to relate the *in vitro* toxicity and cellular uptake with *in vivo* toxicity and biodistribution. In this chapter, we report the biodistribution and pharmacokinetics of SiO_2 in mice as a function of geometry, porosity, and surface characteristics.

5.2 Materials and methods

5.2.1 Materials

Stöber, Meso S, AR8, and their amine-modified counterparts (SA, MA, 8A) were prepared as reported previously [9]. Monoiodinated Bolton-Hunter Reagent, 1 mCi/37 MBq in benzene, was purchased from American Radiolabeled Chemicals (St. Louis, MO). CD-1 mouse serum was a customized bio-specimen order from Charles River Laboratories, from which the CD-1 mice were ordered for this study. All other chemicals were of reagent grade from Sigma-Aldrich.

5.2.2 Premodification of SiO_2 for radiolabeling experiments

Cationic, amine-modified SiO_2 were produced by reacting the nanoparticles with APTES at a weight ratio of 1:1 in anhydrous ethanol for 20 hours at room temperature as described previously [9]. To obtain anionic, slightly amine-modified SiO_2, the same procedure was used except that APTES reacted with SiO_2 at the weight ratio of 1:50 to make sure there were available primary amine groups on the surface to conjugate with monoiodinated Bolton-Hunter Reagent while the surface charge of SiO_2 remained

negative. The nanoparticles were stored in ethanol and thoroughly washed in water and borate buffer immediately before radiolabeling experiments.

5.2.3 SiO_2 radiolabeling experiments

The radiolabeling protocol was adapted from an established Bolton-Hunter method, whereby the primary amine groups available on the nanoparticle surface formed an amide bond with *N*-hydroxysuccinimide group from monoiodinated Bolton-Hunter Reagent [11, 12]. To react with nanoparticles, 20 μL monoiodinated Bolton-Hunter Reagent was transferred to a glass vial and the solvent was allowed to dry in the air for an extended time (1 hour). 10 mg of SiO_2 prepared in the above section (10 mg/mL) in 0.05 M borate buffer (pH 8.5) was quickly added to the glass vial and stirred on ice for 45 minutes. Then the mixture was transferred to a dialysis cellulose ester membrane with a cutoff size of 3.5 – 5 kD (Float-A-Lyzer G2, Spectra/Por, Specutrum Laboratories, Inc) and dialyzed against 4 L water at room temperature for 20 days with water changing on a daily basis. The unreacted Bolton-Hunter Reagent was readily hydrolyzed in the aqueous medium and was removed by dialysis. The hydrolyzed product is referred to as ^{125}I-BHR in this article. Thin layer chromatography (TLC) silica gel was used to check the presence of unbound ^{125}I-BHR in radiolabeled SiO_2 (^{125}I-SiO_2) using methanol water (4:1 volume ratio) solvent as the mobile phase. The radioactivity on silica gel was measured by the Packard Cobra auto-gamma counter (GMI, Ramsey, Minnesota). For SA and slightly amine-modified Stöber, dialysis did not completely remove ^{125}I-BHR from nanoparticles and thus, an alternative centrifugation method described below was used. The mixture from radiolabeling reaction was collected into a 2.0 mL microtube and spun at 15,000 × g for 30 minutes in an Eppendorf centrifuge 5415D (Eppendorf, Hamburg,

Germany). Nanoparticles were extensively washed in water and methanol and finally in water. Then TLC method was applied to check the presence of ^{125}I-BHR in nanoparticles from each washing cycle until unbound ^{125}I-BHR was confirmed to be absent in ^{125}I-SiO_2.

5.2.4 Serum stability of ^{125}I-SiO_2

The stability of radiolabeling on SiO_2 was tested in mouse serum before the biodistribution study. 0.5 mg ^{125}I-SiO_2 was added to 1 ml 50% CD-1 mouse serum in saline and incubated at 37 ^{o}C for 72 hours. The experiment was done in triplicate with ^{125}I-BHR in 50% mouse serum as the positive control. At the end of 72 hours, an aliquot of mixture was withdrawn by a glass capillary and analyzed by TLC. The stability of ^{125}I-SiO_2 was expressed as percentage of radioactivity in the original spotting site out of the total radioactivity on the plate.

5.2.5 Biodistribution and pharmacokinetic analysis

Animal studies were conducted under an approved protocol of the University of Utah IACUC. Female CD-1 mice, 6 – 8 weeks old, were purchased from Charles River Laboratories and housed in standard cages with five animals per cage. All animals were acclimated to the animal facility for at least 1 week prior to experimental procedures. CD-1 mice were injected *via* the lateral tail vein with 20 mg/kg SiO_2 suspension in 200 μL sterile saline. The SiO_2 suspension was a mixture of ^{125}I-SiO_2 and SiO_2 of the same type to make a radioactivity dose of 60,000 cpm per animal for pristine SiO_2 (Stöber, Meso S, AR8) or a radioactivity dose of 120,000 cpm per animal for amine-modified SiO_2 (SA, MA, 8A). The weight content of ^{125}I-SiO_2 which contributed to the dose of SiO_2 in the injection formulation was considered to be negligible [13]. The mice were

sacrificed at 5 minutes, 30 minutes, 2 hours, 24 hours, and 72 hours post-intravenous injection. At each time point, animals were terminated by CO_2 asphyxiation and blood samples were collected *via* the inferior vena cava by a heparin-coated syringe immediately post-euthanasia. The animals were flushed with 20 mL sterile saline to remove blood that remained in the organs in order to obtain accurate tissue accumulation counts based on nanoparticle tissue association or uptake rather than blood content. During necropsy, organs of interest (heart, liver, spleen, lung, kidneys, brain, stomach, small intestine, large intestine, tail, thyroid) and the rest of the carcass (bones, muscle, and skin) were dissected and weighed, followed by tissue radioactivity measurement by a gamma counter. Radioactivity obtained from different organs was calculated as the percentage of the injected dose per gram of tissue. Compartmental analysis of the pharmacokinetic data was performed using WinNonlin Professional, version 5.3 (Pharsight Corporation, CA). A two-compartmental pharmacokinetic model was utilized with first-order elimination.

5.2.6 Urinary and hepatobiliary excretion studies

To measure the excretion of SiO_2 into urine and feces, five animals received the intravenous injection of SiO_2 of each type at 20 mg/kg and were individually housed in special single-mouse metabolic cages. Urine and feces were collected into separate tubes at 2 hours, 24 hours, 48 hours, and 72 hours. The samples were immediately weighed and their radioactivity was measured by a gamma counter. In order to identify the radioactive species in urine, the urine samples, positive controls (950 μL normal urine + 50 μL 2.5 mg/mL SiO_2 + 5 μL 15,000 cpm ^{125}I-BHR), and negative controls (950 μL normal urine + 50 μL 15,000 cpm 2.5 mg/mL SiO_2 injection formulation) were centrifuged at 15,000 ×

g for 20 minutes to obtain the supernatant. The supernatant was removed and measured by a gamma counter. The percentage of radioactivity in the supernatant out of the overall urine sample is indicative of percentage of unbound radioactivity or degraded product in the urine.

5.2.7 Statistical analysis

Experiments were performed in triplicate with results present as average value or mean ± SD. For *in vivo* studies, five animals were used per group and differences in *in vivo* data were analyzed using one-way ANOVA by GraphPad Prism (GraphPad Software, CA). Where detected, Tukey's test was used to evaluate pairwise differences between the groups.

5.3 Results

Stöber, Meso S AR8 were previously synthesized and stored in ethanol[9]. The pristine SiO_2 were further modified with APTES to obtain their highly cationic counterparts (SA, MA, 8A). These amine-modified SiO_2 were directly used in radiolabeling experiments for SA, MA, and 8A. To track the distribution of pristine SiO_2 *in vivo*, the SiO_2 were slightly modified with APTES to generate available primary amine groups for radioisotope conjugation while the anionic surface charge was maintained for comparison with highly cationic, amine-modified SiO_2 in this study (Figure 5.1). The content of unbound ^{125}I-BHR in the ^{125}I-SiO_2 product post-purification was analyzed by TLC. There was minimum presence of unbound radioisotope molecules associated with ^{125}I-SiO_2 product (Figure 5.2). Serum stability study on a typical ^{125}I-SiO_2, ^{125}I-MA, demonstrated that the amide bond formed during radiolabeling reaction was stable in 50%

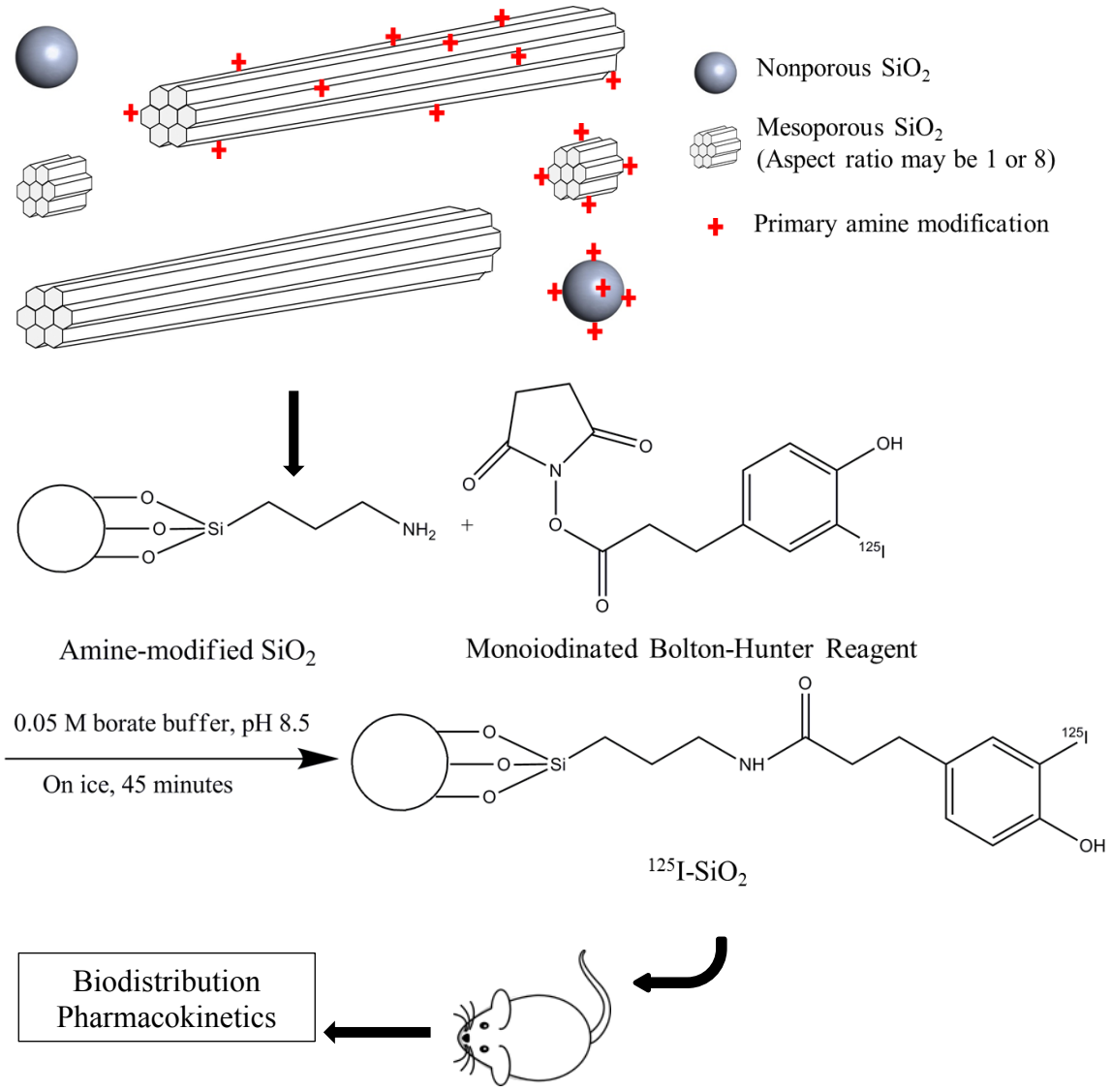

Figure 5.1 Schematic illustration of nanoparticle selection, radiolabeling, and animal administration for biodistribution and pharmacokinetics studies.

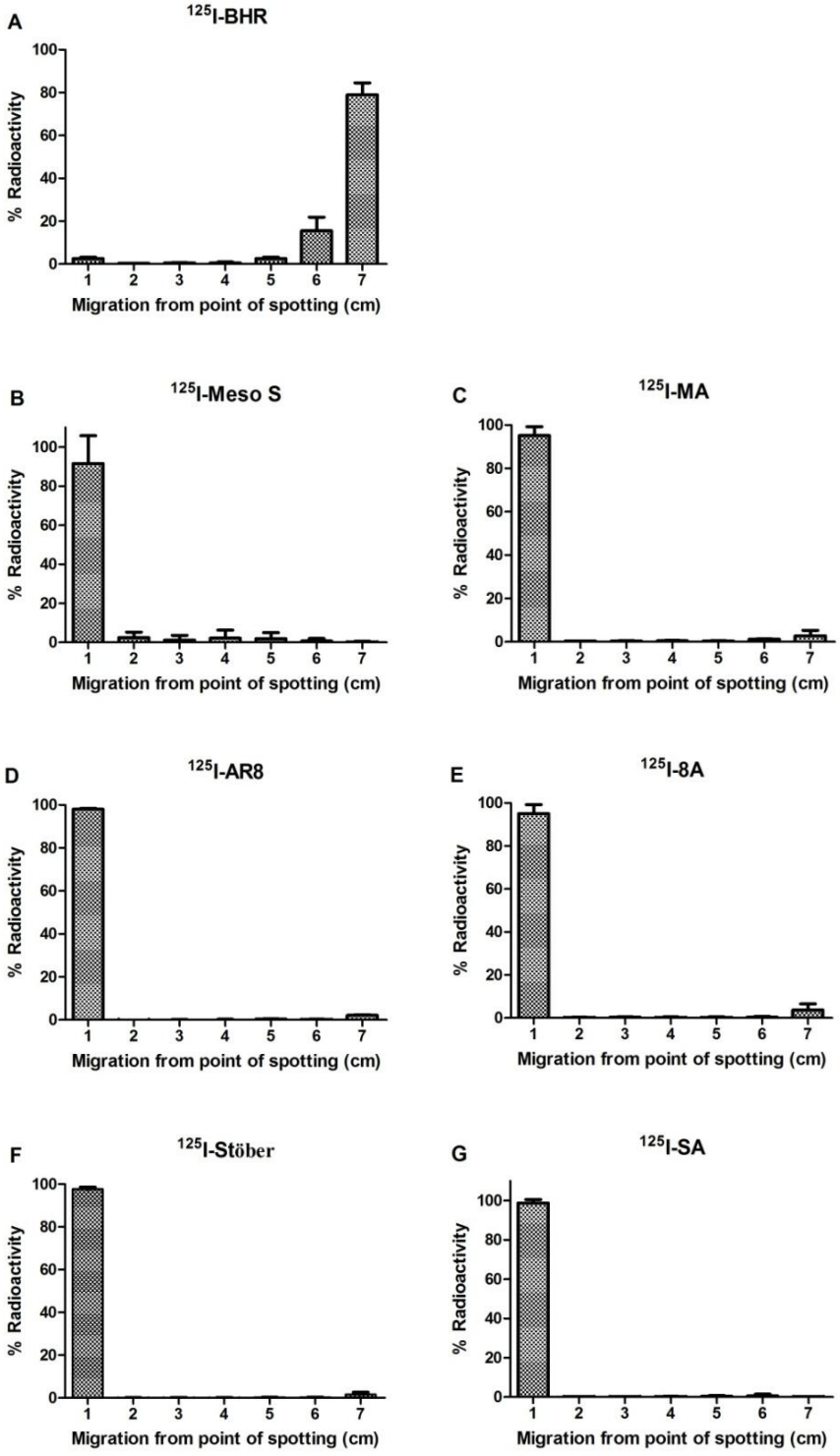

Figure 5.2 TLC analysis of A) ^{125}I-BHR (positive control), or ^{125}I-SiO_2 with various physicochemical properties, B) ^{125}I-Meso S, C) ^{125}I-MA, D) ^{125}I-AR8, E) ^{125}I-8A, F) ^{125}I-Stöber, G) ^{125}I-SA post-purification. Results show that there were minimum unbound radioisotopes in each ^{125}I-SiO_2 product. Data are presented as mean ± SD (n = 3).

mouse serum at 37 ^{o}C for 72 hours (Figure 5.3).

Biodistribution of a series of SiO_2 with varied shapes, porosities, and surface characteristics was evaluated in immune-competent CD-1 mice *via* bolus tail vein injection by tracing the radioactivity distribution. Results show that SiO_2 of various physicochemical properties mainly accumulated in the liver and spleen with differential distribution into the lung (Figures 5.4-5.9). To evaluate the effect of geometry on biodistribution, spherical mesoporous SiO_2 (Meso S, MA) were compared with rod-shaped mesoporous SiO_2 with an aspect ratio of 8 (AR8, 8A). Both Meso S and AR8 exhibited extensive lung accumulation. This accumulation was almost eliminated with amine-modified nanospheres MA but not with amine-modified nanorods 8A. All the accumulation in the lung showed a rapid elimination from this organ within 24 hours post-injection. To examine the influence of porosity on nanoparticle biodistribution, mesoporous nanospheres (Meso S) were compared with nonporous nanospheres (Stöber). Results show that Meso S was primarily accumulated in the lung while Stöber had negligible accumulation in this organ. Stöber also exhibited an increased percentage of liver accumulation out of total recovered dose compared with Meso S. To analyze the surface modification effect, amine-modified SiO_2 were compared with their pristine counterparts. It was revealed that amine modification could efficiently reduce nanoparticle lung accumulation (Figures 5.4-5.9).

The blood profiles of SiO_2 were fitted to a two-compartmental pharmacokinetic model. All nanoparticles studied were rapidly cleared from blood circulation within 2 hours of injection followed by a slow elimination phase which indicated the slow re-distribution between the blood and organs/tissues (Figure 5.10) [14]. There was no

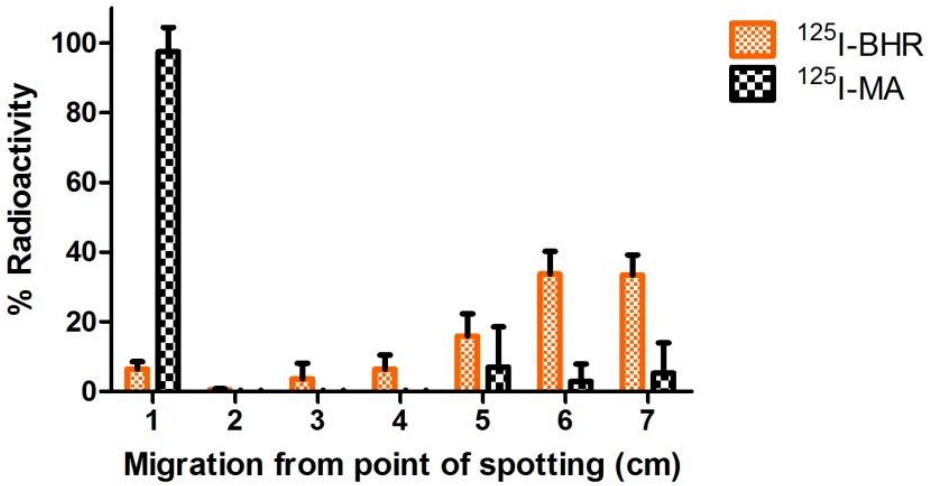

Figure 5.3 Serum stability of ^{125}I-BHR (positive control) and ^{125}I-SiO_2 post-incubation with 50% mouse serum at 37 ^{o}C for 72 hours analyzed by TLC. Results are expressed as percent of radioactivity at different locations from original spotting point out of the total radioactivity on the silica gel plate. Data are presented as mean ± SD (n = 1 in triplicate measurements).

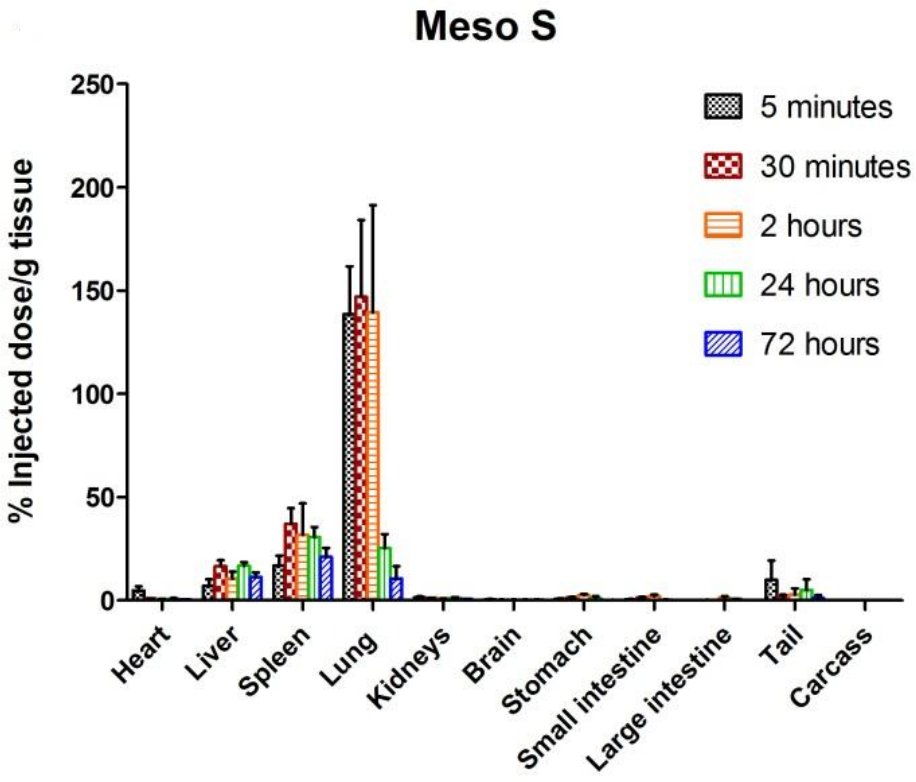

Figure 5.4 Biodistribution of Meso S in healthy mice post-bolus tail vein injection at a dose of 20 mg/kg. Data are presented as mean ± SD (*n* =5).

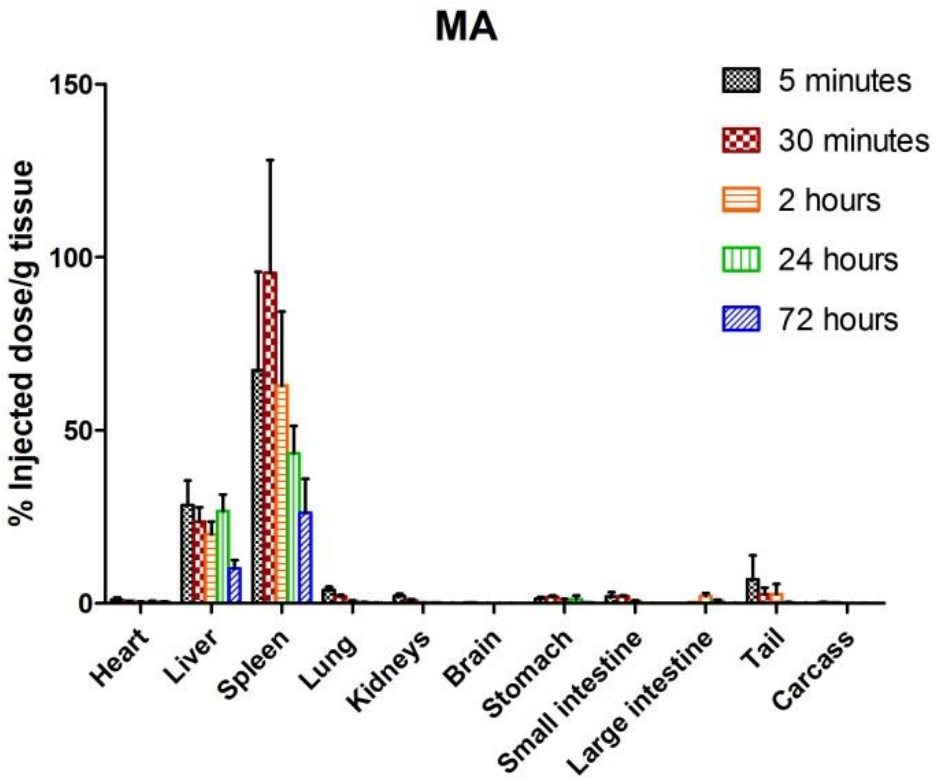

Figure 5.5 Biodistribution of MA in healthy mice post-bolus tail vein injection at a dose of 20 mg/kg. Data are presented as mean ± SD (*n* =5).

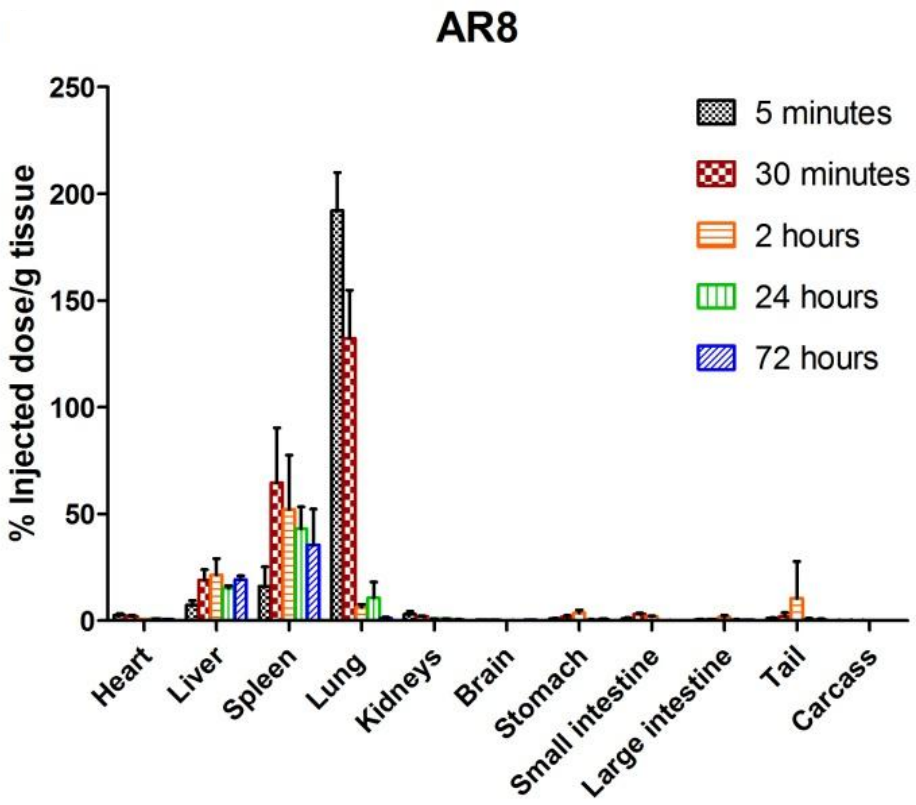

Figure 5.6 Biodistribution of AR8 in healthy mice post-bolus tail vein injection at a dose of 20 mg/kg. Data are presented as mean ± SD (*n* =5).

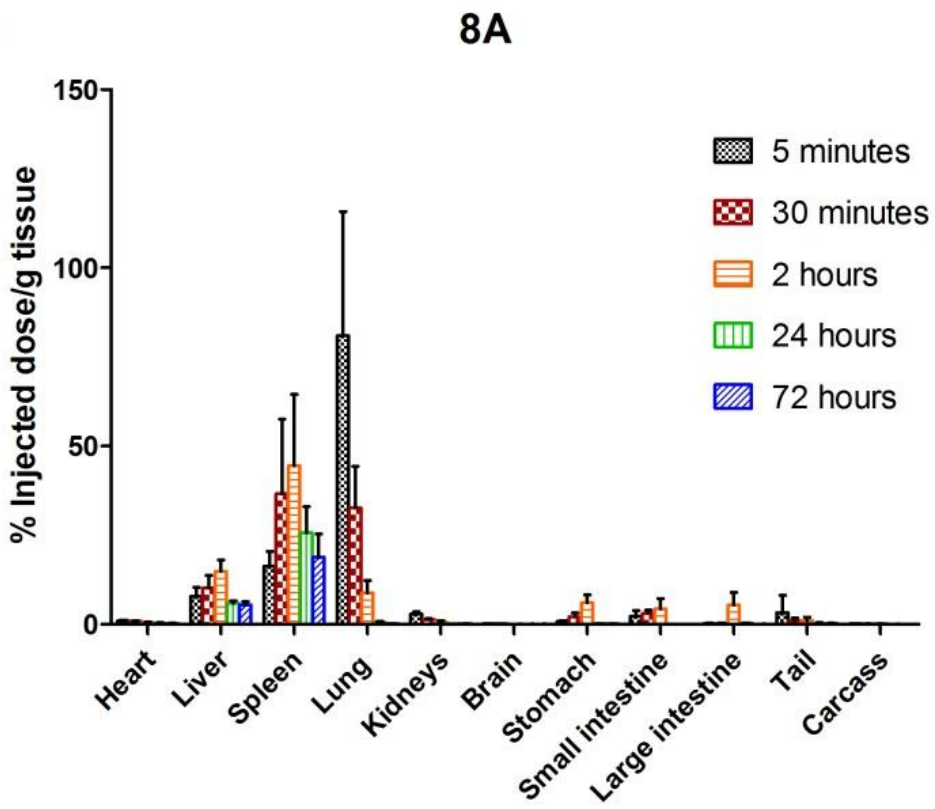

Figure 5.7 Biodistribution of 8A in healthy mice post-bolus tail vein injection at a dose of 20 mg/kg. Data are presented as mean ± SD (*n* =5).

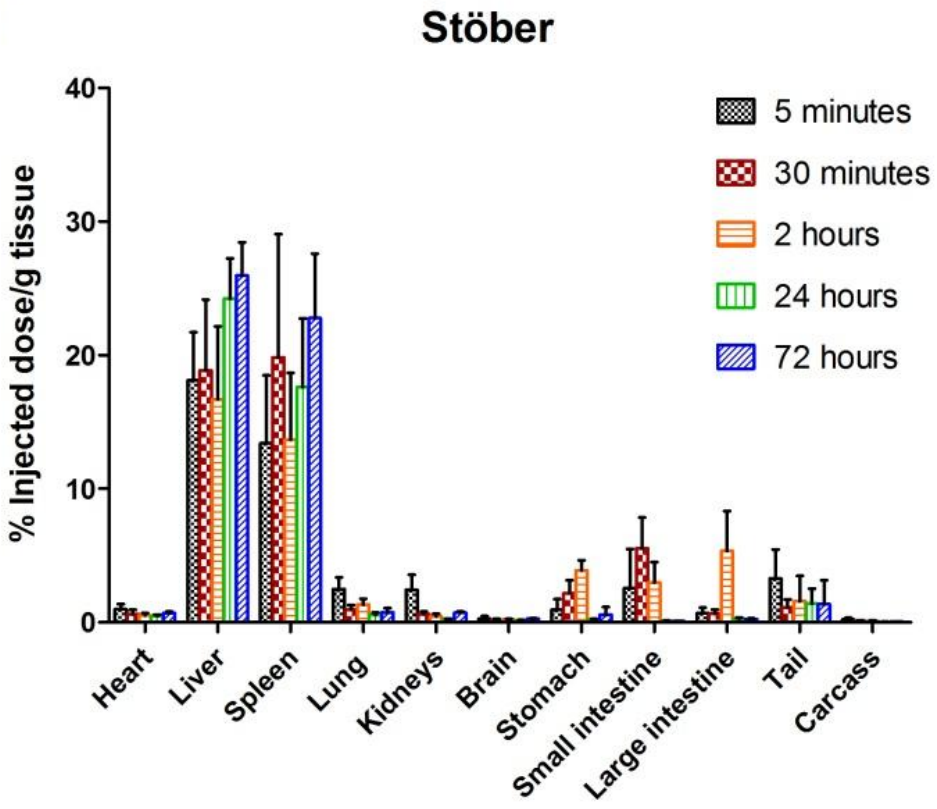

Figure 5.8 Biodistribution of Stöber in healthy mice post-bolus tail vein injection at a dose of 20 mg/kg. Data are presented as mean ± SD (*n* =5).

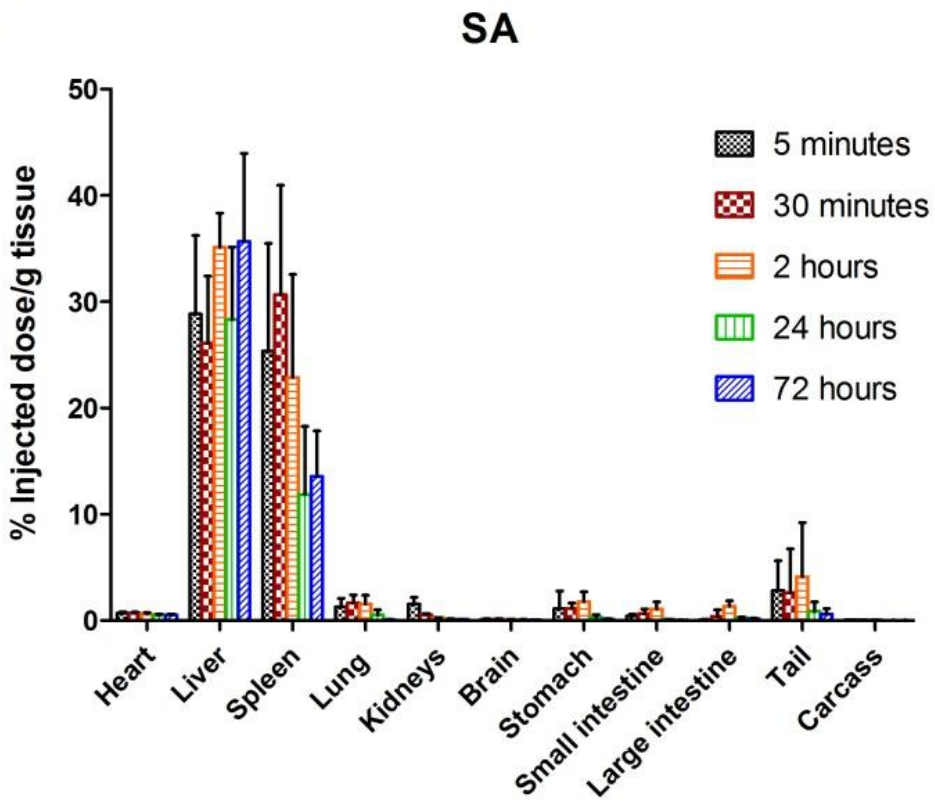

Figure 5.9 Biodistribution of SA in healthy mice post-bolus tail vein injection at a dose of 20 mg/kg. Data are presented as mean ± SD (*n* =5).

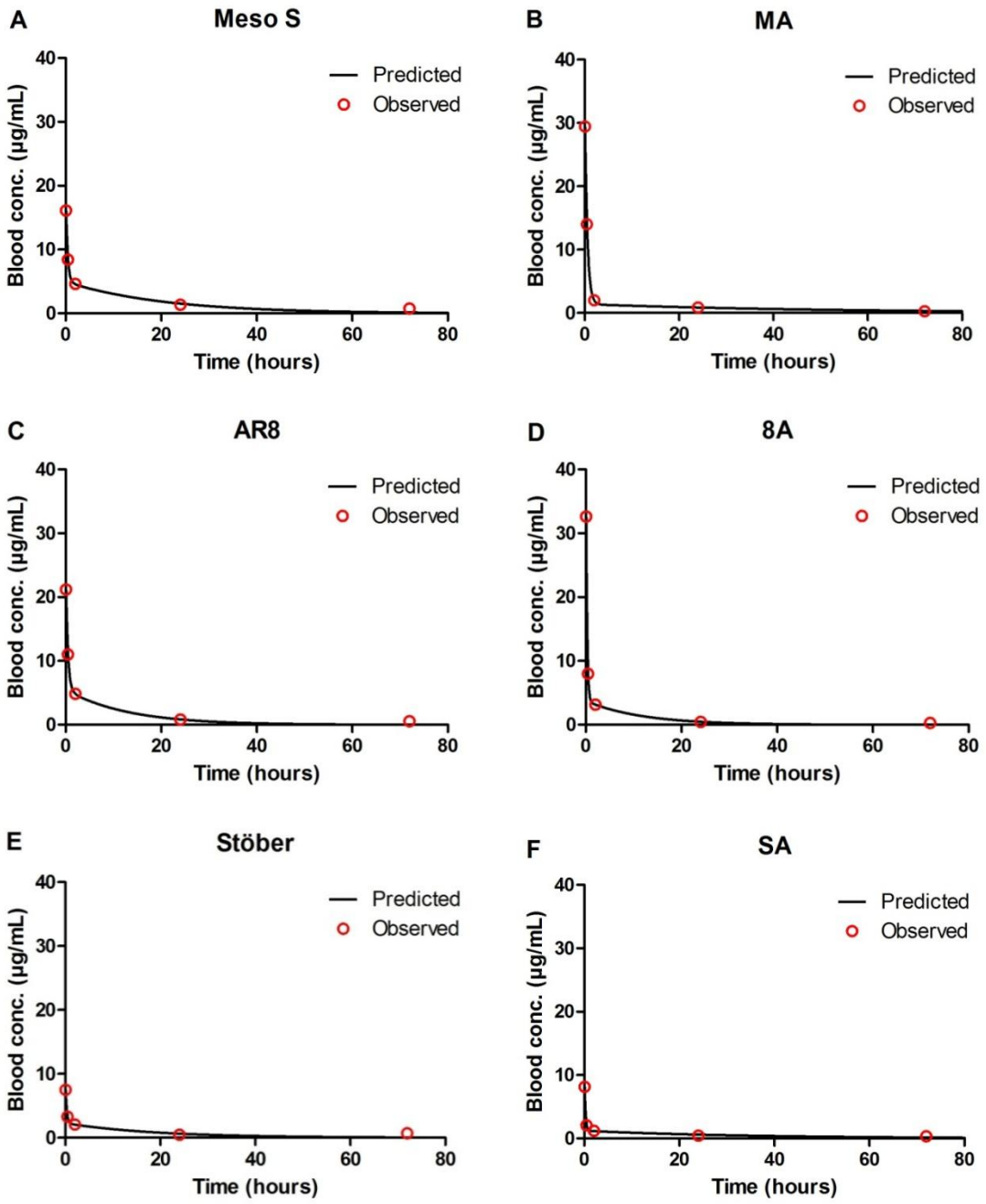

Figure 5.10 Two-compartmental pharmacokinetic analysis of SiO_2 biodistribution: A) Meso S, B) MA, C) AR8, D) 8A, E) Stöber, F) SA in healthy mice. Activity in the blood is converted to nanoparticle concentration using percent injected dose per gram blood and assumes a blood density of 1.0 g/mL.

significant difference in the terminal clearance rates of various types of SiO_2 ($p > 0.05$) (Figure 5.11). Stöber showed a significantly higher volume of distribution at steady state (V_{ss}) than Meso S ($p < 0.05$), while amine-modified, spherical SiO_2 (MA, SA) exhibited a significant increase in V_{ss} compared to their pristine counterparts (Meso S, $p < 0.01$; Stöber, $p < 0.001$) (Figure 5.12).

The tissue affinity indices, calculated as the ratio of area under the curve from a specific organ over area under the curve of blood, reflect the affinity and capacity of nanoparticle association with the specific organ of interest [15]. Various SiO_2 showed high affinity for the spleen and low affinity for the kidneys across the board (Table 5.1). High aspect ratio 8A showed on average higher lung affinity than MA. Stöber and SA had on average higher liver uptake than mesoporous nanoparticles with or without amine modification. Mesoporous SiO_2 showed on average higher affinity to the lung than Stöber. The lung exposure was drastically reduced by amine modification as indicated by decreased tissue affinity indices from amine-modified nanoparticles (SA, MA, 8A) compared with their pristine counterparts (Stöber, Meso S, AR8). The same trend was also observed for kidney exposure of various SiO_2.

The tissue/blood concentration ratio of various nanoparticles in major organs, liver, spleen, lung, and kidneys, was used as an indicator of changes in organ penetrability and retention over time [16]. The SiO_2 across the board generally showed an increase in partitioning in the liver and spleen over time (Figures 5.13-5.14), but the partitioning remained constant in the lung and kidneys over 72 hours (Figures 5.15-5.16). In the lung, mesoporous nanoparticles (Meso S) demonstrated a significantly higher

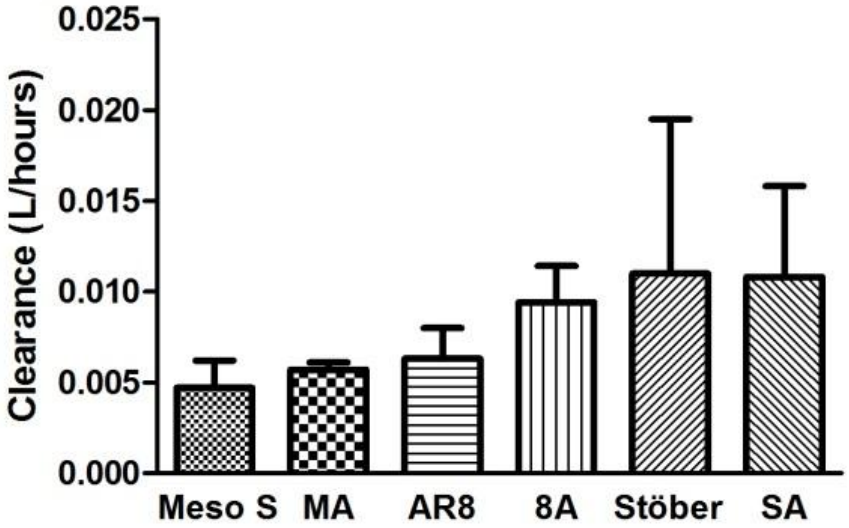

Figure 5.11 Pharmacokinetic parameter clearance based on the two-compartmental analysis for the nanoparticles. There was no significant difference in clearance among all nanoparticles in blood ($p > 0.05$).

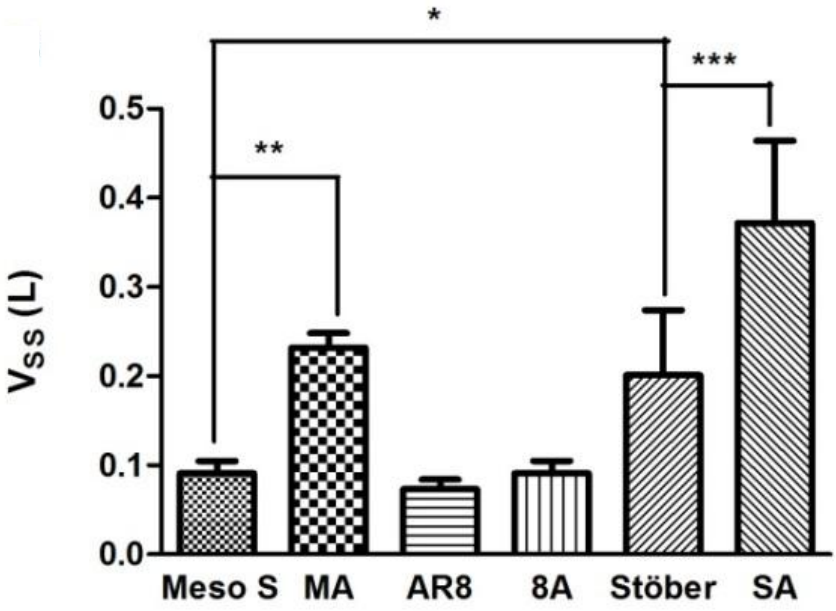

Figure 5.12 Pharmacokinetic parameter V_{ss} based on the two-compartmental analysis for the nanoparticles. Amine-modified SiO_2, MA or SA, exhibited significantly higher V_{ss} than their pristine counterparts, Meso S ($^{**}p < 0.01$) or Stöber ($^{***}p < 0.001$). Stöber showed a significantly higher V_{ss} than Meso S ($^{*}p < 0.05$).

Table 5.1
Tissue affinity indices of SiO_2 of various geometries, porosities, and surface characteristics in major organs of CD-1 mice.

	Tissue affinity index			
Treatment	Liver	Spleen	Lung	Kidneys
Meso S	46.9	93.5	138.9	3.2
MA	82.9	172.3	1.4	0.8
AR8	80.7	193.9	41.8	3.4
8A	49.4	180.5	17.2	2.0
Stöber	186.0	148.1	6.0	3.6
SA	249.5	113.9	4.5	1.3

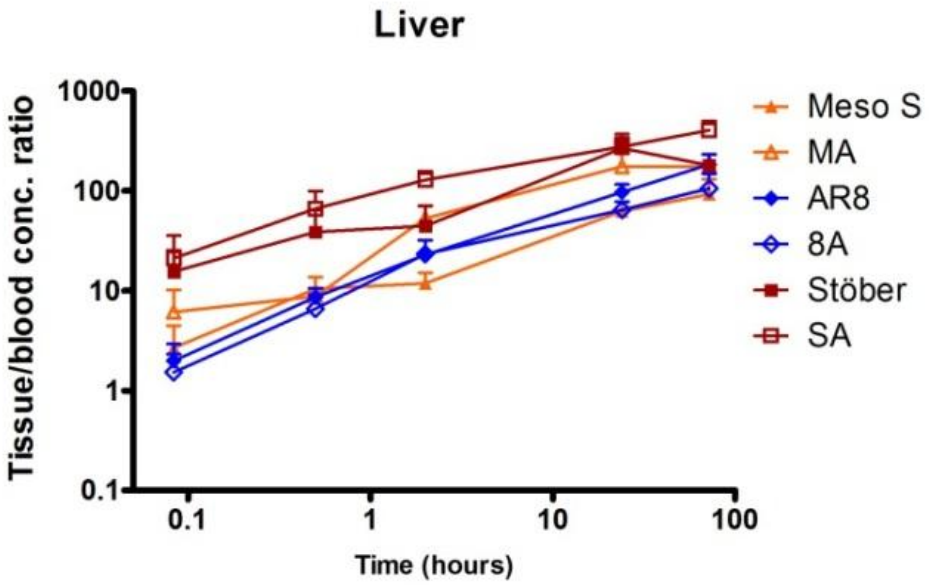

Figure 5.13 Tissue/blood concentration ratio of various SiO_2 in liver. Data are presented as mean ± SD (n = 5).

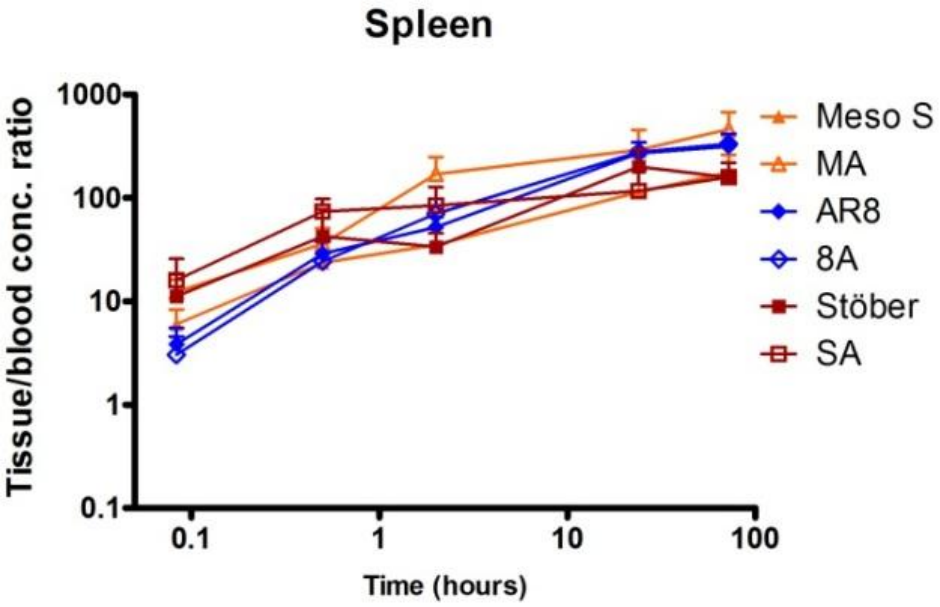

Figure 5.14 Tissue/blood concentration ratio of various SiO_2 in spleen. Data are presented as mean ± SD (n = 5).

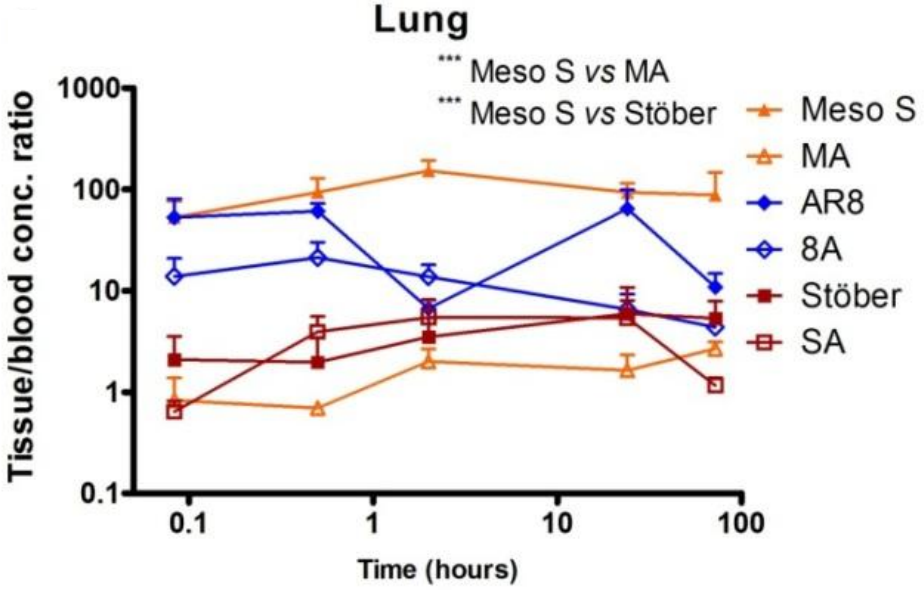

Figure 5.15 Tissue/blood concentration ratio of various SiO_2 in lung. Meso S showed a significantly higher lung/blood concentration ratio than Stöber ($^{***}p < 0.001$) or MA ($^{***}p < 0.001$) within 3 days. Data are presented as mean ± SD ($n = 5$).

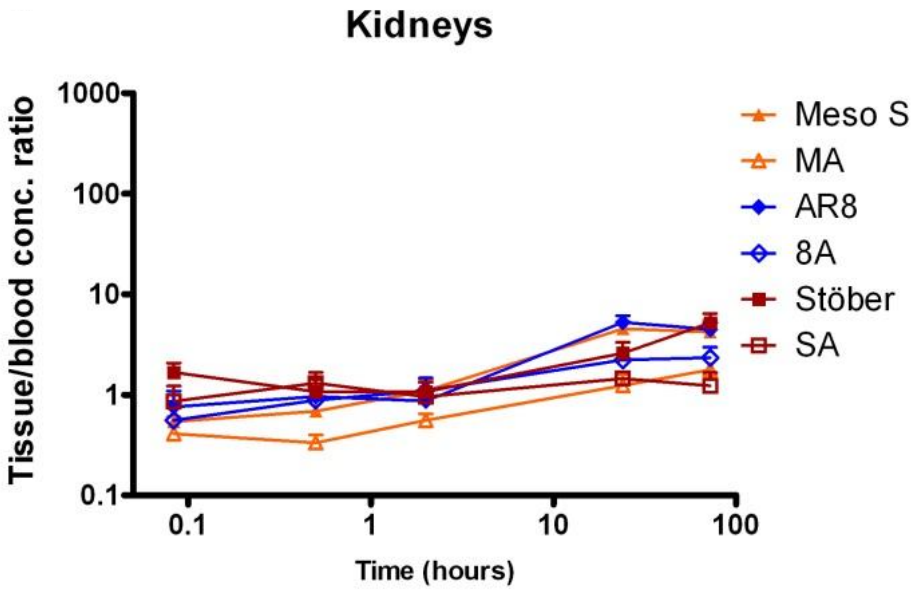

Figure 5.16 Tissue/blood concentration ratio of various SiO_2 in kidneys. Data are presented as mean ± SD (n = 5).

lung/blood concentration ratio than Stöber ($p < 0.001$) or MA ($p < 0.001$) over 3 days (Figure 5.15).

Excretion of the radioactive material through urinary or hepatobiliary routes followed a similar pattern where radioactivity was excreted through urine more than feces at all time-points (2 hours, 24 hours, 48 hours, and 72 hours) and the excretion peaked at 24 hours post injection for both routes (Table 5.2). The overall excreted radioactivity reached 15% - 38% of injected dose by the end of study. To investigate the radioactive species in the excrement, we centrifuged down the urine samples as well as various controls mentioned in the method section to identify radioactive material in the supernatant (Figure 5.17). Results from control groups show that ^{125}I-BHR did not have physical adsorption with SiO_2 and 100% was recovered in the supernatant while 4% of ^{125}I-AR8, a typical ^{125}I-SiO_2, was recovered in the supernatant. This indicates that the 40% recovered radioactivity in supernatant of urine samples from AR8 treatment in mice was most likely to be unbound radioisotopes or small ^{125}I-SiO_2 degraded product. Similar results were found for urine samples from other nanoparticle treatment groups. We also collected the feces from nanoparticle treated animals, suspended in saline followed by centrifugation. Results showed that at least 36% radioactivity in feces was from unbound radioisotopes or small degraded product. The rest of radioactivity recovered in the pellet of urine or feces samples post-centrifugation could be ^{125}I-SiO_2 or their relatively large degraded product [17].

5.4 Discussion

In this chapter, the effect of geometry, porosity, and surface characteristics of SiO_2 on biodistribution and pharmacokinetics upon intravenous injection into healthy

Table 5.2 Urinary or hepatobiliary excretion of radioactivity post-intravenous injection of various SiO_2 in mice

% Injected radioactivity[a]	Urine				Feces			
	2 hours	24 hours	48 hours	72 hours	2 hours	24 hours	48 hours	72 hours
Meso S	1.4 ± 1.4	7.6 ± 2.1	10.2 ± 2.8	13.0 ± 3.3	0.1 ± 0.1	5.1 ± 1.4	7.0 ± 2.6	8.5 ± 2.5
MA	4.4 ± 1.9	10.9 ± 3.4	12.4 ± 3.5	14.8 ± 4.3	0.2 ± 0.1	3.4 ± 1.8	4.3 ± 2.1	5.5 ± 2.8
AR8	1.0 ± 1.0	16.6 ± 8.9	18.9 ± 9.0	22.7 ± 10.9	0.1 ± 0.1	11.1 ± 4.2	12.8 ± 4.5	15.4 ± 4.8
8A	5.1 ± 3.3	18.4 ± 5.5	20.4 ± 5.4	21.9 ± 5.5	0.1 ± 0.1	9.5 ± 2.8	10.6 ± 3.0	12.9 ± 4.1
Stöber	3.7 ± 1.4	9.5 ± 2.1	11.7 ± 2.4	13.5 ± 2.8	0.5 ± 0.3	7.0 ± 1.3	8.9 ± 1.9	11.6 ± 1.6
SA	2.7 ± 0.9	7.7 ± 3.0	9.0 ± 3.3	10.6 ± 2.9	0.1 ± 0.1	2.4 ± 0.7	3.7 ± 0.6	5.2 ± 0.9

[a]Excretion is expressed as percent radioactivity in urine or feces out of the total radioactivity injected. Data are expressed as mean ± SD (n = 5).

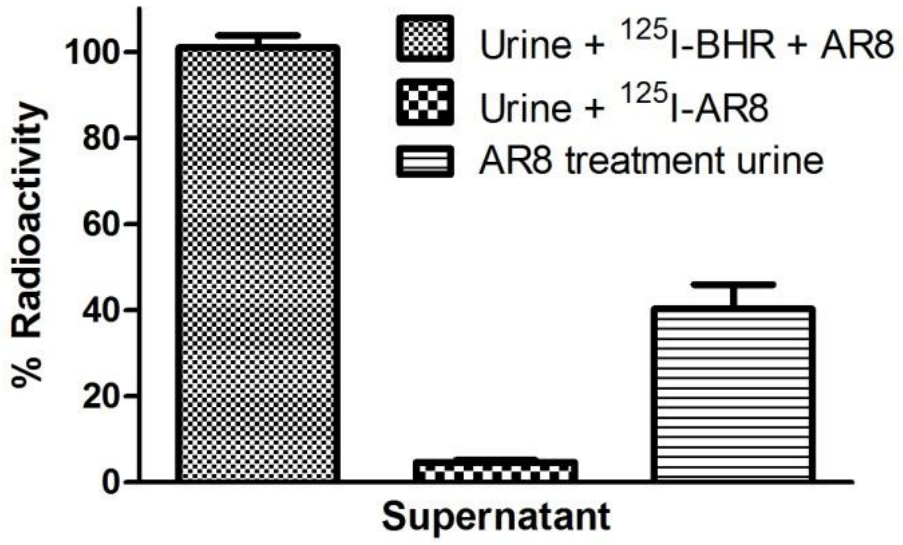

Figure 5.17 The percentage of radioactivity in the supernatant of different groups post-centrifugation. Results are expressed as percent of radioactivity in the supernatant post-centrifugation out of the total radioactivity in the microtubes. Data are presented as mean ± SD (n = 3).

mice was evaluated. The overall effect of physicochemical parameters of nanoparticles on the studied biological systems is summarized in Table 5.3 to enable the relation of biodistribution patterns observed here with cellular uptake and toxicity profiles of similar nanoparticles observed in previous chapters [9, 10].

The biodistribution results show that the majority of SiO_2 accumulated in the liver and spleen post-injection (Figures 5.4-5.9). This is due to the fact that the discontinuous endothelium lining the sinusoidal walls of the liver and spleen allows the passive entrapment of foreign particulates [14, 18]. The continuously increased organ/blood concentration ratios for the liver and spleen indicate that nanoparticles were internalized post-physical sequestration due to the prevalent presence of macrophages in these organs (Figures 5.13-5.14). The difference in accumulation of SiO_2 in various organs corroborates with our previous *in vitro* studies which showed that the cellular response to nanoparticle exposure was cell-type-dependent; macrophages had extensively higher association with the nanoparticles than epithelial cells [9]. Thus, the liver and spleen, where most macrophages reside, showed the most extensive SiO_2 accumulation in the biodistribution study. Nonporous SiO_2 (Stöber) and their amine-modified counterparts (SA) exhibited the highest liver affinity among all types of nanoparticles (Table 5.1). These results agree with *in vitro* studies which showed that porosity played a major role in determining nanoparticle cellular association; nonporous nanoparticles with or without amine modification had the highest cellular association among all types of nanoparticles [9]. The high affinity of Stöber for liver could be responsible for the significant increase in liver enzyme levels in plasma beyond MTDs compared with controls, as shown in previous *in vivo* toxicity studies [10]. It suggests that porosity plays an important role in

Table 5.3
Summary of engineered SiO_2 with various physicochemical properties and their *in vitro* and *in vivo* evaluation results

Nanoparticle type			Stöber	Meso S	AR8	SA	MA	8A
Physico-chemical properties	**Geometry by TEM (nm)**		115	120	136 × 1028	115	120	136 × 1028
	Porosity		Nonpo-rous	Mesopo-rous	Mesopo-rous	Nonpo-rous	Mesopo-rous	Mesopo-rous
	Surface charge in water		----	---	---	++	+++	+++
	DLS size in serum (nm)		121.6	268.9	N/A	N/A	150.3	N/A
***In vitro*[a]**	**IC_{50} (μg/mL)**	**M**	73	89	74	254	182	225
		E	/	/	/	/	/	/
	Cellular association (μg Si/100 μg protein)	**M**	21.2	0.7	0.4	14.8	3.3	4.1
		E	1.5	0	0	1	0.4	0.8
In vivo	**Safety[b]**	**MTD**	450	30	65	450	150	100
		Impaired organ(s) above MTD	Heart, lung, spleen	Kidneys	Kidneys	Lung, kidneys	Lung, kidneys	Lung, kidneys
	Biodistrib-ution	**Geometry**	/	/	/	/	/	Lung
		Porosity	Liver	Lung	/	Liver	/	/
		Surface character-istics	Lung, kidneys	Lung, kidneys	Lung, kidneys	/	/	/
	Pharmaco-kinetics	**V_{ss} (L)**	0.2	0.09	0.07	0.37	0.23	0.09

[a]content adapted from reference [9], surface charge is ranked as ---- highly negative -60 – -40 mV, --- highly negative -40 – -30 mV, ++ moderately positive 10 – 20 mV, +++ highly positive 20 – 40 mV. N/A means not available. M or E refers to macrophages RAW 264.7 or cancerous epithelial cells A549, / means not observed in the study design.

[b]content adapted from reference [10], for column under biodistribution, it means that the physicochemical property (indicated in the corresponding column) of nanoparticles of a specific type (indicated in the corresponding row) led to higher affinity in specific organs (indicated in the crossed cell) than nanoparticles of correspondingly different property (nonporous *versus* mesoporous, pristine *versus* amine-modified, or nanospheres *versus* nanorods). / means that this effect is not observed in the study design.

influencing the nanoparticle biodistribution pattern.

The SiO_2 of various types exhibited differential accumulation in the lung post-injection (Figures 5.4-5.9). The constant lung/blood concentration ratio over time indicated that the accumulation of SiO_2 in the lung was because of transient association with capillary rather than internalization (Figure 5.15). The association was balanced between SiO_2 organ concentration and SiO_2 blood concentration by SiO_2 translocation and redistribution into other organs. Thus, the accumulation in the lung was mostly in capillaries rather than in pulmonary cells. Mesoporous SiO_2 exhibited a higher lung affinity than nonporous SiO_2, and amine modification reduced lung affinity compared with the pristine SiO_2 (Figure 5.15). This pattern could be related to the changes in nanoparticle hydrodynamic size in the presence of serum (Table 5.3). Though produced with similar size as confirmed by TEM, mesoporous SiO_2 had significantly higher hydrodynamic size in the serum, probably due to protein adsorption, than nonporous SiO_2 which were probably stabilized by protein adsorption as suggested previously [10]. The relatively large hydrodynamic size of mesoporous SiO_2 in serum can partially explain the increased lung accumulation compared with nonporous SiO_2 (Figures 5.4, 5.8). Since the lung has the most abundant blood supply among all major organs, nanoparticles with larger hydrodynamic size are more likely to cause obstruction in vessels and increase organ accumulation. The amine-modified SiO_2 showed smaller hydrodynamic sizes in serum, probably due to steric stabilization from adsorbed protein molecules, than their pristine counterparts [10], which causes lower pulmonary accumulation (Figures 5.5, 5.7, 5.9) and decreased tissue affinity indices (Table 5.1). However, amine-modified mesoporous nanorods (8A) showed higher lung affinity than amine-modified mesoporous

nanospheres (MA) (Table 5.1), demonstrating that geometry of these nanoparticles influences biodistribution to a certain extent. In all, lung accumulation of nanoparticles was mostly influenced by porosity and surface characteristics; however, elongated geometrical shape (rods *versus* spheres) increased accumulation in this organ for amine-modified SiO_2.

Our previous *in vivo* toxicity studies showed that the onset of adverse reactions was mainly due to the mechanical obstruction of nanoparticles in the vasculature that led to congestion in organs and subsequent functional failure [10]. It appears that it is the "vasculature impact" rather than cellular toxicity that limits silica nanoparticle safety *in vivo.* In *in vitro* studies, nanoparticle toxicity was mainly influenced by surface characteristics; primary amine modification significantly reduced cellular toxicity, as shown by the increased IC_{50} values compared with pristine nanoparticles, probably due to the differential subcellular localization, whereas porosity and geometry did not seem to affect the IC_{50} [9]. In *in vivo* studies, porosity and surface characteristics influenced hydrodynamic sizes of SiO_2 in circulation, which had an important implication in their vasculature impact and resultant tolerance threshold [10]. Lung and kidneys were shown to be most susceptible to nanoparticle obstruction in vasculature above MTDs, probably due to their abundant blood supply and special anatomic structures [10]. Mesoporous SiO_2, which potentially had the largest hydrodynamic size in circulation as evidenced by hydrodynamic size analysis in serum, were most prone to cause vasculature obstruction and subsequent renal failure, resulting in the lowest MTDs at 30 -45 mg/kg irrespective of geometrical features [10]. Amine modification on mesoporous SiO_2 reduced the hydrodynamic size in serum and raised the MTDs to 100 – 150 mg/kg [10]. Nonporous

SiO_2 had the smallest hydrodynamic size in serum and thus reached the highest MTDs at 450 mg/kg, as observed previously [10]. These previous observations show that porosity and surface characteristics are major factors that influence *in vitro* or *in vivo* toxicity of SiO_2. Our current studies evaluating the biodistribution of these nanoparticles also ascertain the predominant effects of porosity and surface characteristics on organ accumulation.

Pharmacokinetic analysis demonstrates that the majority of SiO_2 of all types were rapidly cleared from circulation at a similar rate (Figure 5.11). Pristine SiO_2 had lower V_{ss} than the amine-modified counterparts while nonporous SiO_2 showed higher V_{ss} than mesoporous SiO_2 (Figure 5.12). This agrees with previous *in vitro* studies on both macrophages and epithelial cells that mesoporous SiO_2 had lower cellular association than their amine-modified counterparts while nonporous SiO_2 showed higher association than mesoporous SiO_2 [9]. These *in vivo* observations suggest that amine-modified SiO_2 or nonporous SiO_2 tended to associate and be taken up by RES in liver or spleen, leading into increased V_{ss}.

Further excretion experiments showed that radioactivity originally from ^{125}I-SiO_2 dosed intravenously was found in urine and feces (Table 5.2), indicating possible excretion of SiO_2 or their degraded product. Nanoparticle accumulation in the kidneys was low (Figures 5.4-5.9) and there was limited affinity of SiO_2 to this organ (Figure 5.16). Due to the very dilute radioactivity concentration in urine and low loading capacity of TLC assays, we could not quantitatively identify each radioactive species in the urine by TLC. Based on the centrifugation method, it was showed that there was possible presence of ^{125}I-SiO_2 or their degraded product in urine, even though a certain extent of

possible unbound radioisotopes from bond breakage from ^{125}I-SiO_2 *in vivo* was detected in supernatant of urine (Figure 5.17). It is possible that nanoparticles were degraded into orthosilicic acid species smaller than the reported renal excretion threshold of 7 nm, and were cleared through the renal route [4, 19]. Previous studies by Tang's group have suggested that intact SiO_2 larger than 100 nm in size can be excreted in urine post-intravenous injection, as evidenced by TEM imaging [20]. The mechanism of large nanoparticle excretion into urine is not fully understood and warrants further studies. The examination into radioactivity in feces indicated a similar fact that SiO_2 was likely excreted through hepatobiliary route into feces as the dense silicate form present in the pellet of feces from centrifugation method, which agrees with previous studies by Lo's group that reported the hepatobiliary excretion of SiO_2 by fluorescence imaging [8]. Our results from excretion experiments suggest that SiO_2 could be biodegraded and excreted out of the body.

5. 5 Conclusion

Of the materials tested in this study, it was demonstrated that SiO_2 biodistribution was influenced more by nanoparticle porosity and surface characteristics, and less by geometry. The nanoparticles across the board showed extensive distribution into the liver and spleen with different concentrations in the lung. Mesoporous SiO_2 accumulated in the lung to a higher extent than nonporous SiO_2 of similar size. Such accumulation was reduced by primary amine modification. However, high aspect ratio amine-modified nanorods showed higher lung accumulation than the amine-modified nanospheres. Results from tissue affinity indices and tissue/blood concentration ratio kinetic analyses suggest that tissue affinity was mainly porosity- and surface characteristics-dependent.

Nonporous SiO_2 exhibited high affinity to the liver, and mesoporous SiO_2 had higher affinity to the lung. Amine modification reduced the affinity of SiO_2 to the lung and kidneys. Two-compartmental pharmacokinetic analysis showed that amine-modified SiO_2 tended to have higher V_{ss} than the pristine counterparts and that nonporous SiO_2 exhibited a higher V_{ss} than mesoporous SiO_2. SiO_2 could be degraded and excreted out of the body by both urinary and hepatobiliary routes. This study enables the systematic understanding of how physicochemical factors affect the living system and facilitates the rational design of SiO_2 for their intended applications in the future.

5. 6 References

[1] S.H. Wu, Y. Hung, C.Y. Mou, Mesoporous silica nanoparticles as nanocarriers, Chem Commun (Camb), 47 (2011) 9972-9985.

[2] F. Tang, L. Li, D. Chen, Mesoporous silica nanoparticles: synthesis, biocompatibility and drug delivery, Adv Mater, (2012).

[3] L. Li, F. Tang, H. Liu, T. Liu, N. Hao, D. Chen, X. Teng, J. He, *In vivo* delivery of silica nanorattle encapsulated docetaxel for liver cancer therapy with low toxicity and high efficacy, ACS Nano, 4 (2010) 6874-6882.

[4] J. Lu, M. Liong, Z. Li, J.I. Zink, F. Tamanoi, Biocompatibility, biodistribution, and drug-delivery efficiency of mesoporous silica nanoparticles for cancer therapy in animals, Small, 6 (2010) 1794-1805.

[5] S.P. Hudson, R.F. Padera, R. Langer, D.S. Kohane, The biocompatibility of mesoporous silicates, Biomaterials, 29 (2008) 4045-4055.

[6] Q. He, Z. Zhang, F. Gao, Y. Li, J. Shi, *In vivo* biodistribution and urinary excretion of mesoporous silica nanoparticles: effects of particle size and PEGylation, Small, 7 (2011) 271-280.

[7] R. Kumar, I. Roy, T.Y. Ohulchanskky, L.A. Vathy, E.J. Bergey, M. Sajjad, P.N. Prasad, *In vivo* biodistribution and clearance studies using multimodal organically modified silica nanoparticles, ACS Nano, 4 (2010) 699-708.

[8] J.S. Souris, C.H. Lee, S.H. Cheng, C.T. Chen, C.S. Yang, J.A. Ho, C.Y. Mou, L.W. Lo, Surface charge-mediated rapid hepatobiliary excretion of mesoporous silica nanoparticles, Biomaterials, 31 (2010) 5564-5574.

[9] T. Yu, A. Malugin, H. Ghandehari, Impact of silica nanoparticle design on cellular toxicity and hemolytic activity, ACS Nano, 5 (2011) 5717-5728.

[10] T. Yu, K. Greish, L.D. McGill, A. Ray, H. Ghandehari, Influence of geometry, porosity, and surface characteristics of silica nanoparticles on acute toxicity: their vasculature effect and tolerance threshold, ACS Nano, 6 (2012) 2289-2301.

[11] N. Malik, R. Wiwattanapatapee, R. Klopsch, K. Lorenz, H. Frey, J.W. Weener, E.W. Meijer, W. Paulus, R. Duncan, Dendrimers: relationship between structure and biocompatibility *in vitro*, and preliminary studies on the biodistribution of ^{125}I-labelled polyamidoamine dendrimers *in vivo*, J Control Release, 65 (2000) 133-148.

[12] G. Thiagarajan, A. Ray, A. Malugin, H. Ghandehari, PAMAM-camptothecin conjugate inhibits proliferation and induces nuclear fragmentation in colorectal carcinoma cells, Pharm Res, 27 (2010) 2307-2316.

[13] S. Sadekar, A. Ray, M. Janat-Amsbury, C.M. Peterson, H. Ghandehari, Comparative biodistribution of PAMAM dendrimers and HPMA copolymers in ovarian-tumor-bearing mice, Biomacromolecules, 12 (2011) 88-96.

[14] S.E. Gratton, P.D. Pohlhaus, J. Lee, J. Guo, M.J. Cho, J.M. Desimone, Nanofabricated particles for engineered drug therapies: a preliminary biodistribution study of PRINT nanoparticles, J Control Release, 121 (2007) 10-18.

[15] S.R. Urva, B.S. Shin, V.C. Yang, J.P. Balthasar, Sensitive high performance liquid chromatographic assay for assessment of doxorubicin pharmacokinetics in mouse plasma and tissues, J Chromatogr B Analyt Technol Biomed Life Sci, 877 (2009) 837-841.

[16] D.L. Thai, L.N. Yurasits, G.R. Rudolph, J.M. Perel, Comparative pharmacokinetics and tissue distribution of the d-enantiomers of para-substituted methylphenidate analogs, Drug Metab Dispos, 27 (1999) 645-650.

[17] X. He, H. Nie, K. Wang, W. Tan, X. Wu, P. Zhang, *In vivo* study of biodistribution and urinary excretion of surface-modified silica nanoparticles, Anal Chem, 80 (2008) 9597-9603.

[18] G. Xie, J. Sun, G. Zhong, L. Shi, D. Zhang, Biodistribution and toxicity of intravenously administered silica nanoparticles in mice, Arch Toxicol, 84 (2010) 183-190.

[19] M. Longmire, P.L. Choyke, H. Kobayashi, Clearance properties of nano-sized particles and molecules as imaging agents: considerations and caveats, Nanomedicine (Lond), 3 (2008) 703-717.

[20] X. Huang, L. Li, T. Liu, N. Hao, H. Liu, D. Chen, F. Tang, The shape effect of mesoporous silica nanoparticles on biodistribution, clearance, and biocompatibility *in vivo*, ACS Nano, 5 (2011) 5390-5399.

CHAPTER 6

CONCLUSIONS AND FUTURE DIRECTIONS

6.1 Conclusions

Porosity and surface characteristics played crucial roles in determining SiO_2 impact on the biological systems. Toxicity was affected to a lesser extent by geometry. Porosity influenced nanoparticle cellular association as nonporous SiO_2 had higher association than mesoporous SiO_2. Porosity also influenced the hydrodynamic size in serum and in turn determined the vasculature impact and the safety dose level. Nonporous SiO_2 had a lower hydrodynamic size in serum and was much better tolerated than mesoporous SiO_2 of similar sizes. Porosity played a critical role in determining the biodistribution and pharmacokinetics of SiO_2 in major organs. Mesoporous SiO_2 had higher lung affinity than nonporous SiO_2, possibly due to larger hydrodynamic size. Nonporous SiO_2 had higher liver affinity and V_{ss} than mesoporous SiO_2, probably because of higher cellular association with the RES. Surface characteristics was the predominant factor that determined the cellular toxicity and association extent *in vitro*. Amine modification on mesoporous SiO_2 increased the cellular association on both macrophages and epithelial cells. However, it significantly reduced the cellular toxicity, probably due to differential cellular localization compared with pristine SiO_2. Surface characteristics also determined *in vivo* nanoparticle safety level, biodistribution, and pharmacokinetics. Amine-modified SiO_2 showing a lower hydrodynamic size than

pristine SiO_2 led to increased MTDs and reduced affinity to lung and kidneys. Amine-modified SiO_2 also showed a higher V_{ss}, probably due to increased association with the RES. Geometry did not seem to play a vital role in determining the cellular uptake, *in vitro* toxicity, and *in vivo* toxicity. However, high aspect ratio 8A did show increased lung accumulation compared with MA, which indicates the influence of geometry of amine-modified nanoparticles in biodistribution. The molecular mechanisms of these geometry, porosity, and surface modification effects need further detailed examination.

6.2 Future directions

The long-term objective of this research is to exploit the effect of physicochemical properties of SiO_2 on the biologically relevant environment to provide a rational design of SiO_2 for their intended applications. Owing to their high surface areas and ordered mesoporous structure, mesoporous silica materials constitute an interesting drug carrier for non-water-soluble drugs as it allows the control of the kinetic delivery of lipophilic drugs [1]. It has been reported that the physicochemical characteristics of silica matrices have substantial influence on drug loading and release profiles [2-4]. Linden's group found that the loading degree is related to the surface area and pore size of the silica matrix and the release kinetics is mainly dependent on porosity [3]. One-dimensional pore structure with cage-like pores is the most promising pore geometry to provide slow release of drugs for time periods varying from hours to weeks [3]. Vallet-Regi's group reported that amine-functionalized MCM-41 microspheres showed a significantly slower drug release rate than irregularly shaped silicate powders, which should facilitate drug delivery over a longer time [4]. Since we have already covered the baseline study on the toxicity and biodistribution of the nanocarrier as a function of

geometry, porosity, and surface characteristics, it is logical to analyze the influence of these characteristics on the drug loading or release profiles for the intended biomedical application. To achieve this goal, ibuprofen, a poorly aqueous soluble molecule, is chosen as the model drug. Engineered SiO_2 were loaded with ibuprofen by soaking them into the pentane solution of ibuprofen under continuous stirring at 37 ^oC. The loaded sample was recovered by filtration, washed with pentane, dried, and compacted to obtain disk pieces. Thermogravimetric and elemental analysis will be used to measure the drug loading in the sample. The *ex vivo* drug release analysis will be conducted by soaking the sample disks into the simulated body fluid at 37 ^oC under continuous stirring. The released ibuprofen concentration will be monitored by UV spectrometry at 273 nm [4]. It is expected that the surface characteristics, porosity, and geometry will have significant influence over drug loading and release from nanoparticles.

In vitro study has shown that amine-modified SiO_2 reduced toxicity to exposed cells compared with the pristine counterparts. It is very important to look into the cause for this toxicity reduction as it is against the main stream knowledge that amine modification on the nanosystem increases toxicity in cells as reported by previous literature [5, 6]. This investigation is crucial for understanding the interaction of nanoparticles with biological systems and which factors, such as amine moiety, interaction of amine groups with nanoparticle surface, surface charge, protein opsonization, *etc.*, determine the consequences of nanoparticle exposure to biological systems. To accomplish this, the nanoparticles could be modified with different amounts of primary amine groups to obtain different zeta potentials. The proliferation inhibition assay can be performed. IC_{50} can be obtained to evaluate the cytotoxicity level of

nanoparticles with different charges. We expect that there is a charge threshold beyond which the nanoparticles start to show reduced IC_{50} compared with the pristine counterparts. To explain the changes in IC_{50}, nanoparticles will be fluorescently labeled to allow imaging by confocal microscopy. It is expected that the differential cellular uptake pathway and subcellular location of nanoparticles causes the difference in IC_{50}.

In vivo toxicity study revealed that the mechanism of adverse reaction in animals was mostly due to obstruction of nanoparticles in vasculature rather than cellular toxicity. It is crucial to analyze the nanoparticle interaction with whole blood which directly reflects a nanoparticle's status in the circulation when injected intravenously. Platelet aggregation studies and neutrophil activation experiments can be performed. Hageman factor- and tissue factor-dependent activation of human blood/plasma coagulation, and binding to human monocytes, endothelial cells, and platelets, can be quantified *in vitro* for various SiO_2. This study could screen nanoparticles with different characteristics to select hemocompatible medical nanodevices for the intravenous route [7].

Since *in vivo* biodistribution study showed the presence of radioactivity in urine and feces and it has been reported previously that nanoparticles with sizes larger than 100 nm could be found as an intact modality in excrement [8, 9], it is necessary to evaluate the mechanism of how these large nanoparticles could be excreted intact considering the renal threshold of several nanometers [10]. Since the biodistribution was done at 20 mg/kg, which was below the MTD of all SiO_2, no histological abnormality was found in kidneys [11]. It is very interesting to analyze the clearance pathway of large size nanoparticles when no physiological damage was seen in kidneys. TEM images could be obtained for kidneys of animals post-intravenous injection of SiO_2 to analyze the possible

presence of intact nanoparticle in the exit route and connect with the physiological status of nephron. This study could generate important data about clearance and biocompatibility of large size nanoconstructs as an *in vivo* delivery system.

6.3 References

[1] C. Charnay, S. Begu, C. Tourne-Peteilh, L. Nicole, D.A. Lerner, J.M. Devoisselle, Inclusion of ibuprofen in mesoporous templated silica: drug loading and release property, Eur J Pharm Biopharm, 57 (2004) 533-540.

[2] S.C. Shen, W.K. Ng, L. Chia, J. Hu, R.B. Tan, Physical state and dissolution of ibuprofen formulated by co-spray drying with mesoporous silica: effect of pore and particle size, Int J Pharm, 410 (2011) 188-195.

[3] J. Andersson, J. Rosenholm, S. Areva, M. Lindén, Influences of material characteristics on ibuprofen drug loading and release profiles from ordered micro- and mesoporous silica matrices, Chem. Mater., 16 (2004) 4160-4167.

[4] M. Manzano, V. Aina, C.O. Are´an, F. Balas, V. Cauda, M. Colilla, M.R. Delgado, M. Vallet-Reg´ı, Studies on MCM-41 mesoporous silica for drug delivery: effect of particle morphology and amine functionalization, Chemical Engineering Journal, 137 (2008) 30-37.

[5] C. Lin, J.F. Engbersen, Effect of chemical functionalities in poly(amido amine)s for non-viral gene transfection, J Control Release, 132 (2008) 267-272.

[6] S.H. Pun, N.C. Bellocq, A. Liu, G. Jensen, T. Machemer, E. Quijano, T. Schluep, S. Wen, H. Engler, J. Heidel, M.E. Davis, Cyclodextrin-modified polyethylenimine polymers for gene delivery, Bioconjug Chem, 15 (2004) 831-840.

[7] R. Tavano, D. Segat, E. Reddi, J. Kos, M. Rojnik, P. Kocbek, S. Iratni, D. Scheglmann, M. Colucci, I.M. Echevarria, F. Selvestrel, F. Mancin, E. Papini, Procoagulant properties of bare and highly PEGylated vinyl-modified silica nanoparticles, Nanomedicine (Lond), 5 (2010) 881-896.

[8] X. Huang, L. Li, T. Liu, N. Hao, H. Liu, D. Chen, F. Tang, The shape effect of mesoporous silica nanoparticles on biodistribution, clearance, and biocompatibility *in vivo*, ACS Nano, 5 (2011) 5390-5399.

[9] X. He, H. Nie, K. Wang, W. Tan, X. Wu, P. Zhang, *In vivo* study of biodistribution and urinary excretion of surface-modified silica nanoparticles, Anal Chem, 80 (2008) 9597-9603.

[10] M. Longmire, P.L. Choyke, H. Kobayashi, Clearance properties of nano-sized particles and molecules as imaging agents: considerations and caveats, Nanomedicine (Lond), 3 (2008) 703-717.

[11] T. Yu, K. Greish, L.D. McGill, A. Ray, H. Ghandehari, Influence of geometry, porosity, and surface characteristics of silica nanoparticles on acute toxicity: their vasculature effect and tolerance threshold, ACS Nano, 6 (2012) 2289-2301.

APPENDIX A

CHARACTERIZATION AND CYTOTOXICITY OF SILICA NANOTUBES

A.1 Introduction

Silica nanotubes (SNTs) are a novel class of inorganic structures with potential applications in imaging and drug delivery [1-10]. The hollow tubular structure obtained with template synthesis [4, 5, 9] can be differentially functionalized on the inner or outer surfaces, enabling the loading of biomolecules inside the tubes and the outer surface modification for targeting or solubility purposes. The open ends of tubes can be functionalized with stimuli-sensitive polymers to act as selective gates to regulate the release of biomolecules based on environmental conditions.

Despite the unique advantages of SNTs, how they interact with biological systems remains largely unknown. Previously, it was shown that SNTs are internalized by cells and that nanotube size and surface charge play crucial roles in determining the extent of cellular uptake [11]. In this pilot study, we aimed to understand the influence of size and surface charge of SNTs on *in vitro* toxicity.

A.2 Methods

A.2.1 SNT characterization

The SNTs were provided by Professor Sang Bok Lee at the University of Maryland, College Park. The zeta potentials of SNTs were measured using a Nanosizer (Malvern, UK). Smoluchowski's model was utilized to calculate zeta potential values from SNTs' electrophoretic migration rates. The SNTs were dispersed in water at a concentration of 2.5 μg/ml with pH of the solution adjusted to 7.4 by adding 1 N HCl or 1 N NaOH and were subject to 10-15 minutes sonication immediately before the measurements. Experiments were done in triplicate and the averaged results are shown.

A.2.2 Cell culture

Human embryonic kidney cells HEK 293T, human large cell lung carcinoma cells H460, human lung fibroblast cells WI-38, and human mammary breast epithelial cells MCF 10A were used in this study. All four cell lines were kindly provided by the late Dr. Angelika Burger (Greenebaum Cancer Center, University of Maryland, Baltimore, MD). HEK 293T cells were cultured in DMEM supplemented with 2 mM L-glutamine, 10% FBS, penicillin, and streptomycin (100 U/ml and 0.1 mg/ml, respectively). H460 cells were cultured in RPMI medium supplemented with 2 mM L-glutamine, 10% FBS, penicillin and streptomycin (100 U/ml and 0.1 mg/ml, respectively). WI-38 cells were maintained in RPMI medium supplemented with 2 mM L-glutamine, 10% FBS, penicillin, and streptomycin (100 U/ml and 0.1 mg/ml, respectively). MCF 10A cells were maintained in mammary epithelial basal medium (Clonetics, Walkersville, MD) with bovine pituitary extract (52 μg/ml), hydrocortisone (0.5 μg/ml), human recombinant epidermal growth factor (10 ng/ml), and

bovine insulin (5.0 μg/ml) (Clonetics, San Diego, CA). All cells were cultured at 37°C in a humidified atmosphere of 5% CO_2.

A.2.3 Cytotoxicity assays

Cells were seeded at a density of 2000 to 10,000 cells per well (100 μl cell suspension) into a 96-well plate. Cells were allowed to adhere for 24 hours before the complete media was replaced with media containing SNTs at different concentrations (0.005 μg/ml, 0.05 μg/ml, 0.5 μg/ml, and 5 μg/ml, quadruplicate for each concentration). Cells were then exposed to the incremental concentrations of SNTs for the following 72 hours at 37°C in a humidified 5% CO_2 atmosphere. After that, the cell media were decanted and MTT solution was added (0.5 mg/ml in the media, 100 μl media per well) into each well. The cells were incubated for an additional 4 hours at 37°C in a humidified 5% CO_2 atmosphere. 100 μl to 200 μl of DMSO was added to dissolve all the formazan crystal. The optical density at 550 nm was measured by SpectraMax M2 microplate reader (Molecular devices, CA) and the viability of the cells was calculated as a percentage of viability of cells grown in complete media in the absence of SNTs.

Plasma membrane integrity was assessed by using Cytoscan-lactate dehydrogenase (LDH) Cytotoxicity Assay Kit (Geno Technology Inc., St. Louis, MO). Exponentially growing MCF 10A cells were exposed to increasing concentrations of SNTs for 24 hours as described above. 10 μl of lysis buffer (9% v/v Triton X-100) was added to cells in positive control group. After incubating at 37 °C for 45 minutes, the plate was centrifuged at 250 × g for 5 minutes. 50 μl of supernatant was used for LDH analysis following the manufacturer's instruction and the absorbance was recorded at 490 nm with a reference wavelength of 680 nm [12]. Toxicity of SNTs was calculated as follows:

$$\text{LDH release (\%)} = \frac{A_{sample} - A_{spont}}{A_{max} - A_{spont}} \times 100\%$$

where A_{sample} is the absorbance of a sample exposed to SNTs, A_{spont} is the absorbance of a sample exposed to complete cell media only, and A_{max} is the absorbance of a sample lysed by lysis buffer (9 % v/v Triton X-100).

LDH absorption was assessed to evaluate the potential interaction of LDH enzyme with SNTs in the cell lysates of MCF 10A cells. Initially, MCF 10A cells were seeded at 10000 cells/well in a 96 well plate as described above. After 24 hours, 10 μl of lysis buffer was added and incubated with cells for 45 minutes at 37^{o}C. Then the plate was centrifuged at 250 × g for 5 minutes and 50 μl of supernatant was transferred to a fresh 96 well plate and incubated with four types of SNTs at the concentration of 5 μg/ml for 24 hours at 37°C, 5% CO_2. After further centrifugation at 250 × g for 5 minutes, 50 μl of supernatant was utilized to determine the LDH release of each type of SNTs following the manufacturer's protocol. Absorbance was recorded at 490 nm with a reference wavelength of 680 nm.

A.2.4 Statistical analysis

Unless otherwise stated, all experiments were conducted in quadruplicate and the results were reported as means ± SD, where statistical significance was determined by two-tailed, unpaired Student's t-test. The level of significance was taken as $p < 0.05$.

A.3 Results and discussion

A series of SNTs of two discrete lengths, namely, 200 and 500 nm, and two different surface charges, namely, unmodified bare (negatively charged) and 3-aminopropyl trimethoxysilane (APTS) modified (positively charged) were previously fabricated and characterized (Figure A.1) [11]. The zeta potentials of the materials at pH 7.4 were shown in Table A.1. Bare SNTs have silanol groups (Si-OH) present on the outer surface and display negative charge due to dissociation of protons from the surface silanol groups at pH values above the isoelectric point (pH 2) in an aqueous solvent [13]. As expected, 200 and 500 nm bare SNTs showed highly negative zeta potential values, implying that the unmodified nanotubes were generally stable and well dispersed in the media. APTS modified SNTs showed almost neutral or positive zeta potential values. APTS modified 200 nm SNTs showed a relatively high positive value, suggesting that these tubes are fairly stable in aqueous solvents. It has been shown [14] that the large aspect ratio of nanotube structures would generally favor increased hydrophobicity and van der Waals interactions, leading to aggregation and sedimentation. In contrast, the limited aggregation tendency of SNTs in aqueous systems is primarily attributed to electrostatic repulsion of like charge on the surface of SNTs. Furthermore, the silanol groups of bare SNTs can readily form the hydroxyl layer with water molecules through hydrogen bonding, which further improves their aqueous dispersibility.

The effect of nanotubes of varying lengths and surface charge on cellular toxicity was determined on a panel of normal cell lines, including embryonic kidney cells (HEK 293T), lung fibroblasts (WI-38), breast epithelial cells (MCF 10A), as well as a cancerous cell line, namely the large cell lung cancer cell line (H460). The rationale for choosing these cell lines

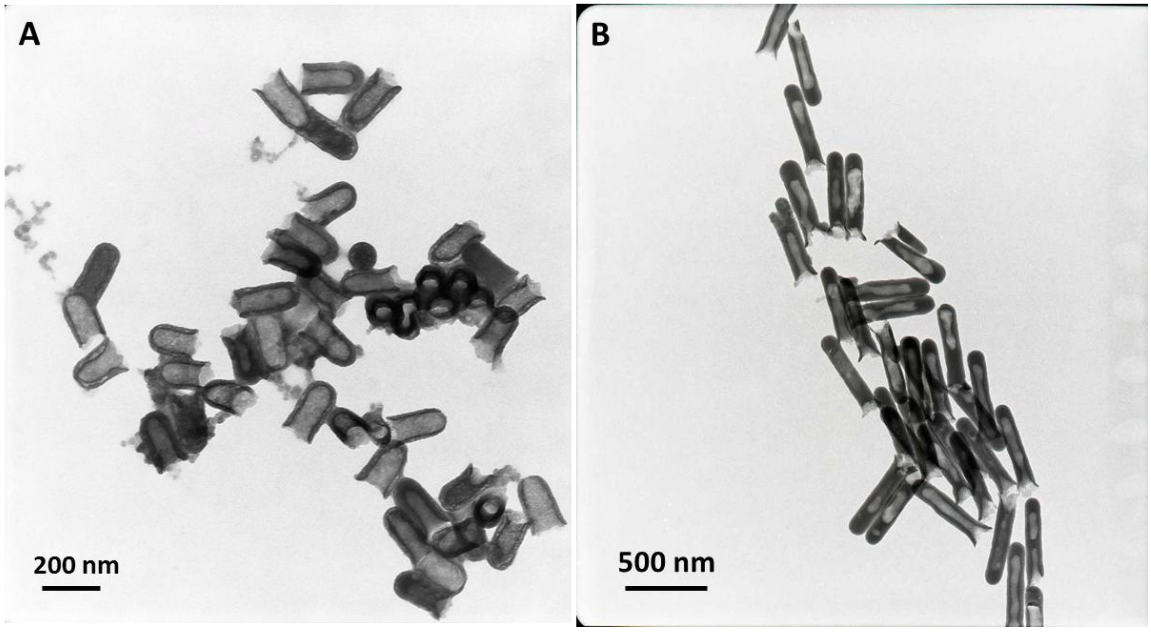

Figure A.1 TEM images of A) 200 nm SNTs and B) 500 nm SNTs (provided by Sungkyoung Kim at the University of Maryland, College Park).

Table A.1 Zeta potential of SNTs (2.5 μg/ml) in deionized water, pH 7.4

Type of SNTs	Zeta potential (mV)
200 nm bare SNTs	-26.80 ± 0.61
200 nm APTS-modified SNTs	8.51 ± 0.31
500 nm bare SNTs	-24.70 ± 1.48
500 nm APTS-modified SNTs	-0.35 ± 1.54

was that these cells could be potentially encountered by SNTs in the *in vivo* biological milieu. A range of concentrations of SNTs (5-0.005 μg/ml) were studied. Based on the results of the MTT assay (Figure A.2), none of the four types of SNTs substantially affected the viability of the four cell lines at all concentrations tested after 72-hour exposure (over 55% or higher viability rates). In general, the 500 and 200 nm bare SNTs showed no significant inhibition on cell growth for all tested cell lines. Surface modification resulted in moderately higher toxicity of APTS-modified SNTs compared with their unmodified counterparts: 200 nm APTS-modified SNTs demonstrated significantly higher growth inhibition compared with 200 nm bare SNTs at 5 μg/ml in HEK 293T, H460, and WI-38 cells ($p < 0.05$). 500 nm APTS-modified SNTs evoked significantly higher inhibitory effect than 500 nm bare SNTs at 5 μg/ml in WI-38 cells ($p < 0.05$).

Apart from the surface charge influence, the impact of size also seems to play an important role on cytotoxicity evaluation: Significantly higher viability of HEK 293T cells and H460 cells was observed when treated with 500 nm APTS-modified SNTs compared with 200 nm APTS-modified SNTs at the highest concentration ($p < 0.05$). This suggests that smaller size of SNTs may be internalized to a higher extent and have greater effects on inhibition of mitochondrial activity. It seemed that toxicity of SNTs is cell-line-dependent: Statistically significant inhibition of cell growth was detected for APTS-modified SNTs in contrast to the unmodified counterparts in WI-38 cells at 0.05 μg/ml or lower concentration ($p < 0.05$). This implies that normal lung fibroblasts are more sensitive to silica nanotube surfaces exposure. In all, toxicity of SNTs to different cell lines was concentration-dependent and toxicity was not observed higher than 45% across the panel of cell lines. Toxicity profiles of SNTs obtained in this evaluation are in good agreement with our previous study [11].

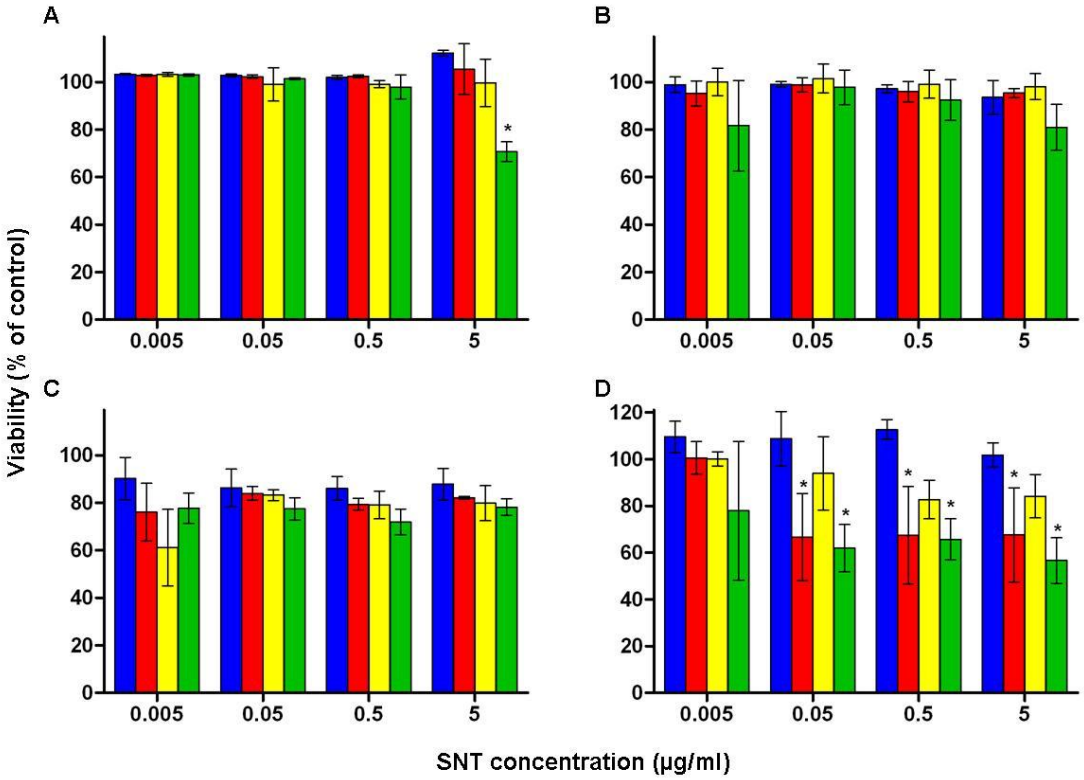

Figure A.2 Viability of different cell lines determined by MTT assay after exposure to 500 nm bare SNTs (■), 500 nm APTS-modified SNTs (■), 200 nm bare SNTs (■), 200 nm APTS-modified SNTs (■) for 72 hours: A) HEK 293T cells; B) H460 cells; C) MCF 10A cells; D) WI-38 cells. Data presented as means ± SD (n = 4). *Statistically different (p < 0.05) from control (cells incubated in complete media only).

The susceptibility of fibroblast cells towards toxicity and cellular injury is increasingly being documented for several engineered nanoparticulate systems such as silica particles, carbon nanotubes [15-17]. The surface area of the particles is also believed to be an important parameter in determining such toxicity which is consistent with our observation with smaller sized SNTs (higher exposed surface area per unit dose).

To evaluate any possible effect of surface charge on cellular membrane integrity, a LDH assay was performed with four types of SNTs in MCF 10A cells. The assay quantitatively measures the amount of stable, cytosolic, LDH enzyme, which is typically leaked out of cells when the cell membrane is damaged. Since all SNTs have surface charges, the possibility that LDH enzyme adsorbs to the surface of particles, thus leading to false negative cytotoxicity results, was also examined [12]. Results revealed that none of the SNTs tested had any significant ($p > 0.05$) LDH absorption at a concentration of 5mg/ml for 24 hours (Figure A.3). LDH assays were also performed on H460 cells and no significant increase in LDH release was detected for all types of SNTs (data not shown).

The 200 nm and 500 nm bare SNTs and 500 nm APTS-modified SNTs caused no significant increase in the LDH release at all concentrations tested after 24-hour exposure (Figure A.4). LDH release was observed only with 200 nm APTS-modified SNTs up to 10% of maximum LDH release from cells, indicating that the observed toxicity with these SNTs might be related to surface charge interaction with plasma membrane. Since plasma membrane injury is one of the physiological characteristics of necrotic cell death, LDH assay illustrated that increasing surface charge may result in more necrotic cells [18].

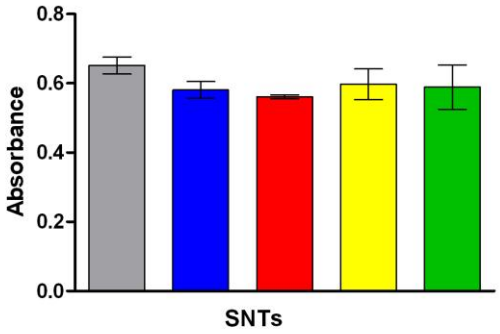

Figure A.3 The absorbance of LDH release from cell lysates incubated with 5 μg/ml of 500 nm bare SNTs (■), 500 nm APTS-modified SNTs (■), 200 nm bare SNTs (■), 200 nm APTS-modified SNTs (■), or control (cell lysates in the absence of SNTs) (■) for 24 hours in MCF 10A cells. No significant difference (p >0.05) was observed between sample absorbance and control absorbance. Data presented as mean ± SD, n = 4.

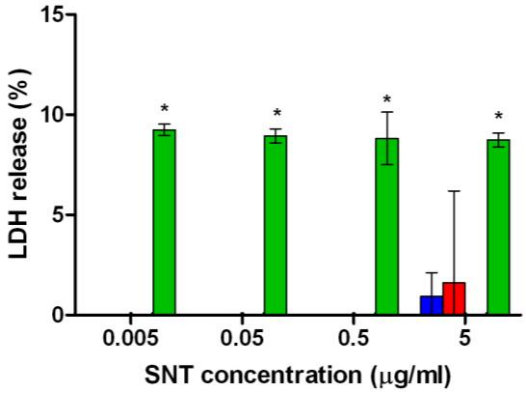

Figure A.4 Effect of 500 nm bare SNTs (■), 500 nm APTS-modified SNTs (■), 200 nm bare SNTs (■), 200 nm APTS-modified SNTs (■) on plasma membrane integrity of MCF10A cells as determined by lactate dehydrogenase (LDH) assay. Results are after 24 hours exposure. Data presented as means ± SD (n = 4). *Statistically different ($p < 0.05$) from control (cells incubated in complete media only).

A.4 Conclusion

In summary, SNTs of discrete length and surface charge were characterized for their physicochemical properties and cytotoxicity *in vitro*. The SNTs showed limited toxicity which was dependent on the cell type but also to a lesser extent on the concentration, surface charge, and length. These studies pave the way for understanding the structural features of SNTs which influence their biocompatibility in cellular environments. Such data can also aid in tailor-designing SNTs for specific biomedical applications in the long run.

A.5 References

[1] X. Bai, S.J. Son, S. Zhang, W. Liu, E.K. Jordan, J.A. Frank, T. Venkatesan, S.B. Lee, Synthesis of superparamagnetic nanotubes as MRI contrast agents and for cell labeling, Nanomed, 3 (2008) 163-174.

[2] F. Buyukserin, C.D. Medley, M.O. Mota, K. Kececi, R.R. Rogers, W. Tan, C.R. Martin, Antibody-functionalized nano test tubes target breast cancer cells, Nanomed, 3 (2008) 283-292.

[3] C.C.L. Chen, Y. C.; Wu, C. H.; Yeh, C. C.; Su, M. T.; Wu, Y. C., Preparation of fluorescent silica nanotubes and their application in gene delivery, Advanced Materials, 17 (2005) 404-407.

[4] H. Hillebrenner, F. Buyukserin, J.D. Stewart, C.R. Martin, Template synthesized nanotubes for biomedical delivery applications, Nanomed, 1 (2006) 39-50.

[5] P.M. Kohli, C. R., Template-synthesized nanotubes for biotechnology and biomedical applications, Journal of Drug Delivery Science and Technology, 15 (2005) 49-57.

[6] C.R. Martin, P. Kohli, The emerging field of nanotube biotechnology, Nat Rev Drug Discov, 2 (2003) 29-37.

[7] S.J. Son, X. Bai, S.B. Lee, Inorganic hollow nanoparticles and nanotubes in nanomedicine Part 2: Imaging, diagnostic, and therapeutic applications, Drug Discov Today, 12 (2007) 657-663.

[8] S.J. Son, X. Bai, S.B. Lee, Inorganic hollow nanoparticles and nanotubes in nanomedicine Part 1. Drug/gene delivery applications, Drug Discov Today, 12 (2007) 650-656.

[9] S.J. Son, X. Bai, A. Nan, H. Ghandehari, S.B. Lee, Template synthesis of multifunctional nanotubes for controlled release, J Control Release, 114 (2006) 143-152.

[10] S.J. Son, J. Reichel, B. He, M. Schuchman, S.B. Lee, Magnetic nanotubes for magnetic-field-assisted bioseparation, biointeraction, and drug delivery, J Am Chem Soc, 127 (2005) 7316-7317.

[11] A. Nan, X. Bai, S.J. Son, S.B. Lee, H. Ghandehari, Cellular uptake and cytotoxicity of silica nanotubes, Nano Lett, 8 (2008) 2150-2154.

[12] J.S. Chang, K.L. Chang, D.F. Hwang, Z.L. Kong, *In vitro* cytotoxicitiy of silica nanoparticles at high concentrations strongly depends on the metabolic activity type of the cell line, Environ Sci Technol, 41 (2007) 2064-2068.

[13] K.N. Pham, D. Fullston, K. Sagoe-Crentsil, Surface modification for stability of nano-sized silica colloids, J Colloid Interface Sci, 315 (2007) 123-127.

[14] M. Foldvari, M. Bagonluri, Carbon nanotubes as functional excipients for nanomedicines: II. Drug delivery and biocompatibility issues, Nanomedicine, 4 (2008) 183-200.

[15] E.R. Kisin, A.R. Murray, M.J. Keane, X.C. Shi, D. Schwegler-Berry, O. Gorelik, S. Arepalli, V. Castranova, W.E. Wallace, V.E. Kagan, A.A. Shvedova, Single-walled carbon nanotubes: geno- and cytotoxic effects in lung fibroblast V79 cells, J Toxicol Environ Health A, 70 (2007) 2071-2079.

[16] V. Pensabene, O. Vittorio, V. Raffa, A. Menciassi, P. Dario, Investigation of CNTs interaction with fibroblast cells, Conf Proc IEEE Eng Med Biol Soc, 2007 (2007) 6621-6624.

[17] H. Yang, C. Liu, D. Yang, H. Zhang, Z. Xi, Comparative study of cytotoxicity, oxidative stress and genotoxicity induced by four typical nanomaterials: the role of particle size, shape and composition, J Appl Toxicol, 29 (2009) 69-78.

[18] M.J. Clift, B. Rothen-Rutishauser, D.M. Brown, R. Duffin, K. Donaldson, L. Proudfoot, K. Guy, V. Stone, The impact of different nanoparticle surface chemistry and size on uptake and toxicity in a murine macrophage cell line, Toxicol Appl Pharmacol, 232 (2008) 418-427.

APPENDIX B

SYNTHESIS AND CHARACTERIZATION OF SILICA-COATED GOLD NANORODS

B.1 Introduction

High aspect ratio, elongated gold nanorods could absorb from the near-infrared through the mid-infrared light at great efficiency, which makes them suitable for multiple applications requiring the conversion of infrared light to heat [1]. The development in gold nanorods synthesis methods enabled the production of nanorods at targeted aspect ratios with high purity [2-8]. It has been reported that 100% high aspect gold nanorods could be obtained by partial dissolution of platelets [9]. Recent studies have also reported successful silica coating on metal nanoparticles [10, 11], which facilitates the production of multifunctional hybrid nanomaterials for biomedical application.

This Appendix describes the synthesis of highly uniform silica-based nanorod structures for comparison with uniform silica nanospheres to evaluate the shape effect on biological systems. The silica coating on gold nanorods could generate high aspect ratio silica-coated nanomaterials as an alternative to silica nanotubes for comparative evaluation of SiO_2 shape effect on biological interface.

B.2 Methods

B.2.1 Synthesis

The gold nanorod synthesis protocol was adapted from reference [9] and the silica coating procedure was adapted from previous reports [10, 12].

Preparation of the growth solution. In a 1 L flask, 64.06 g of CTAB was dissolved in 880 mL water upon gentle heating at 35 ^{o}C. CTAB was dissolved in water upon gentle stirring, the stirring speed was kept slow so that no extensive bubbles were formed. In another 1 L flask, 173.4 mg of gold chloride ($HAuCl_4 \cdot 3H_2O$) (weighted in nitrogen environment) was dissolved in 880 mL water. The CTAB solution was transferred into a 2 L glass bottle. The gold chloride solution was added as well. A 100 mL flask, a 250 mL flask, and a 2 L glass bottle were collected. 45 mL of prepared solution was transferred into a 100 mL flask. 140 mL of prepared solution was transferred into a 250 mL flask. 1575 mL of prepared solution was transferred into the 2 L glass bottle. These containers were left at room temperature (short). 0.1 M ascorbic acid was prepared by dissolving 176 mg of L-ascorbic acid in 10 mL of water. 0.25, 0.77 and 8.75 mL of ascorbic acid solution was added into 100 mL, 250 mL, and 2 L container containing prepared solution. All three containers were hand shaken and the solution turned from golden to colorless.

Preparation of the seed solution (fast). 1.47 mg of sodium citrate was dissolved in 10 mL water. 1.97 mg of $HAuCl_4 \cdot 3H_2O$ was dissolved in 10 mL water. The sodium citrate solution and Au chloride solution were mixed together in a 150 mL flask containing a magnetic stirring bar. To this flask 0.6 mL of 0.1 M ice-cold sodium borohydride ($NaBH_4$) solution (3.78 mg/mL) was added upon vigorous stirring at 1200

rpm. The solution became brownish-red. The seed solution was used within 10 minutes after preparation.

Production of gold nanorods. 4 mL of the seed solution was added to 100 mL flask containing growth solution and gently mixed. Within 3 seconds, 12.4 mL of resulting mixture was transferred to 250 mL flask containing growth solution *via* a 25 mL plastic pipette. The mixture was gently mixed. With 3 seconds, all the content in 250 mL flask was transferred into 2 L glass bottle containing growth solution. The 2 L glass bottle was gently shaken. The glass bottle was left at 27 ^{o}C for additional 14 hours. The color of solution changed to purple in 2-3 minutes and then to dark red in 30 minutes. The high aspect ratio gold nanorods precipitated to the bottom of glass bottle within 12 hours. So the glass bottle was kept at 27 ^{o}C for 12 hours to 14 hours. After the settlement, all supernatant was carefully removed and the invisible layer of nanorods was redispersed into 10 mL of 0.1 M CTAB upon 30 seconds sonication.

Partial dissolution of platelets. An oxidizing Au (III)/CTAB complex for partial dissolution was prepared by dissolving 364 mg of CTAB and 1.97 mg of $HAuCl_4 \cdot 3H_2O$ in 10 mL of DI water. Next, 1 mL of this solution was added to 10 mL Au nanorods and platelets CTAB suspension upon stirring and left undisturbed for 14 hours. Nanorods along with large disks precipitated and form a thin layer on the bottom of flask. The greenish-blue supernatnet containing small disks was carefully collected in a microtube. The layer of precipitate was again redispersed in 10 mL of 0.1 M CTAB solution followed by addition of another 1 mL of Au (III)/CTAB solution. The process was repeated until the supernatant of the suspension post 14 hour sedimentation was no longer in green-blue appearance. The process was repeated for two times in this experiment.

Silica coating on gold nanorods. The Au nanorod solution (0.01 – 0.1 weight% nanorod concentration) was prepared. 10 μL of (3-mercaptopropyl)trimethoxysilane (MPTMS) solution (10 μL MPTMS in 1 mL of ethanol) was added to 1 mL of the nanorod solution and stirred for 20 minutes. Next, 40 μL of a 2.0 M freshly prepared aqueous sodium silicate solution was added and stirring continued for another 20 mintues. The solution was left at room temperature.

B.2.2 Characterization

The gold nanorods or silica coated gold nanorods were added to TEM grids and left dry at room temperature. TEM images were taken with a Philips Tecnai microscope at 120 kV. The absorbance spectrum of gold nanorods in 0.1 M CTAB/D_2O solution was measured on a Cary-17 spectrophotometer.

B.3 Results

Highly uniform gold nanorods were produced at the quantity of ca. 300 μg per batch based on the protocol provided in the method section. The dimension of gold nanorods was 188.08 ± 25.12 nm × 21.89 ± 3.63 nm (length × width) (Figure B.1). The product was 100% nanorods without the presence of other structures (disks, platelets), indicating the successful removal of platelets. The Silica coating resulted in multiple gold nanorods uniformly coated with a silica layer of 10 nm in thickness (Figure B.2). The absorbance spectrum of gold nanorods in 0.1 M CTAB/D_2O solution had the transverse peak at 524 nm (A = 0.25) and longitudinal peak at around 1400 nm to 1600 nm (A ≥ 0.49), indicating the long shape formation (data not shown).

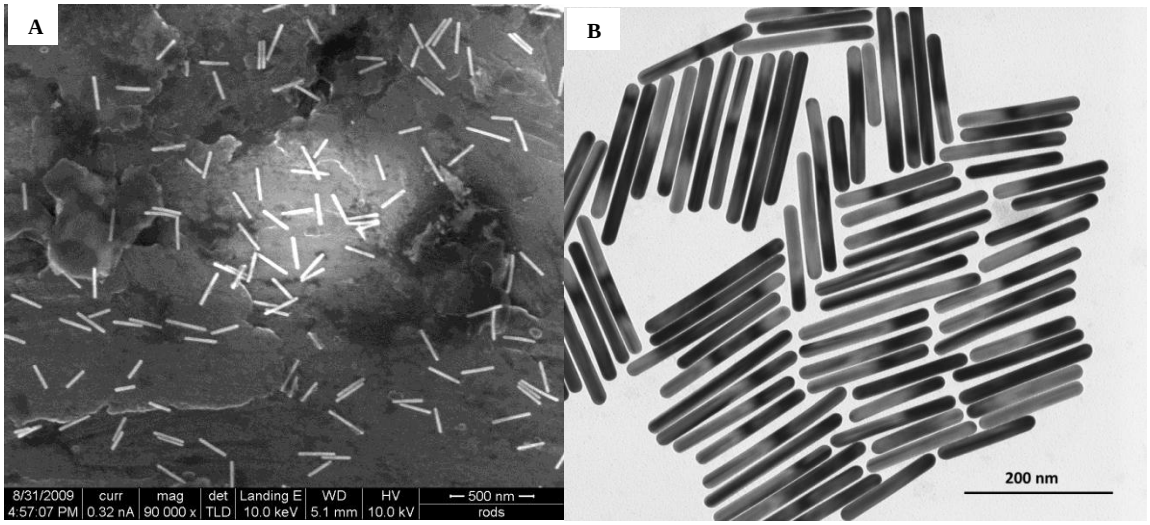

Figure B.1 A) SEM and B) TEM images of highly uniform high aspect ratio gold nanorods.

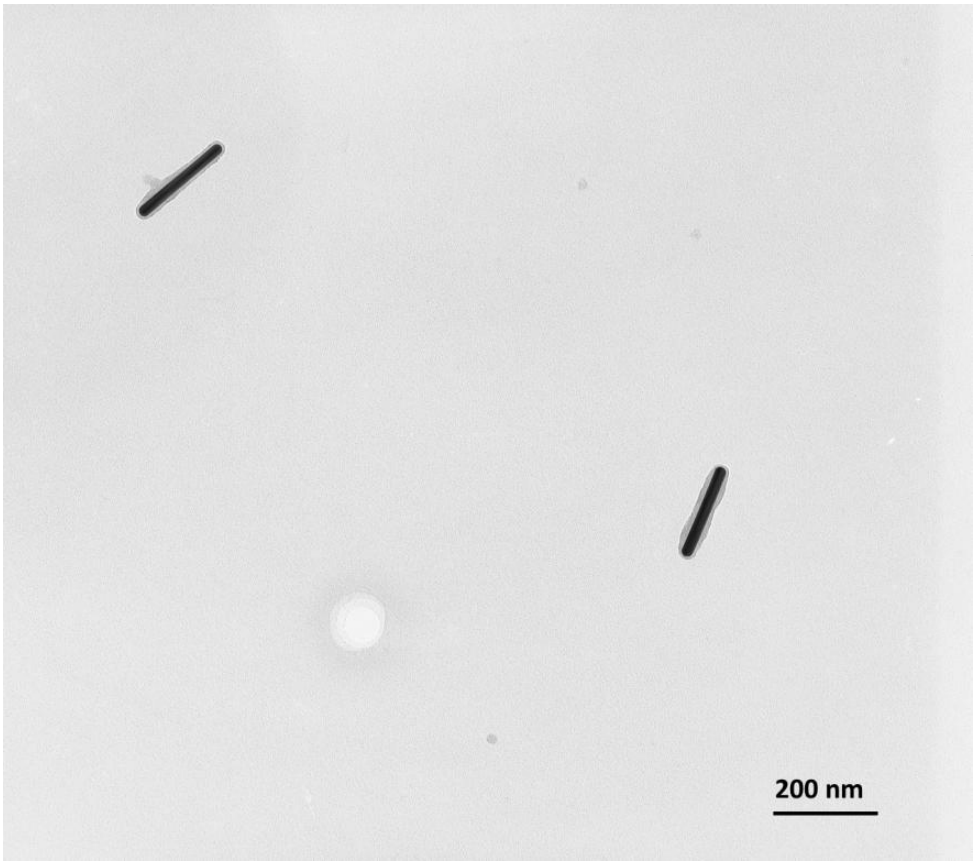

Figure B.2 TEM image of silica-coated gold nanorods.

B.4 Conclusion

Highly uniform, silica coated gold nanorods were obtained with the seed-mediated synthesis. The size of gold nanorods was of biological relevance thus could be further investigated for potential application in nanomedicine. This study provides an effective alternative to obtain silica-based high aspect ratio nanomaterials to evaluate the shape effect of silica materials on biological fate for future evaluations.

B.5 References

[1] X. Huang, I.H. El-Sayed, W. Qian, M.A. El-Sayed, Cancer cell imaging and photothermal therapy in the near-infrared region by using gold nanorods, J Am Chem Soc, 128 (2006) 2115-2120.

[2] B.D. Busbee, S.O. Obare, C.J. Murphy, An improved synthesis of high-aspect-ratio gold nanorods, Adv. Mater., 15 (2003) 414-416.

[3] N.R. Jana, L. Gearheart, C.J. Murphy, Wet chemical synthesis of high aspect ratio cylindrical gold nanorods, J. Phys. Chem. B, 105 (2001) 4065-4067.

[4] D.K. Smith, B.A. Korgel, The importance of the CTAB surfactant on the colloidal seed-mediated synthesis of gold nanorods, Langmuir, 24 (2008) 644-649.

[5] A. Gole, C.J. Murphy, Seed-mediated synthesis of gold nanorods: role of the size and nature of the seed, Chem. Mater., 16 (2004) 3633-3640.

[6] Y. Xia, P. Yang, Y. Sun, Y. Wu, B. Mayers, B. Gates, Y. Yin, F. Kim, H. Yan, One-dimensional nanostrcutures: synthesis, characterization, and applications, Adv. Mater., 15 (2003) 353-389.

[7] V. Kozlovskaya, E. Kharlampieva, B.P. Khanal, P. Manna, E.R. Zubarev, V.V. Tsukruk, Ultrathin layer-by-layer hydrogels with incorporated gold nanorods as pH-sensitive optical materials, Chem. Mater., 20 (2008) 7474-7485.

[8] J. Gao, C.M. Bender, C.J. Murphy, Dependence of the gold nanorod aspect ratio on the nature of the directing surfactant in aqueous solution, Langmuir, 19 (2003) 9065-9070.

[9] B.P. Khanal, E.R. Zubarev, Purification of high aspect ratio gold nanorods: complete removal of platelets, J Am Chem Soc, 130 (2008) 12634-12635.

[10] S.O. Obare, N.R. Jana, C.J. Murphy, Preparation of polystyrene- and silica-coated gold nanorods and their use as templates for the synthesis of hollow nanotubes, Nano Lett, 1 (2001) 601-603.

[11] Z. Wu, J. Liang, X. Ji, W. Yang, Preparation of uniform Au@SiO_2 particles by direct silica coating on citrate-capped Au nanoparticles, Colloids and surfaces A: physicochemical and engineering aspects, 392 (2011) 220-224.

[12] S.-S. Chang, C.-W. Shih, C.-D. Chen, W.-C. Lai, C.R.C. Wang, The shape transition of gold nanorods, Langmuir, 15 (1999) 701-709.